School of Electrical Engineering, Computing and
Mathematical Sciences

Curtin Institute of Radio Astronomy

Targeted searches for prompt radio transients using the Murchison Widefield Array

Jun Tian

This thesis is presented for the Degree of
Doctor of Philosophy
of
Curtin University of Technology

August 2022

To the best of my knowledge and belief this thesis contains no material previously published by any other person except where due acknowledgement has been made. This thesis contains no material which has been accepted for the award of any other degree or diploma in any university.

Jun Tian

"I have been one acquainted with the night. I have walked out in rain—and back in rain. I have outwalked the furthest city light."

— Robert Frost

Acknowledgements

This unforgettable PhD journey is full of challenges and exciting moments. I could not have made it without the encouragement and support of many people.

First and foremost, I would like to thank my supervisors Gemma E. Anderson, Paul Hancock and James Miller-Jones for guiding me through this PhD research. I could not have been luckier having such a wonderful group of supervisors, who have spent tremendous amounts of time and efforts supporting me and keeping me moving in the right direction. I will forever be indebted to you for providing me with invaluable skills and knowledge, encouraging me when I felt frustrated, and shaping me into a better researcher. Thank you for your constant support and patience.

I would also like to thank Marcin Sokolowski, Antonia Rowlinson, Ramesh Bhat, Andrew Williams, Natasha Hurley-Walker, John Morgan, Clancy James and Bradley Meyers for scientific discussions. I really enjoyed working with you, and appreciate your generosity in sharing your experience and expertise with me. All of your kind suggestions and support are invaluable in the progress of this project.

My sincere thanks also goes to my CIRA internal review panel, Randall Wayth, John Morgan and Jess Broderick. You always checked that I felt comfortable with the progress of my project, and provided constructive suggestions that helped evolve my project. I would also like to thank the CIRA administration team, Tina Salisbury, Angela Dunleavy, Emily Johnson, Chamila Thrum and Ali Smith for your constant support during my PhD project.

I made so many friends at CIRA, Steve Raj Prabhu, Kariuki Chege, Torrance Hodgson, Mike Kriele, Jaiverdhan Chauhan, Stefan Duchesne, Pikky Atri, Ronniy Joseph and Jishnu Nambissan Thekkeppatu. We played games together, had parties together, going out for lunch together, and travel for fun together. These are all sweet memories that I will file away somewhere in my mind. I would also like to extend my thanks to the new PhD students, Susmita Sett, Aishwarya Selvaraj and Gayatri Aniruddha. Although we became friends near the end of my PhD, you added lots of fun to this journey.

Finally, I would like to thank my mom and dad. You are always supporting me no matter what kind of life I want to pursue and what place I am going to travel to. Thank you mom for your taking care of me and enduring my naughtiness always. To my dad, you always encourage me to go my own way. Without your constant support, I could not have come so far.

Statement of contribution

Apart from the specific chapters/publications detailed below the remainder of the thesis is all my own work with supervision and advice provided by my supervisory panel - G. E. Anderson, P. J. Hancock and J. C. A. Miller-Jones.

The published paper titled "Early-time Searches for Coherent Radio Emission from Short GRBs with the Murchison Widefield Array" (Tian et al., 2022a, Chapter 3) is my own work except the following. A. Rowlinson fitted the parameters of magnetars to the X-ray light curves of GRB 190627A and GRB 191004A, and provided the code for plotting the model emission. M. Sokolowski provided the code for performing dedispersion with MWA images and simulations. Discussions on the data reduction and implications of the results were contributed by my supervisory panel - G. E. Anderson, P. J. Hancock and J. C. A. Miller-Jones. All Co-authors provided feedback during preparation of the manuscript.

The published paper titled "High time resolution search for prompt radio emission from the long GRB 210419A with the Murchison Widefield Array" (Tian et al., 2022b, Chapter 4) is my own work except the following. M. Sokolowski provided the code of offline correlation for creating visibilities from voltage data. B. W. Meyers provided the code of simulations of MWA tiles. N. Hurley-Walker helped with improving the quality of the MWA image. N. A. Swainston helped in making the strategy for the dispersed pulse search. Discussions on the data reduction and implications of the results were contributed by my supervisory panel - G. E. Anderson, P. J. Hancock and J. C. A. Miller-Jones. All Co-authors provided feedback during preparation of the manuscript.

The published paper titled "A targeted search for repeating fast radio bursts with the MWA" (Tian et al., 2023, Chapter 5) is my own work except the following. The archival VCS data of the SMART survey were provided by N. D. R. Bhat. B. W. Meyers provided the code of simulations of MWA tiles. N. A. Swainston helped in making the strategy for the dispersed pulse search. Discussions on the data reduction and implications of the results were contributed by my supervisory panel - G. E. Anderson, P. J. Hancock and J. C. A. Miller-Jones. All Co-authors provided feedback during preparation of the manuscript.

(Signature of Candidate)

(Signature of Supervisor)

Abstract

This thesis presents our targeted searches for prompt radio transients from gamma-ray bursts (GRBs) and repeating fast radio bursts (FRBs) using the Murchison Widefield Array (MWA), a low frequency ($< 300\,\mathrm{MHz}$) telescope and precursor to the Square Kilometre Array (SKA). Theory suggests that prompt (FRB-like) signals may be produced by GRBs via binary neutron star mergers or core-collapse supernovae, but this GRB/fast radio transient connection is still poorly explored, particularly given the expected short timescales of the emission. Similarly, while the FRB population has rapidly expanded over the last couple years with more than 700 FRBs published so far, low frequency searches for FRB emission have yielded only very few detections, especially at frequencies below $300\,\mathrm{MHz}$. However, both the coherent radio emission predicted to be produced by GRBs and the low frequency FRB emission are very important as they can provide invaluable information on the equation of state of neutron stars and the FRB emission mechanism. In this PhD research, I used the MWA rapid-response observing mode to automatically and rapidly trigger on GRBs within $30\,\mathrm{s}$ of receiving an alert from *Swift* or *Fermi* in order to capture the model-predicted FRB-like emission. I also used archival MWA observations to search for low frequency FRB signals from known repeating FRBs. The results of these searches place significant constraints on the GRB and FRB emission models.

In the GRB triggering experiment, we have successfully followed up ten GRBs (nine short and one long) with the MWA, the largest sample of GRBs studied at such a low frequency. We started recording the observations with the stan-

dard correlator (imaging mode with a time resolution of 0.5 s), which was later upgraded to the Voltage Capture System (VCS; 100μs time resolution) as VCS data are expected to be much more sensitive to prompt radio emission. The main technique used to search for dispersed signals in this thesis is dedispersion in the image domain or the coherently beamformed VCS data. These are some of the most sensitive attempts using dedispersion to search for GRB associated prompt radio emission, demonstrating one of the best sensitivities achieved to date (~ 100 Jy ms). We tested various coherent emission models in the GRB scenario with the upper limits derived from the MWA observations. Specifically, we found the composition of GRB jets is possibly baryon dominated, advancing our understanding of the GRB jet composition problem. Given the predictions of possible dipole spin-down radiation, we also searched for persistent radio emission from each GRB in an MWA image of the full 30 min integration. Our results pose a serious challenge to the magnetar formation assumption though other possibilities cannot be excluded such as the GRBs being at high redshifts or the radiation beam of the magnetar remnant being pointing away from us.

In the case of low-frequency FRB searches, we used 23.3 hr of archival data taken with the MWA VCS between 2014 September and 2020 May, and performed a standard single pulse search with a temporal and spectral resolution of 400 μs and 10 kHz, respectively, over a broad DM range centred at the known DM of each repeating FRB studied in this thesis. This is the first time that the MWA VCS has been used to search for FRB signals from known repeaters, demonstrating a much better sensitivity (~ 100 Jy ms) than previous FRB searches with the standard MWA correlator mode (~ 1000 Jy ms). The fluence upper limits derived from the VCS data enabled us to study the burst rates, low-frequency spectra and local environments of the repeaters.

Finally, this thesis has highlighted the feasibility of MWA in following up GRBs and repeating FRBs for transient searches. We also explored the prospect of following up gravitational wave events with MWA in the future. In the long

term, these transient experiments are paving the way for even more exciting transient science with the more sensitive SKA.

Contents

List of Figures

xxx

Chapter 1

Introduction

Over the past several decades, we have witnessed an explosive growth of extragalactic transients thanks to various all-sky monitor instruments in space or from the ground. These extragalactic transients are energetic, fast and often cataclysmic events, and span across the electromagnetic spectrum from radio to gamma rays, as well as the neutrino and gravitational-wave windows. Radio detection of transients is important as it can provide valuable information about the Universe, such as the baryonic content of the Universe (Macquart et al., 2020), physics of compact binary mergers (Hallinan et al., 2017), and relativistic jets (Fender et al., 2006). One such radio transient is the mysterious fast radio burst (FRB), which is possibly linked to other transients such as gamma-ray bursts (GRBs; Chu et al. 2016; Rowlinson & Anderson 2019) and gravitational wave events (GWs; Kaplan et al. 2016). However, this interconnection is still poorly explored observationally.

1.1 GRBs

GRBs are intense gamma-ray pulses with durations from less than a second to hundreds of seconds produced by relativistic, highly collimated outflows (also called jets). Unlike other astrophysical objects, they usually have most of their

energy output in gamma-ray photons and concentrated into a short period. While their luminosity is not isotropic, we often assume it is so as the isotropic energy does scale with the true energy output (Piran, 2003). Their isotropic luminosity of $10^{51} - 10^{52}$ erg/sec (Kumar & Piran, 2000) makes them the most luminous celestial objects. After the initial burst of gamma rays subside, less energetic and smoothly varying radiation may be still visible up to years (usually called the afterglow), furnishing a wealth of information for GRB studies (e.g. relativistic jets, central engines).

1.1.1 Early history

GRBs were first discovered serendipitously by the military satellite *Vela* in the late 1960s and were thought to be arising from nuclear testing, though the data was published several years later (Klebesadel et al., 1973; Mazets et al., 1974). There are no ground based gamma-ray detectors, as gamma rays emitted by cosmic sources are mostly absorbed by the Earth's atmosphere. Our understanding of the GRB phenomenon progressed very slowly until the launch of the Compton Gamma-ray Observatory with the onboard Burst and Transient Experiment (BATSE) in 1991 (Meegan et al., 1992). The large number of GRBs detected by BATSE unveiled an isotropic distribution of GRBs on the sky, providing strong evidence for their cosmological origin. More importantly, a phenomenological population division in GRB durations was identified in the BASTE catalog: long ($\gtrsim 2$ s) and short ($\lesssim 2$ s), as shown in Figure 1.1 (Kouveliotou et al., 1993).

The cosmological origin of GRBs was further supported by the first signature of cosmological time dilation (i.e. the stretch of burst profiles in time by an amount proportional to the redshift) detected in an analysis of a sample of BATSE GRBs (Norris et al., 1994). However, it was not until the first measurements of GRB redshifts that the cosmological origin of GRBs was confirmed (Metzger et al., 1997). This breakthrough was brought by the Italian-Dutch satellite Beppo-SAX, which could localise a GRB to a small region (~ 10 arcmin) and
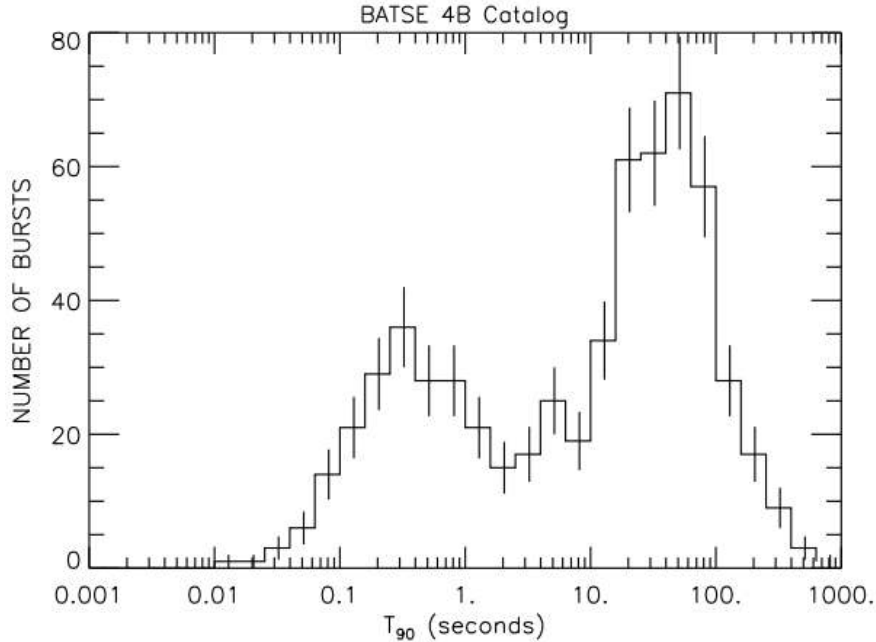
Figure 1.1: The bimodal distribution of durations of BATSE detected GRBs. This figure is adapted from Zhang et al. (2016a).

further pinpoint its X-ray afterglow (if detectable) for optical and radio follow up (Costa et al., 1997; van Paradijs et al., 1997; Frail et al., 1997). The discovery of the optical counterpart to GRB 970508 allowed a spectroscopic analysis of the prominent absorption lines in the spectrum, which suggested the presence of an absorption system in the line of sight at $z = 0.835$ (Metzger et al., 1997). This, coupled with the lack of Lyman-α forest features, constrained the GRB redshift to be $0.835 \leq z \lesssim 2.3$, confirming its cosmological origin. Note that the GRB name follows the convention of YYMMDD. Another optical counterpart discovered from GRB 971214 leads to the identification of a host galaxy at $z = 3.42$ (Kulkarni et al., 1998). Therefore, the long-standing argument on distances of GRBs, i.e. whether GRBs are of Galactic or extragalactic origin, was settled by the identification of optical counterparts.

In 2004, a GRB-dedicated satellite *Swift* was launched by NASA (Gehrels et al., 2004), allowing for arcminute localisation using the Burst Alert Telescope (BAT; operating over an energy range of 15–150 keV with a field of view of 1.4 sr;

Barthelmy et al. 2005a). *Swift* also has two other instruments onboard, X-ray Telescope (XRT; operating over 0.2–10 keV; Burrows et al. 2005) and UV-Optical Telescope (UVOT; operating over 170–600 nm; Roming et al. 2005) that perform automated X-ray and optical follow-up and thus provide arcsecond localisation of the event through detecting the GRB afterglow. This means that we could study the early-time optical and X-ray afterglow, which had been difficult due to the temporal gap between observations of the prompt gamma-ray emission and manually scheduled follow-up observations. *Swift* revolutionalised our understanding of GRB afterglows. Rapid XRT follow-up found that almost all long GRBs have X-ray afterglow detections whereas short GRB X-ray afterglows were fainter and therefore fading more rapidly below its sensitivity. In particular, the XRT light curves revealed that most GRB X-ray afterglows experience a temporal steep-to-shallow transition, i.e. from a bright rapid falling afterglow $\propto t^{-\alpha}$ with $\alpha \gtrsim 3$ to a shallow decay with $\alpha \sim 0.5$ (e.g. O'Brien et al. 2006, Gehrels et al. 2009; see Section 1.1.4). Rapid UVOT follow-up had also revealed unprecedented features in early optical afterglows. The prompt optical emission detected within 100 s of some GRBs was found to be correlated with the prompt gamma-ray emission with a flux density ratio being roughly 1 to 10^5, suggesting their common origin (i.e. internal shocks; Vestrand et al. 2005, 2006; Blake et al. 2005). Additionally, the fast routine response to GRB detections increased the detection rate of optical afterglows to 60% (all observatories combined; Roming et al. 2009), resulting in the measurement of many GRB redshifts (Gehrels & Razzaque, 2013).

In 2008, another gamma-ray satellite *Fermi* was launched. It consists of two instruments: the Gamma-ray Burst Monitor (GBM; Meegan et al. 2009) covering the energy range between 8 keV and 40 MeV and the Large Area Telescope (LAT; Atwood et al. 2009) covering between 20 MeV and 300 GeV. In the pre-*Fermi* era most GRBs were detected in the energy range between 20–1000 keV, with little being known about the behavior of GRBs at higher energies. *Fermi* was launched to explore this domain, i.e. GRB emission above 1 MeV. Unlike *Swift*, *Fermi* is
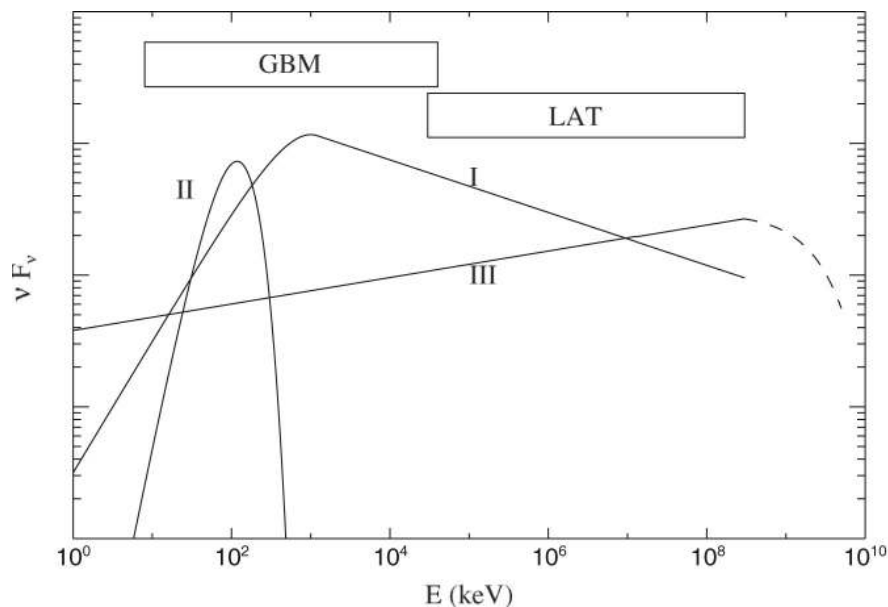
Figure 1.2: The three elemental spectral components that constitute observed spectra of GRBs: a non-thermal Band component (I), a quasi-thermal component (II) and a non-thermal power-law component extending to the LAT band (III). Note that the last component might have a high energy cutoff (Ackermann et al., 2011), as indicated by the dashed line. This figure is adapted from Zhang et al. (2011).

purely a gamma-ray detector, without X-ray or optical follow up for afterglow observations. However, *Fermi* features a much wider field of view (2.4 sr versus 1.4 sr), and thus can detect many more GRBs than *Swift* ($\sim$ 300 compared to $\sim$100 per year; Gehrels & Razzaque 2013) though its localisation capacity is far less accurate ($\sim$degree versus $\sim$arcmin). More importantly, the very high energy photons detected by LAT extended the GRB spectrum up to tens of $\sim$GeV and revealed additional components in the spectrum (Abdo et al., 2009a,b), as shown in Figure 1.2. The LAT detects $\sim$ 10 GRBs per year (Gehrels & Razzaque, 2013), and plausible interpretations for the GeV emission include Synchrotron-Self-Compton scattering (Wang et al., 2009; Bošnjak et al., 2009) and hadronic emission (Razzaque et al., 2010; Asano et al., 2009).

5
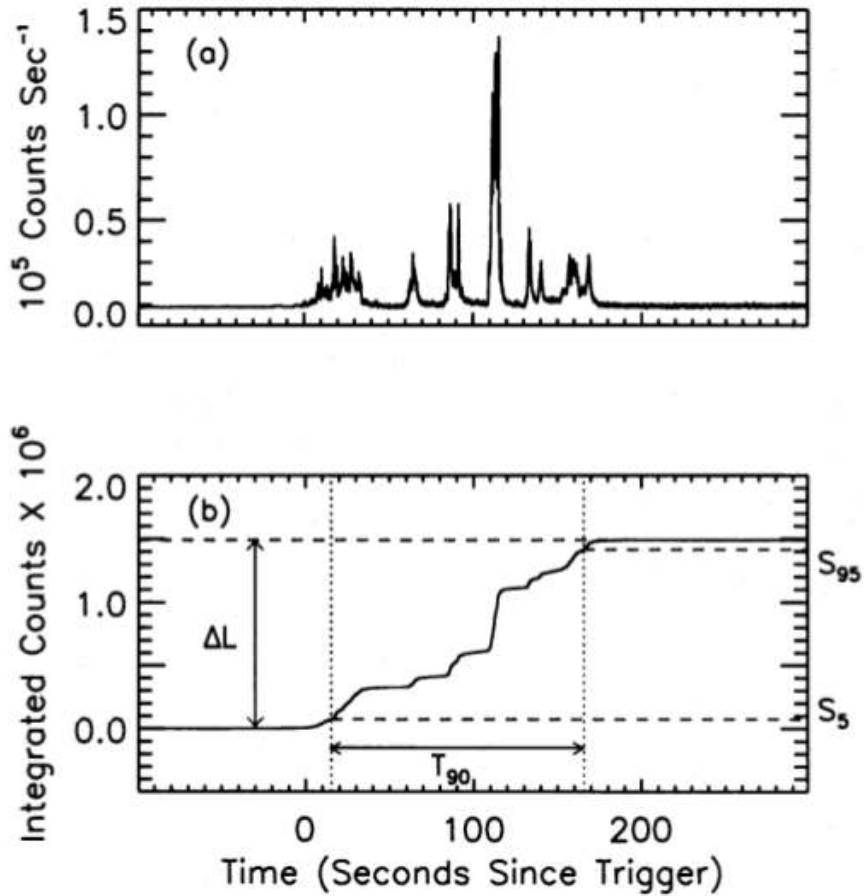
Figure 1.3: Measurement of T_{90} for the prompt gamma-ray emission of burst 3B 940217 with BATSE. The top panel shows the light curve of this burst, and the bottom panel shows the accumulative counts. ΔL represents the total amount of counts observed due to the GRB, and S_5 and S_{95} represent the time when 5% and 95% of the total source counts of the prompt gamma-ray emission have been detected. Therefore, the interval between S_5 and S_{95}, i.e. T_{90}, measures the duration of burst 3B 940217. This figure is adapted from Koshut et al. (1996).

1.1.2 Long and short-duration GRB division

The duration of GRBs is quantified by T_{90}, the duration during which 5% to 95% of the prompt gamma-ray fluence (flux integrated over the duration of the burst) is detected. For an example measurement of T_{90} see Figure 1.3. The value of T_{90} is instrument dependent, depending on the operational energy band and sensitivity of detectors. Detectors that are more sensitive over lower energy bands tend to measure a longer T_{90}. Based on the bimodal distribution of T_{90} in the BATSE band (25–350 keV) as shown in Figure 1.1, GRBs have been classified into a long category and short category with a rough separation at 2 s (Kouveliotou et al., 1993). Later observations with other GRB missions confirmed this bimodal distribution (Sakamoto et al., 2011; Paciesas et al., 2012; Zhang et al., 2012; Lien et al., 2016), though the value of T_{90} separating the two categories varies for different detectors. It is noteworthy that the classification of GRBs based on T_{90} is not clear cut, with some overlap between the long end of the short GRBs and short end of the long GRBs. The bimodal distribution of hardness ratios (HRs) of bursts (i.e. the ratio of total counts in the 100–300 keV and 50–100 keV energy range) adds more evidence to the existence of two populations of GRBs: long-soft and short-hard (Fishman & Meegan, 1995) as shown in Figure 1.4. Although this classification is purely based on phenomenology, broad-band observations spanning X-ray, optical and radio bands link these two types of GRBs to different progenitors: long related to the deaths of massive stars and short to compact binary mergers (Eichler et al. 1989; Paczynski 1991; Narayan et al. 1992; see Section 1.1.3 for more discussion).

1.1.3 GRB progenitors

There is a standard model for GRBs: the "fireball model", invoking internal-external shock scenarios (Rees & Meszaros, 1992; Piran, 1999). A fireball is in essence a large concentration of energy, and can form in an explosion when a large amount of gamma-ray photons are released into a small region. It is supposed
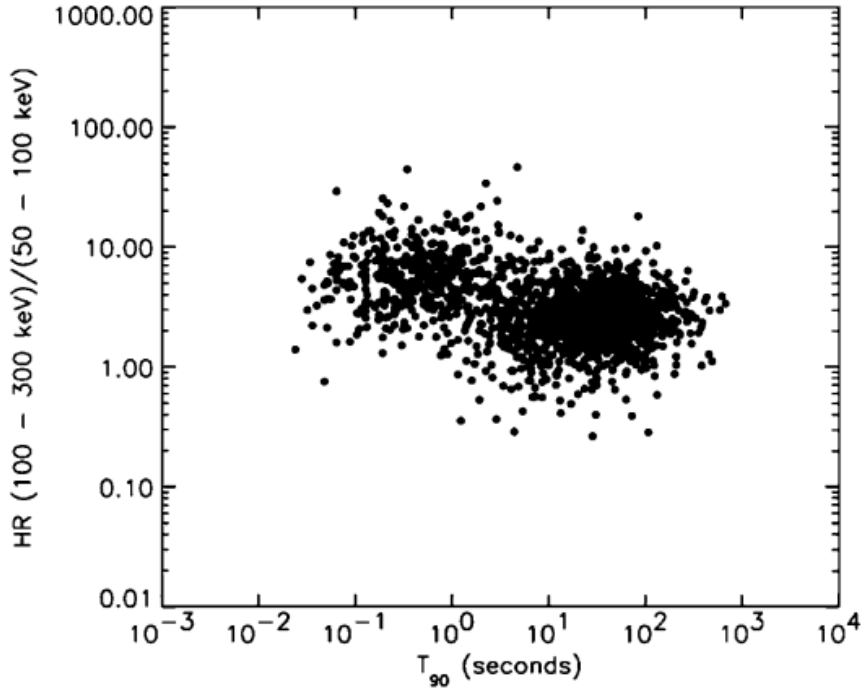
Figure 1.4: The distribution of hardness ratios and durations of BATSE detected GRBs. This figure is adapted from Zhang et al. (2016b).

to be opaque due to the production of electron-positron pairs (for a review see Piran 1999). While the internal shock occurring before the fireball deceleration is responsible for the prompt gamma-ray emission, the external shock at the deceleration radius (i.e. where the relativistic jet launched by the GRB collides with the circumburst medium) can produce the GRB afterglow. Although the process of converting the kinetic energy of relativistic particles into radiation in an optically thin region has been confirmed by various observations, including radio afterglows (Chandra & Frail, 2012; Anderson et al., 2014, 2018a), optical counterparts (Gehrels et al., 2005; Hjorth et al., 2005; Soderberg et al., 2006; Roming et al., 2006; Stratta et al., 2007) and X-ray afterglows (Campana et al., 2006; Falcone et al., 2006; Evans et al., 2009; Margutti et al., 2011; Rowlinson et al., 2013), the central engines are not well understood due to the difficulty in inferring their properties directly from current observations. In this section, I review the different progenitors and central engines of short and long GRBs, and
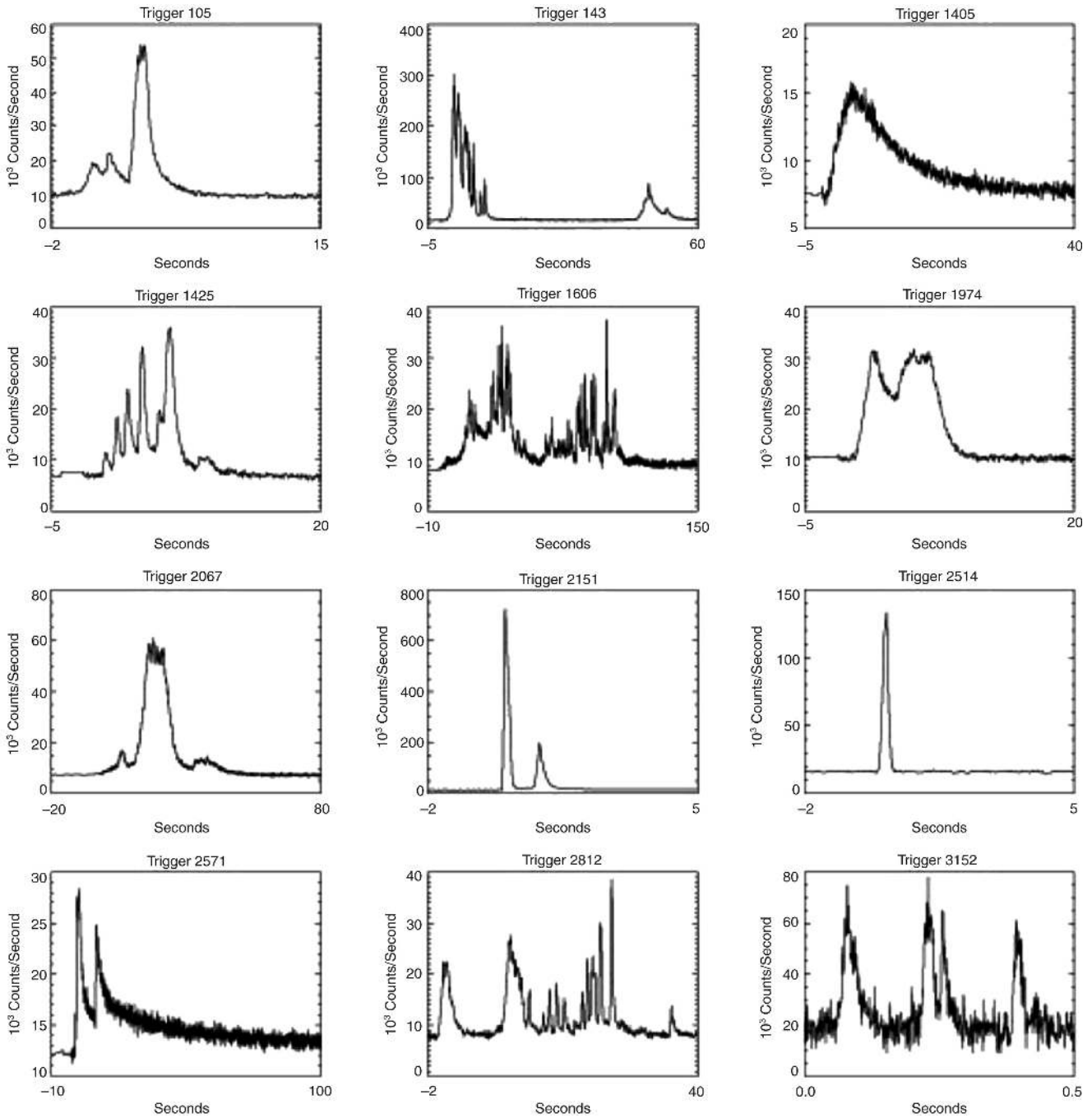
Figure 1.5: Sample light curves of GRBs from the first BATSE catalogue. This figure is adapted from Fishman & Meegan (1995).

their prompt emission mechanism.

1.1.3.1 Long-duration GRBs

Although the classification of long and short GRBs is purely based on phenomenology, there indeed exist two physically distinct types of progenitors: deaths of massive stars related to long GRBs (Hjorth et al., 2003; Cano, 2013; Gehrels et al., 2009) and compact stellar mergers related to short GRBs (Narayan et al., 1992; Nakar, 2007; Eichler et al., 1989; Paczynski, 1991). These connections have been supported by observations of GRB afterglows and identifications of their host galaxies. On the long GRB side, thanks to observations led by BeppoSAX and *Swift*, the host galaxies of most long GRBs were found to be dwarf star-forming galaxies (Galama et al., 1998; Hjorth et al., 2003; Stanek et al., 2003; Campana et al., 2006; Pian et al., 2006; Fruchter et al., 2006), which links long GRBs to the deaths of massive stars (Woosley, 1993). Furthermore, a handful of long GRBs have been firmly associated with spectroscopically identified supernovae of high expansion velocities, such as GRB 980425 (Galama et al., 1998), GRB 030329 (Stanek et al., 2003; Hjorth et al., 2003) and GRB 031203 (Malesani et al., 2004). These associated supernovae, devoid of helium and hydrogen emission, originate from core-collapse massive stars and are thus of the Type Ic (Woosley & Bloom, 2006). With the above considerations, progenitors of long GRBs are most likely to be a rapidly spinning (so a jet can be launched) massive star with relatively low metallicity (required to form a large helium core needed by the collapsar model and diminish the loss of angular momentum) and its hydrogen and helium envelope being stripped (MacFadyen & Woosley, 1999; Smith, 2014).

Given the connection between long GRBs and supernovae, the collapsar model has been proposed to produce the GRB emission (Woosley, 1993). This model predicts the formation of either a black hole or magnetar with a surrounding accretion disk. This central engine provides the necessary energy for the burst

and its late afterglow (see Section 1.1.3.3).

1.1.3.2 Short-duration GRBs

Different from long GRBs, some nearby short GRBs are hosted in elliptical or early type galaxies of minimal star formation, as evidenced by *Swift* observations (Gehrels et al., 2005; Barthelmy et al., 2005b; Berger et al., 2005). Some other short GRBs were localised to star forming galaxies with a large offset from their host galaxies (Fox et al., 2005; Fong et al., 2010). These facts indicate a different progenitor than that of long GRBs, such as neutron star (NS) - black hole (BH) or NS - NS mergers (Eichler et al., 1989; Paczynski, 1991; Narayan et al., 1992). Further evidence for short GRBs being unrelated to supernovae comes from sensitive searches for supernova signatures from nearby short GRBs, which have yielded no detection so far (Kann et al., 2011; Berger, 2014).

The association of short GRBs with compact binary mergers is supported by the identification of kilonova emission from short GRBs (an optical/infrared signal weaker than supernovae; Li & Paczyński 1998). The radioactive elements, produced in a nuclear rich environment provided by merging NSs can produce optical or near infrared excess emission during their decay that lasts longer than the GRB and probably even longer than the afterglow created by the external shocks from the relativistic jet. Note that this optical/infrared emission is far more isotropic than the afterglow. Therefore, short GRBs are expected to have mid to late time re-brightening in their optical/infrared light curves. One example is GRB 130603B (see Figure 1.6; Berger et al. 2013; Tanvir et al. 2013). While its optical afterglow continued to fade away, the decay in infrared was much slower, with a re-brightening consistent with the kilonova model at around 10 days post-burst. Some other short GRBs have also been found to show similar bumps in their light curves (Jin et al., 2015, 2016).

In summary, there are solid evidences that support short GRBs originate from compact binary mergers (for the ultimate confirmation see Section 1.1.4.4, which
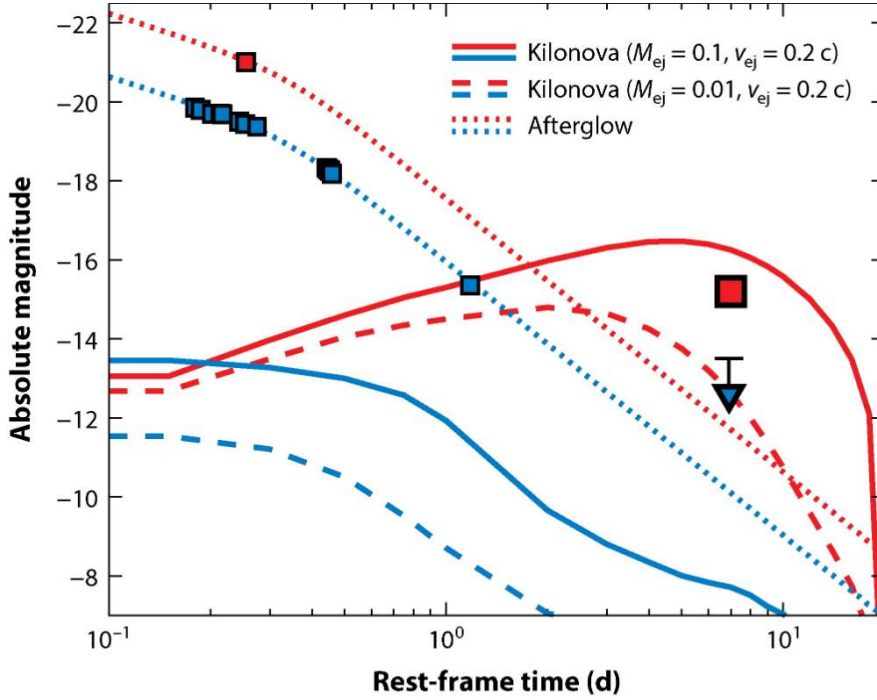
Figure 1.6: An example of kilonova emission from GRB 130603B. The blue and red points represent optical and near-infrared observations of GRB 130603B, respectively. The dotted lines are a fit to the early afterglow evolution. It is clear that there is an excess of near-infrared emission at $\sim 10\,\mathrm{d}$. The solid and dashed lines show the additional emission resulting from an r-process kilonova with two sets of model parameters (the ejecta mass M_{ej} and velocity v_{ej}), respectively, which can account for the excess emission observed in the near-infrared data. This figure is adapted from Berger (2014).

highlights the simultaneous detection of a GRB and GW from a BNS merger). However, it needs to be pointed out that compact binary mergers may not be the only progenitors of short GRBs. Alternative scenarios could include the giant flare from soft gamma-ray repeaters (Palmer et al., 2005) or the collapse of NSs into BHs induced by accretion (Qin et al., 1998; MacFadyen et al., 2005).

1.1.3.3 Central engines

While short and long GRBs differ in their progenitors, their central engines responsible for launching highly energetic and relativistic jets are thought to be of similar nature. Below I introduce the central engine of GRBs without specific reference to short or long GRBs unless a noticeable difference exists.

The GRB central engine is not clearly understood. However, there are several constraints on the properties of the central engine as suggested by observations (Kumar & Zhang, 2015):

1. Capacity to launch extremely luminous (above the Eddington limit) relativistic jets;

2. Limited amount of baryons in the jet (so the energy of individual baryons can be $\gg m_p c^2$), which means outflows can become ultra-relativistic (i.e. Lorentz factors $\Gamma \gtrsim 100$);

3. Intermittent activity of the engine for generating erratic behavior in the GRB light curves;

4. Ability to re-activate as suggested by late-time softer flares (e.g. X-ray flares).

There are two popular candidates of the central engines that satisfy these requirements: a magnetar (i.e. rapidly spinning and highly magnetised NS; Usov 1992; Thompson 1994; Dai & Lu 1998; Kluźniak & Ruderman 1998; Wheeler et al. 2000) or a hyperaccreting BH that is formed via a failed supernova (also called a

hypernova) and surrounded by an accretion disk (Woosley, 1993; Popham et al., 1999; Lee et al., 2000).

The mechanism by which a magnetar powers a GRB has been studied extensively (Bucciantini et al., 2008, 2009; Metzger et al., 2011; Kiuchi et al., 2012; Siegel et al., 2014). Here I give a brief review. There are three phases in the evolution of a new born magnetar. At first, the hot surface of the NS suffers from neutrino-driven mass loss, leading to a baryon-contaminated outflow with a speed insufficient for powering a GRB. About $\sim 10\,\mathrm{s}$ later when the NS cools down, fewer baryons are driven to the outflow, and a Poynting-flux-dominated jet forms. Magnetic instabilities in the jet can dissipate the magnetic energy and power the erratic light curves of a GRB (Kluźniak & Ruderman, 1998; Ruderman et al., 2000). This phase is responsible for the prompt gamma-ray emission phase of a GRB. After this phase, the continuous spindown of the magnetar supplies additional energy that can power X-ray flares (Dai et al., 2006) and plateaus (Rowlinson et al., 2013, 2014).

If a GRB is powered by the spinning down of a magnetar with a period of $P \sim 1\,\mathrm{ms}$ and a surface magnetic field of $B_s \sim 10^{15}\,\mathrm{G}$ (Usov, 1992; Wheeler et al., 2000), the energy output to the GRB should be limited by the total spin energy of the magnetar

$$E_{\mathrm{rot}} \simeq \frac{1}{2} I \Omega^2 \simeq 2 \times 10^{52}\,\mathrm{erg}\,\frac{M}{1.4 M_\odot} R_6^2 P^{-2}, \tag{1.1}$$

where M, R_6 and P are the mass, radius and period of the magnetar, respectively. GRBs with energies exceeding this limit cannot have a magnetar central engine (e.g. Lü & Zhang 2014). In the case of simple dipole radiation from the magnetar, the evolution of the total luminosity with time is given by

$$L(t) = L_0 \frac{1}{(1 + t/t_0)^2} \tag{1.2}$$

where L_0 is the typical spindown luminosity and t_0 is the characteristic spindown

timescale (Usov, 1992).

Another candidate of the central engine of GRBs is an accreting stellar mass BH. In this case, the luminosity of a GRB is given by

$$L_{\mathrm{GRB}} = \zeta \dot{M} c^2 = 1.8 \times 10^{51} \, \mathrm{erg \, s^{-1}} \, \zeta_{-3} \left(\frac{\dot{M}}{1 \, M_\odot \, \mathrm{s^{-1}}} \right), \qquad (1.3)$$

where $\zeta_{-3} = 10^{-3} \zeta$ is the efficiency in transforming the energy released by accreting materials to radiation, and $\dot{M}$ is the accretion rate (0.01–several $M_\odot \, \mathrm{s^{-1}}$ for a typical GRB). Three mechanisms that predict GRB jets to be launched by such hyper-accreting BHs have been proposed: a neutrino-annihilation-driven hot jet along the rotation axis of a neutrino dominated accretion flow (Chen & Beloborodov, 2007), the Blandford–Znajek mechanism (extraction of BH rotational energy electromagnetically via Poynting flux; Blandford & Znajek 1977), or differential accretion within a highly magnetised accretion disk leading to magnetic dissipation (Uzdensky & MacFadyen, 2006). For a review of these mechanisms see, e.g. Zhang & Mészáros (2004), Kumar & Zhang (2015), Berger (2014).

1.1.4 GRB afterglows and association with other transients

In addition to a sudden increase in gamma-ray flux, GRBs have been detected at other wavelengths. These include afterglows in X-ray (Campana et al., 2006; Falcone et al., 2006; Evans et al., 2009; Margutti et al., 2011; Rowlinson et al., 2013), optical (Gehrels et al., 2005; Hjorth et al., 2005; Soderberg et al., 2006; Roming et al., 2006; Stratta et al., 2007) and radio (Frail et al., 1997; Chandra & Frail, 2012; Anderson et al., 2018a; Fong et al., 2015, 2021; Anderson et al., 2021a) bands. More excitingly, a gravitational wave event, GW 170817, has been associated with the short GRB 170817A (Goldstein et al., 2017; Abbott et al., 2017), demonstrating the multimessenger nature of the GRB field. There are also theoretical links between GRBs and FRBs as suggested in Section 1.2. In

this section I review the broad-band afterglows of GRBs and the association with GWs and FRBs. Note that I do not include details relating to optical afterglows as it is not directly related to this thesis.

In the standard internal-external shock (fireball) model, while internal shocks create the prompt gamma-ray emission, external shocks are responsible for the afterglow emission (Rees & Meszaros, 1992; Piran, 1999). Note that in the external shock scenario where a relativistic jet launched by GRBs collides with the ISM, both forward (propagating into the ISM) and reverse (propagating into the relativistic ejecta) shocks can be created, but afterglows are mainly related to forward shocks. It is also common to see jet breaks (achromatic) in GRB afterglow light curves, which is thought to arise from the so-called "edge" effect, i.e. as the relativistic jet decelerates, the observable portion of the jet increases until it becomes comparable to the jet opening angle (Sari et al., 1999; Rhoads, 1999). These theories agree well with GRB afterglow observations, as discussed below.

1.1.4.1 Radio synchrotron afterglow

Radio synchrotron emission (incoherent) has been observed during the ~1–1000 day afterglow phase of long GRBs (Chandra & Frail, 2012; Anderson et al., 2018a) and ~1–10 day afterglow phase of short GRBs (Fong et al., 2015, 2021; Anderson et al., 2021a). This emission likely results from relativistic jet ejecta interacting with the circum-burst media (i.e. external shocks) through forward shocks and/or reverse shocks (Piran, 1999; Sari & Piran, 1999; Kulkarni et al., 1999). These two components of radio afterglows have been detected together for the first time with the Arcminute Mircrokelvin Imager from GRB 130427A, with the reverse shock component dominating the early afterglow (Anderson et al., 2014). There may also be two distinct populations of GRBs: radio bright and radio faint, which differ in their gamma-ray fluences, isotropic energies and X-ray fluxes, suggesting different prompt emission mechanisms, central engines or environments (Hancock et al., 2013). Note that this division applies to both long and short GRBs.
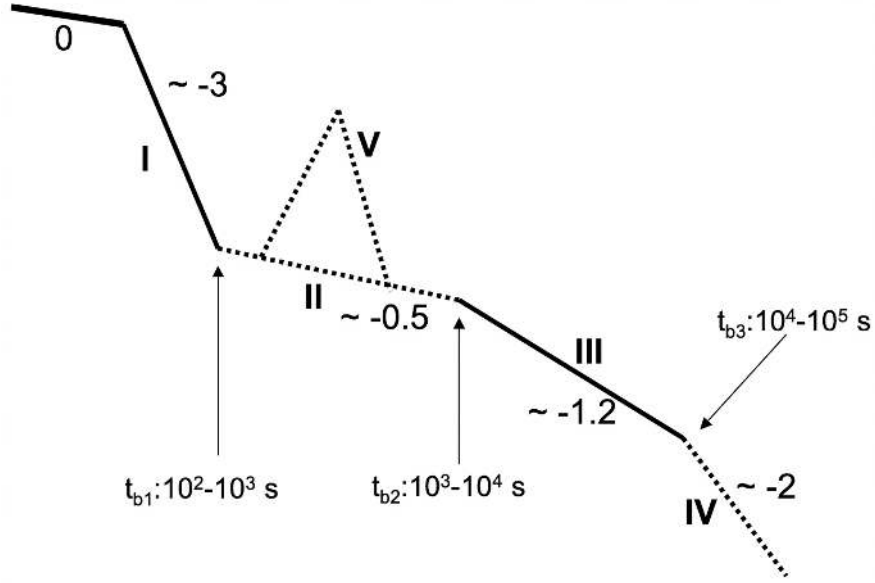
Figure 1.7: A diagrammatic representation of the canonical X-ray light curve of GRB (both long and short) afterglows. The phase 0 represents the prompt emission, and phases I–IV represent four power law light curve segments with different temporal indices and occurrence times as indicated in the figure. Phases I and III are the most common features and are represented by solid lines, while the phase II, which includes a flaring component labelled by V, and phase IV are only observed in a fraction of bursts and marked with dashed lines. This figure is adapted from Zhang et al. (2006).

1.1.4.2 X-ray afterglow

The first X-ray afterglow detection was made by the Beppo-SAX satellite from GRB 970228 (Costa et al., 1997). Since the launch of the *Swift* satellite, a systematic study of X-ray afterglows has been made possible thanks to the rapid and automated follow-up of *Swift* detected GRBs by the *Swift*-XRT. An X-ray analysis of 318 *Swift* GRBs revealed that "canonical" light curves, consisting of a steep decay, a plateau phase and a following standard afterglow phase, can describe a large fraction (42%) of the X-ray light curves (Evans et al., 2009). Other light curves either show only one break (flattening or steepening) or a monotonic decay with a single power law. A diagrammatic representation of the main features of the canonical GRB (both long and short) X-ray light curve is shown in Figure 1.7. The observed features in X-ray afterglows may be summarised as

follows:

I. Steep decay: This X-ray emission is related to the prompt emission phase
(phase 0 in Figure 1.7). The temporal decay slope of this phase is usually
steeper than t^{-3} (Berger et al., 2005; Cusumano et al., 2006). This segment
is considered the tail emission of the prompt gamma-ray emission as it usu-
ally exhibits a smooth transition from the last gamma-ray pulse (Barthelmy
et al., 2005a). There is a strong spectral softening (i.e. smaller hardness
ratio) in the steep decay phase (Zhang et al., 2007; Campana et al., 2006;
Mangano et al., 2007; Butler & Kocevski, 2007; Zhang et al., 2007, 2009).
These features can be attributed to the so-called curvature effect, i.e. pho-
tons emitted from high angular latitude relative to the line of sight travel
longer distances and therefore reach the observer later (Kumar & Piran,
2000; Zhang et al., 2006; Liang et al., 2006).

II. Plateau: This X-ray emission is related to the external shocks. This phase
immediately follows the steep decay, with a slope in the range of t^0 to $t^{-0.5}$,
a typical starting time between 10^2–10^3 s post-burst, a typical duration
of $\sim 10^4$ s and a fluence of $\sim 3 \times 10^{-7}$ erg s^{-1} (Liang et al., 2007). The
spectrum during this phase has a typical photon index of $\Gamma \sim 2.1$ and
shows no sign of spectral evolution (O'Brien et al., 2006; Liang et al., 2007).
This plateau phase suggests continuous energy injection into the blastwave
after the prompt emission phase and can be interpreted within the standard
external shock model (Zhang et al., 2006; Nousek et al., 2006; Zhang et al.,
2011; Yu & Dai, 2007). However, the emergence of "internal plateaus", i.e.
a plateau followed by a very steep decay (slope around t^{-9}), challenges this
interpretation and suggests direct energy dissipation from a long lasting
central engine such as a millisecond magnetar (Troja et al., 2007; Liang
et al., 2007; Lyons et al., 2010; Rowlinson et al., 2010, 2013; Lü & Zhang,
2014; Lü et al., 2015).

III. Normal decay: The normal decay has a typical slope of $\sim t^{-1}$, which agrees with the standard external forward shock model (Mészáros & Rees, 1997; Sari et al., 1998).

IV. Jet break: Some GRBs have one more break after the normal decay phase (Liang et al., 2008; Racusin et al., 2009). The steepening at late times with a slope of $\sim t^{-2}$ can be understood within the jet break (Rhoads, 1999; Sari et al., 1999).

V. X-ray flares: X-ray flares are erratic temporal features superposed on the regular decay of X-ray light curves (e.g. Campana et al. 2006; Falcone et al. 2006; Margutti et al. 2011), and could be explained by the late internal shock model (Meegan et al., 2009). They usually occur from 10^2 to 10^5 s after the prompt emission, with a fluence usually lower than that of the prompt gamma-ray emission and a temporal behavior similar to the gamma-ray pulses (e.g. Chincarini et al. 2007, 2010; Falcone et al. 2007). Thanks to the short slew time of the *Swift* X-ray Telescope (XRT; Burrows et al. 2005), X-ray flares following the prompt gamma-ray emission are commonly observed among *Swift*–BAT triggered GRBs (48%; Swenson & Roming 2014). They indicate the reactivation of GRB central engines (e.g. magnetars) at later times (Burrows et al., 2005; Fan & Wei, 2005; Zhang et al., 2006; Lazzati & Perna, 2007).

The X-ray light curve of GRBs is therefore made up of components from the internal (prompt) emission phase and the external shocks. However, in a large subset of light curves there is evidence of ongoing energy injection (possibly via a magnetar). Understanding the emission mechanisms may hold clues to understanding a subsample of FRBs that could be related to the prompt emission phase and the remnant phase (see the discussion below).

1.1.4.3 Coherent radio emission models for GRBs and potential links with FRBs

Apart from the standard radio afterglows extensively detected and studied, there is another type of radio emission yet to be detected. Here I review the different hypothesised coherent emission mechanisms in the context of binary NS mergers thought to be the progenitors of short GRBs (e.g. Usov & Katz 2000; Totani 2013; Lyutikov 2013; Zhang 2014). I will also discuss which of these models are relevant for prompt radio signal creation in long GRBs.

Depending on the progenitor masses of short GRBs and their equation of state, there are four possible outcomes of merger events: prompt formation of a BH, a hypermassive NS that collapses on timescale of $\sim$ 1s, a supermassive NS surviving 10-10000s, or a stable NS (for a review see Chu et al. 2016). If a NS is produced by the merger, it would have an extremely strong magnetic field powering its high-energy emission. Throughout this thesis, I will refer to this NS remnant as a magnetar. The prompt radio emission could be generated during the inspiral and merger phase or after the formation of a magnetar, and thus could occur within a few seconds after the binary merger. To catch this hypothesised signal, generating GRB alerts without delay and following up rapidly with radio telescopes are most important.

The flux density of radio emission has been predicted by various coherent emission models (see Figure 1.8 for an illustration), and can be compared with the sensitivity of radio telescopes (see figure 9 from Rowlinson & Anderson 2019). There are at least four different mechanisms that have been proposed that could potentially generate radio emission as marked by a,b,c,d in Figure 1.8:

(a) The earliest emission may come from the inspiral of NSs, where interactions of NS magnetic fields just preceding the merger may generate a coherent radio pulse (Lipunov & Panchenko, 1996; Metzger & Zivancev, 2016).

(b) During merger a relativistic jet is launched and interacts with the inter-
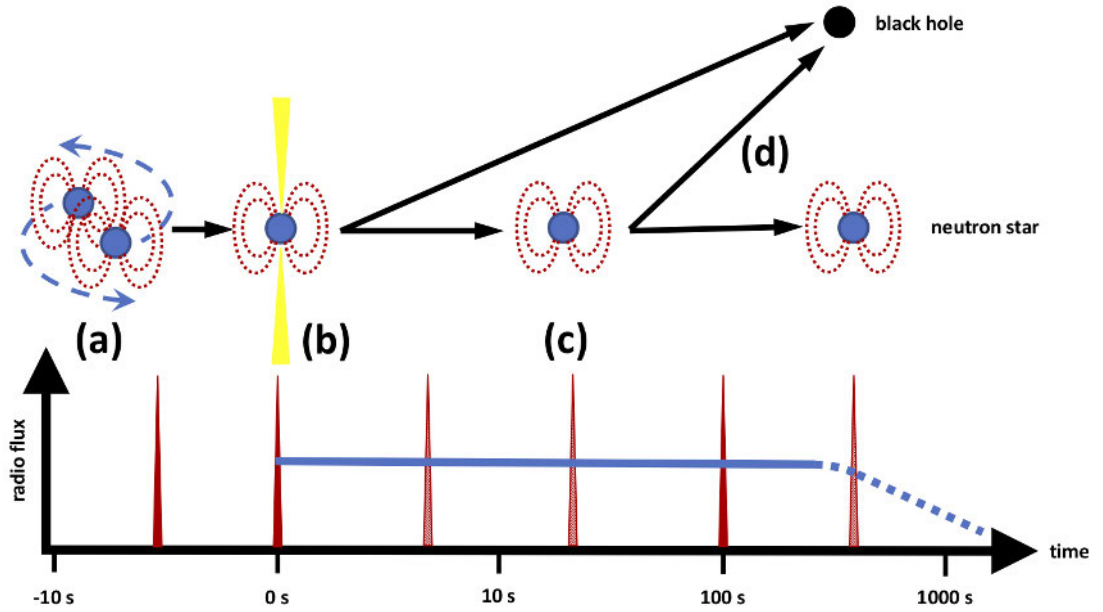
Figure 1.8: Timescales of various coherent emission models (Rowlinson & Anderson, 2019). The red spikes in the light curve represent ∼ ms coherent radio pulses while blue line represents persistent emission (pulsar-like). This figure is adapted from Rowlinson & Anderson (2019).

stellar medium that could produce a coherent radio burst (Usov & Katz, 2000).

(c) If the merger remnant is a magnetar, the coherent radio emission could potentially be powered by dipole magnetic braking and repeat during the lifetime of the magnetar (Totani, 2013; Metzger et al., 2017). If the beam of the magnetar points towards the Earth, persistent radio emission could be detected by us.

(d) At last, if the magnetar cannot support its high mass due to spinning down, a final radio flash may be generated via the release of magnetic energy of the magnetar in its collapse to a BH (Zhang, 2014).

The coherent radio emission mechanism remains a puzzle. Several models, including coherent curvature emission by bunches (Ruderman & Sutherland, 1975; Falcke & Rezzolla, 2014), the synchrotron/cyclotron maser (Lyubarsky, 2014; Be-

loborodov, 2017) and collisionless Bremsstrahlung in turbulent plasma (Romero et al., 2016), have been proposed to explain the extreme brightness temperature of FRBs (see Section 1.2.5.2), which are expected to have similar properties to the prompt radio signals predicted to be generated from BNS mergers. Although all of these models have their own problems, it is likely that NSs could provide the necessary conditions for coherence (Melrose, 2017). Note that BH-NS mergers are not discussed here because several of the emission models are not relevant, including the magnetosphere interaction (which is not possible with just one NS), and the magnetar collapse model as we expect the BH-NS to directly collapse to a BH upon merger.

Many of the above mechanisms may also apply to long GRBs, particularly the GRB jet-ISM interaction and the magnetar (stable or unstable) formation (Usov & Katz, 2000; Bernardini et al., 2012; Totani, 2013; Zhang, 2014). However, such signals, if indeed generated, are less likely to be detected from long GRBs due to their dense surrounding environments preventing the transmission of coherent radiation emitted below the plasma frequency (Zhang, 2014). Nonetheless, it is possible that instances of lower ISM densities and different viewing angles may allow the signal to transmit. Additionally, as the surrounding ISM takes time to react, a single coherent pulse may be able to propagate out from the engine (Lyubarsky, 2008).

1.1.4.4 Association with GW events

Gravitational waves (GWs) are disturbances in spacetime resulting from the most violent and energetic events in the Universe such as compact binary mergers and supernovae. The first GW signal was detected by LIGO from a binary BH merger on September 14, 2015 (Abbott et al., 2016a). It is consistent with the waveform predicted by general relativity for the inspiral and merger of two BHs with masses of 36^{+5}_{-4} and 29^{+4}_{-4} solar masses and a BH remnant of 62^{+4}_{-4} solar masses. Since then more GW signals have been detected with most originating from binary BH

mergers (Abbott et al., 2016b, 2019) and two from BNS mergers (Abbott et al., 2017, 2020a). As the GW detectors have been continually upgraded for better sensitivity, we expect more GW detections in the future (for a review see Abbott et al. 2020b).

Short GRBs are usually considered to be associated with GW events, as they share the same compact binary origin. This has been supported by indirect observational evidence such as kilonova observations (Tanvir et al., 2013) and further confirmed by the near simultaneous detection of GRB 170817A and GW170817 (Goldstein et al. 2017; Abbott et al. 2017; Abbott et al. 2017; see Section 1.1.3). This association was reaffirmed by the later report of a transient optical source in the host galaxy (Coulter et al., 2017) and the ultraviolet transient by *Swift* (Evans et al., 2017), which suggests the kilonova scenario. Recently, continued observations of GW170817 spanning the radio frequency range 0.6-18GHz and lasting 107 days post-merger have revealed a solid climb of the radio light curve and a spectrum explicable in terms of optically-thin synchrotron emission (Mooley et al., 2018c). While the early-time radio observations support the conjecture of a choked jet resulting in a wide-angle outflow moving towards the Earth, the later very long-baseline interferometric observations instead suggest the probable advent of a narrowly collimated and energetic jet about 20 degrees away from the line of sight (Mooley et al., 2018a).

The observations in almost every electromagnetic band since the detection of GW170817 have yielded a huge amount of information on the merger physics including GRB mechanisms (Mooley et al., 2018b; Nakar et al., 2018) and the NS equation of state (Abbott et al., 2018; Raithel et al., 2018), and have ignited a new campaign for joint electromagnetic and gravitational-wave observations. Among the electromagnetic counterparts associated with GW170817 is the theorized prompt radio emission from which we can probe the magnetic configuration during the coalescence, estimate the distance from the DM, and help localise the event. However, observing prompt emission is made difficult by poor locali-

sations provided by GW detectors and announcements of GW candidates more than minutes after the arrival (James et al., 2019). The large field of view of radio telescopes such as the Murchison Widefield Array (MWA; Tingay et al. 2013; Wayth et al. 2018) and automatic triggering system (see Section 1.3) alleviate though do not eliminate these issues, and make it promising to detect any prompt radio emission from BNS mergers.

1.1.4.5 Association with FRBs

The prompt, coherent signals predicted to be produced by GRBs may be similar to fast radio bursts (FRBs) with millisecond durations (Chu et al., 2016; Rowlinson & Anderson, 2019). Currently there is compelling observational evidence that links both repeating and non-repeating FRBs to magnetar engines (CHIME/FRB Collaboration et al., 2020; Bochenek et al., 2020; The CHIME/FRB Collaboration et al., 2021a). Given GRBs could be the progenitors of magnetars, it is natural to make a connection between GRBs and FRBs (e.g. Gourdji et al. 2020). Therefore, detections of FRB-like emission associated with GRBs would support that such events can produce magnetar remnants, and indicate whether these signals may make up a subset of the FRB population.

However, whether the event rate of FRBs is consistent with short GRBs and/or BNS mergers is still under debate (Thornton et al., 2013; Totani, 2013). A certain fraction of the whole FRB population is suggested to be merger associated (Zhang, 2020a). Searching for FRBs temporally and spatially coincident with GRB candidates can further test such an association (DeLaunay et al., 2016). While DeLaunay et al. (2016) claimed an association detection of FRB 131104 and a transient gamma-ray counterpart, an arcsecond localisation of the FRB source is really needed for a confident association. More details on FRBs are introduced in Section 1.2.

1.1.5 Targeted searches for coherent radio emission from GRBs

As described in Section 1.1.4.3, coherent radio emission (either prompt or persistent) has been predicted for GRBs. This emission could provide valuable information on the composition of the GRB jet and the equation of state of NSs (Ravi & Lasky, 2014; Lasky et al., 2014). Moreover, the detection of prompt radio emission would shed light on the origin of some FRBs (see Section 1.1.4.5). Therefore, searching for coherent radio emission from GRBs is well motivated scientifically.

There have been many searches for prompt radio emission associated with GRBs but so far none have yielded a detection. One of the earliest searches was at 151 MHz between 1970 and 1973 but no signals were observed over a sensitivity limit $\sim 10^5$ Jy from GRBs detected by the *Vela* satellites (Baird et al., 1975). Later observations have also showed no prompt radio emission from GRBs (see Dessenne et al. 1996, Obenberger et al. 2014, Bannister et al. 2012, Palaniswamy et al. 2014 and Kaplan et al. 2015). Recently, Anderson et al. (2018b) performed a low-frequency search (below 100 MHz) using the Owens Valley Radio Observatory Long Wavelength Array (OVRO-LWA), which, as an all-sky instrument, continuously monitored all GRBs. They performed an image de-dispersion analysis and found no simultaneous radio emission associated with short GRB 170112A above 4.5 Jy on 13 s timescales. Another telescope, the LOw Frequency ARray (LOFAR; van Haarlem et al. 2013), was used to trigger rapid-response observations on *Swift* GRB 180706A (long) and GRB 181123B (short), resulting in deep limits of 1.7 mJy and 153 mJy, respectively over a 2 hr timescale on associated coherent, persistent radio emission from a magnetar remnant (Rowlinson et al., 2019, 2020). In addition, the NS merger origin has also been investigated from the FRB context, where the properties of two non-repeating FRBs and their host environments were used to constrain merger models, make electromagnetic light curve predictions, and were searched for evidence of temporally coincident,

sub-threshold gamma-ray counterparts (Gourdji et al., 2020).

The MWA (see Section 1.3) has been used to perform triggered observations of GRBs since 2015 (e.g. Kaplan et al. 2015). The first triggered MWA observation on a short GRB was performed by Kaplan et al. (2015), and yielded an upper limit of 3 Jy on 4 s timescales. Anderson et al. (2021b) reported the first short GRB trigger with the upgraded MWA triggering system, and performed a search for dispersed signals using images with a temporal and spectral resolution of 0.5 s/1.28 MHz, obtaining a fluence upper-limit range from 570 Jy ms at a dispersion measure (DM) of 3000 pc cm^{-3} ($z \sim 2.5$) to 1750 Jy ms at a DM of 200 pc cm^{-3} ($z \sim 0.1$), corresponding to the known redshift range of short GRBs (Rowlinson et al., 2013). Note that although DeLaunay et al. (2016) claimed a detection of a transient gamma-ray counterpart to FRB 131104, I caution against this association given its low confidence (3.4σ).

There are several possible reasons for the non-detections in these previous efforts. While all-sky instruments can continuously monitor for GRB occurrences, they usually have lower sensitivity. The more sensitive pointed observations are prone to miss the earliest signal because they often take a few minutes to slew/re-point and begin observing the event. Moreover most previous searches have focused on the more common long GRBs. Although long GRBs have some of the same expected mechanisms to short GRBs for producing coherent radio emission (e.g. the impact of the gamma-ray jets into the ISM and the formation of a magnetar; Usov & Katz 2000, Evans et al. 2009), such signals may not penetrate through the dense medium surrounding core-collapse supernovae (Zhang, 2014) and would therefore be difficult to detect.

1.2 FRBs

There is another type of transients, FRBs, which have a much shorter history than GRBs. Nonetheless, it can teach us important physics. As coherent signals from mostly extragalactic origins, FRBs are expected to be dispersed by the

medium in the Universe. That means FRBs can be used to probe the density of the intergalactic medium and the density profiles of galaxy halos (Macquart et al., 2020).

Also FRBs could potentially be linked to GRBs. Both transient events are potentially associated with compact objects such as magnetars. Moreover, there are several theories that predict the production of prompt radio emission (FRB-like) by GRBs (see Section 1.1.4.3) though observational evidence is still missing. Therefore, some of the GRB models could potentially be applied to FRB studies. In this section, I provide a brief overview of the current status of the FRB field including both observations and theories.

1.2.1 Brief history

One of the earliest searches for extragalactic radio pulses can trace back to Phinney & Taylor (1979). They performed the first sensitive high-time-resolution search for millisecond pulsed signals associated with distant supernovae and primordial BHs using the Arecibo telescope, and detected no signals over a fluence sensitivity of $3\,\mathrm{Jy\,ms}$. However, it was not until several decades later that FRBs were first discovered in radio pulsar surveys (Lorimer et al., 2007). The single pulse (known as the "Lorimer burst"; Figure 1.9) was so bright (peak flux density $> 30\,\mathrm{Jy}$) that it saturated the detector. Several theories were proposed for explaining the Lorimer burst, including a giant pulse from radio pulsars (short duration pulses with a high peak luminosity; Hankins et al. 2003), a rotating radio transient (a subset of radio pulsars that can be discovered by single pulse search; McLaughlin et al. 2006) or even a artificial signal from terrestrial sources (Burke-Spolaor et al., 2011). However, the large dispersion measure (DM) of the "Lorimer" burst (DM $\sim 375\,\mathrm{pc\,cm^{-3}}$) could not be contributed by the electron content of the Milky Way between the burst and the Earth (about $30\,\mathrm{pc\,cm^{-3}}$), ruling out the above conjectures and suggesting an extragalactic origin. This discovery implied that there should exist more radio pulses of extragalactic origin
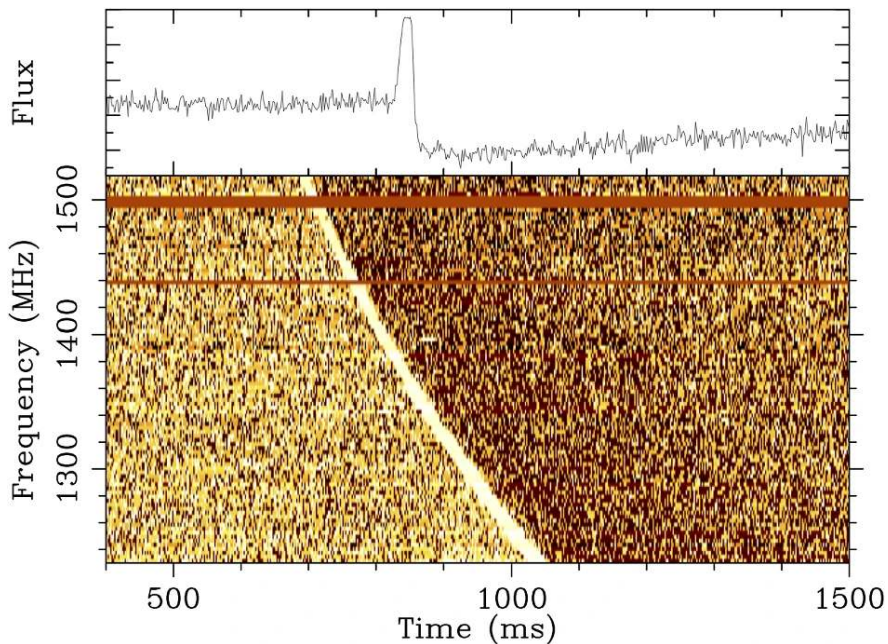
Figure 1.9: The Lorimer burst as seen in the beam of the Parkes receiver. The top panel shows the pulse profile summed over all frequency channels. The bottom panel shows the burst as a function of time and frequency (i.e. dynamic spectrum). The horizontal red lines are frequency channels flagged due to RFI corruption. There is a time/frequency sweep in the dynamic spectrum, suggesting the signal was dispersed by a total DM of $\sim 375\,\mathrm{pc\,cm^{-3}}$. The bright pulse saturated the detector, resulting in a drop in flux after the pulse occurred. This figure is adapted from Lorimer et al. 2007.

(Thornton et al., 2013).

In the early days of FRB discoveries, a peculiar class of artificial signals were mistaken for FRBs (also called "Perytons"). These "Perytons" (discovered only at Parkes) showed the similar dispersive sweep of a real astrophysical signal, but can be pinpointed to a local origin through multi-beam coincidence (Burke-Spolaor et al., 2011). Because of the occurrence of these false signals, some astronomers once suspected all FRBs were artificial in origin. Later investigation into a large sample of "Perytons" revealed they resulted from microwave ovens being opened while still in operation at the site (Petroff et al., 2015), which put the controversy of the Peryton phenomenon to rest and allowed further studies of the real astrophysical FRBs.

A few years later, a transient source similar to the Lorimer burst was discov-

ered by Keane et al. (2011). However, given the sightline of this event in the Galactic plane, it was considered to have a Galactic origin like Rotating Radio Transients (RRATs; Bannister & Madsen 2014). A milestone in FRB discoveries was made by Thornton et al. 2013, who discovered four pulses in the High Time Resolution Universe survey using Parkes. Like the Lorimer burst, these bursts have a large dispersive delay and thus an extragalactic origin. Since then the interest in FRB searches has increased substantially. In addition to searches with Parkes (through archival or new data; Burke-Spolaor & Bannister 2014; Ravi et al. 2015; Champion et al. 2016), there are also searches with other telescopes such as the Arecibo Observatory (Spitler et al., 2014), the Green Bank Telescope (Masui et al., 2015), the Upgraded Molonglo Synthesis Telescope (UT-MOST; Caleb et al. 2016), the Australian Square Kilometer Array Pathfinder (ASKAP; Bannister et al. 2017; Shannon et al. 2018), the Canadian Hydrogen Intensity Mapping Experiment (CHIME; CHIME/FRB Collaboration et al. 2018, 2019b,c,a, 2020; Fonseca et al. 2020a; Amiri et al. 2021), and the Low-Frequency Array (LOFAR; Pleunis et al. 2021b).

The first FRB discovered by a telescope other than Parkes is FRB 121102 (Spitler et al., 2014). It was discovered by the Arecibo telescope in the Galactic anticenter ($l = -0.2°$, $b = 175°$) with a DM value of $557\,\text{cm}^{-3}\,\text{pc}$. More excitingly, this is the first FRB that was observed to repeat (Spitler et al., 2016), resulting in the proposal of two different FRB source classes, repeating and non-repeating FRBs. The discovery of repeat bursts from FRB 121102 also led to the very first FRB localisation to $\sim 100\,\text{mas}$ precision using radio interferometers, which enabled the identification of FRB 121102's host galaxy and confirmed conclusively its extragalactic nature (Chatterjee et al., 2017; Marcote et al., 2017). Since then, more repeating FRBs have been discovered, one with ASKAP (Kumar et al., 2019) and dozens with CHIME (CHIME/FRB Collaboration et al., 2019b,c; Fonseca et al., 2020b; Amiri et al., 2021). This phenomenologically divides bursts into two empirical FRB populations, though it is still under debate whether all

29

FRBs are actually repeating.

Most recently, an FRB-like signal has been detected from the Galactic magnetar SGR 1935+2154 (CHIME/FRB Collaboration et al., 2020; Bochenek et al., 2020), which is the first detection of such bursts in our own galaxy. This burst, with an intrinsic luminosity comparable to the faintest known bursts from extragalactic FRBs, bridges the gap in luminosity between Galactic radio pulse emitters and extragalactic FRBs. This discovery provides an important clue on the origin of FRBs, i.e. FRBs could arise from magnetars (for FRB models see Section 1.2.5).

1.2.2 Observed properties

1.2.2.1 Localisations

Localisations of FRBs can reach (sub-)arcsecond precision thanks to long baseline interferometers (see Section 2.2), which allow the identification of host galaxies associated with FRBs at ∼Gpc distances (e.g. Vedantham et al. 2016; Eftekhari et al. 2018). Currently, around two dozen FRBs have been localised to a wide range of host galaxies at redshifts between $z = 0.03$–0.66 and with a stellar mass of 10^8–$10^{10}\,\mathrm{M_\odot}$ and a star formation rate of 0.05–$10\,\mathrm{M_\odot\,yr^{-1}}$ (e.g. Chatterjee et al. 2017; Bannister et al. 2019; Ravi et al. 2019; Law et al. 2020; Marcote et al. 2020; Heintz et al. 2020). While the diversity of FRB host galaxies makes it difficult to infer the progenitor channels of these mysterious sources, the redshift measurements for localised FRBs can be used for deriving FRB energetics (see below).

1.2.2.2 Energetics

The isotropic equivalent source luminosity of an FRB can be expressed as

$$L = \frac{4\pi\,d_{\mathrm{L}}^2\,S_\nu\,\Delta\nu}{1+z},$$
(1.4)

where d_{L} is the luminosity distance of the source, S_ν is the differential flux per unit logarithmic frequency interval, and $\Delta\nu$ is the bandwidth over which an FRB is observed[1] (so $S_\nu \, \Delta\nu$ is the total flux of a source with a flat spectrum; Hogg 1999). The (1+z) factor accounts for the redshifting of frequencies between the frame of the source and the observer. The isotropic-equivalent spectral luminosity (i.e. $L/\Delta\nu$) of FRBs spans more than six orders of magnitude from $\sim 10^{28}\,\mathrm{erg\,s^{-1}\,Hz^{-1}}$ to $\sim 10^{34}\,\mathrm{erg\,s^{-1}\,Hz^{-1}}$ (Nimmo et al., 2022), as shown in Figure 1.10. This luminosity range is only slightly higher than observed from the nano-shots of the Crab pulsar and the radio bursts of the Galactic magnetar SGR 1935+2154, suggesting in terms of energetics that extragalactic FRBs could be produced by young pulsars or magnetars (CHIME/FRB Collaboration et al., 2020; Bochenek et al., 2020).

1.2.2.3 Brightness temperature

The radiation brightness temperature is commonly quoted to characterise the emission nature of radio sources such as pulsars. The brightness temperature of a radio source is defined as the effective blackbody temperature releasing the same luminosity as the radio source. Following arguments commonly used in pulsar astronomy, the brightness temperature is given by

$$T_{\mathrm{B}} \simeq 10^{36} \left(\frac{S_{\mathrm{peak}}}{\mathrm{Jy}}\right) \left(\frac{\nu}{\mathrm{GHz}}\right)^{-2} \left(\frac{W}{\mathrm{ms}}\right)^{-2} \left(\frac{d_{\mathrm{L}}}{\mathrm{Gpc}}\right)^{2} \mathrm{K}, \qquad (1.5)$$

where S_{peak} is the peak luminosity of the radio emission, ν is the observing frequency, and W is the pulse width (often measured at 50% and 10% of the peak; Lorimer & Kramer 2012). As can be seen from Figure 1.10, the brightness temperature of FRBs spans from $\sim 10^{32}\,\mathrm{K}$ to $\sim 10^{40}\,\mathrm{K}$, much larger than $T_{\mathrm{B}} \sim 10^{24}\,\mathrm{K}$ for a Galactic pulsar (e.g. Cordes & Chatterjee 2019). This strongly supports the coherent nature of FRB emission (see Section 1.2.5.2) as $T_{\mathrm{B}} \sim 10^{12}\,\mathrm{K}$ is the maxi-

---

[1]Actual FRBs are often not broadband, and assuming so can lead to damaging conclusions in more in-depth analyses (e.g. Aggarwal 2021).
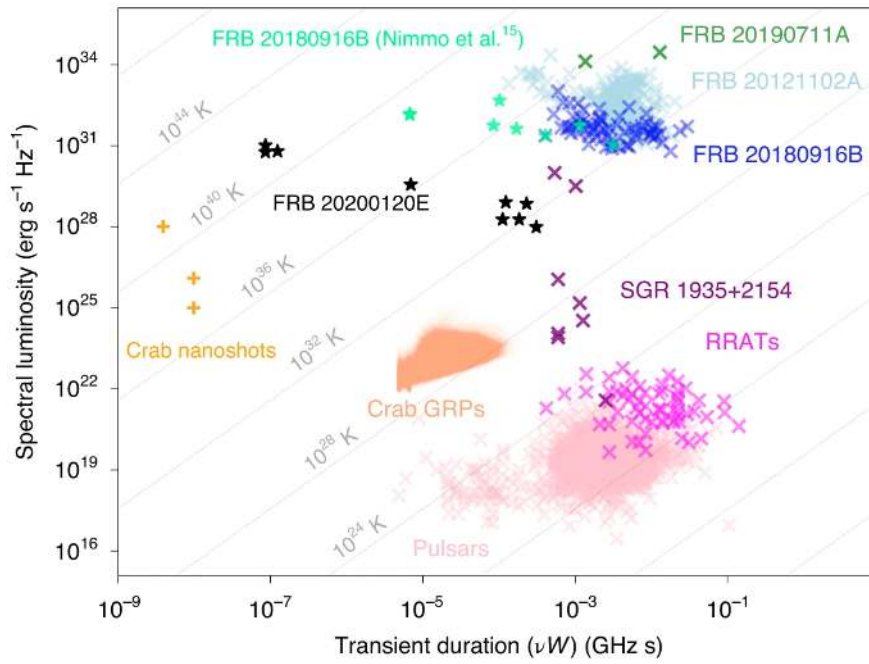
Figure 1.10: Energetics and duration of different coherent radio transients. The x-axis is the transient duration W multiplied by the observing frequency ν, and the y-axis is the isotropic-equivalent spectral luminosity. Different transients are marked by stars or crosses in different colors, and the labels are in the same colors as the marks. The grey lines indicate different brightness temperatures. This figure is adapted from Nimmo et al. 2022.

mum temperature incoherent radiation can achieve (Kellermann & Pauliny-Toth, 1969).

1.2.2.4 Spectral properties

FRBs have been detected at frequencies between 110 MHz and 8 GHz (mainly through targeted observations of repeating FRBs; Gajjar et al. 2018; Michilli et al. 2018; Majid et al. 2020; Pilia et al. 2020; Chawla et al. 2020; Pastor-Marazuela et al. 2021; Pleunis et al. 2021b), and some of them may be detectable even at lower frequencies (< 100 MHz) as suggested by Pleunis et al. (2021b). However, FRB emission is found to have narrow-band nature (Gourdji et al., 2019), and repeaters are even narrower in bandwidth than non-repeaters (Pleunis et al. 2021a; also see Section 1.2.4 for the differences between repeating and non-repeating FRBs). Observations of the repeating FRB 20190711A with the Parkes Ultra-Wideband Low receiver of an instantaneous frequency coverage between 0.7–4 GHz discovered a burst with a spectral extent of only 65 MHz (Kumar et al., 2021a). Other multi-band observations of repeating FRBs show similar behavior (Chawla et al., 2020; Majid et al., 2020; Pearlman et al., 2020; Pastor-Marazuela et al., 2021; Pleunis et al., 2021b).

The narrow-band nature of FRBs makes it difficult to characterise their spectrum, which is fundamental for studying the emission mechanism. However, it is possible to combine the detected emission from different FRBs to construct an average broadband spectrum (Macquart et al., 2019; Bhattacharyya et al., 2021). The average spectral index of FRB emission has been determined to be $-1.5^{+0.2}_{-0.3}$ from the summed power of 23 ASKAP FRB sources (Macquart et al., 2019) and $-1.53^{+0.29}_{-0.19}$ by a simulation on a sample of 82 FRBs detected by Parkes, ASKAP, CHIME and UTMOST (Bhattacharyya et al., 2021). These values agree with the spectral index derived for millisecond and slow pulsars (typically between -1.4 and -1.6; Bates et al. 2013; Jankowski et al. 2018), which might imply a similarity between the FRB emission mechanism and the pulsar emission mechanism (see

Section 1.2.5 for more discussion).

1.2.2.5 Sky rate

Thanks to the large number of FRBs discovered recently by CHIME (Amiri et al., 2021), a detailed analysis of the FRB sky rate is possible. As shown in Amiri et al. (2021), the FRB sky rate can be expressed as a power-law function of frequency ν and fluence F as below:

$$R = R_0 \times \left(\frac{\nu}{600\,\text{MHz}}\right)^{-\alpha\beta} \times \left(\frac{F}{5\,\text{Jy ms}}\right)^{\beta-1} \text{sky}^{-1}\,\text{day}^{-1}, \qquad (1.6)$$

where α is the average spectral index (see the section above), $\beta = -1.40 \pm 0.11^{+0.06}_{-0.09}$ is the power-law index parameterizing the fluence distribution, and $R_0 = 820 \pm 60^{+220}_{-200}\,\text{sky}^{-1}\,\text{day}^{-1}$ is the sky rate of FRBs with a fluence $> 5\,\text{Jy ms}$ and a scattering time $< 10\,\text{ms}$ at 600 MHz. This estimation is consistent with the rate reported from the Green Bank North Celestial Cap survey in the 300–400 MHz band ($3.4^{+15.4}_{-3.3} \times 10^3\,\text{sky}^{-1}\,\text{day}^{-1}$ with a fluence $\gtrsim 2\,\text{Jy ms}$; Parent et al. 2020).

1.2.2.6 Burst rate of repeating FRBs

Repeating FRBs usually exhibit highly variable burst rates, depending on their episodic bursting behavior. For example, FRB 201124A has been observed to emit 48 bursts within three hours (Marthi et al., 2021), while its rate prior to discovery is as low as $< 3.4\,\text{day}^{-1}$ (Lanman et al., 2021). However, there is tentative evidence for periodic activity from two repeaters, FRB 20121102A with a period of 161 ± 5 days (Rajwade et al., 2020b; Cruces et al., 2021) and 20180916B with a period of 16.35 ± 0.15 days (Chime/Frb Collaboration et al., 2020). This might reflect an orbital (Ioka & Zhang, 2020), rotational (Beniamini et al., 2020) or precessional (Levin et al., 2020) period.

There also seems to be an increasing trend of burst rates towards lower frequencies (Pearlman et al., 2020). This has been investigated in detail for FRB 20180916B. Assuming Poisson statistics for the bursts of FRB 20180916B, Pearl-

man et al. (2020) demonstrates the burst rate around the peak activity window of FRB 20180916B at 1.5 GHz, 2.3 GHz and 8.4 GHz is $1.2^{+2.8}_{-1.8}\,\text{hr}^{-1}$, $0.3^{+1.0}_{-0.6}\,\text{hr}^{-1}$ and $0.006^{+0.038}_{-0.023}\,\text{hr}^{-1}$, respectively. Note that the burst rate depends not only on frequency and the statistical spectral index, but also on the fluence detection threshold and instantaneous spectral index [2]. This trend suggests that there could be more bursts at low frequencies ($< 300\,\text{MHz}$). Note that extrinsic effects such as propagation effects (see the section below) and increased sky temperature may affect the detectability of low-frequency FRB emission.

1.2.3 Propagation effects

FRBs, as extragalactic events, travel through large volumes of intergalactic and interstellar media before reaching us. Several propagation effects therefore influence the observed properties of FRBs, and allow us to place constraints on their distance and probe the intergalactic medium and the density of galactic halos and hosts (Macquart et al., 2020). Here, I review a few of these effects that are of most importance to FRB observations.

1.2.3.1 Dispersion

Dispersion is due to the velocity difference among frequencies when electromagnetic waves travel through the intervening plasma between the emitter and the Earth. The space is made dielectric by inter-galactic and -stellar electrons. The time delay of a signal with respect to infinite frequency is quantified by the dispersion measure (DM) as

$$\tau = \frac{\text{DM}}{241.0\,\nu^2_{\text{GHz}}}\,\text{s}, \tag{1.7}$$

where ν_{GHz} is the observing frequency in GHz (Taylor et al., 1993). The DM of

---

[2]The statistical spectral index portrays the spectrum of the overall burst rate, and is different from the instantaneous spectral index which describes the differential energy distribution of individual bursts.

an FRB can be measured from the dispersive sweep in the dynamic spectrum (see Figure 1.9). Following the convention in FRB astronomy, DM is in units of $\mathrm{pc\,cm^{-3}}$. For a typical $\mathrm{DM} \sim 500\,\mathrm{pc\,cm^{-3}}$ (e.g. FRB 140514; Petroff et al. 2014), the dispersion delay at an observing frequency of $100\,\mathrm{MHz}$ and $1\,\mathrm{GHz}$ is $\sim 200\,\mathrm{s}$ and $\sim 2\,\mathrm{s}$, respectively, demonstrating that lower frequency components arrive later than higher frequency components.

The dispersion measure of FRBs can be used to study the medium in the Universe (e.g. Macquart et al. 2020) as the DM value depends on the content of electrons along the line of sight

$$\mathrm{DM} = \int_0^d n_{\mathrm{e}}(l)\,dl, \tag{1.8}$$

where n_{e} is the electron number density as a function of the path length l, and d is the distance to the source.

The observed DM of an FRB can be decomposed into three components

$$\mathrm{DM_{obs}}(z) = \mathrm{DM_{MW}} + \mathrm{DM_{IGM}}(z) + \frac{\mathrm{DM_{Host}}}{1+z}, \tag{1.9}$$

where $\mathrm{DM_{MW}}$ is the Galactic contribution along the FRB direction, which can be estimated by the electron density model NE2001 (Cordes & Lazio, 2002) or YMW16 (Yao et al., 2017), $\mathrm{DM_{IGM}}$ is contributed by the intergalactic medium (IGM), and $\mathrm{DM_{Host}}$ is by the host galaxy. The factor $(1+z)$ takes into account time dilation for a cosmological source. $\mathrm{DM_{IGM}}$ is dependent on cosmic baryons in the path between the source and the Earth. Assuming a homogeneous distribution for all baryons and a constant ionization fraction (Deng & Zhang, 2014), we can estimate the value of $\mathrm{DM_{IGM}}$ using $\mathrm{DM_{IGM}} \sim 1200z\,\mathrm{pc\,cm^{-3}}$ (Ioka, 2003; Inoue, 2004; Lorimer et al., 2007; Karastergiou et al., 2015; Yang & Zhang, 2016). However, recently there has been an estimation of the relation between $\mathrm{DM_{IGM}}$ and z using eight (sub-)arcsecond localised FRBs (Macquart et al., 2020), as shown in Figure 1.11. $\mathrm{DM_{Host}}$ is difficult to measure as it depends on the local
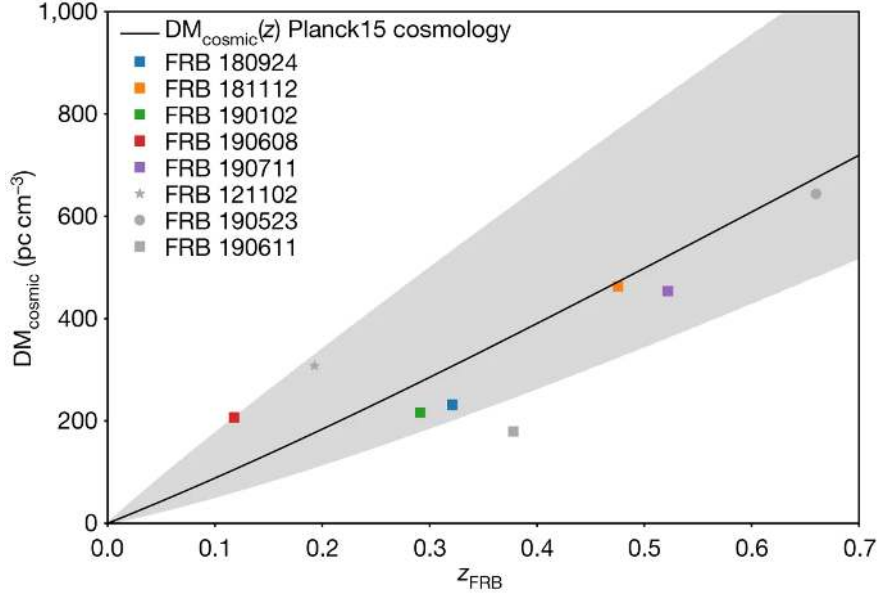
Figure 1.11: Relation between intergalactic (cosmic) DMs and redshifts of eight (sub-)arcsecond localised FRBs (data points). The solid line represents the expected relation between DM_{cosmic} and z assuming the Plank15 cosmology, with the shaded region encompassing 90% of the expected DM_{cosmic} value. This figure is adapted from Macquart et al. (2020).

environment of FRBs and the relative position in the host galaxy. However, with the knowledge of DM_{MW} and DM_{IGM} and the measured DM of an FRB, we can infer DM_{Host} using Eq. 1.9.

1.2.3.2 Scattering

Scattering of FRBs is due to density variations and turbulence in the plasma along the line of sight. It causes multi-path propagation of radio waves and pulse broadening proportional to $\sim \nu^{-4}$ (Bhat et al., 2004). Scattering has been observed for many FRBs (CHIME/FRB Collaboration et al., 2019b; Fonseca et al., 2020b; Amiri et al., 2021). Usually the scattering feature of FRBs can be identified as an exponential decay in the pulse profile and fit by an exponential function (McKinnon, 2014) except when the FRB has a complex pulse structure (e.g. Day et al. 2020). A clear example is the temporal scattering in FRB 110220 (Thornton et al., 2013; Petroff et al., 2019), as shown in Figure 1.12. The one-sided expo-
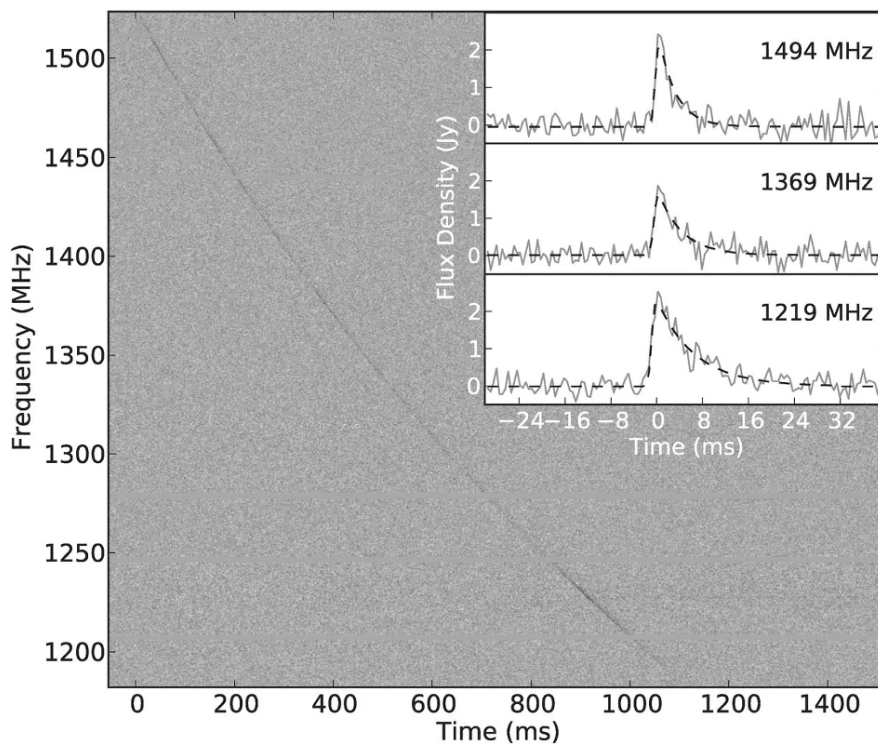
Figure 1.12: Example of scattering in FRB 110220. The main panel shows the dynamic spectrum of the burst, and the inset shows the frequency resolved pulse profiles. There is a trend of more asymmetrical broadening in the pulse towards lower frequencies, which can be well explained by the scattering effect. This figure is adapted from Thornton et al. (2013).

nential decay in the pulse profile increases towards lower frequencies as $\nu^{-4.0\pm0.4}$ (Thornton et al., 2013), consistent with the predicted frequency dependence (Bhat et al., 2004).

Scattering with a timescale larger than the intrinsic burst width reduces the burst amplitude (fluence is conserved) and thus the detectability of FRBs. This is particularly true in low-frequency searches for FRBs. If an FRB has a scattering timescale of 10 ms at 600 MHz (Amiri et al., 2021), we would expect it to increase to > 160 ms at an observing frequency below 300 MHz. This means more sensitive telescopes are needed to detect these signals as they get smeared at lower frequencies. Note that other factors such as free-free absorption (see below) also plays a prominent role in the detectability of the signal at low radio frequencies.

1.2.3.3 Free-free absorption

Free-free absorption is caused by the absorption of incoming radio waves by free electrons. The amount of free-free absorption of radio emission is determined by the density n_e and temperature T of the free electrons along the line of sight as well as the observational radio frequency ν. The opacity of a radio source due to free-free absorption in the source environment can be expressed as the optical depth (e.g. Condon & Ransom 2016)

$$\tau \equiv \ln \frac{E_0}{E_{\text{obs}}} \approx 3.28 \times 10^{-7} \left(\frac{T}{10^4 \text{K}} \right)^{-1.35} \left(\frac{\nu}{\text{GHz}} \right)^{-2.1} \left(\frac{\text{EM}}{\text{pc cm}^{-6}} \right), \qquad (1.10)$$

where E_0 is the amount of energy emitted by the source, E_{obs} is the observed amount after free-free absorption, and EM is the emission measure defined by the integral of n_e^2 along the line of sight:

$$\frac{\text{EM}}{\text{pc cm}^{-6}} = \int \left(\frac{n_e}{\text{cm}^{-3}} \right)^2 d \left(\frac{l}{\text{pc}} \right). \qquad (1.11)$$

If FRBs are produced in dense environments such as active star forming re-

gions and supernova remnants (e.g. FRB 121102 and FRB 20201124A, Bassa et al. 2017; Piro et al. 2021), free-free absorption may affect the detectability of the FRB emission at low frequencies ($< 1\,\mathrm{GHz}$) as the opacity of free-free absorption scales with frequency as $\nu^{-2.1}$. Therefore, free-free absorption may explain the shortage of FRB detections at low frequencies though the intrinsic spectra of FRBs and scattering induced temporal broadening are also limiting factors (Sokolowski et al., 2018). Conversely, any detections of low-frequency FRB emission would provide important probes of the source environments.

1.2.4 Repeater and non-repeater population properties

There is an empirical difference dividing of FRBs: repeaters (Spitler et al., 2016) and non-repeaters (Petroff et al., 2015; Shannon et al., 2018), and their progenitors and/or emission mechanisms could potentially be different (CHIME/FRB Collaboration et al., 2019b; Fonseca et al., 2020b). The existence of two populations of FRBs is further supported by recent studies using a large sample of CHIME FRBs (Amiri et al., 2021; Pleunis et al., 2021a). While the intrinsic burst widths and bandwidths of repeating FRBs are found to differ significantly from the non-repeating population, the sky distributions, DM and scattering distributions and signal strengths of these two populations are quite similar.

Currently, there are 24 sources known to repeat (Spitler et al., 2016; CHIME/FRB Collaboration et al., 2019b,c; Kumar et al., 2019; Fonseca et al., 2020b; Amiri et al., 2021), and there is tentative evidence for periodic activity from two of them, FRB 20121102A (Rajwade et al., 2020b) and 20180916B (Chime/Frb Collaboration et al., 2020). Note that the periodicity here refers to long-term and periodic episodes of increased burst rates, and is distinct from sub-second periodicity observed among sub-pulses within a single burst (The CHIME/FRB Collaboration et al., 2021b). FRB 20180916B, first discovered by CHIME (CHIME/FRB Collaboration et al., 2019c), is the best characterised repeating FRB. Its burst rate was found to vary with a period of $16.35 \pm 0.15\,\mathrm{days}$ (Chime/Frb Collaboration
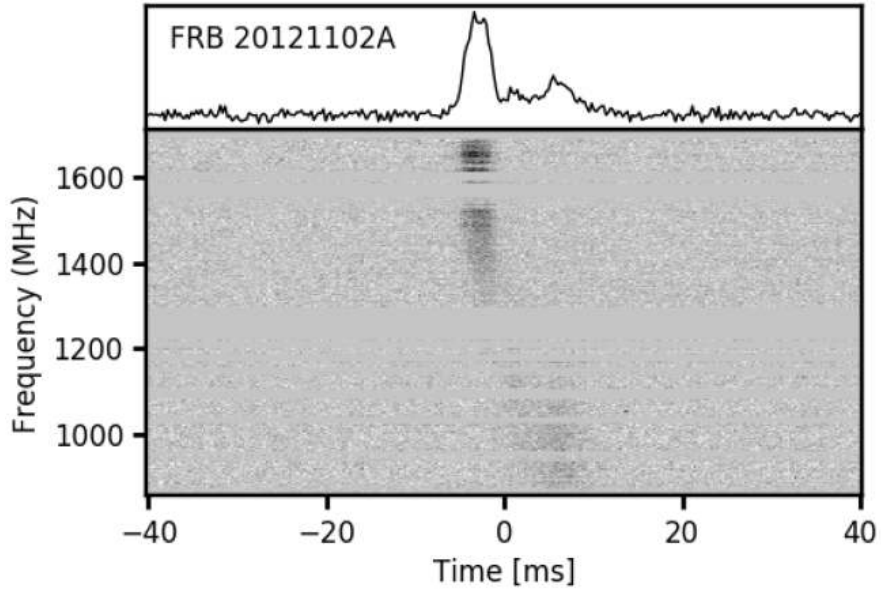
Figure 1.13: The dynamic spectrum of one burst detected by MeerKAT from the repeating FRB 121102A. The top panel shows the integrated burst profile in arbitrary units. The sub-bursts can be seen drifting downward in radio frequency with time (i.e. the "sad trombone" effect; Hessels et al. 2019). This figure is adapted from Caleb & Keane 2021.

et al., 2020). Similarly, FRB 20121102A was found to have a ~ 160 day burst rate variance period (Rajwade et al., 2020b; Cruces et al., 2021). This periodic activity might indicate an orbital (Ioka & Zhang, 2020), rotational (Beniamini et al., 2020) or precession (Levin et al., 2020) period.

Repeating and non-repeating FRBs often show different features in their burst properties. For example, on average, repeating FRBs are likely to have longer burst durations than non-repeating FRBs (Scholz et al., 2016; CHIME/FRB Collaboration et al., 2019c; Fonseca et al., 2020b). The downward drifting of sub-pulses in frequency with time, i.e. the "sad trombone" effect as shown in Figure 1.13, appears to be a common feature among repeating FRBs (Hessels et al., 2019; CHIME/FRB Collaboration et al., 2019a). While some repeating FRBs share flat polarisation position angles within and between bursts, such as FRB 20121102A and FRB 20180916B (Michilli et al., 2018; Nimmo et al., 2021), the bursts of FRB 180301 show a diversity of polarisation position angle swings (Luo

et al., 2020). In-depth polarimetric and spectrotemporal studies of more FRBs are needed to confirm and explain these features.

1.2.5 FRB models

1.2.5.1 FRB engine

There is a diversity of progenitor theories proposed as source models of FRBs, which until the CHIME catalogue was released was even more than the number of detected FRBs (Petroff et al., 2019). These models include exploding BHs (Barrau et al., 2014), superconducting cosmic strings (Yu et al., 2014; Thompson, 2017a,b), technosignatures from extraterrestrial intelligences (Lingam & Loeb, 2017), magnetic reconnection in magnetars induced by axion quark nuggets (Van Waerbeke & Zhitnitsky, 2019), NS - white dwarf binaries (Gu et al., 2016), binary NS mergers (Yamasaki et al., 2018), white dwarf - BH mergers (Li et al., 2018), and collapse of a supermassive rotating NS to a BH (Falcke & Rezzolla, 2014) among others. Detailed reviews of these theories can be found in Katz (2016) and Popov et al. (2018). Here I focus on theories involving magnetars, which have been a plausible candidate for FRB engines since the early days of FRBs, with additional encouragement through the detection of FRB-like signals from the magnetar SGR 1935+2154 (CHIME/FRB Collaboration et al., 2020; Bochenek et al., 2020).

The association of FRBs with magnetars can be made from a simple dimensional argument. The characteristic length scale of FRB engines may be defined as

$$l_{\mathrm{eng}} \lesssim cw, \tag{1.12}$$

where c is the speed of light, and w is the observed pulse duration[3]. For a typical FRB duration of milliseconds, we expect $l_{\mathrm{eng}} \lesssim 10^7 \, \mathrm{cm}$. NSs are fa-

---

[3]This is an argument based on causality, but it is not a hard limit.

vored over BHs due to their strong magnetic fields and large rotational energies, both of which can provide enough energy for FRB emission (for FRB energetics see Section 1.2.2.2). Additionally, NSs, well-known emitters of coherent radio emission (though the underlying emission mechanism remains unknown; see Section 1.2.5.2) can naturally account for similar characteristics observed between FRB and pulsar emission, such as high brightness temperature, a variety of linear and circular polarisation fractions, pulse widths and structures, and spectra.

Despite the previously noted strengths of the magnetar model, there is a challenge to the magnetar model. Up until very recently, the radio luminosity seen from known Galactic magnetars were many orders of magnitude lower than that required for FRBs (see Figure 1.10). This vast luminosity gap between magnetars and FRBs has been substantially narrowed by the recent discovery of unusually bright FRB-like emission from the Galactic magnetar SGR 1935+2154 (CHIME/FRB Collaboration et al., 2020; Bochenek et al., 2020). The radio burst detected from the magnetar SGR 1935+2154 with a burst energy at 400–800 MHz of approximately 3×10^{34} erg is more than three orders of magnitude more energetic than the brightest magnetar radio bursts previously seen (Olausen & Kaspi, 2014; Esposito et al., 2020), and could satisfy the energy budget for the two nearest FRBs, FRB 181030 (CHIME/FRB Collaboration et al., 2019c) and FRB 141113 (Patel et al., 2018). It should be noted that distant FRBs can be much more energetic (e.g. FRB 180110 with a burst energy of 10^{42}–10^{43} erg; Pol et al. 2019; Shannon et al. 2018), and whether magnetars could generate such energetic events is still unclear.

1.2.5.2 Radiation mechanisms

As magnetars (either existing or newly created) are at least one of the likely progenitors of FRBs as discussed above, in this section I specifically consider FRB emission mechanisms in the context of magnetars. Generally speaking, there are two types of FRB emission mechanisms depending on the emission site

with respect to the magnetar: in the magnetosphere (i.e. pulsar-like) or in the relativistic jet powered by the magnetar (i.e. GRB-like). Here I briefly review these two types of models. More details can be found in Zhang (2020b).

Pulsar-like models are promising for addressing the high brightness temperature observed in FRBs through, e.g. plasma maser effects. One such model suggests that magnetic reconnection in the magnetosphere (possibly induced by magnetic pulses propagating away from the magnetar) can generate radio waves compatible with FRB observations (Lyubarsky, 2020). Another model relies on the assumption that a collection of charged particles can radiate in-phase due to their clustering in momentum and position spaces. However, in such models, it remains unclear how the bunched particles can be maintained in coherence over the observed timescale of FRBs (Melrose, 1978). Plasma lensing, induced by plasma structures in the host galaxy of FRBs, is also a possible explanation for the high apparent luminosity of FRBs given the lens amplification can be as large as ~ 100 as observed in pulsars (Cordes et al., 2017). It could also explain the strongly episodic burst detections and highly variable spectra observed in repeating FRBs. Nonetheless, more FRB observations, especially those of ultra wide band that can cover FRBs from ~ 0.1–$10\,\mathrm{GHz}$, are needed to test these ideas.

In GRB-like models, FRBs are suggested to be produced via synchrotron maser emission in relativistic jets, which has been explored in depth in GRB models (Usov & Katz, 2000; Sagiv & Waxman, 2002). A realistic version of the synchrotron maser model invokes either a weakly magnetised plasma where negative absorption could happen within a narrow frequency range (Waxman, 2017) or a highly magnetised jet containing ordered magnetic fields that allow energetic electrons to emit in phase (Plotnikov & Sironi, 2019). During the outward propagation of shocks in media with a density decreasing with distance from the magnetar, the maser frequency is expected to decrease with time. This could account for the frequency downwards drifting in some repeating FRBs

(CHIME/FRB Collaboration et al., 2019a,c; Hessels et al., 2019). However, the highly ordered magnetic field required by such models seems contrived (Plotnikov & Sironi, 2019). Therefore, while a variety of models have been proposed, the radiation mechanism of FRBs is still a question needing further research. A comparison of the pulsar-like and GRB-like models can be found in Zhang (2020b).

1.2.6 FRB searches at low frequencies

Since the first discovery in 2007, the FRB field has been one of the most active research areas in astronomy, with the FRB population expanding at an incredible rate, and our understanding of their origins and mechanisms rapidly evolving. FRBs (both repeating and non-repeating) have been detected at frequencies from 300 MHz (Chawla et al., 2020; Pilia et al., 2020; Parent et al., 2020) up to 8 GHz (Gajjar et al., 2018). However, while FRB searches at low frequencies (< 300 MHz) are ongoing (Coenen et al., 2014; Karastergiou et al., 2015; Tingay et al., 2015; Rowlinson et al., 2016; Law et al., 2017; Sokolowski et al., 2018; Sanidas et al., 2019; Houben et al., 2019; Sokolowski et al., 2021), the only detection has been of the repeating FRB 20180916B, where Pleunis et al. (2021b) reported the detection of 18 bursts between 110–188 MHz with LOFAR. This confirms the existence and the detectability of low-frequency FRB emission from cosmological distances (not limited by propagation effects or the FRB emission mechanism).

The MWA has been previously employed to search for FRBs in the image domain (Tingay et al., 2015; Rowlinson et al., 2016; Sokolowski et al., 2018), which is constrained to a balance between survey speed and sensitivity. Tingay et al. (2015) performed a pilot search for FRBs in the frequency range between 139–170 MHz using 10.5 hr of observations recorded in the imaging mode with a spectral and temporal resolution of 1.28 MHz and 2 s over a sky area of $400 \deg^2$, and found no FRB candidates above a threshold of 700 Jy ms. Rowlinson et al. (2016) performed a pilot transient survey on timescales of 28 s using 100 hr of MWA ob-

servations, and identified no FRB candidates above a threshold of 7980 Jy ms. This search was less sensitive, and could be improved using high time resolution data or image dedispersion (Anderson et al., 2021b) though at the expense of processing speed. In other words, Tingay et al. (2015) sacrificed surveyed area to increase sensitivity, while Rowlinson et al. (2016) sacrificed sensitivity to increase the amount of surveyed data. Apart from the blind FRB searches in the wide field of view of the MWA, there is also a targeted search. Sokolowski et al. (2018) conducted a coordinated campaign with the MWA to specifically shadow the bright FRBs detected by the ASKAP. A dedispersion search over simultaneous MWA observations of seven ASKAP FRBs with a temporal and spectral resolution of 0.5 s and 1.28 MHz across the 170–200 MHz band yields no candidates within the ASKAP error regions exceeding a 5σ threshold, corresponding to a fluence upper limit of 450–6500 Jy ms. This work concluded that there must be either a break in the spectrum (> 200 MHz) or a thick absorbing medium in the environment of the ASKAP FRBs. While FRB searches with the MWA have not yielded a real detection yet, there has been a significant improvement on the sensitivity, which results in important constraints on the FRB emission mechanism and environment.

1.3 MWA

As described in Section 1.1.5 and 1.2.6, MWA has been used to search for coherent radio emission associated with GRBs and low-frequency FRB emission, placing significant constraints on the coherent emission models applicable to GRBs and FRB emission mechanisms. In this thesis, I further exploit the capacity of MWA (e.g. the rapid-response mode and high time resolution data), and continue these searches to further advance our understanding of GRB and FRB physics. In this section, I introduce the MWA instrument and how I am going to use it for targeted searches for prompt radio transients.

The MWA is a precursor of the Square Kilometre Array (SKA; Dewdney

et al. 2010), located at the Murchison Radio-astronomy Observatory (MRO) in the Murchison region of Western Australia. The MRO has been chosen to host the MWA due to its low-level radio frequency interference made by humans, particularly in the FM band covered by the operating frequency range of MWA.

The MWA commenced science operations in 2013 (i.e. phase I; Tingay et al. 2013). Its operational frequency range is between 80 and 300 MHz with an instantaneous bandwidth of 30.72 MHz, and its standard correlator has a time and frequency resolution of 0.5 s and 10 kHz (Tingay et al., 2013). It contains 128 tiles with a minimum baseline of 7.7 m and maximum baseline of 2864 m, corresponding to a field of view ranging from $\sim 300 - 1000 \deg^2$ and angular resolution of ~ 1 arcmin at 185 MHz (for a full description see Tingay et al., 2013). The phase II upgrade of MWA in 2018 doubles the number of antenna tiles to 256 with half of them operational at a time due, and enables two distinct array configurations with 72 of the new tiles arranged near the MWA core increasing the sensitivity to diffuse emission, and the remaining 56 long baseline tiles improving the angular resolution and reducing the confusion noise (Wayth et al., 2018). There are two configurations of the 128 operating tiles: extended and compact. While the extended configuration employs the long baseline tiles and the core, the compact configuration employs only the tiles near the MWA core. Most of the baselines in the compact configuration are shorter than 200 m, leading to the much lower angular resolution of ~ 10 arcmin (Wayth et al., 2018). An illustration of the MWA phase I and phase II baseline configurations is shown in Figure 1.14.

Apart from the standard correlator, there is another observing mode of the MWA: the Voltage Capture System (VCS; Tremblay et al. 2015). Unlike the standard correlator, the VCS records channelised data (3072 channels across 30.72 MHz of bandwidth) for each tile (4×4 dipole array) instead of correlated visibilities. This allows for the capture of high temporal and frequency resolution raw voltage data ($100 \, \mu s/10$ kHz). The MWA VCS observations are most sensitive to millisecond-duration transient signals (for a comparison of sensitivity
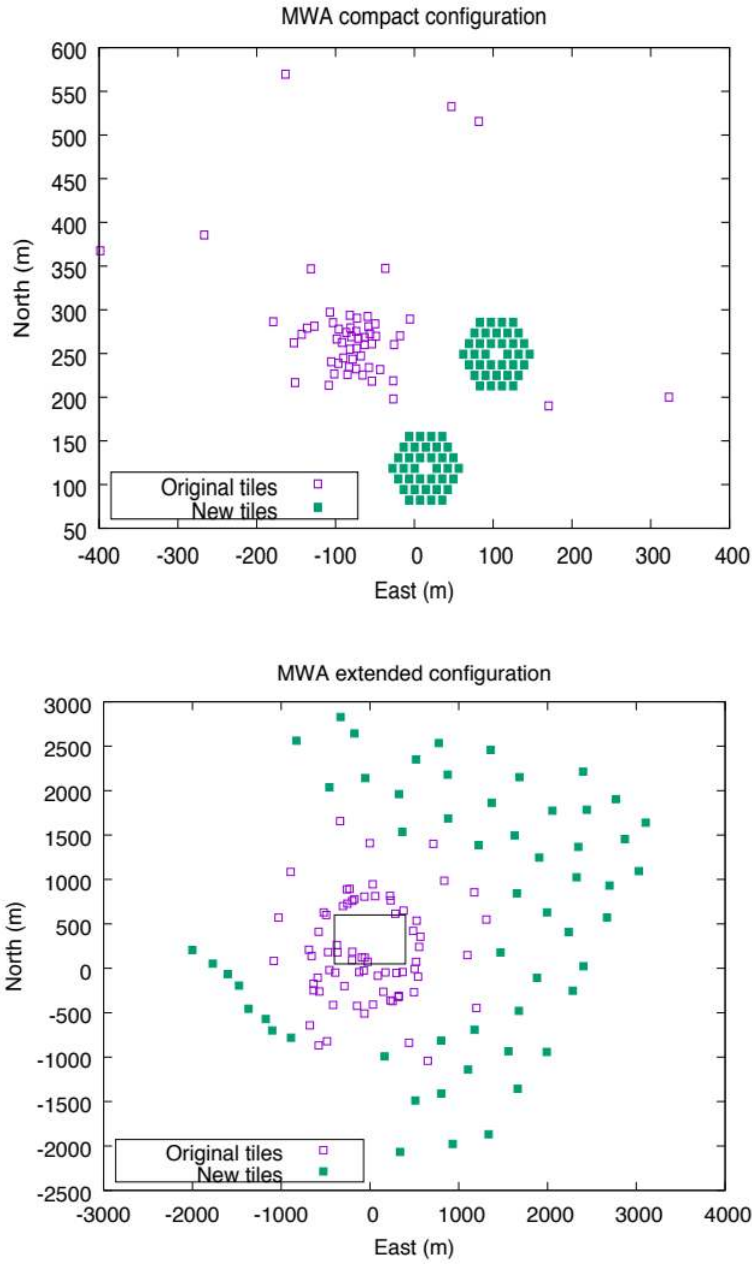
Figure 1.14: Compact (top) and extended (bottom) configurations of the MWA phase II upgraded from the MWA phase I. The top panel shows the 72 new tiles (green squares) arranged for the compact configuration, and the bottom panel shows the 56 new tiles (green squares) arranged for doubling the maximum baseline of the extended configuration. This figure is adapted from Wayth et al. (2018).

between the standard MWA correlator and the VCS see Chapter 3), and have been extensively used for pulsar searches (Bhat et al., 2016; Xue et al., 2017; McSweeney et al., 2017; Meyers et al., 2018; Swainston et al., 2021). However, the VCS data are also suitable for FRB searches. An FRB search with the MWA VCS would be more promising for detecting low-frequency FRB emission than previous works using the standard correlator (see Section 1.2.6).

1.3.1 Rapid response

The rapid-response mode of MWA is most important in searching for the earliest radio emission associated with GRBs. Given the dispersion delay of radio signals, low-frequency telescopes can potentially capture prompt radio signals produced simultaneously or even prior to GRB events as long as their response to transient alerts are fast enough. The rapid-response system on the MWA can receive and analyse incoming GRB alerts from *Swift* and *Fermi*, and automatically schedule 30 min of standard observations centered at the source position. Note that simultaneous radio emission of GRBs is expected to arrive 18 s–6 min after GRBs for an observing frequency of 185 MHz (the central frequency of the MWA observing band; Tingay et al. 2013) and a redshift of $0.1 < z < 2.5$ (the observed redshift range of short GRBs; see Eq. 1.7; Gompertz et al. 2020).

The MWA has been used for performing triggered observations of GRBs since 2015 (e.g. Kaplan et al. 2015). In 2018, the MWA triggering system was upgraded to enable it to trigger on VOEvents (Virtual Observatory Events, which is a standard information packet for the communication of transient celestial events; Seaman et al. 2011), allowing the MWA to point to a GRB position and begin observations within 20 s of receiving an alert (Hancock et al., 2019a). There are three capabilities that make MWA a competitive telescope for searching for the earliest radio signatures from GRBs:

(1) With a large number of closely spaced receiving antennas the MWA features a high sensitivity over a wide field of view ($> 300 \, \mathrm{deg}^2$; Tingay et al. 2013)

and thus is capable of covering the large positional errors of *Fermi* GRBs ($\sim$ 10°; Meegan et al. 2009) and a large portion of the even larger LIGO/Virgo positional uncertainties.

(2) The upgrade from a GCN packet based notification system (on target within 23s of *Swift* GRB 150424A; Kaplan et al. 2015) to a VOEvent based automatic trigger system further reduces the response time of the MWA to 20–30 s after receiving a transient alert and allows us to filter out *Swift* and *Fermi* events more efficiently (Hancock et al., 2019a). Given that signals at low frequencies arrive later than high-frequency signals (see Section 1.2.3.1), this rapid-response capability makes the MWA a promising instrument for catching radio emission associated with a GRB.

(3) The upgraded triggering system is now capable of triggering observations in the VCS mode, which boosts the time resolution to 0.1ms and thus increases our sensitivity to FRB-like signals which would otherwise be smeared out over the 0.5s coarse sampling of correlated observations.

The rapid-response and VCS mode of the MWA is currently employed for searching for GRB associated radio emission. Given that the data rate of VCS observations is high ($\sim$28 TB/hr), it is not practical to continuously observe one GRB for more than $\sim$100 min (Tremblay et al., 2015), making it difficult to probe prompt signals predicted to be produced at late times (e.g. by the collapse of an unstable magnetar remnant into a BH, which may not occur for up to 2 hr post-merger; Zhang 2014). However, a 15 min integration with the VCS will allow us to search for prompt, coherent emission predicted to occur either just prior, during, or shortly following GRBs for a wide range of DMs (150-2500 pc cm^{-3}) to much deeper sensitivities than the standard correlator while still creating a manageable data volume.

A comparison between the rapid-response mode of MWA and other telescopes of low radio frequencies is shown in Figure 1.15 (Anderson et al., 2021a). The ex-

pected dispersion delays of radio signals at the observing frequencies of different telescopes are also included. We can see that MWA and LWA1 HAL are able to be on target in time to capture any signals produced simultaneously with GRBs. Whereas the response time of LOFAR (4–5 min; Rowlinson et al. 2019, 2020) is insufficient for probing the earliest predicted prompt signals, it is the most sensitive telescope among all those listed in Figure 1.15, making LOFAR more suitable for searching for persistent emission from magnetar remnants formed hours after GRBs. Therefore, the MWA's reasonable sensitivity and rapid-response time make it the most competitive instrument for searching for and detecting prompt, coherent radio signals from GRBs.

1.3.2   Experimental setup

An illustration of the experimental setup for triggering rapid-response observations of GRBs with the MWA is shown in Figure 1.16. When a GRB event happens, it first triggers GRB detectors such as *Swift*-BAT or *Fermi*-GBM. These detectors then send out a transient alert to the astronomy community (i.e. VOEvents, described in the section above) with detailed information including event position, alternative classifications and the probability of being a genuine GRB. Note that *Swift* has a superior localisation capability than *Fermi*, with GRBs localised by these two detectors having typical positional uncertainties of $1 - 4$ arcmin (Gehrels et al., 2004) and 1–10 deg (Meegan et al., 2009), respectively. After receiving such an alert, the MWA rapid-response front-end service parses the information contained, and in the case of identifying it as a real GRB starts repointing the telescope to the event position and schedules either a 30 min observation in the imaging mode or a 15 min VCS observation (the latter for the well localised *Swift* detected GRBs only).
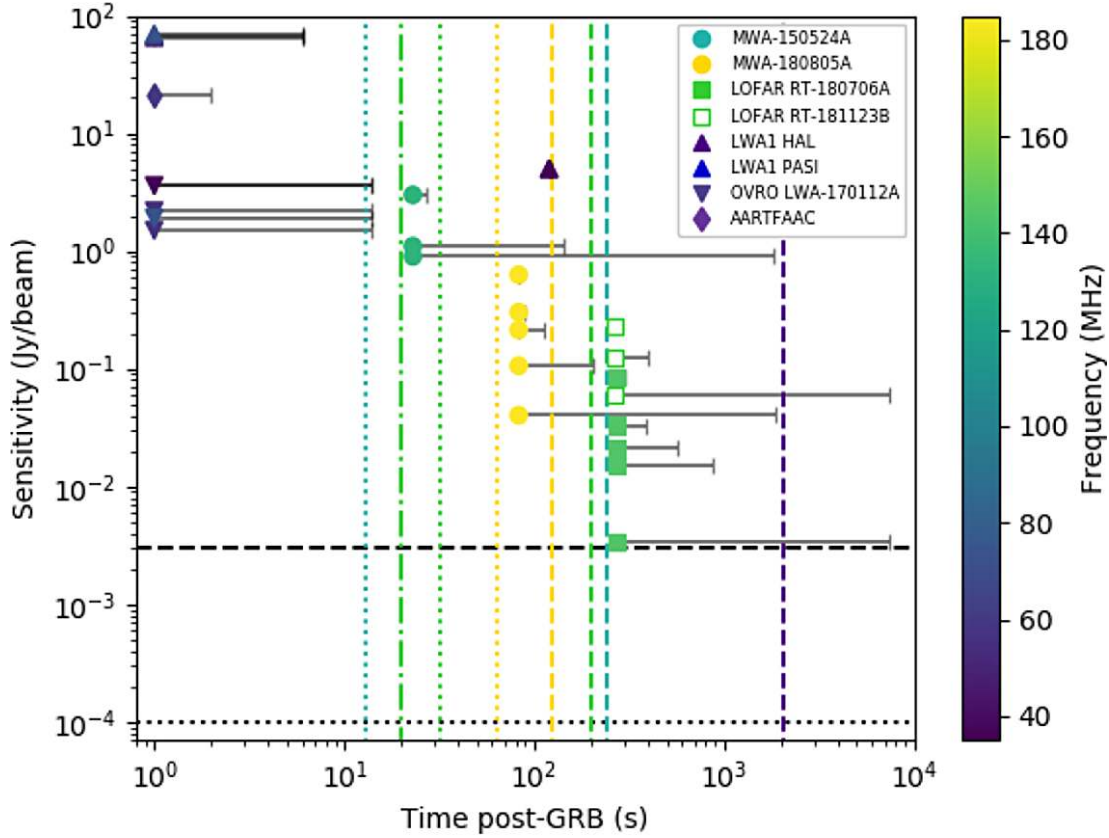
Figure 1.15: Comparison of response time and sensitivity between MWA and other low-frequency telescopes. Different telescopes are represented by different symbols, and those continuous monitoring programs (all-sky) that obtain simultaneous observations of GRBs are plotted at 1 s post-burst. The dotted and dot-dashed vertical lines indicate the expected arrival times of radio signals associated with GRB 150424A (dark green) and GRB 180805A (yellow) for the MWA and GRB 180706A (light green) and GRB 181123B (light green) for LOFAR, with colors matching the observing frequency. The black horizontal dashed and dotted lines show the expected sensitivity for the MWA at 185 MHz and LOFAR at 150 MHz. This figure is adapted from Anderson et al. (2021a).
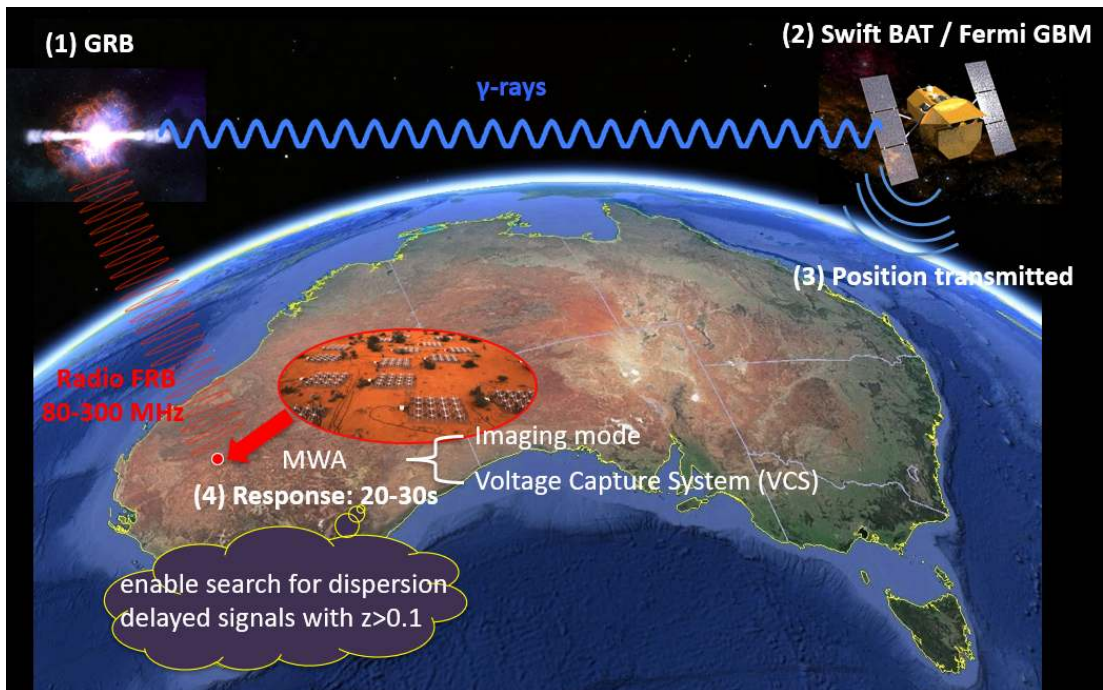
Figure 1.16: The experimental setup for triggering rapid-response observations of GRBs with the MWA. Given the dispersion delay of radio signals (18 s for an observing frequency of 185 MHz and a redshift of $z = 0.1$; see Section 1.3.1), the response time of the MWA (20–30 s) enables us to search for simultaneous radio emission of GRBs at a redshift of $z > 0.1$.

1.4 Motivation for this thesis

There have been lots of theoretical models that predict coherent radio emission from GRBs, either produced by BNS mergers (short GRBs) or core-collapse supernovae (long GRBs; see Section 1.1.4.3). Despite extensive searches for this predicted emission, no detection has been claimed yet. Possible reasons for previous non-detections include a low sensitivity of the telescope or a slow response to GRB detections. In order to increase our chance of detection and better understand the radio emission mechanisms in the GRB scenario, a sensitive telescope with a fast response is needed. The MWA is the desired telescope. It features a rapid response to GRB detections by *Swift* and/or *Fermi* that is capable to capture the dispersed low-frequency radio emission produced concurrently with the prompt gamma-ray emission. Additionally, the high sensitivity of the MWA high time resolution VCS data would allow us to detect the predicted prompt radio emission assuming typical model parameters. Therefore, searching for prompt radio transients using the MWA would be very productive in studying the GRB associated radio emission.

Given that GRBs could form magnetar remnants (see Section 1.1.3) and that FRB progenitors are likely magnetars (see Section 1.2.5), there is potentially a link between GRBs and FRBs. We can use the VCS data to search for low-frequency FRB emission, which is expected to be more sensitive than previous works using the imaging data (see Section 1.2.6). In particular, we can perform a targeted search for low-frequency emission from repeating FRBs, which is motivated by the recent LOFAR repeating FRB detection (Pleunis et al., 2021b). This search would either make a detection or place further constraints on the poorly known FRB origin.

This thesis presents a low-frequency search for prompt radio transients from a sample of GRBs and repeating FRBs. In Chapter 2, I provide a brief overview of the theory of interferometry and data reduction and analysis used in this work. I also describe the search for dispersed prompt emission using image dedisper-

sion techniques and standard FRB searching software. In Chapter 3, I present a low-frequency (170–200 MHz) search for coherent radio emission associated with nine short GRBs using the MWA imaging data, which is the biggest sample yet. I combine this sample with the upper limits of other GRBs in the literature and place constraints on BNS merger coherent radio emission models. Chapter 4 presents the first VCS trigger on a GRB to search for prompt radio emission associated with a long GRB 210419A. I also discuss constraints on the X-ray flare model of GRBs. Chapter 5 focuses on a targeted search for low-frequency (144–215 MHz) FRB emission from five known repeating FRBs discovered by CHIME and ASKAP using archival VCS data from the MWA. I also discuss the implications for the spectrum and environment of repeating FRBs. I conclude with Chapter 6, where I revisit the radio emission mechanisms in the GRB scenario and low-frequency bursts of repeating FRBs, and conclude with a view towards the future.

Chapter 2

Methodology

Radio telescopes collect and record information about the phase and amplitude of radio waves with the use of antennas and receivers. Because electromagnetic waves at radio frequencies can be manipulated easily, the radio telescopes have been developed into different forms, including single dishes (either parabolic or parabolic sections) which concentrate incoming radiation at the focus and amplify it with a radio receiver, and interferometry telescopes which collect signals at separated antennas and combine these signals electronically to form an image. This research project has made use of astronomical data taken by the radio interferometer, MWA. In this chapter, I give a brief overview of the fundamentals of radio interferometry. Then I describe the data reduction procedure for MWA observations.

2.1   Single-dish radio telescopes

I start with single-dish radio telescopes as they can be considered fundamental units of more complex interferometry telescopes. The performance of a radio dish can be characterised by its angular resolution and sensitivity. The angular resolution of a dish is limited by the size that is practical to build. For example, a telescope with a diameter of $D = 100\,\mathrm{m}$ and observing at a wavelength of

57

$\lambda = 20\,\mathrm{cm}$ has an angular resolution of $\theta \sim 1\,\mathrm{deg}$ based on the relation $\theta \sim \lambda/D$ (corresponding to the half-power point of an approximate Gaussian sensitivity pattern). The sensitivity of a dish is determined by the collecting area as well as other factors such as system temperature and bandwidth. To overcome the limitation of physical dish size and sensitivity, interferometric telescopes are needed (see Section 2.2).

The calibration of single-dish radio telescopes, i.e. determining the conversion between voltage response and incident radio flux as a function of sky position and frequency, is simple. As all signals from a given direction are reflected by the parabolic surface of the dish to the focus and thus combined in phase, we only need to calibrate the telescope gain (i.e. the amplitude of the voltage response to incident radiation; see below). Usually, we can observe a nearby ($< 30°$ from the target source) bright and persistent source with stable flux to calibrate the telescope gain. More details on the fundamentals of radio astronomy and radio telescopes can be found in Marr et al. (2015) and Condon & Ransom (2016).

2.1.1 Beam response

The beam response (i.e. response to the area of the sky where radiation can be detected) of a single-dish radio telescope as a function of source directions can be calculated using the Fourier transform. A basic diagram of a one-dimensional aperture is shown in Figure 2.1 (generalization to a two-dimensional aperture is straightforward). The plane waves emitted by a source at infinity induce an electric field pattern at the aperture antenna

$$f(l) = \int_{\mathrm{aperture}} g(u)e^{-i2\pi lu}du, \tag{2.1}$$

where $l \equiv \sin\theta$, $u \equiv x/\lambda$, and g is the position dependent field strength (i.e. illumination function) and stays constant for uniform illumination. Note that the response of a single dish is a single value, but incorporates some kind of weighted average over the entire beam area (Condon & Ransom, 2016). This expression

can be easily generalized to the more realistic case of a two-dimensional aperture

$$f(l, m) = \int \int_{\text{aperture}} g(u, v) e^{-i2\pi(lu+mv)} du\, dv, \qquad (2.2)$$

where m and v are second dimension analogs of l and u, respectively. In summary, the beam pattern of a two-dimensional aperture is the two-dimensional Fourier transform of the illumination function. A basic diagram of a two-dimensional circular aperture and the corresponding beam pattern (Airy disk) is shown in Figure 2.2.
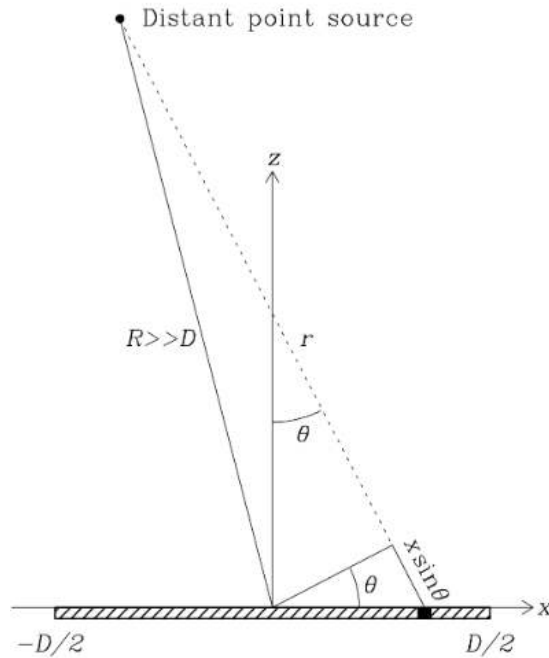
Figure 2.1: Basic diagram of a one-dimensional aperture spanning $-D/2 < x < D/2$ and a distant point source ($R \gg D$) in the direction θ (with respect to the normal of the aperture). This figure is adapted from Condon & Ransom (2016).

2.2   Interferometry

In order to increase the angular resolution of radio telescopes and enable the association of radio sources with optical counterparts, radio interferometry is
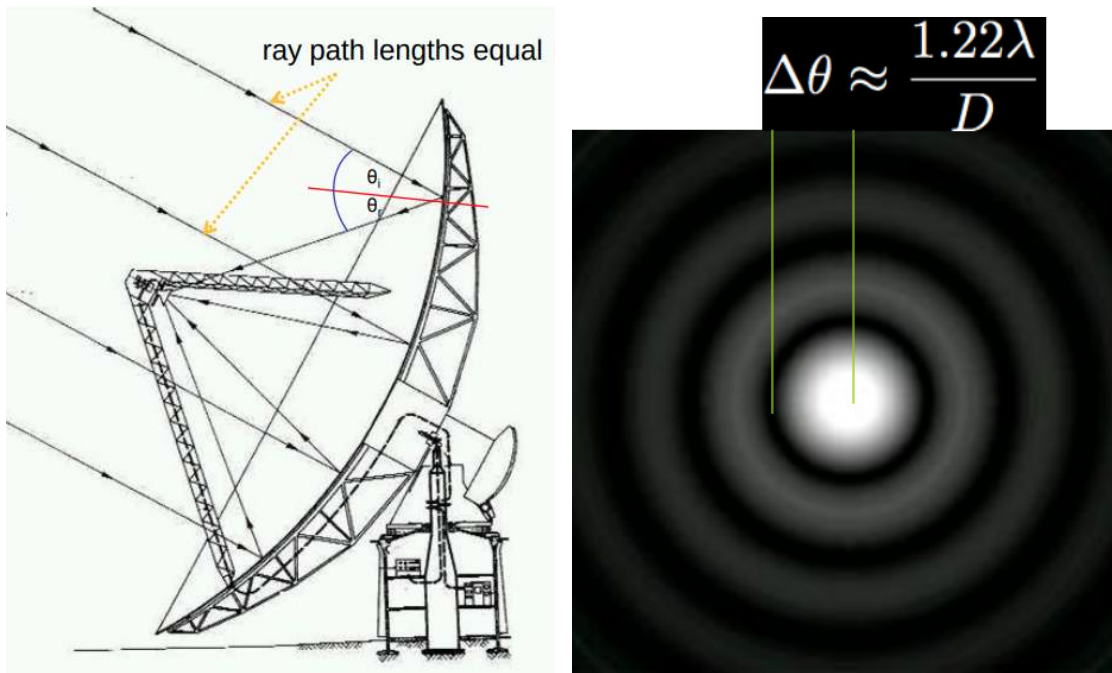
Figure 2.2: Schematic of a two-dimensional circular aperture (left) and the corresponding beam response (right). In the left panel, incident plane waves along ray paths (black arrowed lines) are reflected by the parabolic dish to the focal point. In the right panel, the beam response of the two-dimensional circular aperture is shown as the Airy disk. Source: John Reynolds, Radio Astronomy School 2015 in Narrabri, NSW Australia.

used. This is a technique that uses two or more radio antennas in an array to collect and combine electromagnetic signals. The fundamental unit of a synthesis array is a two-element interferometer formed by each pair of antennas. The main advantage of the synthesis array is angular resolution, as any pair of antennas can be placed an arbitrary distance apart. Note that Earth-based interferometers are inherently limited by the diameter of the Earth. While single-dish telescopes still have strength in pulsar discovery and spectral line analysis, high-resolution radio images can only be made by the multi-antenna radio interferometer. At a wavelength of $\lambda = 10\,\text{cm}$, an array of radio telescopes with a maximum separation of $D = 5\,\text{km}$ can achieve arcsec angular resolution.

Interferometry telescopes have made great astrophysical discoveries, such as the discovery and investigation of apparent superluminal motions in quasars by the "Goldstack" interferometer (Whitney et al., 1971; Cohen et al., 1971), the measurement of proper motions and distances of H_2O maser sources by the Very-long-baseline interferometry (VLBI; Genzel et al. 1981b,a), the first image of the supermassive black hole at the centre of the Milky Way revealed by the Event Horizon Telescope (EHT; Akiyama et al. 2022a,b,c,d), and the recent discovery of a large population of FRBs by CHIME in the beamforming mode (Amiri et al., 2021). Moreover, the upcoming SKA, with unprecedented angular resolution and sensitivity is expected to make most revolutionary contribution to the astronomy field, including EOR, transients and galaxy evolution.

While interferometry telescopes have big advantages over single-dish telescopes, their calibration is more complicated. As the interferometer consists of individual antennas distributed at different locations, the observing conditions such as the atmospheric conditions or the elevation of the source are different for different parts of the array. For example, the ionosphere above the MWA has been found to vary over a length scale of ≈ 3–$8\,\text{km}$ (Jordan et al., 2017), longer than the baseline of the MWA phase II (see Section 1.3). Apart from the antenna dependent calibration, a single calibration for the whole telescope is needed to

determine the absolute gain and its evolution with time. Therefore, it is necessary to calibrate the data from each antenna before making images. More details on interferometric techniques can be found in Taylor et al. (1999) and Thompson et al. (2017).

2.2.1 Antennas

An antenna is a detection element of radio telescopes that converts incident electromagnetic waves into electrical currents. There are various forms of antennas, such as dipoles (a straight wire) and parabolic reflectors (for a complete review see Balanis 2005). As this thesis research is conducted with an interferometer made up of dipoles, here I give a brief introduction to dipole antennas.

A simple dipole antenna consists of two collinear wires, as shown in Figure 2.3. When the dipole is driven by an oscillating current source, it can radiate with a radiation power dependent on the amplitude and frequency of the oscillating current. In order to maximise the radiation power, half-wave dipoles ($l \approx \lambda/2$), which have a nearly resistive load (i.e. all electric power is dissipated in the form of radiation) due to resonance, are commonly used. Practical forms of dipole antennas are more complicated as we need to consider the finite conductor thickness and frequency dependent radiation characteristics. Examples of dipoles for practical use include bow-tie antennas (used for MWA; Lonsdale et al. 2009; see Section 1.3), inverted V-shaped dipoles (used for LOFAR; Ellingson 2005), log-periodic antennas (used for the SKA-Low station; Bolli 2020), triangular sheets (used for Shaped Antenna measurement of the background RAdio Spectrum; Nambissan T. et al. 2021) and cylindrical dipoles (used for the Tianlai interferometer; Cianciara et al. 2017). More details can be found in Balanis (2005).

2.2.2 Interferometer response

We start with an analysis of the simplest case, i.e. two-element interferometers. A schematic diagram is shown in Figure 2.4. The plane waves emitted by a source
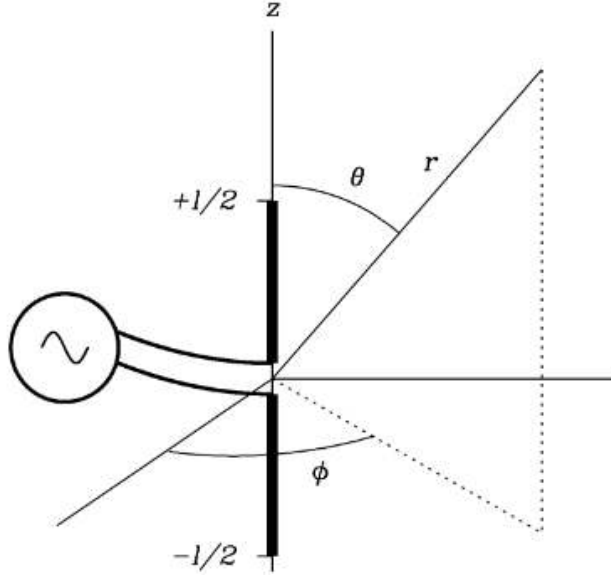
Figure 2.3: A short dipole made up of two wires of length $l/2$ (total length $l \ll$ one wavelength λ). When the dipole is driven by an oscillating current source, it can create a radiation field in the surrounding space described by the coordinate system (r, θ, ϕ).

at infinity are sampled by two antennas with a separation vector $\vec{B}$. There is a path delay between the arrival times of the plane waves at the two antennas, $\vec{B} \cdot \vec{s}$, where $\vec{s}$ is a unit vector in the source direction. Given the wave number of the plane waves $k = 2\pi/\lambda$, that path delay can be converted to a phase delay of $k\vec{B} \cdot \vec{s}$. If we combine the signals from the two antennas by multiplying them electronically, it can be shown that the response of the interferometer is

$$R = \int I(\vec{\sigma}) e^{ik\vec{B}\cdot(\vec{s}+\vec{\sigma})} d\vec{\sigma}, \tag{2.3}$$

where $d\vec{\sigma}$ represent a small part of the source, and $I(\vec{\sigma})$ is the emission intensity (i.e. the sky emission pattern) of the small part. If we move the term $e^{ik\vec{B}\cdot\vec{s}}$ independent of the source out of the integral, the response can be written as

$$R = e^{ik\vec{B}\cdot\vec{s}} \int I(\vec{\sigma}) e^{ik\vec{B}\cdot\vec{\sigma}} d\vec{\sigma}. \tag{2.4}$$

Therefore, the amplitude of the response is simply given by the Fourier transform
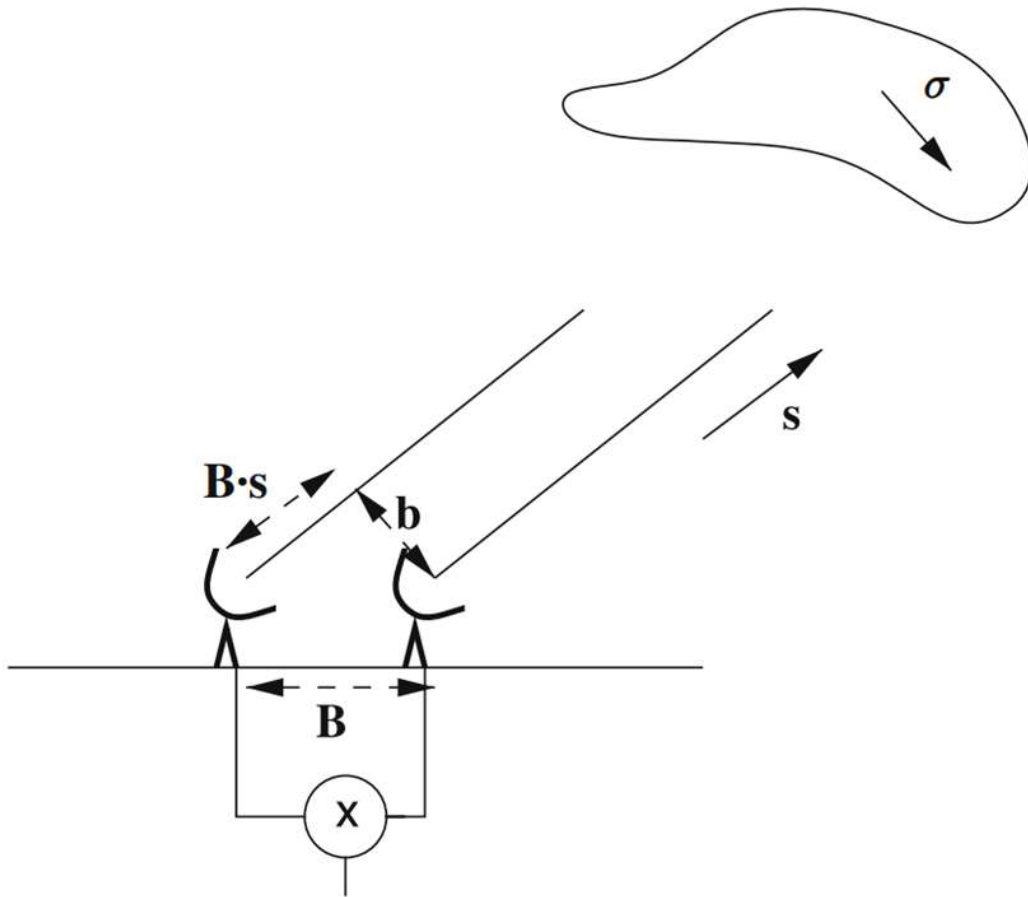
Figure 2.4: Basic diagram of an interferometer with a baseline $\vec{B}$ observing a source in the direction $\vec{s}$. The vector $\vec{b}$ is the baseline vector projected on the sky plane, and $\vec{B} \cdot \vec{s}$ is the path delay between the two waves arriving at the two antennas. This figure is adapted from Jackson (2008).

of the source intensity distribution. It is noteworthy that the phase in the term $e^{ik\vec{B}\cdot\vec{s}}$ depends on the relative direction between the baseline vector and the source, which is known to vary sinusoidally with the Earth rotation, so this phase rotation can be removed by the insertion of electronic delays (i.e. adding a time lag to one antenna to artificially change $\vec{B}\cdot\vec{s}$). The source information is all contained in the Fourier transform response, which is a complex quantity (also called visibility).

The response of the interferometer given by Eq. 2.5 can be further decomposed using Cartesian coordinates. $\vec{\sigma}$ is a vector on the sky plane, and can be easily decomposed into $\vec{\sigma} = x\vec{i} + y\vec{j}$, where $\vec{i}$ and $\vec{j}$ are unit vectors in the east-west and north-south directions, respectively. If we decompose $\vec{B}$ using the same coordinates into $\vec{B} = u\vec{i} + v\vec{j}$ (note that the component perpendicular to the sky plane makes no contribution to $\vec{B} \cdot \vec{\sigma}$), the response after phase compensation becomes

$$R(u,v) = \int\int I(x,y)e^{2\pi i(ux+vy)}dxdy, \qquad (2.5)$$

where u and v are in units of wavelength. The physical interpretation of uv is quite straightforward: imagine we are on the source looking at the baseline, it would appear as a line drawn on the Earth that can be decomposed into two components, one is parallel to the equator (i.e. u) and the other towards the north pole (i.e. v). The above equation means that the interferometer response (or measured "visibilities") is simply a 2D Fourier transform of the source intensity distribution. An example of this transform is shown in Figure 2.5, where the top panel shows a model image of a supernova remnant, and the bottom panel shows the interferometer response in the uv plane.

As the Earth rotates, the u and v components change, tracing out an ellipse in uv space in one Earth rotation. This change provides useful information on the sky, enabling us to work backwards to recover the source structure if the source remains constant over the duration of the observation (for details see Jackson 2008). The ellipse of the uv track is characterised by a semi-major and semi-
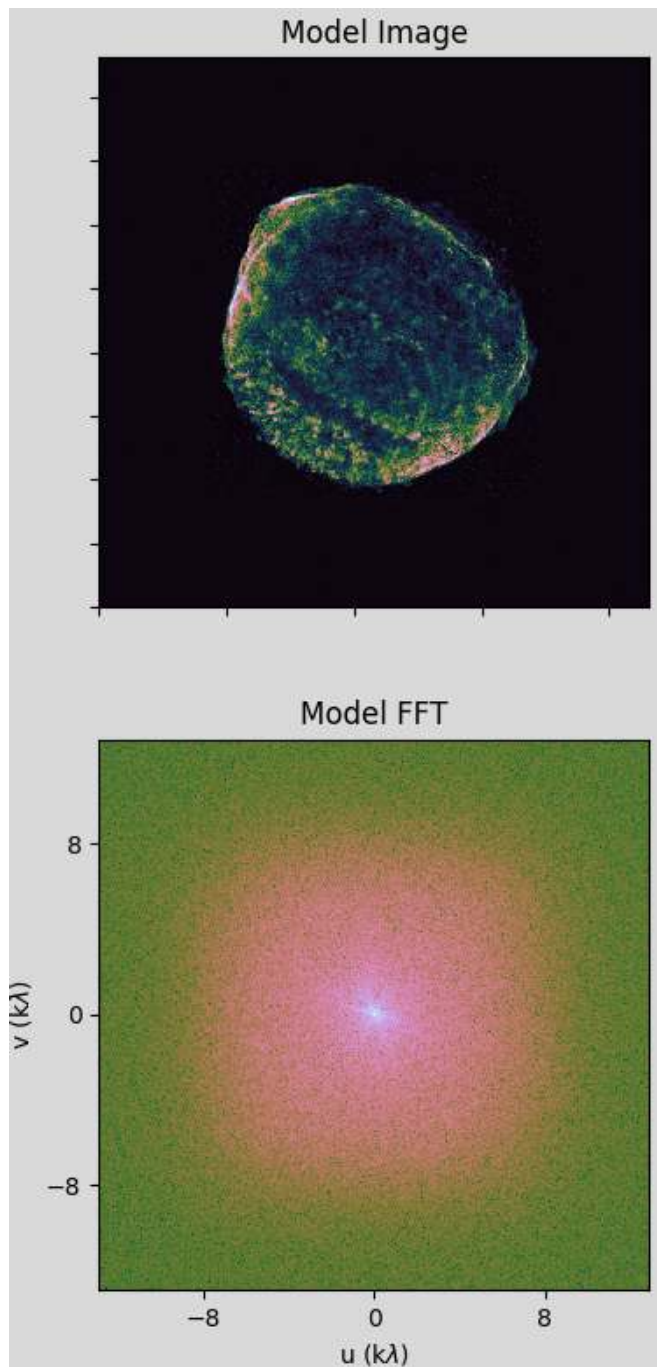
Figure 2.5: Model image of a supernova remnant (top) and the real part of the 2D Fourier transform of the model image in the uv plane (bottom). The u and v axes are in units of wavelengths. This figure was created using the Friendly Virtual Radio Interferometer tool (see https://github.com/crpurcell/friendlyVRI).

minor axis of $\frac{L}{\lambda} \cos \delta$ and $\frac{L}{\lambda} \cos \delta \sin D$ in the u and v directions respectively, where L is the baseline length, and δ and D are the declinations of the baseline and the source, respectively. While an interferometer does not fully sample the uv plane, resulting in the inferred images being incomplete, the rotation of the Earth can help to fill in the uv plane by effectively rotating the array.

The best uv coverage for an interferometer is a full elliptical track. Note that since the response function evaluated at position (u,v) is conjugate to the one at $(-u,-v)$, a single measurement covers two values in the uv plane (e.g. Moldon 2012). Therefore, a full track only requires 12 hr of continuous observation. In the case of shorter observations, the more complete the coverage of the uv plane is, the more information we will obtain for the source brightness distribution on the sky. Note that the MWA does not require such an observing strategy due to the large number of well placed tiles resulting in lots of baselines and therefore good instantaneous uv coverage. The recovery of the true sky brightness using the incomplete uv coverage is discussed in Section 2.2.4.

Now we move to more realistic interferometers consisting of more than two antennas. Given more than one baseline is present, visibilities corresponding to different tracks on the uv plane can be measured simultaneously. So interferometers with more antennas (and thus baselines) are expected to fill the Fourier plane more quickly. However, the 2D uv plane may be insufficient for describing the large number of antennas unlikely to be located in the same plane, particularly as the Earth rotates. In this case, a third dimension, w, parallel to the line of sight is needed. The visibility in the (u, v, w) coordinate system can be written as

$$R(u,v,w) = \int \int \frac{I(x,y)}{\sqrt{1-x^2-y^2}} e^{2\pi i(ux+vy+wz)} dx\, dy. \qquad (2.6)$$

Note that the above integral is not a 3D Fourier transform as the variable z implicitly depends on x and y (Condon & Ransom, 2016). However, it may be approximated as a 2D Fourier transform if the field of view of instruments is

sufficiently small ($w \approx 0$ and $\sqrt{1 - x^2 - y^2} \approx 1$). For a large field of view, several methods have been developed to account for the w term, such as W-Projection (Cornwell et al., 2005, 2008) and W-Stacking (Offringa et al., 2014). More details can be found in, e.g. Thompson et al. 2017 and Condon & Ransom 2016.

2.2.3 Calibration

The calibration consists of phase calibration and amplitude calibration. Note that we assume all antenna locations are fixed and known so that the true visibilities of a source can be mathematically calculated and compared to measured visibilities to derive a calibration solution. The amplitude calibration is to derive the scaling factors that make all the visibility amplitudes consistent with known source models, the same as the calibration of a single-dish instrument (see Section 2.1). Note that the scaling factors can be antenna dependent. The bright source observed for amplitude calibration can also be used for phase calibration, by which we recover source positions. Possible causes of phase errors include atmospheric effects, instrumental errors such as pointing and tracking errors, and random noise. Ideally, the phase calibrator should be a point source at the observing frequency, which means we known its phase should be zero. We first calibrate the phases of the observation of the calibrator, and then transfer the phase corrections to the target source. Note that in this process, the phases of the calibrator are set to zero, so the reference direction of the calibrator is different from its real direction. In order to diminish the difference in atmosphere conditions between the target source and the calibrator so the phase solution can be transferred, we should choose a calibrator near the target for calibration (e.g. Pradel et al. 2006). Note that this is more critical for GHz frequency interferometers than for the MWA.

2.2.4 Imaging and deconvolution

The recovery of the sky brightness distribution $I(x, y)$ from the interferometer response function is called deconvolution. Ideally, we would like a fully filled
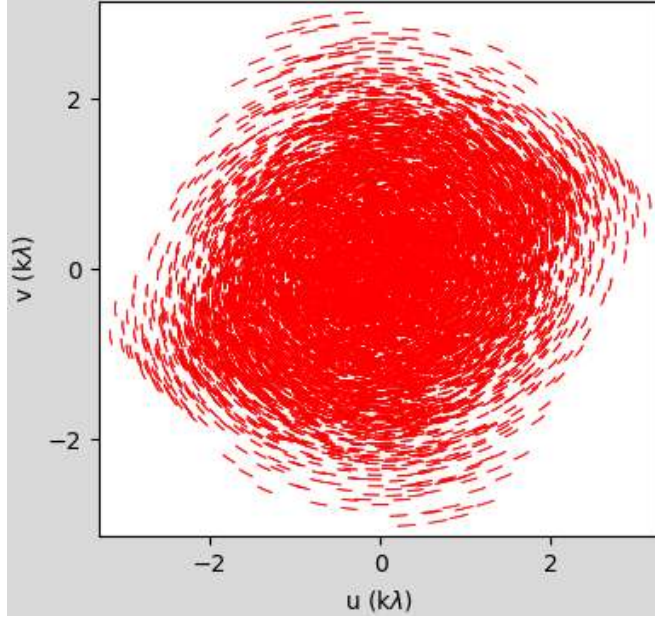
Figure 2.6: Example uv coverage of a 30 min MWA observation at a frequency of 185 MHz. This figure was created using the Friendly Virtual Radio Interferometer tool.

uv plane that can fully sample the intensity distribution of the target source. However, this is not practical because an interferometer is constructed of separate antennas forming fixed baselines[1]. We can only have discrete samples of the uv plane. For an array composed of N antennas, the number of uv samples is equal to the number of baselines, i.e. $N_b = \frac{1}{2}N(N-1)$. The lack of information from unsampled baselines means there are uncertainties in the deconvolved images due to the missing parts of the uv plane. An example of the uv coverage of a 30 min MWA observation is shown in Figure 2.6.

The "dirty image" resulting from the imperfect sampling of the uv space is given by

$$I_D(x,y) = \int \int I(u,v)S(u,v)e^{2\pi i(ux+vy)}dudv, \qquad (2.7)$$

where $S(u,v)$ is the sampling function, set to 1 in the parts of the uv space

---

[1]The MWA has effectively two levels of interferometry, i.e. 4×4 dipoles form a tile and 128 tiles form the array (see Figure 2.8).
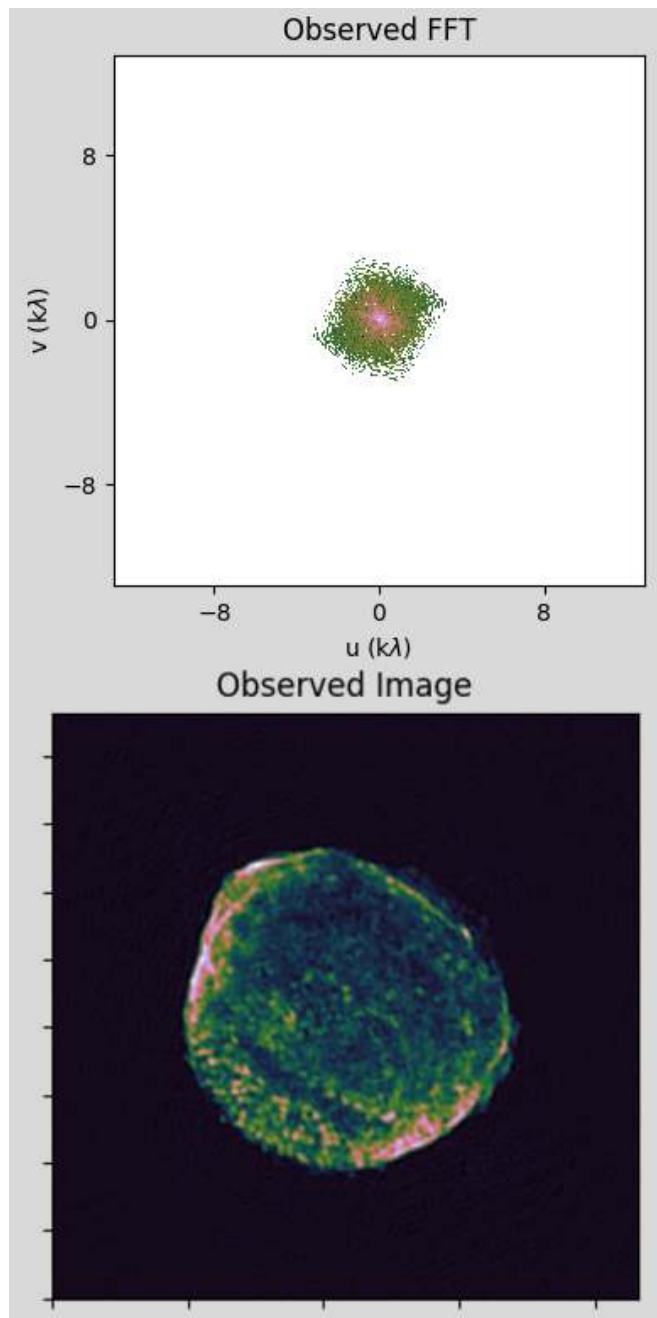
Figure 2.7: Visibilities of a 30 min MWA observation of the supernova remnant shown in Figure 2.5 in the uv plane (top) and the inverted image (bottom). The uv coverage here is incomplete with long baselines for $uv \gtrsim 2\mathrm{k}\lambda$ (responsible for collecting small-scale information; see Section 2.2.2) being missing, meaning that we are losing fine structures in the inverted image when we compare it to the original image in Figure 2.5. This figure was created using the Friendly Virtual Radio Interferometer tool.

that have been sampled and 0 in the other parts. Note that this equation can be considered an inverse Fourier transform of Eq. 2.5 (except for the insertion of the sampling function). Based on the convolution theorem (i.e. the Fourier transform of the multiplication of two functions is equal to the convolution of their respective Fourier transforms), the dirty image can be expressed as

$$I_D(x, y) = I(x, y) * B(x, y),$$ (2.8)

where

$$B(x, y) = \int \int S(u, v) e^{2\pi i (ux + vy)} du dv,$$ (2.9)

is the "dirty beam" (the Fourier transform of the sampling function). Therefore, deconvolution (including cleaning) is basically a process of making additional assumptions (e.g. the sky is mostly blank with occasional real sources that can be modelled by delta functions) to recover the image $I(x, y)$. An example of this deconvolution process is shown in Figure 2.7, where the top panel shows the visibilities of a 30 min MWA observation of the supernova remnant in Figure 2.5, and the bottom panel shows the deconvolved image. As the uv coverage of the MWA observation is incomplete (but far better than most other instruments; see Figure 2.6), we can see some details missing in the deconvolved image (compared to the original image in Figure 2.5).

It is worth mentioning that there are three different weighting schemes in the imaging process that combines visibility data from all baselines: uniform weighting, natural weighting and robust weighting (also known as Briggs' weighting; Briggs 1995). While the uniform weighting applies the same weight on every scale, resulting in a high resolution but non-optimal system noise, the natural weighting allows the scales with more baselines to dominate the image and provides the best nominal sensitivity. This can reveal more large scale features due to the large number of short baselines in the array, but is likely to introduce more
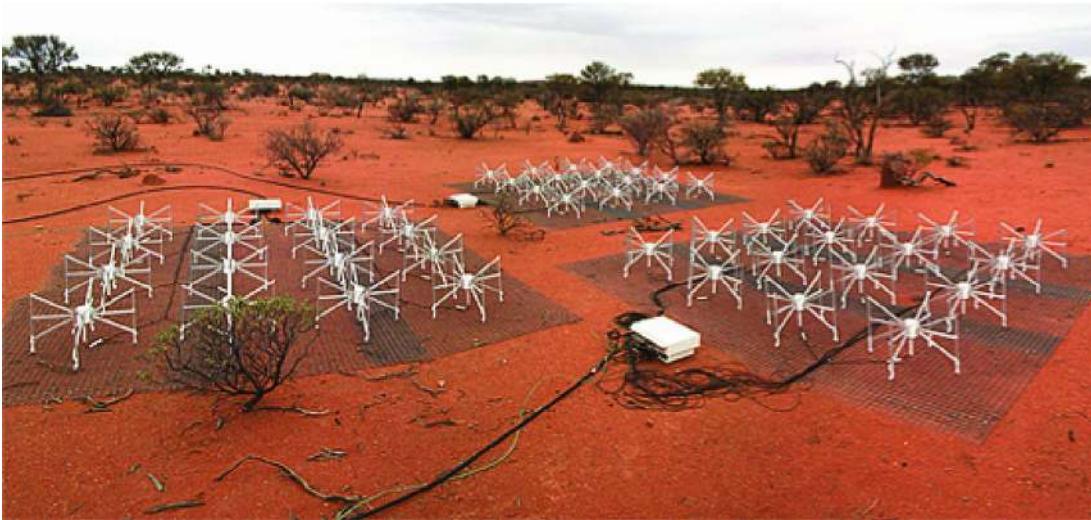
Figure 2.8: Example of MWA tiles and analog beamformers. This figure is adapted from Tingay et al. (2013).

sidelobes to the image. The robust weighting is a trade-off between the above two weighting schemes, and could provide a compromise between resolution and sensitivity (Briggs, 1995). For point sources (e.g. the prompt radio transients investigated in this thesis), a uniform-like robust weighting is commonly used (see Chapter 3).

2.3 Data collection

The radio observations processed and analysed in this PhD project were all recorded by the MWA. In this section, I introduce the data collection process for both voltage data and correlated data.

2.3.1 Voltage data

The antennas of the MWA record celestial signals as electric signals. When an electromagnetic wave arrives at the MWA antennas, it will induce electric signals in the antennas. The signals from a set of 4×4 antennas (forming a "tile") are fed to an analog beamformer attached to the tile (see Figure 2.8). Different tiles

have different signals due to their different locations and orientations. We call the power produced in each tile the raw voltage data. It records the first information about celestial signals.

The voltage data are 4-bit + 4-bit raw complex voltages from every antenna, polarisation, and $100\,\mu$s and $10\,$kHz sample. These data were inaccessible in the initial digital system design of the MWA, but enabled by the Voltage Capture System (VCS) after 2015 (Tremblay et al., 2015). During the data acquisition, the VCS passes the voltage data to a group of 16 servers made up of Redundant Arrays of Independent Disks (RAIDs; amounting to $46\,$TB of storage in total). Given that the voltage data rate is high ($\sim 28\,$TB/hr), these data can be continuously written out to the RAIDS for $\sim\,100\,$min at most before reaching the storage limit. These temporarily stored data will eventually be transferred to the MWA data archive hosted by the Pawsey supercomputer center for long-term storage. This could take a significant amount of time because higher priority is given to archiving correlated visibilities (see below). More details can be found in Tremblay et al. (2015).

2.3.2 Correlated data

The raw voltage data can also be transferred to hardware correlators for signal correlation. At the correlation center (Ord et al., 2015), the voltage data from each pair of the 128 MWA tiles are correlated to form baselines with different lengths (for the correlation process see Eq. 2.3–2.6). The final product of correlation is visibility data, which are then transmitted back from the telescope site to the data center. Note that the correlated data are averaged to a lower time resolution of $0.5\,$s to facilitate storage. The biggest difference between voltage data and correlated data is time resolution. As the voltage data have a much higher time resolution, they are more suitable for prompt radio transient searches (see Chapters 4 and 5).

2.4 Imaging

The MWA-correlated data can be used for imaging. The standard procedure consists of flagging, calibration, cleaning and imaging. In this section, I describe each of these processing steps.

Before data reduction, I briefly introduce data downloading. The command line client MANTA-RAY-CLIENT[2] is used to download data from the MWA All-Sky Virtual Observatory[3] (ASVO) server. There are some options in the tool that allow us to change the time and frequency resolution of the downloaded data, apply COTTER (Offringa et al., 2015) for detecting and flagging RFI, and convert the observation to Common Astronomy Software Application (CASA; McMullin et al. 2007) measurement sets. The downloaded data are all stored at Pawsey Supercomputing Center, and most of the processing I am going to discuss in the following are built as high performance computing workflows.

The first step in data reduction is identifying any corrupted data for flagging and discarding. There are several causes for data corruption, such as radio-frequency interference (RFI), broken hardware or software, and scheduling errors. As the bad data would introduce artefacts to the visibilities, we need to flag and remove them. There are various methods for data flagging, either in the hardware (Kocz et al., 2010; Barnbaum & Bradley, 1998; Briggs et al., 2000; Fridman & Baan, 2001; Hellbourg et al., 2014) or software (Golap et al., 2005; Athreya, 2009; Pen et al., 2009; Offringa et al., 2012; Sekhar & Athreya, 2018) domain. In this PhD project, I used the software AOFLAGGER[4] (Offringa et al., 2012) to flag the MWA data for its effective RFI rejection and fast performance.

The calibration is a process of determining the antenna dependent complex gains. There are two calibration methods: in-field calibration (mainly used in this thesis) and a standard calibrator. The in-field calibration uses the GaLactic and Extragalactic All-sky MWA (GLEAM) survey (Hurley-Walker et al., 2017,

---

[2]https://github.com/mwatelescope/manta-ray-client.git
[3]https://asvo.mwatelescope.org/
[4]https://sourceforge.net/projects/aoflagger/

2019) as a source model within the field of view, and avoids the bulk refractive offset resulting from transferring solutions from dedicated calibration observations. However, for the target field with bright sources such as Pictor A or Centaurus A within the primary beams, the in-field calibration was not possible as these sources were not included in the GLEAM catalogue. Instead, we derived the calibration solution from a nearby calibrator that had been observed within 12 hours of the MWA observation. Note that in 2020 the GLEAM sky model was updated to include the bright calibrator (A team) sources and the GLEAM Galactic plane catalogue so now it can be applied to more MWA observations, especially those near the Galactic plane with bright sources in the field.

The in-field calibration is performed as follows:

1. Create a catalogue that contains all GLEAM sources in the field of view of the MWA observation using the script CROP_CATALOGUE.PY. Usually we selected those sources from the GLEAM catalogue with a flux density above 1 Jy and within a radius of 30° of the MWA pointing center. If there are too few sources (e.g. $\lesssim 10$), we can increase the radius until enough sources are included.

2. Create a sky model for all the selected sources using the script VO2MODEL.PY. For each source, there are four important parameters we need for calibrating the antenna response, i.e. the coordinates (RA and Dec), the flux density at 200 MHz (the reference frequency in the GLEAM survey), and the spectral index. These parameters constitute the sky model for the in-field calibration.

3. Calibrate the visibilities using the local sky model. This is to find the best solution of the amplitude and phase corrections needed to apply to each antenna that minimise the difference between the corrected data and the model. After the fitting, we can inspect the solution for each antenna, and flag the antennas with abnormal solutions such as divergent phase solutions

over the processed bandwidth. If all solutions look consistent, i.e. varying continuously with frequency without any abrupt jumps, we can apply the solution to the downloaded data.

The standard calibration method is similar to the process described above, with the only difference being the number of calibrators incorporated in the sky model. With only one calibrator, the standard method usually generates inferior solutions to the in-field calibration, which can be attributed to variations of conditions (e.g. ionosphere) with time and sky location, or a poor model of the calibrator source.

During both in-field and standard calibration, we have assumed the antenna based gains are constant with time. However, that may not be the case. In practice, the phases on the target can vary with time, which may be caused by an unstable ionosphere or an inadequate model of the source structure. In that case, self-calibration is introduced to mitigate these fluctuations as it can be performed on a shorter timescale than that of the variations (Cornwell, 1995; Walker, 1995; Cornwell & Fomalont, 1999). A prerequisite step for self-calibration is in-field or standard calibration. We need to make a first image of the target field, which is used as an input to the self-calibration. The self-calibration makes use of the point sources in the image as a new sky model to re-calibrate the visibilities. This whole process can be repeated a few times until we see little further improvement in the image quality. The main purpose of the self-calibration is to make the most reliable image by improving the calibration using a better source model that is appropriate for the time and direction of the target observations.

After obtaining a good calibration solution, we can continue to make images with the calibrated visibility data. In this PhD project, I used the WSCLEAN algorithm (Offringa et al., 2014; Offringa & Smirnov, 2017) to image and deconvolve the MWA visibility data. There are lots of parameters in the WSCLEAN command line program, including the image size and resolution, image weighting, number of iterations, and noise threshold[5] (for the choice of these parameters see Chap-

---

[5]More details can be found on https://wsclean.readthedocs.io/en/latest/

ter [3]). After the cleaning, WSCLEAN outputs XX and YY polarisation images, which can be converted into primary beam corrected total intensity (i.e. Stokes I) images using the fully embedded element MWA beam model (Sokolowski et al., 2017).

2.4.1 Ionospheric distortion correction

When observing celestial radio sources with low frequency telescopes like MWA, a common issue is ionospheric distortions to the incident radio waves, resulting in shifts of the measured positions of the radio sources from their real positions. The total electron content (TEC) in the atmosphere along the line of sight induces a constant phase shift to all interferometric antennas, and thus does not affect the source positions. It is the gradient of the electron density in the direction perpendicular to the line of sight $\Delta_\perp \mathrm{TEC}$ that contributes an angular shift to the source positions, which is given by

$$\Delta\theta = -\frac{1}{8\pi^2} \frac{e^2}{\eta_0 m_e} \frac{1}{\nu^2} \Delta_\perp \mathrm{TEC}, \tag{2.10}$$

where e and m_e are the electron charge and mass, η_0 is the vacuum permittivity, and ν is the radio frequency (Thompson, 2017a). For MWA, the offsets in source positions due to ionospheric effects are usually $\sim$ arcmin (e.g. Hurley-Walker et al. 2017; Hurley-Walker & Hancock 2018). An example of the ionosphere induced variations is shown in Figure 2.9.

We used the algorithm FITS_WARP[6] (Hurley-Walker & Hancock, 2018) to correct for the shifts in source positions in the MWA images. There are two tasks performed by FITS_WARP: cross-matching the sources found in the MWA image with a reference catalogue, i.e. the GLEAM catalogue (Hurley-Walker et al., 2017, 2019), and warping the image. The second task involves calculating the offsets from the reference position in the GLEAM catalogue for all matched sources, fitting a smooth function to the offsets and applying the fitted model to the entire

---

[6]https://github.com/nhurleywalker/fits_warp

Source position offsets / pixels
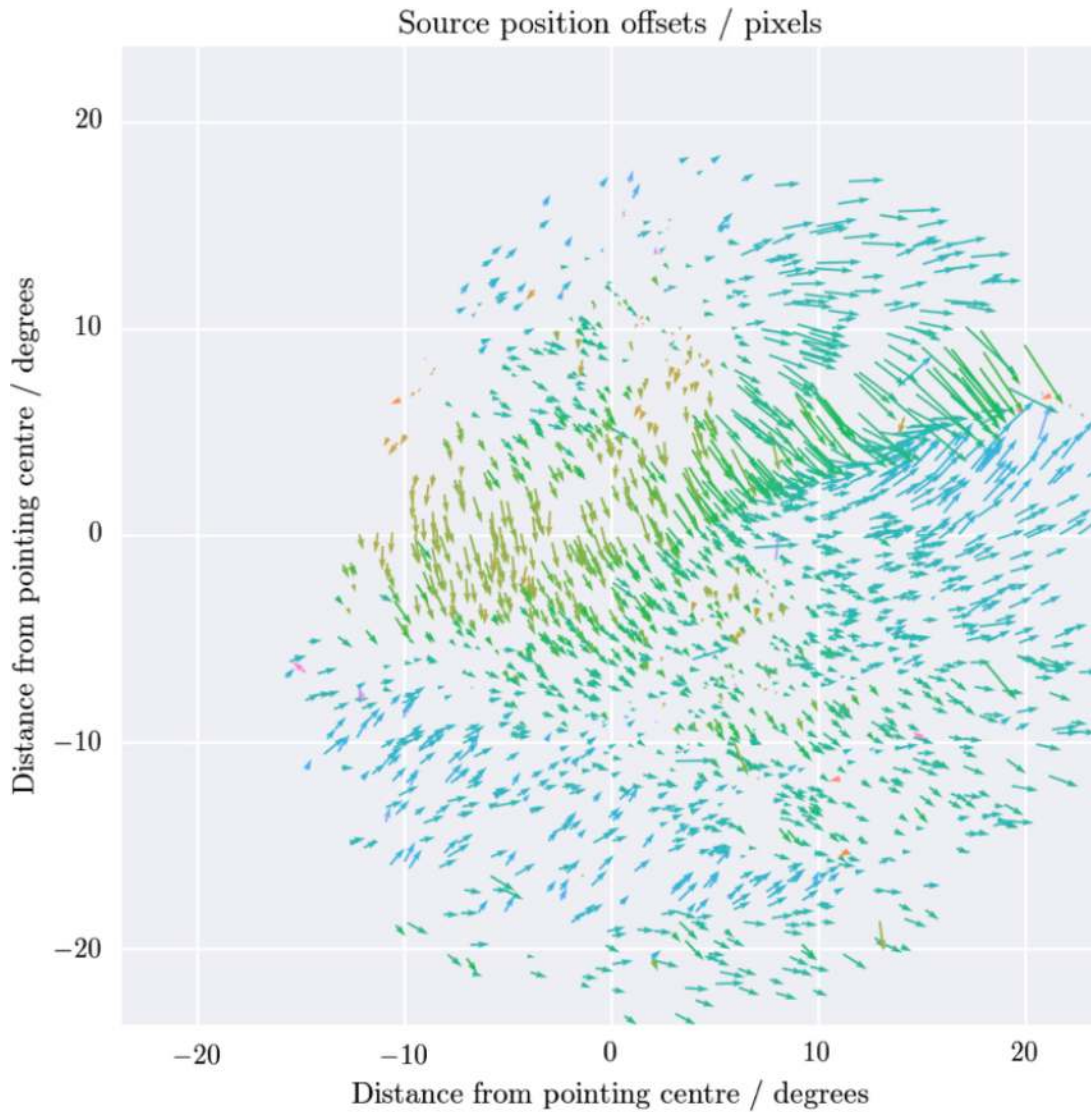
Figure 2.9: Example of source position offsets induced by ionospheric effects. The vectors indicate the direction and magnitude of the offsets of the sources from their reference positions. Note that the vector lengths are in units of pixels rather than degrees. This figure is adapted from Hurley-Walker & Hancock (2018).

image. This algorithm has been fully tested on MWA data, demonstrating an improvement in the mean offset of sources positions by a factor of 3 after applying FITS_WARP (Hurley-Walker & Hancock, 2018).

2.4.2 Flux calibration

In the MWA images calibrated by the in-field calibration or a standard calibrator, the flux scales can deviate from the input amplitude calibration model by $\leq 50\%$ (Duchesne et al., 2020). The reasons could be an inaccurate calibrator model, residual primary beam model errors, or the existence of bright sources other than the calibrator being dominant in the field (for details see Duchesne et al. 2020).

We used the FLUX_WARP software package[7] (Duchesne et al., 2020) to correct for the absolute flux density deviations in the MWA images. Similar to what FITS_WARP did, FLUX_WARP used the GLEAM catalogue as a reference catalogue, and cross-matched it with the sources found in the MWA images to determine the absolute flux density deviations. Then FLUX_WARP fits a smooth function to the deviations and applies the corrections to the MWA images. The fitting functions available in the software include a mean or median of the flux offset, or a linear function of the elevation or declination of the image (Duchesne et al., 2020). For simplicity, we adopted the mean offset for flux correction.

2.5 Image data processing

For my data processing I used the MWA-fast-image-transients pipeline[8], which automates the reduction of MWA data of transient events, including downloading, calibration and imaging on different timescales (for details about the pipeline see Anderson et al. 2021b). The final data products are images on timescales of $2\,\mathrm{m}$, $30\,\mathrm{s}$, and $5\,\mathrm{s}$ for the full bandwidth of $30.72\,\mathrm{MHz}$. The MWA-fast-image-transients pipeline can also produce sub-band images for every $0.5\,\mathrm{s}$ time step,

---

[7]https://gitlab.com/Sunmish/flux_warp
[8]https://github.com/PaulHancock/MWA-fast-image-transients
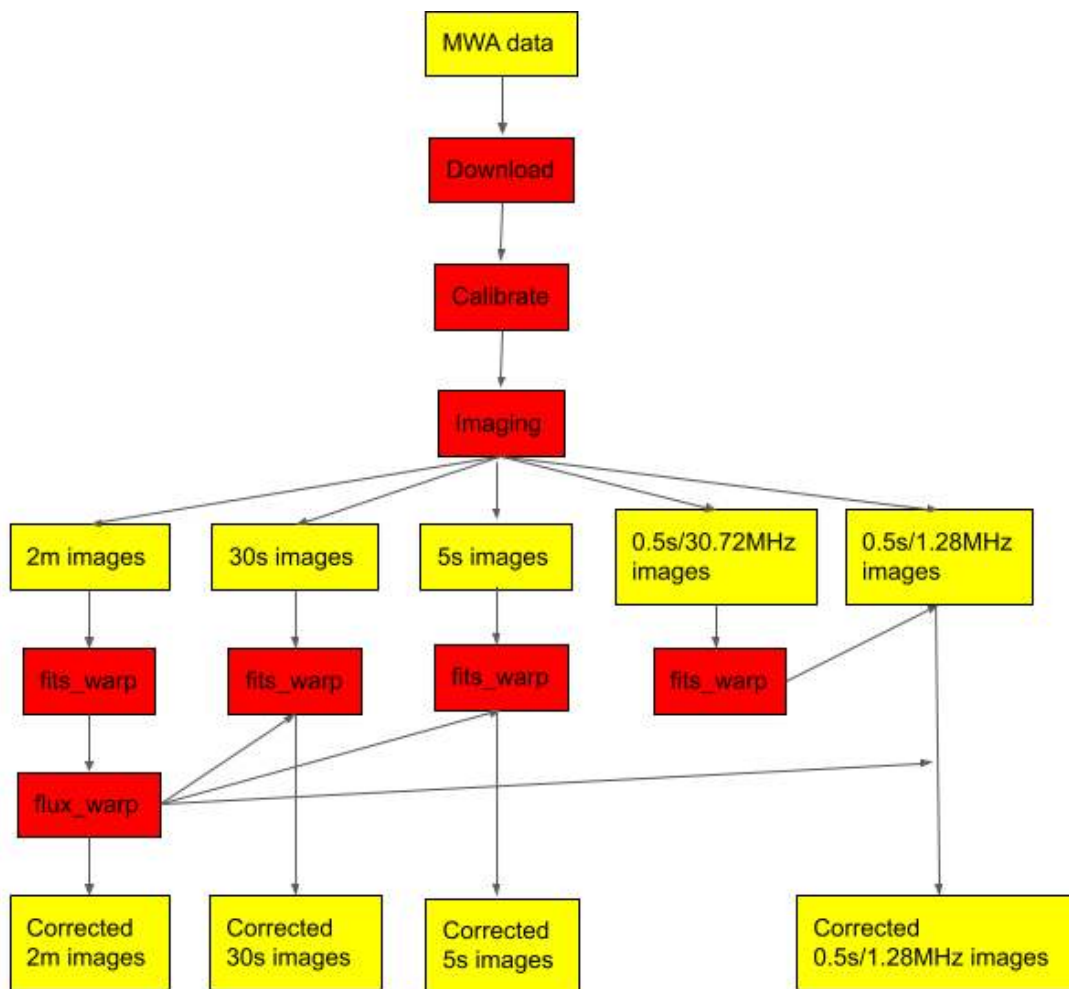
Figure 2.10: A schematic diagram showing the MWA data reduction work-flow. Red boxes represent a script or process, and yellow boxes represent input, intermediate or final data products.

where the bandwidth is split into its constituent 1.28 MHz coarse channels. While there is no universal data processing pipeline for the MWA, I put together specific tools such as FITS_WARP, FLUX_WARP and ROBBIE (a work-flow for detecting transients and variables in the image domain; Hancock et al. 2019b) for my transient reduction case. Here I describe my own custom workflows used to process the MWA data.

Figure 2.10 shows the MWA data reduction work-flow. First we downloaded the measurement sets from the ASVO server. We selected our calibration method (infield or external calibrator) depending on the location of the GRB relative to

bright sources in the sky and the Galactic plane (see Section 2.4). The WSClean algorithm (Offringa et al., 2014; Offringa & Smirnov, 2017) was used to image and deconvolve the 2 min observations of each GRB. Next we made images on 30 s and 5 s timescales, which accommodate the expected dispersive broadening of a prompt radio signal across the MWA observing bandwidth for a redshift of $z \sim 0.1$ (DM$\sim 120\,\mathrm{pc\,cm^{-3}}$; see Section 1.2.3.1) and $z \sim 0.7$ (DM$\sim 840\,\mathrm{pc\,cm^{-3}}$), the lowest and average redshift known for short GRBs (Rowlinson et al., 2013). This was done by splitting each 2 min observation into 4 intervals of 30 s, which were imaged and cleaned separately. We then split the 2 min observation into 22 intervals of 5 s starting from the first timestamp with real data (i.e. abandoning the first 4 s and last 6 s of data, see Anderson et al. 2021b), and created the 5 s images without cleaning due to their high noise levels.

To allow for a de-dispersion search for prompt signals (see Chapter 3), we created sub-band images by splitting the 2 min observation into 0.5 s intervals and the 30.72 MHz bandwidth into 24 1.28 MHz channels, which is the native coarse channel resolution of the MWA correlator (for the MWA system design see Tingay et al. 2013). We also created 0.5 s full band images, which could be used to correct source positions in the 0.5 s sub-band images as discussed below. We performed no cleaning on the 0.5 s timescale images.

Source position offsets caused by ionospheric effects and the errors in the absolute flux density calibration were corrected using FITS_WARP (Hurley-Walker & Hancock, 2018) and FLUX_WARP (Duchesne et al., 2020), which apply corrections to the MWA images via comparisons to the GLEAM catalogue. Ionospheric corrections using FITS_WARP were applied to each individual 2 min, 30 s, and 5 s image. There were too few sources found in the 0.5 s / 1.28 MHz images to perform a reliable position correction, so instead we generated a solution from each 0.5 s / 30.72 MHz image and applied it to the sub-band images in the same time bin. We did not apply a chromatic correction to the frequency dependent ionospheric position offsets ($\propto 1/\nu^2$). At our central observing frequency of 185 MHz,

the relative difference in the position offset within the 30.72 MHz bandwidth is expected to be $\sim 18\%$. Given the ionospheric position offset has a typical value of $\sim$arcmin (Hurley-Walker & Hancock, 2018), this difference would be smaller than the MWA synthesized beam size (see Section 1.3) and thus negligible. However, the flux density calibration was computed by running FLUX_WARP on the ionospherically corrected high signal-to-noise 2 min images, with the resulting solutions then being transferred to the 30 s, 5 s and 0.5 s images.

We did not correct the source positions and flux scales for the observations taken in the compact configuration as their low angular resolution meant that few sources could be matched to the GLEAM catalogue. We expected the ionospheric correction, typically of $\sim$ arcmin, to be much smaller than the ~ 10 arcmin resolution of the compact configuration and thus should not distort our images or analysis. We also expected a consistent flux calibration for the different timescale images across the 30 min compact configuration observations of GRBs as all snapshots were calibrated using a single solution derived from an external calibrator. Note that the flux scale in these images may be incorrect (see Section 2.4.2), but that should not affect our transient and variable search (see below).

2.5.1 Transient and variable search

We adopted the ROBBIE[9] (Hancock et al., 2019b) work-flow, which was further updated in Anderson et al. (2021b) to process the MWA images and search for variable and transient events. For each MWA dataset, ROBBIE first creates a mean image, which is then used to extract a persistent source catalogue and corresponding light curves. Comparisons between the mean and individual images, and a statistical analysis of the catalogue, are then used to identify variable and transient candidates. We can also add a monitoring position into the catalogue of persistent sources, which forces ROBBIE to perform prioritized fitting and extract a light curve at the position to search for associated radio emission (Hancock

---

[9] https://github.com/PaulHancock/Robbie

et al., 2018). Note that the monitoring position could be of a known transient (e.g. a well localised GRB; see Chapter 3).

We characterised the variability of all light curves output by ROBBIE through the derivation of three parameters: the modulation index (m); the de-biased modulation index (m_d), which takes into account the errors on the flux densities; and the probability of being a non-variable source (p_val). The first two parameters are calculated as (Hancock et al., 2019b):

$$m = \frac{\sigma}{\mu}, \tag{2.11}$$

$$m_d = \frac{1}{\mu}\sqrt{\frac{\Sigma_i(\mu - S_i)^2 - \Sigma_i\sigma_i^2}{N}}, \tag{2.12}$$

where S_i and σ_i are the flux density and uncertainty measured from the image at epoch i, N is the total number of epochs, μ and σ are the mean and standard deviation of the measured flux densities. p_val is calculated differently from described in Hancock et al. (2019b). First we normalise the light curve to

$$Z_i = \frac{x_i - \mu}{\sigma_i}, \tag{2.13}$$

which has a zero mean and unit variance. Then we can compute p_val by performing a Kolmogorov-Smirnov test of the normalised light curve $\{Z_i\}$ against a normal distribution. In this way, we account for the effect of varying uncertainties caused by the telescope changing its pointing centre throughout the observation, which changes the local noise for a given sky position (more details can be found in Anderson et al. 2021b). For variable candidates, we followed the threshold set in Hancock et al. (2019b), i.e. p_val $< 10^{-3}$ and $m_d > 0.05$, to distinguish variables from non-variables.

2.6 Beamforming

For the VCS data processing we used the VCS data processing pipeline, which was initially developed for pulsar searches (e.g. Bhat et al. 2016, McSweeney et al. 2017, Meyers et al. 2017 and Ord et al. 2019). This pipeline automates the reduction of MWA VCS data of targeted sources, including downloading, calibration and beamforming at the target positions. The final data product is a time series of Stokes parameters packed into the PSRFITS format (Hotan et al., 2004), which can be further analyzed by the PRESTO software package[10] (Ransom, 2001). Here I present specific details regarding calibrating the VCS data and beamforming at the positions of the target sources.

First is calibration. For each MWA observation, we need to determine the direction independent complex gains, including amplitudes and phases, for each constituent tile (4×4 dipole array) through the calibration process (for details see Ord et al. 2019). We selected a bright source that had been observed in the standard correlator mode within 12 hours of the VCS observation as the calibrator source. The Real Time System (RTS; Mitchell et al. 2008) was used to generate a calibration solution for the amplitude and phase for each of the 24×1.28 MHz sub-bands and each tile from visibilities. We inspected these solutions and discarded tiles showing poor calibration solutions. We also excised the edge channels (0–7 and 120–127) of each of the 24 sub-bands to alleviate the aliasing effects resulting from the channelisation process. We applied this calibration process to each MWA observation before coherently summing the power from the constituent tiles.

Next is beamforming. In order to maximize our sensitivity to any millisecond-duration signals coming from certain directions, we coherently summed the voltages from individual MWA tiles to form a tied-array beam in the signal directions (i.e., coherent beamforming; Swainston et al. 2022). This can be viewed as the interferometer response to a single direction rather than the whole sky (see Section 2.2.2). Relative to incoherent beamforming (which simply sums up the power

---

[10]https://github.com/scottransom/presto

from each tile to preserve a large field of view), this can potentially gain more than an order of magnitude in sensitivity for each phase centered beam (Bhat et al., 2016). The performance of coherent beamforming is affected by a few factors, such as the quality of the calibration solution (for the possible causes of poor solutions see Section 2.4) and the pointing direction of the telescope.

Here I briefly summarise the beamforming process (for more details see Swainston et al. 2022). The essential step is converting cable and geometric delays to the pointing center into phase shifts for each tile. With the knowledge of the delay model and the complex gain information from the calibration solution derived in the calibration process, we can obtain the tile based gain solution to equalise the tile gains and phase all tiles to the same direction. Note that this is different from what the correlator does given that I do not need to choose sweet spots for the observing direction center.

2.7   Time series data processing

Using the VCS tied-array beamformer, we produced time series data with a temporal and frequency resolution of $100\,\mu s$ and $10\,kHz$ for the MWA VCS observations. As the prompt, coherent radio emission we are searching for will be dispersed in time by the medium it propagates through, it was necessary to perform a de-dispersion search to increase our sensitivity to any short-duration ($\sim ms$) signals.

There are quite a few publicly accessible software packages that are designed for dispersed pulse searches, i.e. reading in instrument data and outputting single pulse candidates. Some examples of popular pipelines include HEIMDALL[11] primarily used for FRB searches with Parkes and UTMOST (Champion et al., 2016; Caleb et al., 2017), PRESTO[12] used at Arecibo and Green Bank (Ran-

---

[11]https://sourceforge.net/projects/heimdall-astro/
[12]https://github.com/scottransom/presto

som, 2001), FREDDA used at ASKAP (Bannister et al., 2017), AMBER[13] used at the Westerbork Telescope (Sclocco et al., 2016; Mikhailov & Sclocco, 2018), BURST_SEARCH[14] for the GBT telescope, and BONSAI for CHIME (CHIME/FRB Collaboration et al., 2018). Different software packages implement different algorithms, and they have been optimised for specific survey configurations. Therefore, they are differently sensitive to single pulse signals, and the sensitivity could change in different regions of the parameter space (Keane & Petroff, 2015). So far there has been no universal standard to compare these codes and their efficiency in single pulse searches. More details can be found in Petroff et al. (2019).

We chose the PRESTO software package for the dispersed pulse search because it has been thoroughly tested in pulsar searches using the MWA VCS observations (Bhat et al., 2016; McSweeney et al., 2017; Meyers et al., 2017, 2018; Ord et al., 2019; Xue et al., 2019). PRESTO uses sub-band dedispersion techniques, which performs tree dedispersion over the subbands within the full bandwidth (Ransom, 2011; Spitler et al., 2014). As an incoherent dedispersion method, it is not as accurate as the coherent dedispersion method in recovering the intrinsic pulse shape, but computationally simpler and faster (Zackay & Ofek, 2017).

First we dedispersed the time series using the PREPDATA routine in PRESTO. Compared to other radio telescopes traditionally used for high-time resolution analysis, the MWA is generally less affected by RFI (Offringa et al., 2015). Therefore, we did not perform any RFI excision that is often used at higher observing frequencies (see procedures outlined in Swainston et al. 2021). Nonetheless, any spurious events caused by RFI can be identified from the final candidates by visual inspection. We determined the DM search range of each observation based on the potential DMs of the target source. Then we found out the optimal DM trials using the DDPLAN.PY algorithm in PRESTO using the parameters passed: central frequency, bandwidth, number of channels, and sampling time. As the dispersive channel smearing increases with the DM value, the data could be down

---

[13]https://github.com/TRASAL/AMBER
[14]https://github.com/kiyo-masui/burst_search

sampled to match the smearing time. The DM step size was increased when the DM smearing would cause a loss in sensitivity equal to a DM error the size of half a DM step.

We searched for single pulses from each of the de-dispersed time series using PRESTO's matched-filtering based SINGLE_PULSE_SEARCH.PY routine, which convolves the time series with boxcars of different widths. Single pulse events detected with an S/N above six were classified as candidates (e.g. Chawla et al. 2020, Meyers et al. 2018, Bannister et al. 2012). We adopted the definition of σ, i.e. the noise level, as output by PRESTO for our S/N value (e.g. Zhang et al. 2020). Note that the statistics of this S/N may be complicated by a few facts, mainly that the matching algorithm is difficult to model statistically and the search over different DM trials and pulse widths is not necessarily independent (e.g. Bannister et al. 2012).

Chapter 3

Early-time searches for coherent radio emission from short GRBs with MWA

This chapter is a reproduction of J. Tian, G. E. Anderson, P. J. Hancock, J. C. A. Miller-Jones, M. Sokolowski, A. Rowlinson, A. Williams, J. Morgan, N. Hurley-Walker, D. L. Kaplan, Tara Murphy, S. J. Tingay, M. Johnston-Hollitt, K. W. Bannister, M. E. Bell, B. W. Meyers (2022), "Early-time Searches for Coherent Radio Emission from Short GRBs with the Murchison Widefield Array", Publications of the Astronomical Society of Australia, Volume 39, article id. e003, DOI: https://doi.org/10.1017/pasa.2021.58. I have adapted the chapter to make it better fit into this thesis, avoiding repetition of the materials already included in Chapters 1 and 2 and keeping all references consistent within this thesis.

3.1 Introduction

As discussed in Section 1.1.4.3, there are several models that predict that short GRBs may produce coherent low-frequency radio emission. However, these signals

remain undetected even though there have been many searches for prompt radio emission associated with GRBs (see Section 1.1.5). The MWA, equipped with a rapid-response mode, combined with its wide field-of-view and high sensitivity (see Section 1.3), is an ideal instrument for searching for the model predicted emission via triggered observations of GRBs. In this chapter, we present a low frequency (170–200 MHz) search for coherent radio emission associated with nine short GRBs detected by the *Swift* and/or *Fermi* satellites using the MWA rapid-response observing mode. The MWA began observing these events within 30 to 60 s of their high-energy detection, enabling us to capture any dispersion delayed signals emitted by short GRBs for a typical range of redshifts. Using MWA observations, we conducted transient searches at the GRB positions on different timescales that can accommodate the expected dispersive smearing of a prompt radio signal over the MWA observing bandwidth for typical short GRB redshifts. We also searched for dispersed signals at a temporal and spectral resolution of 0.5 s and 1.28 MHz using the image dedispersion technique, which could improve our sensitivity to any prompt radio signals. Then the fluence and persistent emission upper limits derived from the MWA observations of the nine short GRBs were compared to the short GRB coherent emission models, allowing us to place constraints on key parameters of the models, including the radio emission efficiency of the nearly merged neutron stars, the fraction of magnetic energy in the GRB jet, and the radio emission efficiency of the magnetar remnant (assuming the formation of magnetar remnants by these GRBs). Finally, we discussed how this GRB triggering experiment can be further improved using the MWA VCS mode (to be demonstrated in Chapter 4).

In Section 3.2, we describe the sample of short GRBs analysed in this chapter. We describe the processing pipeline in Section 3.3, followed by data analysis methods we used to search for prompt radio emission on 2 min, 30 s, and 5 s timescales in Section 3.4. We also describe our search for dispersed prompt emission using image de-dispersion techniques with an image temporal and spectral

resolution of 0.5 s and 1.28 MHz in Section 3.4. Our results are then presented in Section 3.5. We compare the flux density and fluence upper limits derived from different GRBs and select the best ones to constrain the models of BNS mergers, as shown in Section 3.6. We focus on GRB 190627A, which is the only GRB in our sample with a redshift measurement and therefore represents the most sensitive low frequency, short timescale limit among the population of short GRBs included in this chapter. In Section 3.7, we discuss how our sample along with other low frequency radio limits on prompt and persistent coherent emission from short GRBs constrain some of the explored emission models, and how these studies can be improved in the context of the MWA.

3.2 GRB sample

As discussed above, in order to search for GRB associated coherent radio emission we have been using the MWA to perform triggered observations of GRBs detected by *Swift* and/or *Fermi* since 2015 (see Section 1.3). There were 22 short GRBs detected by *Swift* and/or *Fermi* during the period from April 2017 to September 2020 that triggered MWA rapid-response observations. After inspecting their images individually, we selected nine GRBs with good image quality to be included in this chapter as listed in Table 3.1 (for their image quality see Figure A.1 and A.2 in Appendix A). Most of the GRBs were discovered by *Fermi*–GBM as it monitors 50% of the sky at any one time (Meegan et al., 2009), much larger than the 1.4 sr field of view of *Swift*–BAT (Gehrels et al., 2004). Among the GRBs not chosen for analysis, six were contaminated by the Sun (these observations were taken before we implemented the Sun suppression algorithm; Hancock et al., 2019a), three were close to the Galactic plane (these may be analysed in the future when we have a good MWA Galactic plane sky model), three *Fermi* GRBs had final positions outside the MWA primary beam (before we implemented real-time pointing updates as the *Fermi* position is improved; Hancock et al., 2019a), and GRB 180805A was published in a previous paper (Anderson et al., 2021b).

The MWA configuration in which each GRB was observed is listed in Table 3.1.

3.2.1 *Swift* triggers

MWA rapid-response observations were triggered on *Swift*–BAT events GRB 190627A (Sonbas et al., 2019a) and GRB 191004A (Cenko et al., 2019a). The advantage of *Swift*–BAT detected GRBs over *Fermi* detected events is that they are often localised by the *Swift* X-ray Telescope (XRT; Burrows et al. 2005), which provides arcsec position localisations and makes afterglow detections/redshift determinations much more likely. The XRT also performs these observations rapidly following the BAT trigger (109.8 s and 81.5 s for GRB 190627A and GRB 191004A, respectively; Sonbas et al. 2019b, Cenko et al. 2019b), with the resulting X-ray light curves allowing us to constrain coherent radio emission models (see Section 3.6.1).

GRB 190627A has a brief duration of 1.6 s (Barthelmy et al., 2019), placing it in the short GRB category based on the usual criterion $T_{90} \leq 2\,$s (Kouveliotou et al., 1993). Nonetheless, there are a few caveats about this identification. Despite the short duration of GRB 190627A, the relative softness of its spectrum makes it intermediate between most short and long bursts detected by *Swift*–BAT (Barthelmy et al., 2019). GRB 190627A is the only event with a spectroscopic redshift of $z = 1.942$ (Japelj et al., 2019) in our sample, which helps us to constrain its DM when searching for associated dispersed signals as described in Section 3.4.3. However, this redshift is unusually high for a short GRB, requiring a very high efficiency to produce observable emission given the limited energy reservoir of binary mergers (Berger, 2014). Additionally, GRB 190627A has a bright optical afterglow (Japelj et al., 2019), making it unusual in the population of short GRBs (Kann, 2013). Therefore, there is ambiguity in classifying GRB 190627A as being short.

GRB 191004A has been included in our sample as one of our rare triggers on *Swift* short GRBs, though it had a duration of 2.44 s (Sakamoto et al., 2019). We

calculated its hardness ratio (i.e., fluence in 50–100 keV over fluence in 25–50 keV) to be ≈ 1.6, intermediate between the short and long population of *Swift* GRBs (see figure 8 in Lien et al. 2016). There is no other information available for determining whether it is short or long, such as rest-frame duration (Zhang et al., 2009; Belczynski et al., 2010) or the isotropic gamma-ray energy and spectral peak (Lü et al., 2010). A few high-redshift long GRBs with rest-frame durations shorter than 2 s have been found to possess the properties of short GRBs, such as a hard spectrum and a large offset from the host galaxy centre (e.g. Ahumada et al. 2021). Given there is no clear distinction in the durations of long and short GRBs (Berger, 2014) and the rest-frame duration of GRB 191004A would be < 2 s should it occur at $z > 0.2$, we treated GRB 191004A as if it were short. Note that the first three 2 min observations following the *Swift* trigger were corrupted so our first MWA observation of this source was delayed 6.35 min with respect to the GRB detection as shown in Table 3.1.

3.2.2 *Fermi* triggers

Seven GRBs were triggered by the *Fermi*–GBM and detected only in the gamma-ray band. For five out of the seven events, we were able to obtain 15 continuous MWA snapshot observations, covering 30 min post-burst. During our MWA observation of GRB 190804A, the source coordinates were updated by *Fermi* by more than 20 deg, resulting in the first few MWA pointing centres being well separated from the final GRB position, and subsequently discarded. Note that in Table 3.1, the quoted start time is the earliest time that the MWA was actually pointed at the GRB, with the time post-burst corresponding to this delay with respect to the GRB detection by the *Fermi*–GBM. We also discarded the last few observations of GRB 190420.98, of which the pointing centres were driven away from the GRB location (beyond 50% of the primary beam) by the Sun suppression algorithm (Hancock et al., 2019a). Among the seven *Fermi* GRBs, three were further localised by the Interplanetary Network (IPN; Hurley et al. 2013),

GRB	Detector	Trigger No.	Start Time (UT)	Time (sec) post-burst	Config.	RA (deg)	Dec (deg)	Uncertainty	T$_{90}$ (sec)	Localisation instrument	Calibrators
170827B	Fermi	525555489	19:38:38	34	I	30.39	-47.86	1.29°	0.18	IPN	PicA
190420.98	Fermi	577495949	23:33:18	53	IIE	319.29	-66.41	2.04°	1.47	Fermi–GBM	IF
190627A	Swift	911609	11:19:26	55	IIE	244.828	-5.289	1.7''	1.6	Swift–XRT	HerA+3C353
190712.02	Fermi	584583925	00:26:06	46	IIE	341.06	-38.41	9.21°	1.79	Fermi–GBM	IF
190804A	Fermi	586574612	01:32:54	567	IIE	108.02	-64.86	12.02°	2	Fermi–GBM	IF
190903A	Fermi	589223981	17:20:30	54	IIC	63.95	-59.485	0.46°	0.27	IPN	PicA
191004A	Swift	927825	18:13:34	392	IIC	31.668	-36.933	1.7''	2.44	Swift–XRT	PicA
200325A	Fermi	606799116	03:19:26	54	IIE	31.72	-31.816	4'	0.96	Swift–BAT	IF
200327A	Fermi	607035413	20:57:50	62	IIE	236.574	-4.217	13.7'	0.64	IPN	IF

Table 3.1: Short GRBs that triggered the MWA rapid-response mode. GRB 191004A had a burst duration slightly longer than 2 s but is assumed to be short (see the text in Section 3.2.1).

1: The GRB detector that triggered the MWA rapid-response mode;

2: The unique number assigned to each GRB detected by Fermi or Swift.

3: The start time in UT of the first MWA observation that contained the position of the GRB within 50% of the MWA primary beam. Note that the date is given by the GRB name in the first column with the convention of YYMMDD;

4: The delay of the MWA observation with respect to the GRB detection by Fermi or Swift;

5: The MWA array configuration of the GRB observation, including phase I ('I'), or phase II extended ('IIE') or compact ('IIC');

6: The uncertainty corresponds to the 1σ and 90% positional confidence for Fermi- and Swift-detected GRBs, respectively;

7: The time taken to accumulate 90% of the burst fluence starting at the 5% fluence level (short GRBs are usually considered to have a T$_{90} \leq$ 2 s; Kouveliotou et al. 1993): a: Svinkin et al. (2017); b: Fermi–GBM burst catalog at HEASARC: https://heasarc.gsfc.nasa.gov/W3Browse/fermi/fermigbrst.html; c: Barthelmy et al. (2019); d: Ghumatkar et al. (2019); e: Mailyan & Meegan (2019); f: Sakamoto et al. (2019);

8: The instrument that provides the best localisation for the GRB: g: the IPN GRB database table: https://heasarc.gsfc.nasa.gov/w3browse/all/ipngrb.html; h: Fermi trigger information: https://gcn.gsfc.nasa.gov/fermi_grbs.html; i: Swift trigger information: https://gcn.gsfc.nasa.gov/swift_grbs.html;

9: The calibration of the MWA observation was either performed using an external calibrator (named) or via an infield calibration (IF) using the GLEAM survey (Hurley-Walker et al., 2017) as a sky model.

one was later localised by *Swift*–BAT, whereas for the other four events, the only position was provided by the *Fermi*–GBM. The positional information contained in the GBM Final Position Notice usually have uncertainties of about a 1–10 deg radius, which are less accurate than the IPN and BAT localisations.

3.3   Data Processing

For our data processing we used the MWA-fast-image-transients pipeline, which automates the reduction of MWA data of transient events, including downloading, calibration and imaging on different timescales (for details see Chapter 2). The final data products are images on timescales of 2 min, 30 s, and 5 s as well as 0.5 s/1.28 MHz (coarse channel, i.e. splitting the 30.72 MHz bandwidth into 24) images. It should be noted that every 2 min observation actually means 112 s of data due to the flagging of data at the beginning and end of each observation (see Anderson et al. 2021b for details). Here we present specific details regarding the image calibration and cleaning of the nine short GRBs in our sample.

3.3.1   Calibration

We used two calibration methods (infield calibration or single calibrator) depending on the location of the GRB relative to bright sources in the field (for details see Chapter 2). The calibration methods adopted for each of the nine GRBs are listed in the last column of Table 3.1. We applied the in-field calibration to five GRBs. Since there was a significant amount of extended emission in the region of GRB 190712.02, we discarded the baselines shorter than 500 m before applying the in-field calibration. Self-calibration was applied on GRB 190420.98 to improve the image quality. For the other four GRBs, we derived calibration solutions using calibrator observations of a single bright source including PicA, HerA, and 3C353.

3.3.2 Imaging

The MWA-fast-image-transients pipeline, which incorporates the WSClean algorithm (Offringa et al., 2014; Offringa & Smirnov, 2017), was used to image and deconvolve the 2 min observations of each GRB. We adopted a pixel scale of 32 arcsec for the observations taken in the MWA phase I configuration, 16 arcsec for the phase II extended configuration, and 1.6 arcmin for the phase II compact configuration. The default image size was 4096×4096 pixels. For the *Fermi* GRBs in our sample with poor localisations, we increased the image size to as large as 8000×8000 pixels. For the GRBs observed with the lower angular resolution compact configuration, we made smaller images of 1000×1000 pixels. See Figure A.1 and A.2 in Appendix A for the first 2 min snapshots of the nine short GRBs in our sample.

We also created full band images on 30 s and 5 s timescales (for accommodating dispersed prompt radio signals) and 0.5 s/1.28 MHz sub-band images (for image dedispersion). Details on the imaging process and corrections of ionosphere induced source position offsets and flux scales can be found in Chapter 2.

3.4 Data Analysis

In this section we first describe the software used to search for transient and variable candidates in the MWA images, followed by the criteria we set to remove invalid candidates. We consider transient candidates as sources that appear in individual epochs and variable candidates as sources that remain detectable in multiple epochs but with a variable flux density, both of which may be coherent radio emission associated with GRBs.

3.4.1 Transient and variable search

We adopted the Robbie (Hancock et al., 2019b) work-flow to process the MWA images and search for variable and transient events within the positional error

regions of each GRB (for more details on running Robbie see Chapter 2). We devised two analysis methods depending on the GRB localisation accuracy. The two *Swift* GRBs in our sample were localised by XRT, which resulted in smaller position errors than the angular resolution of MWA (Wayth et al., 2018). Therefore, we can force Robbie to perform priorized fitting and extract a light curve at the best known position of the GRB to search for associated radio emission (Hancock et al. 2019b; also see Chapter 2 for details on prioritized fitting).

For the less well localised *Fermi* GRBs, we assumed that any associated variable or transient candidates were located within the *Fermi*–GBM 1σ error region (Narayana Bhat et al., 2016) if they were not further localised by *Swift*–BAT or the IPN. In addition, since the noise level increases towards the edge of the MWA primary beam that can create spurious signals, we restricted our source search to the inner part of the MWA primary beam, within 50% of the maximum sensitivity. Among the different MWA pointings in the $15 \times 2\,\mathrm{min}$ snapshot observations of a GRB, we picked the first pointing to determine the MWA primary beam as the prompt radio emission we are targeting is most likely to appear in the first few snapshots (see Section 2.1). We therefore only searched for candidates within the overlap between these two regions. An example of the overlap region between the IPN position of GRB 170827B and 50% of the MWA primary beam within which we searched for transients and variables is shown in Figure 3.1 (for other *Fermi* GRBs see Figures A.1 and A.2 in Appendix A). The final list of variable and transient candidates within the region of interest (ROI) of all *Fermi* GRBs were retained for further inspection.

3.4.2 Transient and variable selection

For the *Swift* GRBs, we looked for any transients or variables detected by Robbie at their known positions. We also inspected the light curves and corresponding variability statistics as output by Robbie that were generated via priorized fitting at the GRB positions for evidence of transient or variable behaviour.
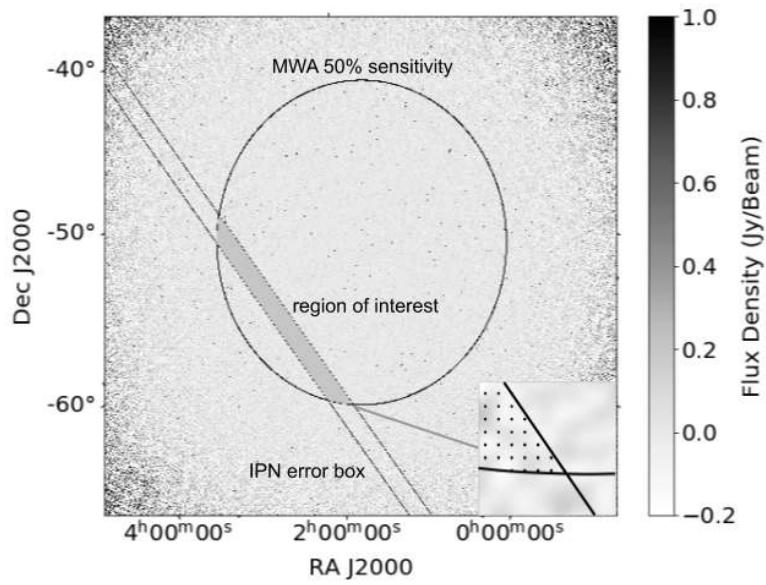
Figure 3.1: MWA image of the field of GRB 170827B. The image size is $30° \times 30°$, and the integration time is $2\,\mathrm{min}$ beginning 34s post-burst. The boundaries of the MWA primary beam and the IPN error box are shown with black lines, where the overlap (grey shaded area) shows the region of interest (ROI) we searched for transients and variables. The inset at the bottom right corner is a zoomed in view to display the black dots that illustrate the independent pixels selected for the de-dispersion analysis (see Section 3.4.3).

For the *Fermi* GRBs, we inspected the Robbie transient and variable candidates found within the ROI. In order to make a first cut on transient and variable candidate selection, we devised a set of tests to filter out false positives (such as noise fluctuations or imaging artefacts) as described in the following.

All transient candidates had to have a signal-to-noise ratio (SNR) ≥ 6, which corresponds to a false positive rate of $\sim 10^{-9}$ under the assumption of Gaussian noise that is independent in both the space and time dimensions. The number of trials was estimated by the number of synthesised beams in the ROI. For example, for GRB 190420.98 there were $\sim 2 \times 10^5$ synthesised beams in the ROI, and there were ten 2 min snapshots, resulting in a final trial number of $\sim 2 \times 10^6$. Therefore, we expected a false positive transient rate of 2×10^{-3} at a $6\,\sigma$ level in the ROI for GRB 190420.98 for the full 20 min observation. See Table B.2 in Appendix B, which lists the number of synthesised beams, the transient false positive rate $\geq 6\sigma$ within each ROI for each transient timescale (2 min, 30 s, and 5 s) assuming Gaussian statistics, and the total number of transient candidates detected by Robbie for each *Fermi* GRB.

In order to check the accuracy of the Gaussian noise assumption, we compared the distribution of real noise in the MWA image of GRBs to the Gaussian distribution. Figure 3.2 shows an example of the noise distribution observed in the ROI of the first 2 min image of GRB 190420.98 (see Figure A.2 in Appendix A). Note that we have subtracted the mean value from the noise and normalised the noise using the RMS within the ROI. We observed a rate of 3×10^{-3}, 8×10^{-4}, 2×10^{-4} and 0 for events with a SNR above 3, 4, 5 and 6, respectively, against the expected false positive rate of 1×10^{-3}, 3×10^{-5}, 3×10^{-7} and 1×10^{-9} under the Gaussian noise assumption. Furthermore, we subtracted a standard Gaussian function from the observed noise distribution to demonstrate the actual variation in probability density $\lesssim 0.002$, as shown in the bottom panel of Figure 3.2. The above comparisons suggest the Gaussian distribution is a reasonable approximation of the real noise, and thus could be used to estimate noise induced false
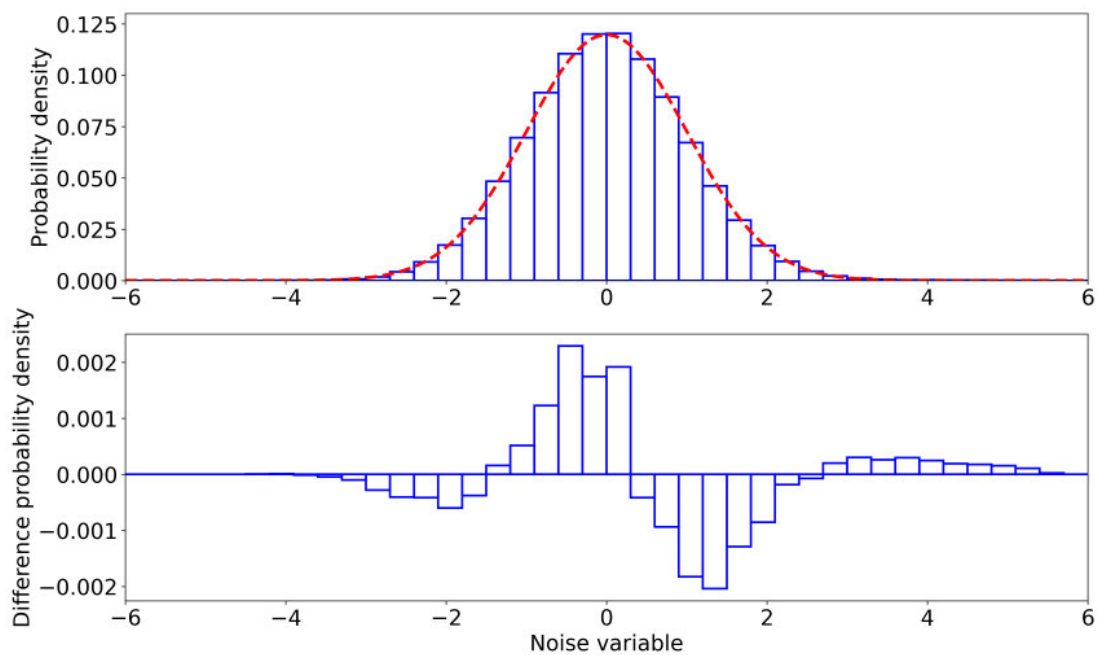
Figure 3.2: Distribution of the noise observed in the ROI of the first 2 min image of GRB 190420.98 (top; see Figure A.2 in Appendix A) and difference between the observed noise distribution and the ideal Gaussian function (bottom). The dashed red line is a standard Gaussian curve, and shows how close the noise distribution is to Gaussian noise (see Section 3.4.2).

signals.

As a sanity check, we used another method to estimate the expected transient false positive rate in each GRB ROI. Again assuming the image noise conforms to Gaussian statistics, we estimated the expected number of false positive events in the ROI by taking the number of candidates found in a larger image region defined by the 50% MWA primary beam and then multiplying by the ratio of the region areas. In the case where more transient candidates were detected by ROBBIE in the ROI than predicted via this method, we inspected the individual images and removed any candidates that were consistent with sidelobes from bright sources or other imaging artefacts. For example, while we detected a transient candidate in the ROI for GRB 190420.98, there were significant sidelobe artefacts from the nearby radio galaxy PKS 2153-69, indicating the candidate was unlikely to be real. The expected transient false positive rate within the ROI of each of the seven *Fermi* GRBs based on comparisons to the number of false events in the MWA 50% primary beam can be found in Table B.2.

For variable candidates, we followed the threshold set in Hancock et al. (2019b), i.e. p_val $< 10^{-3}$ and $m_d > 0.05$, to distinguish variables from non-variables. As a sanity check, we again computed the number of variables in the MWA 50% primary beam to estimate the expected variable false positive rate in the ROI as we did for transient candidates. In the case of an excess of variables in the ROI, we compared their light curves with the light curves of nearby sources. If a variable candidate showed the same trend of variation as the nearby sources, the variation was probably caused by short-timescale calibration, measurement, or instrumental errors rather than being intrinsic to the source (Bell et al., 2019). All variable candidates found by ROBBIE and the expected variable false positive rate within each *Fermi* GRB ROI are listed in Table B.2.

Following this analysis, no transients or variables were identified in the ROIs of the *Fermi* GRBs. Based on minimising the false positive rate assumed from Gaussian statistics, we quote $6\,\sigma$ flux density upper limits (6 times the average

GRB	Upper limit (Jy/beam)			
	30 min	2 min	30 s	5 s
170827B	0.41	0.94	2.1	2.1
190420.98	0.29	0.27	0.58	1.1
190627A	0.027	0.084	0.29	0.42
190712.02	0.33	0.86	2.1	4.6
190804A	0.21	0.58	2.1	4.1
190903A	2.9	11	15	20
191004A	1.1	2.0	1.9	1.9
200325A	0.19	0.39	0.81	1.7
200327A	0.2	0.71	1.4	3.2

Table 3.2: Upper limits on the radio flux density of transient and variable emission associated with the nine short GRBs in our sample. We quote $6\,\sigma$ upper limits (6 times the average RMS within the ROI) for *Fermi* GRBs and $3\,\sigma$ for *Swift* GRBs. Given the noise evolves with time for each GRB, we quote the maximum value for the upper limit. We also include the 3σ deep limit derived from the 30 min full observation for each GRB.

RMS within the ROI) for each of the *Fermi* GRBs on timescales of 2 min, 30 s, and 5 s, as shown in Table 3.2. As the light curves generated at the position of the *Swift* GRBs on different timescales are consistent with the noise, we quote $3\,\sigma$ flux density upper limits. We also include a $3\,\sigma$ deep limit derived from the 30 min full observation for each GRB in Table 3.2, which can be used to constrain persistent emission models (see Section 3.6.2.3).

3.4.3 Search for dispersed signals

Our observations are specifically targeting prompt, coherent radio signals predicted to be associated with short GRBs, which will be dispersed in time by the intervening medium between their origin and the Earth. We therefore perform a search for dispersed signals across a wide range of DMs over the entire ~ 30 min triggered observation. A technique has been developed to search for dispersed signals in short timescale, sub-band radio images of a transient event, which generates a de-dispersed time series in units of SNR at a single sky position (for details see Anderson et al. 2021b). The de-dispersion code has four main steps for creating de-dispersed time series, which was run on all relevant sky positions

within the ROI of each short GRB.

1. *Create a dynamic spectrum at each relevant sky position using the 0.5 s sub-band images.* For *Swift* GRBs, we created a dynamic spectrum at the pixel coincident with the GRB position. For *Fermi* GRBs with large positional errors, we only processed the independent sky/field positions within the ROI, which were essentially one position per synthesised beam as illustrated in Figure 3.1. The search areas of GRB 190712.02 and GRB 190804A were prohibitively large (see Figure A.2 in Appendix A) so we did not perform this analysis on these two *Fermi* GRBs.

2. *Create a de-dispersed time series from each dynamic spectrum.* For every $0.5\,\mathrm{s}$ time step and $12\,\mathrm{pc\,cm^{-3}}$ DM trial across the whole $30\,\mathrm{min}$ observation (see details in the next paragraph) we calculated the average de-dispersed flux density over the dynamic spectrum pixels crossed by the dispersive sweep (see Anderson et al. 2021b for a visualisation of the dynamic spectrum and de-dispersed time series).

3. *Estimate the noise levels of the de-dispersed time series.* For *Swift* GRBs, this was calculated by running the de-dispersion code on 100 nearby position pixels (in addition to the signal pixel) to create 100 de-dispersed time series. To remove any persistent emission that may be at that position, we averaged each of the 101 de-dispersed timeseries in time and subtracted this mean from their corresponding parent timeseries. We then calculated the standard deviation of the 100 mean subtracted timeseries (not including the signal pixel), which we defined as the de-dispersed time series of the noise. For *Fermi* GRBs, the noise was estimated in the same way but by averaging the de-dispersed time series created at each independent pixel in the ROI.

4. *Create the final de-dispersed time series in SNR units.* This was done by dividing the de-dispersed time series at the signal pixel (*Swift*) or indepen-

dent pixels in the ROI (*Fermi*) by the de-dispersed time series of the noise derived in the previous step.

The DM resolution of our search for dispersed signals ($12\,\mathrm{pc\,cm^{-3}}$) was chosen by equating the expected dispersion smearing across the full $30.72\,\mathrm{MHz}$ bandwidth to the temporal resolution of $0.5\,\mathrm{s}$ (see eq. 1 in Anderson et al. 2018a). All but one of the GRBs in our sample have no redshift measurement so we searched for dispersed signals across the DM space that covers the known redshift range of short GRBs ($0.1 < z < 2.5$; Rowlinson et al. 2013). The contribution of the intergalactic medium to the DM of a short GRB can be estimated from the redshift for the cosmological paradigm of a flat universe. We adopted the method described by Macquart et al. (2020) to calculate $\mathrm{DM_{IGM}}$, taking into account the redshift evolution of the fraction of cosmic baryons in diffuse ionized gas. The redshift range corresponded to a range of $90 < \mathrm{DM_{IGM}} < 2400\ \mathrm{pc\,cm^{-3}}$. Considering the typically large offset of short GRBs from the centers of their host galaxies (Fong & Berger, 2013), we assumed the DM contribution from their host galaxies to be small ($\mathrm{DM_{host}} \sim 30\,\mathrm{pc\,cm^{-3}}$; Cordes & Lazio 2002). Assuming a similarly small contribution from the Milky Way based on the YMW16 DM model ($\mathrm{DM_{MW}} \sim 30\,\mathrm{pc\,cm^{-3}}$; Yao et al. 2017), we adopted a DM range of 150–2500 $\mathrm{pc\,cm^{-3}}$ for our search for dispersed signals associated with GRBs without a known redshift.

The redshift of GRB 190627A corresponded to a $\mathrm{DM_{IGM}}$ of $\sim 1800\,\mathrm{pc\,cm^{-3}}$. However, this value can vary depending on the number of galactic halos intersected by the line of sight, corresponding to a possible DM range between 1400 and 2400 $\mathrm{pc\,cm^{-3}}$, which encompasses 90% of the expected values (Macquart et al., 2020). The DM contribution from the Milky Way in the direction of GRB 190627A ($l = 8.17°$, $b = 30.26°$) is estimated to be $\mathrm{DM_{MW}} \sim 50\,\mathrm{pc\,cm^{-3}}$ based on the YMW16 electron-density model (Yao et al., 2017). We therefore estimate a DM of $\mathrm{DM_{host}} + \mathrm{DM_{MW}} + \mathrm{DM_{IGM}} = 1900^{+600}_{-400}\,\mathrm{pc\,cm^{-3}}$ for GRB 190627A.

In order to set a threshold for selecting dispersed signal candidates for further

investigation in the resulting de-dispersed time series, we first considered the *Swift* GRBs and determined the number of trials based on the time and DM steps used in our analysis. Given that there are $\sim 3 \times 10^6$ trials for GRB 191004A and $\sim 10^6$ for GRB 190627A, we set a threshold of 5σ, corresponding to less than one false positive for each *Swift* GRB. In the case of *Fermi* GRBs, which are not localised to a single pixel, we assessed the noise statistics of the de-dispersed time series in the ROI for each event by creating a set of time series from the same dataset using (nonphysical) negative DM values. If the GRB error region contains only noise, a de-dispersion analysis with positive and negative DMs (same range of absolute values) should give similar SNR distributions. Table 3.3 shows a comparison of the maximum SNR and number of high SNR events above 5σ for the set of positive and negative DMs for each *Fermi* GRB. We also include the expected number of false positive events $> 5\,\sigma$, along with the maximum SNR for which we expect there to be only one false positive event assuming a Gaussian distribution. From Table 3.3, one can see that the high SNR events observed in our dataset are consistent with noise. There are fewer detected events above 5σ than the expected number of false positive events, which may be caused by an overestimation of the noise. The noise calculated in our data using the standard deviation of a population of pixels was affected by the sensitivity changing across the image, which is higher than the value expected in the case of an unchanged sensitivity. If any signals are detected with a higher SNR in the positive de-dispersed time series than the maximum measured in the negative de-dispersed time series, then it is possible that they are real signals.

In the case of no dispersed signal detections in the de-dispersed time series, we derived an upper limit for each *Swift* GRB using signal simulations (see Section 3.4.4) and adopted a 7σ upper limit for each *Fermi* GRB given less than one event above 7σ is expected from Gaussian statistics (see Table 3.3). We present our dispersed signal search results in units of fluence (Jy ms, the integrated flux density over the pulse width), which is common in the fields of FRB and pulsar

astrophysics (see Tables 3.3 and 3.4).

3.4.4   Dispersed signal simulations for well localised GRBs

As GRBs 190627A, 191004A, and GRB 200325A were well localised by *Swift* (*Fermi* GRB 200325A was localised by *Swift*–BAT to within 50 synthesised beams), we were able to inject simulated pulses into the de-dispersed time series to determine our sensitivity to such signals in each MWA observation, thereby allowing us to derive fluence limits as a function of DM (as done by Anderson et al. 2021b). As GRB 191004A and GRB 200325A have no known redshift, we simulated pulses over a large DM range, including 150, 500, 1000, 1500, 2000 and 2500 pc cm^{-3}. As the redshift is known for GRB 190627A, we simulated pulses over a smaller DM range between 1500 and 2500 pc cm^{-3}. By injecting signals over a wide range of fluence values, we were able to test the efficiency of our detection algorithm in the three GRB datasets, which are plotted in Figure 3.3. The fluence limits quoted in Table 3.4 are the signal fluence corresponding to the 90% detection efficiency of our algorithm. The performance of our algorithm was different for each MWA observation depending on many factors such as the presence of bright sources in the field, the GRB location within the primary beam, and the elevation of the observation.

3.4.5   Fluence limits for *Fermi* GRBs

Signal injection was not a viable method for calculating the fluence limits of the *Fermi* GRBs as their poorer localisations means that the sensitivity changes significantly across the ROI, and the performance of our algorithm is dependent on the sky position we choose to inject the signals. Although we could provide a fluence limit as a function of DM and signal position in the ROI using the signal injection technique for a given *Fermi* GRB, it would be hugely computationally expensive. Instead we created a de-dispersed time series for each of the independent positions in the ROI and derived a 7σ fluence upper limit for each of the

GRB	DM	Trial number	Maximum SNR	Critical SNR for 1 event	Detected events above 5σ	Expected false events above 5σ	Fluence limit (Jy ms)
170827B	P	$\sim 2 \times 10^{10}$	6.564	6.5	1920	5733	610–1616
	N		6.662		1395		
190420.98	P	$\sim 10^{11}$	6.936	6.9	15195	28665	609–1609
	N		6.750		15375		
190903A	P	$\sim 10^{9}$	5.237	6	40	287	2067–12110
	N		5.351		50		
200327A	P	$\sim 10^{10}$	6.190	6.4	2415	2866	166–2064
	N		6.177		2324		

Table 3.3: Results following the search for dispersed signals associated with *Fermi* GRBs. This includes a comparison of high SNR events arising from the positive and negative DM time series analysis described in Section 3.4.3. We also list the 7σ upper limits on the fluence for each GRB in the last column. Given the noise varies with DM, time and the GRB position within the ROI due to the MWA primary beam, we present a range for the fluence upper limits (see details in Section 3.4.5). GRB 190712.02 and GRB 190804A are not included in this analysis due to their poor localisations (see Section 3.4.3), and GRB 200325A is analyzed along with the *Swift* GRBs (see Section 3.4.4).

1: The positive (P) or negative (N) DMs used to create the de-dispersed time series;

2: The trial number estimated from the number of time steps, DM trials and synthesised beams (for which a de-dispersed time series was generated) within the ROI;

3: The maximum SNR event detected;

4: The critical SNR beyond which we expect there to be just one event;

5: The number of events detected with SNRs above 5σ in the positive and negative DM de-dispersed time series;

6: The expected false positive event rate above 5σ assuming a Gaussian distribution.

7: The 7σ fluence limits on dispersed signals associated with each GRB.

GRB	fluence limit (Jy ms)
190627A	80–100
191004A	1300–1600
200325A	600–1200

Table 3.4: The fluence limit on dispersed signals for the two *Swift* GRBs and one *Fermi* GRB. These limits correspond to the 90% detection efficiency of our detection algorithm to simulated signals injected into the dedispersed timeseries of these three events (see Section 3.4.4).

Fermi GRBs using the noise calculated from these de-dispersed time series, corresponding to a false positive rate of $\sim 10^{-12}$ under the assumption of Gaussian noise (see Table 3.3). Given the noise varies with DM, time, and the position in the MWA primary beam, we present a range for the fluence upper limits for the *Fermi* GRBs.

3.5 Results

3.5.1 *Swift* GRBs

The light curves derived at the position of the two *Swift* GRBs using priorized fitting showed no evidence of variable or transient radio emission over any of the timescales investigated (see Table B.1 in Section B for the corresponding variability parameters described in Section 3.4.1) and were consistent with the local rms noise. For both events we quote the 3σ upper limits on the flux density of an associated radio transient on timescales of $30\,\mathrm{min}$, $2\,\mathrm{min}$, $30\,\mathrm{s}$, and $5\,\mathrm{s}$ in Table 3.2.

We also performed a search for dispersed signals at the position of the two *Swift* GRBs but none were detected above $5\,\sigma$ (which is well below our detection threshold of $7\,\sigma$). In order to calculate the efficiency of our detection algorithm to dispersed signals, we injected simulated pulses covering a fluence range of 30–$140\,\mathrm{Jy\,ms}$ and a DM range of 1500–$2500\,\mathrm{pc\,cm^{-3}}$ into the dedispersed timeseries of GRB 190627A (see Sections 3.4.3 and 3.4.4). The variation of detection
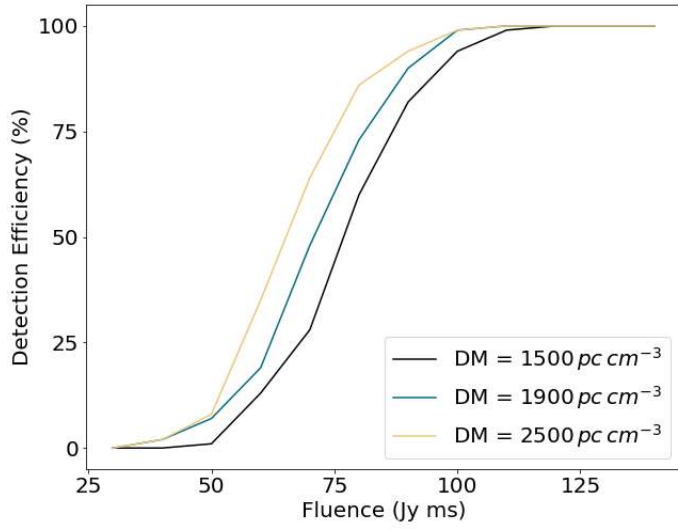
(a) GRB 190627A
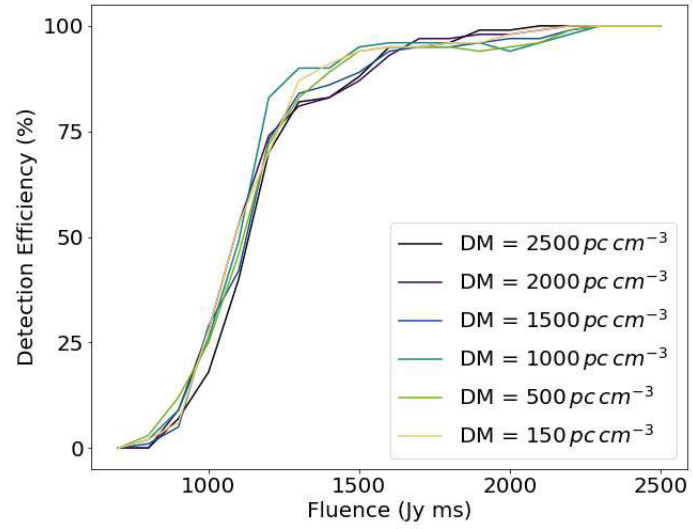
(b) GRB 191004A
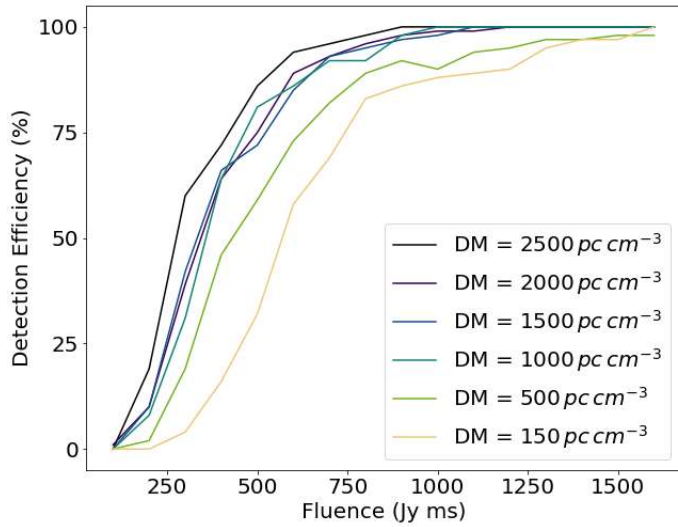
(c) GRB 200325A

Figure 3.3: Detection efficiency of dispersed signals as a function of fluence for GRB 190627A, GRB 191004A and GRB 200325A calculated through signal injection (see Section 3.4.4). The DM ranges of the simulated signals were based on the known redshift of GRB 190627A (see Section 3.4.3) or in the case of GRB 191004A and GRB 200325A, the known redshift range of short GRBs.

efficiency as a function of fluence for this GRB is shown in Figure 3.3(a), which increases with increasing DM. For this DM range, we found a 90% detection efficiency for signals with a fluence of 80–100 Jy ms. Note that the 90% detection efficiency is commonly used as a threshold in FRB simulations to validate FRB search pipelines (e.g. Farah et al. 2019; Gupta et al. 2021). As GRB 191004A has no known redshift, we performed this simulation over a much broader DM range of 150–2500 pc cm^{-3} (see Section 3.4.3). The detection efficiency of dispersed signals in the GRB 191004A dataset as a function of fluence for various DM values are also shown in Figure 3.3(b), which indicates a 90% detection efficiency between 1300 and 1600 Jy ms within the DM range explored. The GRB 191004A dataset is therefore less sensitive than that of GRB 190627A, which reflects the different noise levels in the images of these two GRBs (see Figure A.1 in Appendix A). The much higher noise in the field of GRB 191004A is caused by the sidelobes from a nearby bright source (Fornax A). We use the 90% detection efficiency as the fluence limit in our analysis in Section 3.6 for both *Swift* GRBs, which are also listed in Table 3.4.

3.5.2 *Fermi* GRBs

We inspected the transient candidates detected on timescales of 2 min, 30 s, and 5 s from the seven *Fermi* GRBs (see Table B.2). We used two different methods to estimate the expected false positive detection rate (see Section 3.4.2). Given that there was no transient candidate passing our inspection, we quote a 6σ upper limit on the flux density for the *Fermi* GRBs, as shown in Table 3.2.

We inspected the variable candidates detected from the seven *Fermi* GRBs (see Table B.2), and found the number of variables detected in each GRB ROI to be consistent with the expected false positive event rate. Further inspection revealed that all candidates showed similar light curve variations to nearby sources, with larger flux density variations likely due to errors associated with ionospheric positional corrections (GRB 190712.02 and GRB 190804A) or errors associated

with the flux density scale correction (GRB 190420.98). No variable candidates passed our inspection.

We searched for dispersed signals from the *Fermi* GRBs (excluding GRB 190712.02 and GRB 190804A for the reason given in Section 3.4.3) following the procedure described in Sections 3.4.3, 3.4.4 and 3.4.5. *Fermi* GRB 200325A was localised by *Swift*-BAT to within 4 arcmin (DeLaunay et al., 2020a) so we can assume that the image noise did not change over this small region (see Figure A.1 in Appendix A). We therefore performed the same simulation analysis as for *Swift* GRBs at the best known GRB position. We found no signal above 5σ in the de-dispersed time series. Our detection efficiency of the simulated signals as a function of fluence is shown in Figure 3.3(c), which yields a fluence upper limit of 600–1200 Jy ms for the DM range of 150–2500 pc cm^{-3} (90% detection efficiency, see Table 3.4). The four events GRB 170827B, GRB 190420.98, GRB 190903A and GRB 200327A were localised by *Fermi*-GBM or IPN, and had large positional errors (see Figure A.2 in Appendix A). We compared the high SNR events observed in the real data to the SNRs produced by negative DMs. The SNR of the brightest dispersed signal detected by our algorithm for these four *Fermi* GRBs is given in Table 3.3, which are all SNR< 7. Given the similar maximum SNR values resulting from the processing of both the positive and negative DM datasets, we conclude there is no compelling evidence of any dispersed signals. The range in 7σ fluence upper limits derived from the de-dispersed time series created for each independent pointing in the ROI for the above four *Fermi* GRBs are given in Table 3.3.

In summary, no associated radio emission was observed for any of the nine short GRBs. Table 3.2 shows the flux density upper limits derived from the transient/variable analysis of the nine GRBs over different timescales, and Table 3.3 and 3.4 show the fluence upper limits derived from a search for dispersed signals via an image dedispersion analysis and signal simulations. The most stringent limits are from GRB 190627A as it was located close to the MWA

pointing centre with no nearby bright sources. All these upper limits can now be used to constrain the theoretical coherent radio emission models applicable to BNS mergers (e.g. Rowlinson & Anderson 2019).

3.6 Constraints on emission models

We discuss the implications of our fluence and flux density upper-limits with respect to three models that predict coherent radio emission arising from BNS mergers within the context of our sample of short GRBs. Two of the models described in the following predict emission that results from the production of a (quasi-)stable magnetar so we assume that such a remnant was formed by each of the short GRBs studied in this chapter. In this section, we first discuss the magnetar parameters derived or assumed for each event before describing each model. We then discuss the coherent emission constraints placed by individual short GRBs and by the whole sample.

3.6.1 Central engine activity

The positions of the two *Swift* GRBs are well known due to their XRT detections, with the resulting X-ray light curves allowing us to derive additional parameters for any remnant. The plateau phase observed in many GRB X-ray light curves is often interpreted as energy injection from a (quasi-)stable magnetar remnant formed from the BNS merger (Zhang & Mészáros, 2001). We consider two different magnetar models: stable and unstable. If the magnetar remnant possesses a mass less than the maximum mass allowed for a NS (depending on the equation of state; Lasky et al. 2014), the merger product would be a stable magnetar. In the other case, the magnetar is unstable as its mass is initially supported by its rapid spin. However, it soon collapses into a BH as it spins down, resulting in a steep decay in the X-ray light curve.

In order to determine the magnetar parameters (for the method see Rowlin-

son et al. 2013), we created the rest-frame X-ray light curves for GRB 190627A and GRB 191004A by combining their *Swift*-BAT and XRT data from the *Swift* Burst Analyser (Evans et al., 2010). Although the *Fermi* GRB 200325A was also detected by *Swift*-BAT, this observation lasted only $\sim 150\,\mathrm{s}$ (DeLaunay et al., 2020b), insufficient for fitting the magnetar model. Since we do not know the redshift of GRB 191004A, we assumed a value of 0.7, the average redshift for short GRBs. We also applied a *k*-correction (Bloom et al., 2001) to obtain the 1–10000 keV rest-frame luminosity light curves, as shown in Figure 4.1. Considering that the decay phase following the plateau in both X-ray light curves does not agree with the simple curvature effect expected for the collapse of an unstable magnetar into a BH (Rowlinson et al., 2010, 2013), we fitted a stable magnetar model to these data to determine the bolometric luminosity of the magnetar (see eq. 8 in Rowlinson & Anderson 2019). This bolometric luminosity and the duration of the X-ray plateau are used to calculate the magnetar magnetic field strength and the initial spin period, assuming a magnetar mass of $2.1\,\mathrm{M_\odot}$, a radius of $10^6\,\mathrm{cm}$, and an efficiency factor of $f = 3.45$ (see eq. 6, 7 and section 2.2.2 in Rowlinson & Anderson 2019). Table 3.5 shows the fitted magnetar parameters for the two *Swift* GRBs. Compared to the typical range of magnetar parameters proposed by Rowlinson & Anderson (2019), the fitted magnetar remnant for GRB 191004A may be considered typical, while for GRB 190627A it has a much faster spin period and weaker magnetic field. Note that in our modelling we assumed the magnetar spins down solely through magnetic dipole radiation. Incorporating other radiative losses such as gravitational wave emission (e.g. Sarin et al. 2020) may further improve our fitting results.

We caution that there is significant uncertainty in the magnetar properties, only a fraction of which has been included in the quoted uncertainties in Table 3.5. Specifically, the unknown redshift z (for GRB 191004A) and efficiency factor f could introduce substantial uncertainty to the fitted magnetar period P and magnetic field B. Therefore, the model predicted coherent radio emission de-

GRB	P (ms)	B (10^{15} G)
190627A	$1.353^{+0.047}_{-0.042}$	$0.668^{+0.052}_{-0.045}$
191004A	$6.16^{+0.32}_{-0.25}$	$17.4^{+1}_{-0.9}$

Table 3.5: Magnetar parameters derived from magnetar model fitting to the X-ray light curves of GRB 190627A and GRB 191004A, assuming a NS mass of $2.1\,M_\odot$ (as described in Section 3.6.1). P and B represent the spin period and magnetic field with $1\,\sigma$ uncertainties.

pendent on the magnetar properties (i.e. the GRB jet-ISM interaction, persistent pulsar emission and magnetar collapse; see Section 3.6.2) could be much fainter than those presented for GRB 190627A and GRB 191004A in Section 3.6.3.1 and 3.6.3.2, which means our conclusions on model constraints could be relaxed in certain circumstances, e.g. a high redshift of GRB 191004A of $z > 0.7$ or a large efficiency factor $f > 3.45$.

As the *Fermi* GRBs in our sample do not have X-ray data for deriving the magnetar parameters, we assumed the formation of a 'typical' stable magnetar remnant, which, from the distribution of the magnetar parameters fitted to known X-ray plateaus (see figure 8 in Rowlinson & Anderson 2019), may be defined as possessing a magnetic field of $2.4^{+4.6}_{-1.6} \times 10^{16}$ G and a spin period of $9.7^{+20.8}_{-6.6}$ ms. In addition, given the lack of X-ray data, we cannot make any assumptions regarding the stability of the magnetar remnant resulting from the *Fermi* GRBs, so we do not consider coherent emission produced by the collapse of the magnetar into a BH (e.g. Zhang 2014).

3.6.2 Coherent emission models

Various models have predicted the production of coherent radio emission associated with short GRBs (for a review see Rowlinson & Anderson 2019). The emission predicted to be produced by the alignment of the merging NS magnetic fields is independent of the magnetar remnant (see Section 3.6.2.1), while the other models require us to derive magnetar parameters from X-ray data (see Sec-
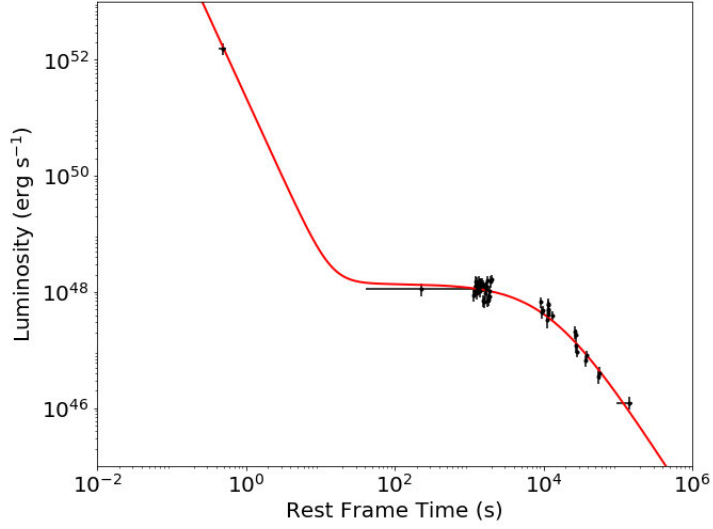
(a) GRB 190627A
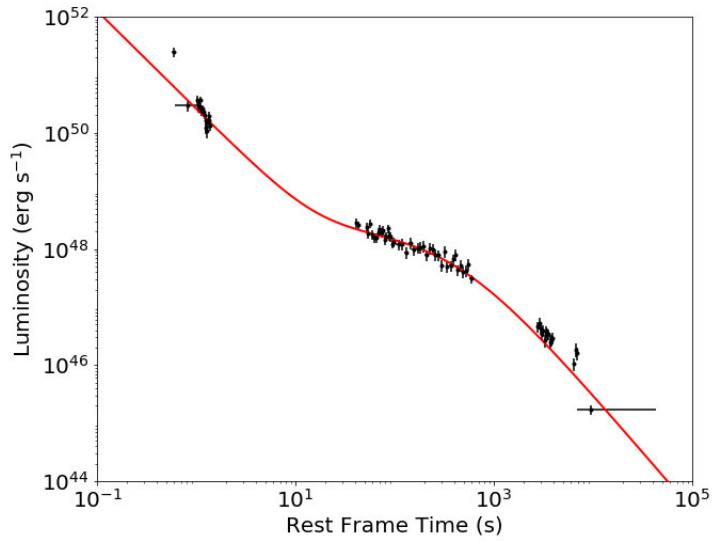
(b) GRB 191004A

Figure 3.4: The rest-frame *Swift*–BAT and –XRT light curves of GRB 190627A and GRB 191004A. The black points represent the BAT and XRT data, and the red lines show the fit to the magnetar central engine powering the plateau phase (see Section 3.6.1). We used the redshift $z = 1.942$ for GRB 190627A and assumed a typical short GRB redshift of $z = 0.7$ for GRB 191004A.

tions 3.6.2.2 and 3.6.2.3). Here we briefly review the four emission mechanisms we have chosen to test.

3.6.2.1 Interactions of NS magnetic fields

The earliest coherent radio emission may come from the inspiral phase, where interactions between the NS magnetospheres just preceding the merger may spin them up to millisecond spin periods and lead to a revival of the pulsar emission mechanism (Lipunov & Panchenko, 1996; Metzger & Zivancev, 2016). The emission starts from a few seconds prior to the merger and peaks at the first contact of the NS surfaces, giving rise to a short duration radio flash. Its flux density is predicted to be

$$F_\nu \sim 2 \times 10^8 \, (1+z) \, \frac{B_{15}^2 M_{1.4}^3}{R_6 \nu_{9,\mathrm{obs}} D^2} \, \epsilon_\mathrm{r} \, \mathrm{Jy}, \qquad (3.1)$$

where $\nu_{9,\mathrm{obs}}$ is the observing frequency in units of $10^9 \, \mathrm{Hz}$, D is the distance to the binary system in Gpc, the radio emission efficiency (ϵ_r) is the fraction of the wind luminosity being converted into coherent radio emission (typically 10^{-4} for known pulsars; Taylor et al., 1993), and we assume typical NS parameters for the magnetic field of $B_{15} = 10^{-3}$ in units of $10^{15} \, \mathrm{G}$, a mass of $M_{1.4} = 1$ in units of $1.4 \, \mathrm{M}_\odot$, and a radius of $R_6 = 1$ in units of $10^6 \, \mathrm{cm}$ (Rowlinson & Anderson, 2019). Note that the parameters B_{15}, $M_{1.4}$ and R_6 are assumed properties of the merging NSs, not of the magnetar remnant. The distance can be estimated from the redshift z using the predefined cosmology parameters (Wright, 2006).

3.6.2.2 Interaction of relativistic jets with the ISM

If a Poynting flux dominated wind is produced by the magnetar remnant formed following the binary merger (Usov, 1994; Thompson, 1994), its interaction with the ISM would generate a low frequency, coherent radio pulse at the highly magnetised shock front (Usov & Katz, 2000). As this emission is linked to the relativistic gamma-ray jet and only propagates through the pre-existing low density

surrounding medium, it should be detectable within the first few minutes of a GRB trigger. The radio fluence is given by

$$\Phi_\nu \sim \frac{0.1\epsilon_B(\beta - 1)}{\nu_{\max}} \left(\frac{\nu}{\nu_{\max}}\right)^{-\beta} \Phi_\gamma \, \mathrm{erg\, cm^{-2}\, Hz^{-1}} \qquad (3.2)$$

where ϵ_B is the fraction of magnetic energy in the relativistic jet, and $\beta \simeq 1.6$ is the spectral index (Usov & Katz, 2000). The peak frequency of the coherent radio emission ($\nu_{\max}$ in GHz) is determined by the magnetic field at the shock front (see equations 11-13 in section 2.4 of Rowlinson & Anderson, 2019), and Φ_γ is the observed gamma-ray fluence in $\mathrm{erg\, cm^{-2}}$.

3.6.2.3 Persistent emission following the formation of a magnetar

If the merger remnant is a magnetar, the coherent radio emission powered by dipole magnetic braking may be detectable during the lifetime of the magnetar (Totani, 2013; Metzger et al., 2017). If the beam of the magnetar aligns with the GRB jet and points towards the Earth, the coherent emission will be detected as persistent emission. The flux density of this emission is given by

$$F_\nu \sim 8 \times 10^7 \, \nu_{\mathrm{obs}}^{-1} \, \epsilon_r \, D^{-2} \, B_{15}^2 \, R_6^6 \, P_{-3}^{-4} \, \mathrm{Jy}, \qquad (3.3)$$

where P_{-3} is the magnetar spin period in units of 10^{-3} s (Totani, 2013; Rowlinson & Anderson, 2019). This persistent radio emission may only be detectable for up to a few hours following the merger as its rapid spin-down rate would cause the dipole radiation to weaken very quickly or (if unstable) it collapses into a BH (which is $\lesssim 2$ h, depending on the magnetar parameters B and P derived in Section 3.6.1).

3.6.2.4 Collapse of the magnetar remnant

Finally, as the magnetar remnant spins down in its conversion of rotational energy to radiation power (see the section above), it may collapse into a BH, resulting in

a short-duration coherent radio signal via magnetic reconnection (Zhang, 2014). This magnetar collapse may not occur until 2 hr post-burst (Zhang, 2014). The radio fluence is given by

$$\Phi_\nu \sim -\frac{10^{-23}\epsilon\,E_{\mathrm{B}}}{4\pi D^2}(\alpha+1)\nu_{\mathrm{p}}^{-(\alpha+1)}\frac{\nu_{\mathrm{obs}}^\alpha}{1+z}\,\mathrm{Jy\,ms}, \qquad (3.4)$$

where ϵ is the efficiency of converting the magnetic energy of the magnetar remnant E_{B} (in units of erg) to radio emission, α is the spectral index if we assume a power-law spectrum for the radio emission (i.e. $\propto \nu^\alpha$), and ν_{p} is the plasma frequency of the emitting region of an electron number density n (i.e. $\nu_{\mathrm{p}} \simeq 9n\,\mathrm{kHz}$; Rowlinson & Anderson 2019; Rowlinson et al. 2021). Note that this model is unlikely to be probed by our 30 min MWA observations immediately following GRBs, and thus not discussed in the following sections of this chapter. We will explore the detectability of this model emission in Chapter 6.

3.6.3 Constraints from individual GRBs

3.6.3.1 GRB 190627A

GRB 190627A is the only event amid our nine short GRBs that has a known redshift ($z = 1.942$). Thanks to the redshift measurement, we can calculate a luminosity distance of 15.2 Gpc and directly constrain the fundamental parameters of the emission models, such as the efficiency of radio emission ϵ_{r}, which directly scales with the predicted flux densities from the interaction of the merging NS magnetic fields, and that of the persistent pulsar emission from the magnetar remnant (Eq. 1 and 3). We can also constrain the fraction of magnetic energy ϵ_B that directly scales with the predicted fluence from the interaction between the relativistic jet and ISM (Eq. 2). This has not been possible in previous works as low frequency radio upper limits of coherent radio emission have only poorly constrained these emission parameters under a presumed redshift (e.g. Rowlinson et al. 2019, Rowlinson et al. 2020, Anderson et al. 2021b). In addition, as this

Swift GRB has also been localised to within an MWA synthesised beam, we are able to derive a constraining dispersed signal (fluence) limit.

In Figure 3.5 we plot the predicted flux density of a signal produced by the alignment of the merging NS magnetic fields in GRB 190627A, as a function of the radio emission efficiency ϵ_r (see Eq. 1 in Section 3.6.2.1). We compare this prediction to the upper limit derived from the 2 min snapshots of GRB 190627A as this timescale is comparable to the dispersive smearing of a prompt, coherent signal across the MWA observing band for a redshift of 1.942 (~ 90 s). We can see from Figure 3.5 that this coherent emission would only be detectable on a 2 min timescale if it has an efficiency $\gtrsim 10^{-2}$. We also plot the deeper limit derived from the dispersed signal simulations (see Section 3.4.4) in Figure 3.5. In this case, the emission would be marginally detectable for a typical pulsar efficiency.

In Figure 3.6 we plot the predicted fluence produced by the relativistic jet and ISM interaction as a function of the fraction of magnetic energy ϵ_B (see Eq. 2 in Section 3.6.2.2). The gamma-ray fluence of GRB 190627A was measured to be $(9.9 \pm 2.2) \times 10^{-8}$ erg cm^{-2} by *Swift*–BAT in the 15–150 keV energy band (Barthelmy et al., 2019). In this case, the jetted outflow is assumed to be a magnetised wind that is powered by a magnetar central engine (Usov & Katz, 2000) so is dependent on the magnetar parameters derived for GRB 190627A (see Table 3.5). By also adopting a typical value of 10^{49} erg for the kinetic energy from short GRBs (Fong et al., 2015), $\Gamma = 1000$ for the Lorentz factor of the relativistic wind (Ackermann et al., 2010), and $n = 10^{-2}$ cm^{-3} for the poorly known electron density of the surrounding medium (Fong et al., 2015) we were able to derive ν_{max} (see Section 3.6.2.2 and Rowlinson & Anderson, 2019). We then compared the fluence upper limit we derived through our de-dispersion analysis (Table 3.4; horizontal dotted line in Figure 3.6) to the fluence prediction (solid line), constraining the fraction of magnetic energy in the relativistic jet launched by GRB 190627A to $\epsilon_B < 2 \times 10^{-4}$, which is consistent with the limit $\epsilon_B \lesssim 10^{-3}$ given by the requirement that the magnetic stress at the shock front should not disrupt the
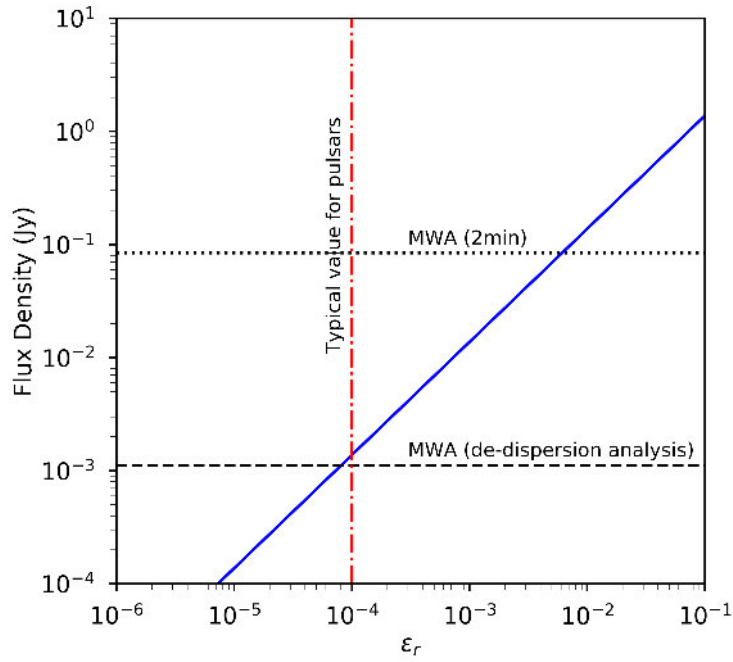
Figure 3.5: The predicted 185 MHz flux density (blue line) of the prompt signal emitted by the alignment of the merging NS magnetic fields (Section 3.6.2.1) in GRB 190627A as a function of the radio emission efficiency (ϵ_r). The horizontal dotted line shows the least constraining flux density upper limit derived from the 2 min snapshots of GRB 190627A (Table 3.2). The horizontal dashed line shows the flux density upper limit converted from the least constraining fluence limit derived from the image de-dispersion analysis (Table 3.4), and the vertical line shows the typical efficiency observed for known pulsars ($\epsilon_r \sim 10^{-4}$).
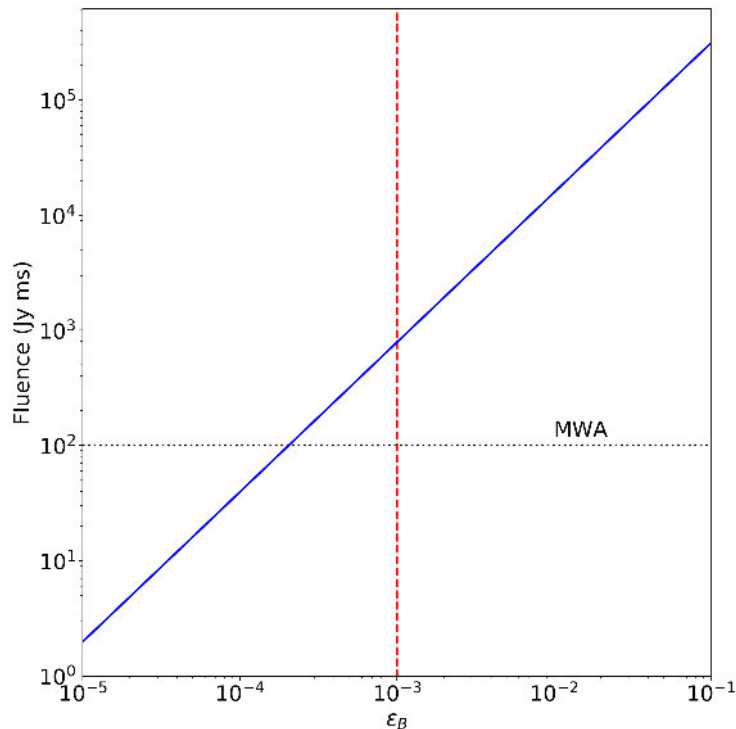
Figure 3.6: The predicted fluence (blue line) of a prompt signal produced by the relativistic jet and ISM interaction (Section 3.6.2.2) for GRB 190627A as a function of the fraction of magnetic energy in the GRB jet (ϵ_B). The horizontal dotted line shows the least constraining fluence upper limit derived from our image de-dispersion analysis (Table 3.4), and the vertical dashed line shows a typical value for the magnetic energy fraction of $\epsilon_B = 10^{-3}$ (Katz, 1997).

thin colliding shells in internal shock models (vertical dashed line in Figure 3.6; Katz 1997).

In Figure 3.7 we plot the predicted flux density of persistent pulsar emission from the magnetar remnant as a function of the radio emission efficiency ϵ_r using the magnetar parameters listed in Table 3.5 and Eq. 3 in Section 3.6.2.3. We use the upper limit obtained from the 30 min integration of GRB 190627A to constrain our detection of the persistent emission (Table 3.2). Figure 3.7 shows that for our limit, the magnetar remnant likely has a radio emission efficiency of $\epsilon_r \lesssim 10^{-3}$.

From the above comparison between the upper limits and the theoretical predictions, we obtained the following constraints on the model parameters for
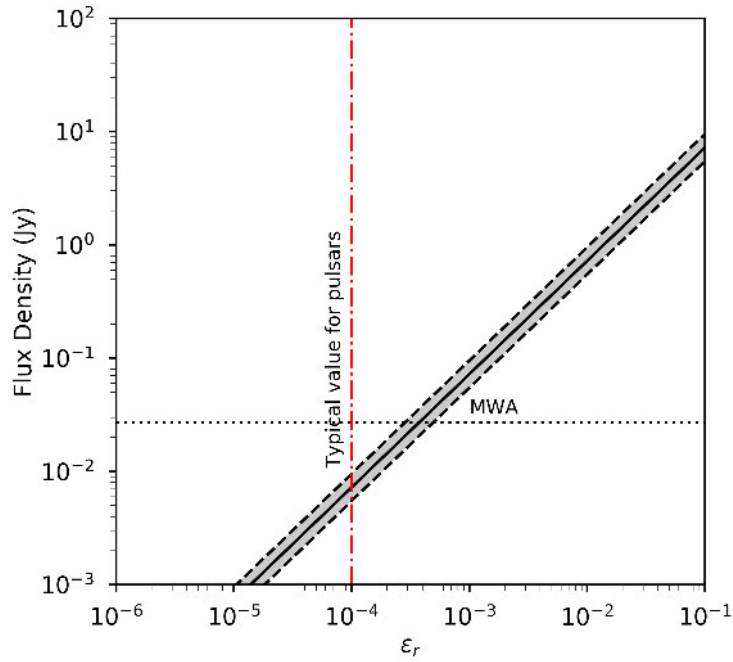
Figure 3.7: The predicted flux density of the persistent emission from a magnetar remnant (Section 3.6.2.3) resulting from GRB 190627A as a function of the radio emission efficiency (ϵ_r). The shaded region corresponds to the $1\,\sigma$ uncertainty on the fitted magnetar remnant parameters listed in Table 3.5 (see Section 3.6.1). The horizontal line shows the flux density upper limit obtained from the 30 min integration of GRB 190627A (Table 3.2), and the vertical line shows the typical efficiency observed for known pulsars.

GRB 190627A: the radio emission efficiency of the nearly merged NSs $\epsilon_r \lesssim 10^{-4}$; the fraction of magnetic energy in the GRB jet $\epsilon_B \lesssim 2 \times 10^{-4}$; and the radio emission efficiency of the magnetar remnant $\epsilon_r \lesssim 10^{-3}$. While the merging NSs are predicted to have a lower radio emission efficiency than typical pulsars, the magnetar remnant may have a higher efficiency. The constraint on the fraction of magnetic energy in the GRB jet is consistent with the range $10^{-6} \lesssim \epsilon_B \lesssim 10^{-3}$ resulting from a systematic study of GRB magnetic fields (Santana et al., 2014). GRB afterglow analyses also show that ϵ_B downstream of the shock is much larger than 10^{-9}, which is the typical value in the surrounding medium of short GRBs, assuming a density of $1\,\text{cm}^{-3}$ and a magnetic field of $\sim \mu G$ similar to the Milky Way (e.g., Panaitescu & Kumar 2002, Yost et al. 2003 and Panaitescu 2005). If the magnetic field in the surrounding medium of GRB 190627A has a similar value to that of the Milky Way, the amplification factor of the magnetic energy fraction for this GRB would be $\lesssim 2 \times 10^5$. Several magnetic field amplification mechanisms have been proposed, including the Weibel instability, the cosmic-ray streaming instability, and the dynamo effect (e.g., Lucek & Bell 2000, Medvedev et al. 2005, Milosavljević & Nakar 2006, Inoue et al. 2011, Mizuno et al. 2011).

3.6.3.2 GRB 191004A

GRB 191004A is one of the two events detected by *Swift*. Given that the first three 2 min snapshots were corrupted, the delay between the MWA first being on-target with respect to the GRB detection (see Section 3.2.1) has meant we cannot test coherent emission models that predict the production of prompt radio signals either just prior to, or concurrent with, the merger (see Section 3.6.2.1 and 3.6.2.2) for redshifts $z \lesssim 2.7$. We are therefore only able to constrain the persistent emission from a magnetar remnant for this GRB, which is the model presented in Section 3.6.2.3. Given we don't know the redshift of this event, we need to explore how the predicted flux density changes between redshifts of $0.1 < z < 2$. The magnetar parameters were derived by fitting the magnetar

model to the rest frame X-ray light curve (assuming $z = 0.7$; see Section 3.6.1). These parameters therefore vary with redshift (Rowlinson & Anderson, 2019), with the magnetic field and spin period scaling according to

$$B_{15} \propto D^{-1} (1 + z),$$ (3.5)

$$P_{-3} \propto D^{-1} (1 + z)^{1/2}.$$ (3.6)

Figure 3.8 shows the predicted persistent pulsar emission from a magnetar remnant produced by GRB 191004A as a function of redshift. We used the fitted magnetar parameters derived for GRB 191004A (listed in Table 3.5) and the above scaling relations (Eq. 3.5 and 3.6) to calculate the predicted flux density. Otherwise, we assumed the same parameters as adopted for GRB 190627A in Section 3.6.3.1. Since the observations of GRB 191004A were conducted with the MWA compact configuration, the confusion noise caused the upper limit on the 30 min integration to be less constraining compared to other GRB observations taken in the extended configuration. Our MWA flux density limit for GRB 191004A is therefore insufficient for constraining this model.

3.6.3.3   *Fermi* GRBs

The other GRBs in our sample were detected by *Fermi*–GBM so no follow-up X-ray data are available to derive their magnetar remnant parameters. Assuming a typical magnetar remnant for all the *Fermi* GRBs (see Section 3.6.1), we now compare the radio emission upper limits derived from our MWA observations to theoretically predicted values described by models presented in Section 3.6.2.2 and 3.6.2.3. Note that since none of the *Fermi* GRB fluence upper limits place constraints on the NS magnetic field interactions described in Section 3.6.2.1, we do not consider this model further (see discussion in Section 3.7.1.1).

Figure 3.9 shows the predicted prompt radio emission produced by the GRB
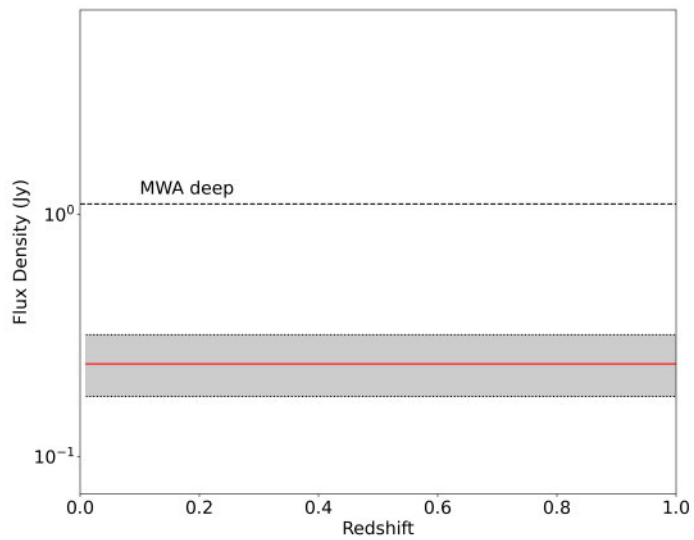
Figure 3.8: The flux density of persistent emission (solid red line) predicted to be produced by a remnant magnetar resulting from GRB 191004A as a function of redshift (Section 3.6.2.3). The shaded region corresponds to the $1\,\sigma$ uncertainties on the fitted magnetar parameters (see Section 3.6.1 and Table 3.5). The radio emission efficiency is assumed to be $\epsilon_r = 10^{-4}$, which is the typical value for pulsars. The horizontal dashed line indicates the flux density upper limit of $1.104\,\mathrm{Jy}$ derived from the $30\,\mathrm{min}$ integration of GRB 191004A.
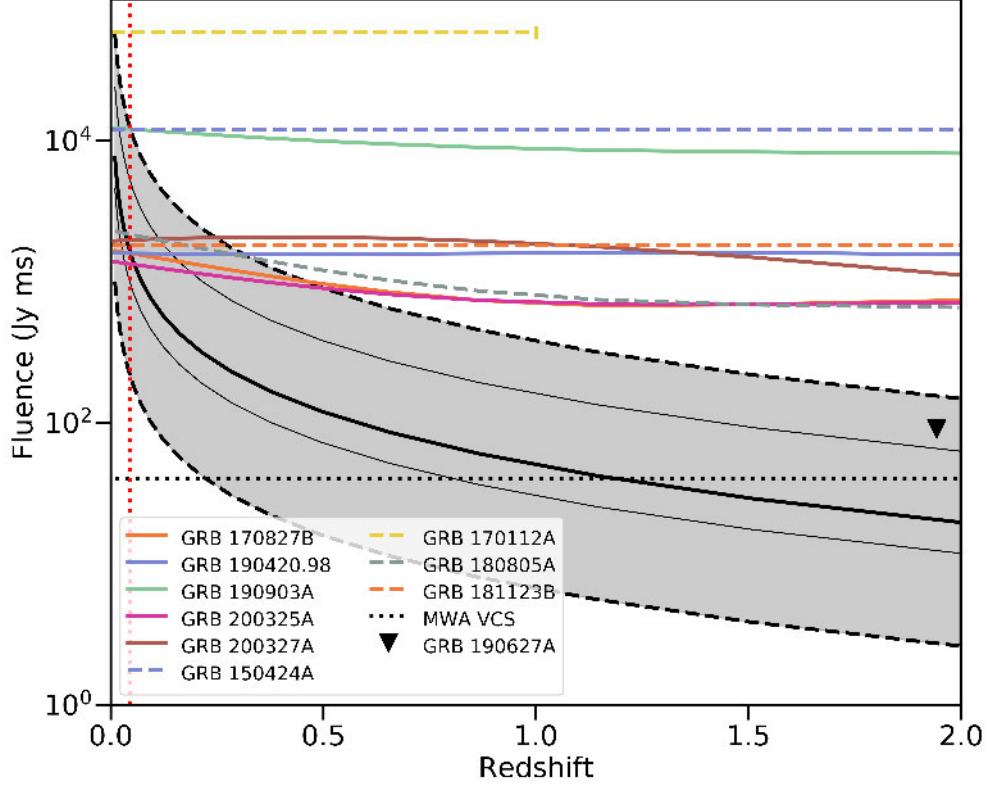
Figure 3.9: The fluence of the prompt radio signal predicted to be produced by the relativistic jet and ISM interaction using the mean values of the magnetic field and spin period of known magnetar remnants (see figure 8 in Rowlinson & Anderson 2019) and assuming the median value of the gamma-ray fluences measured for different *Fermi* GRBs in Table 3.6 (thick black curve). The two thin black curves show the radio fluence predictions corresponding to the minimum and maximum gamma-ray fluence measured for the *Fermi* GRBs, and the shaded region corresponds to the $1\,\sigma$ scattering in the distribution of the parameters of typical magnetars. Different from Figure 3.8, there is no rescaling of magnetic field and spin period with redshift. The fluence limit for GRB 190627A is plotted as a black triangle. The solid coloured curves represent the fluence upper limits as a function of DM (redshift) derived from the de-dispersion image analysis performed on the *Fermi* GRBs. We also include the fluence upper limits published for individual short GRBs (dashed coloured curves), including GRB 150424A (132 MHz; Kaplan et al. 2015), GRB 170112A (56 MHz; Anderson et al. 2018b), GRB 180805A (185 MHz; Anderson et al. 2021b) and GRB 181123B (144 MHz; Rowlinson et al. 2020). The dotted black line indicates a potential fluence limit we could achieve if we instead trigger observations using the MWA Voltage Capture System (VCS; see further details in Section 3.7.1.2.)

jet–ISM interaction as a function of redshift assuming a typical magnetar remnant was formed. The large uncertainties (the shaded region) come from the scatter in the distribution of the spin period and magnetic field strength of magnetar remnants from previously studied short GRBs (Rowlinson et al., 2013; Rowlinson & Anderson, 2019). The predicted radio fluence directly scales with the gamma-ray fluence (see Eq. 3.2), which we list in Table 3.6 for each GRB as measured by *Fermi*–GBM in the 10–1000 keV energy band. For this comparison, we adopt the median gamma-ray fluence value, i.e. $7.8 \times 10^{-7} \, \mathrm{erg \, cm^{-2}}$, for predicting the prompt emission fluence (thick black curve in Figure 3.9). We also plot the model radio fluence predictions corresponding to the minimum and maximum gamma-ray fluence in our sample (Table 3.6) in Figure 3.9 (thin black curves). Note that the uncertainty in the predicted emission due to the magnetar parameters encompasses the range in predictions caused by different gamma-ray fluence measurements. The other model parameters are assumed to be the same as for GRB 190627A.

We overplot all the fluence limits derived from our GRB sample (Tables 3.3 and 3.4) on Figure 3.9 to constrain the GRB jet-ISM interaction model (Section 3.6.2.2). Only those GRBs for which MWA was on-target $\lesssim 1 \, \mathrm{min}$ post-burst were included in this Figure as any prompt signals emitted at cosmological distances at the time of burst would have been dispersion delayed by up to $\sim 2 \, \mathrm{min}$ at MWA frequencies. We incorporated the dependence of the fluence upper limits on the DM value and redshift, as was done in Anderson et al. (2021b). In each case, we plot the maximum fluence limit in the range quoted in Tables 3.3 and 3.4. It can be seen that the majority of our fluence limits in this chapter are constraining for GRBs at low redshifts $z \lesssim 0.5$ for a subset of magnetar parameters. In Section 3.7.1.2, we further explore the implications of our upper limits on this emission model.

Figure 3.10 shows the predicted persistent dipole radiation from a typical magnetar as a function of redshift (thick black curve). Again, the shaded region

GRB	γ-ray fluence ($10^{-7}\,\mathrm{erg\,cm^{-2}}$)
170827B	4.7 ± 0.1[a]
190420.98	6.5 ± 0.3[a]
190903A	7.8 ± 0.6[b]
200325A	24.9 ± 1.2[c]
200327A	15.3 ± 0.6[d]

Table 3.6: The gamma-ray fluences (10–1000 keV) measured by *Fermi*–GBM for those *Fermi* events for which we derived radio fluence limits. References include: a: Fermi–GBM burst catalog at HEASARC: https://heasarc.gsfc.nasa.gov/W3Browse/fermi/fermigbrst.html; b: Mailyan & Meegan (2019); c: Veres et al. (2020a); d: Veres et al. (2020b).

illustrates the uncertainty in the prediction due to the scatter in the distribution of known magnetar parameters (Rowlinson & Anderson, 2019), which spans six orders of magnitude. We plot the flux density upper limits derived from the 30 min integrations of the GRBs as listed in Table 3.2. For a typical magnetar remnant, the majority of our MWA observations could have detected persistent dipole radiation up to a redshift of $z \sim 0.6$. We explore this further in Section 3.7.1.3.

3.7 Discussion

We have performed a search for coherent radio emission associated with BNS mergers on the biggest sample of short GRBs at low frequencies using the MWA rapid-response system, obtaining radio fluence and flux density upper limits on this predicted emission (see Tables 3.2 3.4, and 3.3). The de-dispersion analysis in the image space (see Section 3.4.3) accommodates the dispersive smearing of the prompt signals across the MWA observing band for a range of short GRB redshifts, and thus is more sensitive to these signals than just imaging on different timescales (5 s, 30 s, 2 min). Thanks to the rapid response time of the MWA (for a comparison of response times of different low frequency facilities see figure 10 in Anderson et al. 2021b), we are able to use these fluence upper limits to constrain
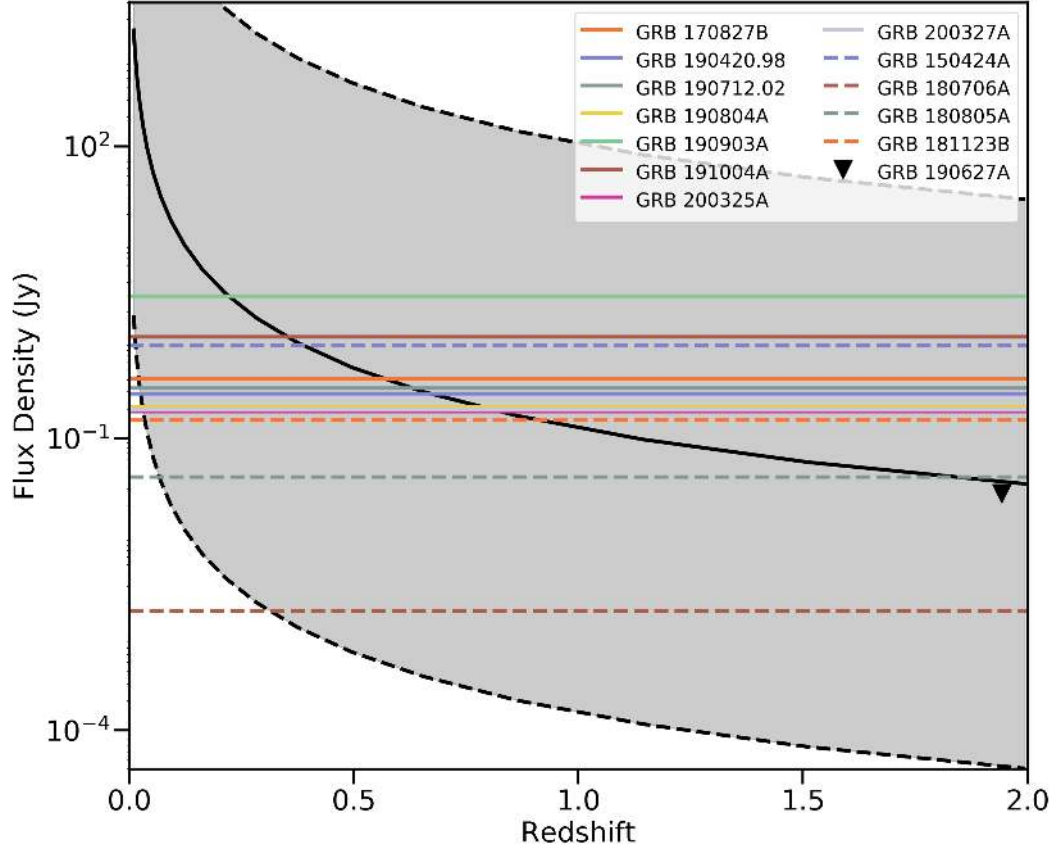
Figure 3.10: Similar to Figure 3.9, here we plot the predicted flux density for the persistent radio emission from the dipole radiation of a magnetar remnant (see Section 3.6.2.3). The solid black curve represents the predicted emission from a typical magnetar with the shaded region corresponding to the 1σ scatter in the distribution of magnetar parameters. The solid coloured curves represent the flux density upper limits derived from the 30 min integration of our sample of short GRBs. We also plot the flux density upper limits from observations of other individual GRBs (dashed coloured curves), including GRB 150424A (Kaplan et al., 2015), GRB 180706A (a long GRB; Rowlinson et al., 2019), GRB 180805A (Anderson et al., 2021b) and GRB 181123B (Rowlinson et al., 2020).

the prompt radio emission models in the early stages of BNS mergers. With the flux density upper limits obtained from the 30 min observations, we are able to constrain the persistent emission model (see Section 3.6.2 for a summary of these models).

3.7.1   Constraints on the tested coherent emission models

In this section, we consider the implications of the constraints the nine short GRBs in our sample place on the emission models described in Section 3.6.2. The upper limits we obtained for the *Swift* GRB 190627A demonstrates the best sensitivity MWA can achieve with triggered observations using the standard correlator mode, as can be seen from Figure 3.9 and 3.10 (black triangle). As part of this investigation, we also compare our results to the low frequency fluence and flux density upper limits obtained from investigations of individual short GRBs. In Figure 3.9, we include the fluence upper limits on the prompt radio emission from individual short GRBs, including 1.2×10^4 Jy ms for GRB 150424A observed by the MWA (Kaplan et al., 2015), 5.85×10^4 Jy ms for GRB 170112A observed by OVRO-LWA (Anderson et al., 2018a), 570–1750 Jy ms for GRB 180805A observed by the MWA (Anderson et al., 2021b) and 1824 Jy ms for GRB 181123B observed by LOFAR (Rowlinson et al., 2020). In Figure 3.10, we chose to include the flux density upper limits on the persistent radio emission from individual GRBs, including 0.9 Jy on a 30 min timescale for GRB 150424A observed by MWA (Kaplan et al., 2015), 1.7 mJy on a 2 h timescale for GRB 180706A observed by LOFAR (a long GRB; Rowlinson et al., 2019), 40.2 mJy on a 30 min timescale for GRB 180805A observed by MWA (Anderson et al., 2021b), and 153 mJy on a 2 h timescale for GRB 181123B observed by LOFAR (Rowlinson et al., 2020). Even compared to previous surveys and triggered observations, our triggered MWA observations of GRB 190627A obtained the most stringent limits on both prompt and early-time persistent coherent emission to date from a short GRB within a few hours post-burst at low frequencies.

3.7.1.1 Interaction of NS magnetic fields

In Section 3.6.2.1, we described that one of the earliest prompt, coherent signals predicted from a short GRB may be produced by the alignment of the NS magnetic fields prior to the merger. Here we compare the model prediction to the fluence upper limits derived from our short GRB sample. From Table 3.3 and 3.4, we can see the fluence upper limits range from 80 to 12, 110 Jy ms. According to Eq. 3.1, assuming typical NS properties, we predict the fluence to be $\lesssim 10$ Jy ms at a reasonable redshift. Therefore, none of our observations are sensitive enough to detect this predicted emission.

3.7.1.2 Relativistic jet and ISM interaction

As outlined in Section 3.6.2.2, we expect the collision of a relativistic jet with the ISM to produce prompt, coherent radio emission. This model is dependent on the properties, i.e. the spin period and the magnetic field strength of the newly formed magnetar remnant. Considering a typical magnetar as proposed by Rowlinson & Anderson (2019), we compared the fluence upper limits obtained from our sample of short GRBs (solid curves) and those from previous triggered observations (dashed curves) to the model prediction in Figure 3.9. Note that the de-dispersion analysis performed for GRB 170112A by Anderson et al. (2018a) covers a limited range of DM values so the corresponding dashed lines spans a limited range of redshift.

Among all these searches at low frequencies, our observation of GRB 190627A is the most sensitive, and even at a redshift of $z = 1.942$, we were sensitive enough to detect the predicted prompt signal from the jet-ISM interaction for some range of typical magnetar remnant parameters. The majority of fluence limits obtained from our sample and other triggered observations of short GRBs are sensitive enough to search for prompt signals up to a redshift of $z \sim 0.5$ for a subset of typical magnetar remnant parameters. Considering the magnetic energy fraction was assumed to be $\epsilon_B = 10^{-3}$ for the predicted emission in Figure 3.9, our non-

detection might suggest a constraint of $\epsilon_B \lesssim 10^{-3}$, comparable to the theoretical limit on ϵ_B for GRBs with narrow subpulses in internal shock models (Usov & Katz, 2000). Compared to previous constraints on ϵ_B using radio observations of short GRBs, our limit is comparable to the $\epsilon_B \lesssim [10^{-4}–10^{-2}]$ (depending on pulse widths) derived for GRB 150424A (Rowlinson & Anderson, 2019), but less constraining than the $\epsilon_B \lesssim [3 \times 10^{-5}–2 \times 10^{-4}]$ derived for GRB 181123B (Rowlinson et al., 2021). While it is unlikely that the majority of short GRBs are at $z > 0.5$ (Gompertz et al., 2020), overall, our non-detection of prompt radio emission from such a big sample of short GRBs is consistent with model predictions when considering the full parameter space covered by the potential diveristy in both magnetar parameters and gamma-ray fluences and (see shaded region in Figure 3.9).

In Figure 3.9 we also compared the expected sensitivity of the MWA Voltage Capture System (VCS; Tremblay et al., 2015) to the model prediction and short GRB fluence limits. The VCS mode has a temporal and spectral resolution of $100\,\mu$s and $10\,$kHz, respectively, making it specifically sensitive to narrow ($\sim 10\,$ms) pulsed and therefore dispersed signals. Rapid-response MWA observations of short GRBs using the VCS would therefore be sensitive enough to detect prompt emission from a large subset of magnetar remnant parameters over a large redshift range (see further discussions in Section 3.7.2).

3.7.1.3 Persistent pulsar emission

If a magnetar is formed via the BNS merger, it is predicted to emit in the same way as pulsars (see Section 3.6.2.3). Again, this emission is dependent on the magnetar remnant properties. In Figure 3.10, we compared the flux density upper limits obtained from our sample of short GRBs (solid curves) and those from previous works (dashed curves) to the predicted flux densities assuming the formation of a typical magnetar remnant.

Our observation of *Swift* GRB 190627A provides the second most sensitive

limit on the persistent emission from a magnetar remnant. With this sensitivity, we are able to detect the predicted persistent emission from a typical magnetar up to a redshift of ~ 2. Note that when plotting the limits for this GRB and the other *Swift* GRB 191004A, we did not assume typical magnetar parameters but used those derived from their X-ray light curves in Section 3.6.1.

One can see that Rowlinson et al. (2019) performed the most sensitive search for persistent emission from the long GRB 180706A using LOFAR. A LOFAR observation with over a 2 h integration can reach mJy sensitivities thanks to its large number of antennas and long interferometric baselines (van Haarlem et al., 2013). This sensitivity is sufficient to detect the predicted persistent emission over a broad range of redshifts and a large magnetar parameter space. However, as GRB 180706A is a long GRB, the dense surrounding medium may prevent the transmission of low-frequency radio signals (Zhang, 2014).

For the 11 short GRBs in Figure 3.10 (excluding the long GRB 180706A), it is somewhat surprising to see no detection of any persistent emission given that all the flux density upper limits are comparable to the model predictions for a large subset of typical magnetar parameters over a wide range of redshifts, at least up to $z \sim 0.6$. The non-detections from such a big sample provide new implications for this persistent emission model. It is possible that these short GRBs did not produce any persistent radio emission, given that the probability of a BNS merger forming a magnetar remnant is between 5 and 97%, depending on the NS equation of state (Ravi & Lasky, 2014). However, if all the 11 short GRBs in Figure 3.10 actually formed typical magnetars, then either their pulsar beams were pointed away from the Earth and/or they were located at redshifts of $z \gtrsim 0.6$. In the population of short GRBs with known redshifts (see table 1 in Gompertz et al. 2020), only one third have redshifts of $z > 0.6$. Therefore, it is unlikely that all the 11 short GRBs are located at high redshifts, which suggests that either some of the short GRBs did not form magnetars or their radio emission is not aligned with our line of sight. There is still another possibility that the short GRBs

formed magnetars that deviate from the assumed typical parameters, given the typical parameters are drawn from the distribution of a small population of fitted magnetars (see figure 8 in Rowlinson & Anderson 2019). For an ideal case, we might expect two thirds of the 11 short GRBs to be located at $z < 0.6$, half of which formed magnetars with persistent emission brighter than what we are considering a 'typical' magnetar remnant, and all of which have their emission beams pointed towards us. If that were the case, then we might have predicted to detect dipole radiation from the magnetar remnants of approximately four short GRBs.

We therefore conclude that the non-detection of persistent emission from these 11 short GRBs could be related to the simplicity of the model, our assumption that the majority of short GRBs form a magnetar remnant is invalid, and/or our assumption that the magnetar's radio beam is aligned with the rotational axis and remains pointed towards Earth following the merger is invalid. It is also possible that some GRBs in the sample, such as GRB 190627A and 191004A (see Section 3.2.1) may actually be long GRBs, which means their higher density environments could prevent the radio emission from escaping.

3.7.2 Future improvements

The biggest improvement to this experiment will be to perform triggered observations on short GRBs using the VCS as its high temporal resolution ($100\,\mu$s) will increase our sensitivity to FRB-like signals (~ 10ms width), which would otherwise be diluted by the 0.5 s coarse sampling of the standard correlator. Given that the data rate of VCS observations is high ($\sim 28\,$TB/hr), we would not be able to continuously observe one GRB for more than $\sim 100\,$min (Tremblay et al., 2015), making it difficult for us to detect prompt signals predicted to be produced at late times (e.g. by the collapse of an unstable magnetar remnant into a BH, which may not occur for up to 2 hr post-merger; Zhang 2014). However, a 15 min integration with the VCS will allow us to search for prompt, coher-

ent emission predicted to occur either just prior, during, or shortly following the merger (see the models described in Sections 3.6.2.1 and 3.6.2.2) for a wide range of DMs (150-2500 $\mathrm{pc\,cm^{-3}}$) to much deeper sensitivities while still creating a manageable data volume. This is demonstrated in Figure 3.9 where we include the estimated VCS sensitivity limit calculated by Rowlinson & Anderson (2019). While the standard correlator (0.5 s temporal resolution) observations can probe the prompt radio emission produced by the jet-ISM interaction up to a redshift of $z \sim 0.5$ for a typical magnetar remnant, the more sensitive VCS observation can probe this emission up to redshifts of $z > 1$ for a much wider range of magnetar parameters. Therefore, VCS triggered observations of short GRBs is the most promising method for searching for associated prompt, coherent emission.

The poorly known magnetar remnant properties result in uncertainties in the predicted persistent emission that spans six orders of magnitude, as shown in Figure 3.10. As the population of short GRBs detected by *Swift* keeps growing, we expect more of their X-ray light curves to be fitted by the magnetar model in the future. This will help narrow down the model parameters and better constrain the detectability of the emission. Additionally, more redshift measurements on short GRBs would allow us to constrain the key parameters of the emission models, as what we have done for GRB 190627A in Figure 3.5, 3.6 and 3.7 (see also Section 3.6.3.1).

3.7.2.1 Implications for GW follow-up

As BNS mergers are plausible GW emitters, we plan to search for the predicted coherent radio emission using MWA triggered observations of GW events. Compared to short GRBs detected by *Swift* and/or *Fermi*, GW events detected by aLIGO/Virgo are much closer ($\lesssim 190\,\mathrm{Mpc}$ in observing run O4 likely commencing mid-2022; Abbott et al. 2020b), which means their associated radio emission would be much brighter. In Figure 3.9 we plot the expected maximum redshift of GWs with a vertical dotted red line. While observations with the standard MWA

correlator have an almost 50% chance of detecting the predicted emission from GWs based on the largely uncertain magnetar parameters, the VCS mode would either make a detection or rule out the jet-ISM interaction model undoubtedly.

The proximity of GW events also means less dispersion delay, which means we may require a faster response time than what is currently possible with MWA. As discussed in Anderson et al. (2021b), the MWA may only be on-target fast enough for frequencies $\lesssim 130\,\mathrm{MHz}$, the lower end of the MWA observing band. However, a strategy proposed by James et al. (2019) for triggering MWA on 'negative latency' aLIGO/Virgo alerts of BNS mergers (generated by detections of GWs during the inspiral phase before the merger) could help alleviate the requirement on response times, allowing the MWA enough time to capture any associated prompt, coherent radio emission. For further details on MWA follow-up strategies of GWs, see Kaplan et al. (2016), James et al. (2019), and Anderson et al. (2021b).

3.7.2.2 Prospects for SKA-Low

The low-frequency component of the Square Kilometre Array (SKA-Low; Dewdney et al. 2009) is a radio telescope covering the frequency range 50–350 MHz and of an unprecedented sensitivity, resulting from the enormous number of dual-polarisation antennas (Sokolowski et al., 2021). Given the model predictions shown in Section 3.6.3.3, the far greater sensitivity of the SKA-Low will rigorously test these models. Therefore, it is plausible to implement our rapid-response system on the SKA-Low to search for coherent radio emission associated with GRBs. A future plan to enhance the SKA-Low system with the triggering capability to react to external transient alerts has been proposed by Sokolowski et al. (2021).

3.8　Conclusions

In this chapter, we have searched for coherent radio emission from nine short GRBs in the frequency range of 170 and 200 MHz using MWA rapid-response observations. These observations began within 30 s to 10 min postburst (7 of the 9 events within ~ 1 min post-burst), integrating for a maximum of 30 min. We have inspected the images of these nine GRBs that were made on timescales of 30 min, 2 min, 30 s, and 5 s but found no associated transient or variable emission within the GRB positional error regions, quoting flux density upper limits in Table 3.2. We have also performed a de-dispersion search for transients using 0.5 s / 1.28 MHz sub-band images, but found no FRB-like signals associated with the GRBs, quoting a range of fluence upper limits in Tables 3.3 and 3.4. Our fluence and flux density limits on transient emission associated with our nine short GRBs were compared to model predictions of coherent prompt and persistent emission applicable to BNS mergers. As a result of this work, we come to the following main conclusions:

1. The MWA rapid-response observations of *Swift* GRB 190627A provides the most constraining upper limits on coherent emission associated with short GRBs in our sample. By fitting the stable magnetar model to its X-ray light curve (see Figure 4.1), we were able to acquire the magnetar remnant parameters (see Table 3.5). As GRB 190627A is the only event in our sample with a known redshift, we were able to constrain key parameters of the emission models described in Section 3.6.2, including the radio emission efficiency of the nearly merged NSs ($\epsilon_r \lesssim 10^{-4}$), the magnetic energy fraction in the GRB jet ($\epsilon_B \lesssim 2 \times 10^{-4}$), and the radio emission efficiency of the magnetar remnant ($\epsilon_r \lesssim 10^{-3}$, see Figures 3.5, 3.6 and 3.7).

2. The fluence upper limits derived from the de-dispersion analysis of our MWA standard observations were sensitive enough to detect the predicted prompt radio emission produced by the GRB jet-ISM interaction (see Sec-

tion 3.6.2.2) up to a redshift of $z \sim 0.5$ for a subset of typical magnetar parameters (see Figure 3.9). While it is unlikely that the majority of short GRBs are at $z > 0.5$ (Gompertz et al., 2020), our sensitivity is not very constraining when considering the full regime of predictions (shaded region in Figure 3.9) so non-detections may not be unexpected. However, future MWA rapid-response observations using the VCS will be more sensitive to narrow, FRB-like signals, enabling us to probe this emission up to a much higher redshift for a larger range of potential magnetar parameters.

3. The flux density upper limits derived from the 30 min observations of a sample of short GRBs suggest that we should be able to detect the persistent radio emission produced by a typical magnetar remnant (see Section 3.6.2.3) up to a redshift of $z \sim 0.6$ (see Figure 3.10). Given that $\sim 2/3$ of short GRBs have redshifts of $z \leq 0.6$ (Gompertz et al., 2020), our non-detection of persistent radio emission from this sample of short GRBs implies one or more of the following: that some GRBs are not genuinely short, no magnetar remnant was formed, the magnetar remnants do not have typical properties defined by Rowlinson & Anderson (2019), their radiation beams are pointing away from us, or the model is too simplistic.

The MWA, with its large field of view and rapid-response triggering mode, is currently one of the most competitive radio telescopes for performing rapid follow-up observations of short GRBs in search of coherent prompt or persistent emission associated with BNS mergers. In the next chapter, we employ the VCS mode to trigger on GRBs, which is more sensitive to prompt, FRB-like signals. Furthermore, our experiment with the MWA demonstrates the importance of incorporating rapid response capabilities into other low frequency facilities to enable programs that search for prompt radio emission associated with transients, particularly the SKA-Low, which will have superior instantaneous sensitivity on shorter timescales (discussed in Section 6.3.4).

Chapter 4

High time resolution search for prompt radio emission from the long GRB 210419A with MWA

This chapter is a reproduction of J. Tian, G. E. Anderson, P. J. Hancock, J. C. A. Miller-Jones, M. Sokolowski, N. A. Swainston, A. Rowlinson, A. Williams, D. L. Kaplan, N. Hurley-Walker, J. Morgan, N. D. R. Bhat, D. Ung, S. Tingay, K. W. Bannister, M. E. Bell, B. W. Meyers, M. Walker (2022), "High time resolution search for prompt radio emission from the long GRB 210419A with the Murchison Widefield Array", Monthly Notices of the Royal Astronomical Society, Volume 514, Issue 2, page 2756-2768, DOI: https://academic.oup.com/mnras/article-abstract/514/2/2756/6595331. I have adapted the chapter to make it better fit into this thesis, avoiding repetition of the materials already included in Chapters 1 and 2 and keeping all references consistent within this thesis.

4.1 Introduction

In Chapter 3 we performed a search for GRB associated coherent radio emission using the rapid-response mode and the standard correlator (imaging mode)

of the MWA. In this chapter we continue our search for these coherent signals by performing triggered observations on GRBs using the MWA VCS, which, as discussed in Chapter 3, is expected to be more sensitive to prompt radio signals than the imaging mode due to the high time resolution of VCS data. Here we present the first MWA VCS observation triggered on the long GRB 210419A for coherent signal search. Although the long GRB 210419A is more likely to have a denser environment than the sample of short GRBs studied in Chapter 3 (Zhang, 2014), we might still expect there to be a chance for prompt radio signals emitted by GRB 210419A to be able to escape (e.g. Rowlinson et al. 2019; Rastinejad et al. 2022; also see Section 6.1). Note that the different coherent emission models investigated with MWA observations of short GRBs in Chapter 3 are also applicable to long GRBs except for the interaction of NS magnetic fields (see Section 1.1.4.3).

The MWA began observing GRB 210419A within $89\,\mathrm{s}$ of its detection by *Swift*, enabling us to capture any dispersion delayed signal emitted by this GRB for a typical range of redshifts. Using the MWA observation, we conducted a standard single pulse search with a temporal and spectral resolution of $100\,\mu\mathrm{s}$ and $10\,\mathrm{kHz}$ over a broad range of dispersion measures. By deriving fluence upper limits from the VCS observation and comparing these limits to the GRB jet-ISM interaction model, we can place constraints on the fraction of magnetic energy in the GRB jet, as was done in Chapter 3. It is noteworthy that while in Chapter 3 we assumed the formation of magnetar remnants by GRBs, which acted as central engines capable of powering coherent radio emission, we do not make the same assumption in this chapter. Interestingly, we observed an X-ray flare in the light curve of GRB 210419A. Assuming the X-ray flare was emitted as part of the prompt emission, it could also drive coherent radio emission via ISM interactions similar to that of the gamma-ray jet as suggested by Starling et al. (2020). This motivated us to perform a search for signals during the X-ray flaring activity of GRB 210419A, and derive an intensity upper limit for constraining the fraction of

magnetic energy during X-ray flares. Finally, this chapter highlights the prospect of the MWA VCS triggering program in searching for GRB associated coherent signals (to be discussed in detail in Chapter 6).

For the rest of this chapter, we describe the observation of GRB 210419A obtained using *Swift* in Section 4.2 and the VCS triggering mode of the MWA in Section 4.3. We describe the data processing in Section 4.4, followed by analysis methods we used to search for prompt radio emission in Section 4.5. Our results are then presented in Section 4.6. We use the upper limit derived from our VCS observation of GRB 210419A to constrain coherent radio signals associated with the relativistic jet during the prompt gamma-ray emission phase and from an X-ray flare in Section 4.7.

4.2   GRB 210419A

The GRB 210419A was first detected by *Swift* Burst Alert Telescope (BAT; Barthelmy et al. 2005a) at 06:53:41 UT on 2021 April 19 (trigger ID 1044032; Laha et al. 2021). Refined analysis of the BAT light curve determined a T_{90} of 64.43 ± 11.69 s (Palmer et al., 2021), unambiguously placing this GRB in the long GRB category ($T_{90} \gtrsim 2$ s; Kouveliotou et al. 1993). The time-averaged gamma-ray spectrum from T+21.92 to T+95.01 s is best fit by a simple power-law model with an index of 2.17 ± 0.24, consistent with typical long GRBs (Lien et al., 2016), and the gamma-ray fluence in the 15–150 keV band is $(7.8 \pm 1.2) \times 10^{-7}$ erg cm^{-2} (Palmer et al., 2021).

A subsequent detection of the X-ray afterglow by the *Swift*-XRT localised this GRB to the position α(J2000.0) $= 05^h47^m24^s.23$ and δ(J2000.0) $= -65°30'9''0$ with an uncertainty of $2''0$ (90% confidence; Osborne et al. 2021). The XRT X-ray spectrum ($0.3 - 10$ keV) at ~ 1 h post-burst is best fit by a power law with a photon index of $2.60^{+0.29}_{-0.27}$ and an absorption column of $1.9^{+0.7}_{-0.6} \times 10^{21}$ cm^{-2} in the Photon Counting (PC) mode (Beardmore et al., 2021).

Combining the *Swift*–BAT and –XRT data from the *Swift* Burst Analyser

([Evans et al., 2010](#)), we created the X-ray light curve for GRB 210419A in the 0.3–10 keV energy band in the observer frame, as shown in Figure [4.1](#). The light curve is characterised by a power law decay with an X-ray flare peaking at $\sim 4 \times 10^2$ s (shaded region), followed by a plateau phase starting from $\sim 10^3$ s. In order to calculate the duration and fluence of the X-ray flare of GRB 210419A, we fitted the flare with a smooth broken power-law function plus a declining power-law to model the underlying X-ray emission decay (see eq. 1 & 2 in [Yi et al. 2016](#)), as shown in Figure [4.2](#). The duration of the flare (248 s) is defined as the interval between the two intersections of the flare component and the underlying power law decay (335–583 s; [Yi et al. 2016](#)). Integrating the flux density over this duration, we obtained a fluence of 1.58×10^{-7} erg cm^{-2} for the X-ray flare, which is a typical value among observed X-ray flares (see figure 1 in [Starling et al. 2020](#)). For the analysis, results and interpretation of the X-ray flare see Sections [4.4.3](#), [4.6.2](#) and [4.7.2.2](#), respectively. We do not see a steep decay following the plateau phase in the X-ray light curve, which might suggest it is powered by a stable magnetar ([Rowlinson et al., 2013](#)). No redshift was obtained for GRB 210419A. An optical follow-up of this GRB with the Las Cumbres Observatory (LCO) 1-m Sinistro instrument did not detect any uncatalogued optical source within the XRT error region ([Strausbaugh & Cucchiara, 2021](#)).

4.3 MWA observation

The MWA triggered observation of GRB 210419A was taken at a central frequency of 185 MHz with a bandwidth of 30.72 MHz in the phase II compact configuration ([Wayth et al., 2018](#)) using the VCS mode, which has a temporal and frequency resolution of 100 μs and 10 kHz, respectively. The size of the MWA synthesised beam in this configuration is ~ 10 arcmin, much larger than the GRB positional error. The GRB position was continuously observed for 15 min. Note that 45/128 tiles were offline during this observation, which resulted in a noticeable sensitivity loss (see Section [4.5.2](#)).
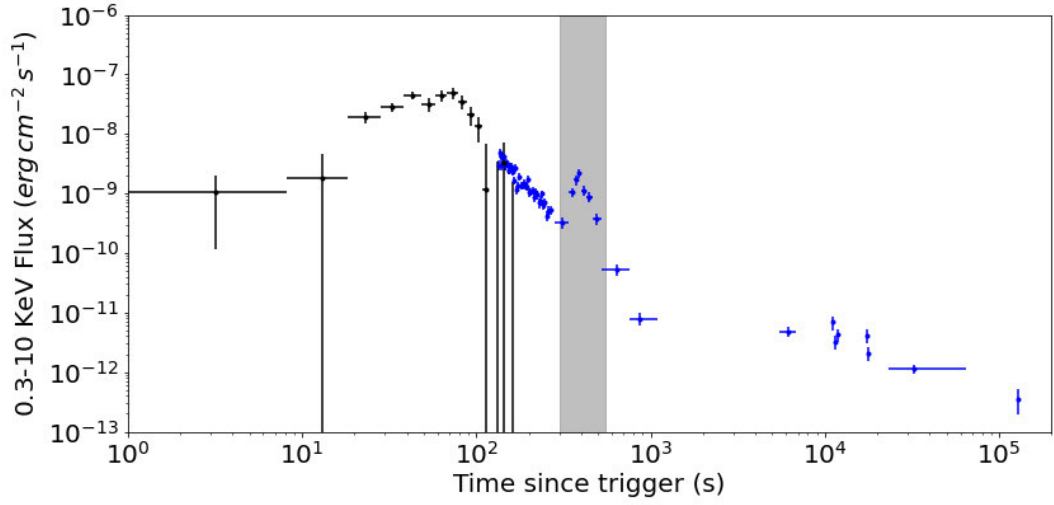
Figure 4.1: 0.3–10 keV flux light curve of GRB 210419A. The black and blue data points were obtained by the *Swift*-BAT (extrapolated to 0.3-10 keV) and the *Swift*-XRT, respectively. The shaded region indicates the period covering the X-ray flare investigated in Section 4.7.2.2. The X-ray plateau phase starts around 1000 s post-burst.
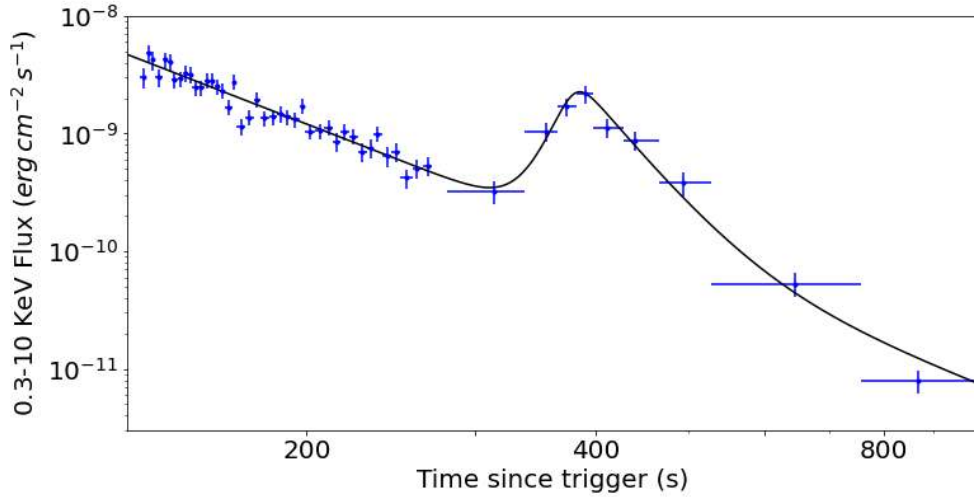
Figure 4.2: The fit to the X-ray flare from GRB 210419A used to calculate its duration of 248 s (between 335–583 s post-burst). We used a smooth broken power-law function to fit the flare plus a declining power-law to fit the underlying X-ray light curve observed by *Swift*–XRT (blue points), with the fitting result being shown as the black line.

143

UT Time (2021-04-19)	Latency (s)	Event (#)	Description
06:53:41	0	1	*Swift*–BAT detects GRB 210419A
06:54:57	76	2	*Swift* VOEvent alert notice circulated
06:54:57.5	76.5	3	MWA front-end receives VOEvent
06:54:57.8	76.8	4	VOEvent handler parses VOEvent and sends trigger to schedule observations
06:54:59.1	78.1	5	MWA schedule is updated
06:55:06.2	85.2	6	MWA is on target
06:55:10.0	89	7	MWA sets up the VCS mode and begins observations

Table 4.1: Timeline for MWA triggered observation of GRB 210419A

The VOEvent broadcasting the *Swift*–BAT detection of GRB 210419A was circulated 76 s post-burst. Just 0.5 s later, the MWA rapid-response front-end web service received the VOEvent. The VOEvent handler took 0.3 s to parse this VOEvent, identifying it as a real GRB, and triggered MWA VCS observations, with the subsequent update of the MWA observing schedule taking 1.3 s. The telescope then took a further 10.9 s to re-point and begin collecting data in the VCS mode. Therefore, the total latency between the *Swift* broadcast of the VOEvent and the MWA being on target was 13 s. Overall, the MWA observation of GRB 210419A started at 06:55:10 UT, just 89 s following the *Swift* detection. A time-line of the triggering process is summarised in Table 4.1.

4.4   Data processing

Since GRB 210419A was localised to within the MWA phase II compact configuration tied-array beam, we could coherently beamform the VCS data at the GRB position. Here we present specific details regarding the calibration and beamforming of the VCS observation of GRB 210419A (for details see Chapter 2).

4.4.1   Calibration

We selected a bright source (Hydra A) that had been observed in the standard correlator mode three hours after the VCS observation of GRB 210419A as the calibrator source. For each of the 24×1.28 MHz sub-bands and each tile of the

GRB observation, a calibration solution for the amplitude and phase was generated from the visibilities using the RTS (Mitchell et al., 2008). After inspecting each solution, we discarded a further nine tiles due to their poor calibration solutions. We also excised the edge channels to alleviate the aliasing effects (see Chapter 2).

4.4.2 Coherent beamforming

After calibration, we used the coherent beamforming to phase all tiles of the MWA observation of GRB 210419A to the GRB position. This requires the knowledge of cable and geometric delays to the pointing centre (i.e. the position of GRB 210419A) for each tile (for details see Chapter 2). Combining the delay model and the complex gain information from the calibration solution derived above, we obtained the tile based gain solution to phase all tiles to the same direction of GRB 210419A.

4.4.3 Imaging over a long integration time

While the high time resolution data are most suitable for searching for the prompt radio emission, snapshot images on $\sim$ min timescales can be used for detecting dispersed long duration signals (see Section 4.7.2.2). Compared to MWA imaging in the standard correlator mode (see Chapter 3), there is a prerequisite step for imaging the VCS data, i.e. offline correlation for creating visibilities (Sett et al., 2022). We used the same calibration observation as in Section 4.4.1 for calibrating the visibilities, and made an image with 248 s of data that covers the duration of the X-ray flare (highlighted in Figure 4.1 and fitted in Figure 4.2). To take into account the dispersion delay in the arrival time of any associated radio emission with respect to the X-ray flare, we offset the start time of the image. Given the unknown redshift of GRB 210419A, we made images starting from 347 s, 582 s and 820 s post-burst, corresponding to the dispersion delay for a typical long GRB at low, mean, and high redshift (Le & Mehta, 2017), including $z = 0.1$, 1.7 and

4 respectively, and inspected them for any associated signals.

For the image we adopted a pixel scale of 2 arcmin and size of 2048×2048 pixels, and used the WSClean algorithm (Offringa et al., 2014; Offringa & Smirnov, 2017) for deconvolution. This imaging exercise also provides a check on the data quality and the calibration solution despite the relatively poor imaging performance in the compact configuration. The final MWA image covering the period of the X-ray flare assuming a redshift of $z = 1.7$ is shown in Figure 4.3. For the results and interpretation see Sections 4.6.2 and 4.7.2.2.

4.5 Data Analysis

The coherent beamforming of the VCS observation of GRB 210419A resulted in a time series with a temporal and frequency resolution of $100\,\mu s$ and $10\,kHz$. As any prompt radio signals emitted by GRB 210419A would be dispersed in time by the medium it propagates through, we need to perform a de-dispersion search (see Chapter 2). Considering this emission may be linked to different emission models and thus have different start times following the GRB (see Section 4.7.2), we performed the search across the entire 15 min observation.

4.5.1 Dispersed pulse search

The de-dispersion search was performed using the PRESTO software package (Ransom, 2001). Note that we did not perform RFI excision (see Chapter 2). We used the PREPDATA routine in PRESTO to de-disperse the time series. Since there is no redshift measurement for GRB 210419A, we searched over a broad DM range from 1 to $5000\,pc\,cm^{-3}$, corresponding to a redshift range up to $z \sim 4$ using the DM–redshift relation $DM \sim 1200z\,pc\,cm^{-3}$ (e.g. Ioka 2003; Inoue 2004; Lorimer et al. 2007; Karastergiou et al. 2015). This DM range covers up to 90% of long GRBs detected by *Swift* per year based on their known redshift distribution (Le & Mehta, 2017). The DM trials used for de-dispersion were determined

by the DDPLAN.PY algorithm in PRESTO, and the time series data were down sampled by up to a factor of 16 to match the dispersive channel smearing (see Chapter 2). This results in 4401 DM trials and a temporal resolution ranging between 0.1–1.6 ms. Finally, we used PRESTO's SINGLE_PULSE_SEARCH.PY routine to search for single pulses in the de-dispersed time series. More details can be found in Chapter 2.

Following this analysis, PRESTO identified 143 trials with a SNR> 6, with a maximum SNR of 7.1 (for the distribution of the SNRs see Figure C.2 in Appendix C). As a further test on the sample of $> 6\sigma$ trials and the likelihood of some being real, we performed another single pulse search by creating a set of time series on the same dataset using (unphysical) negative DM trials (see Chapter 3 for further details). We found 119 candidates and a maximum SNR of 6.7 for the negative DM trials. Given the similar maximum SNR values resulting from the processing of both the positive and negative DM datasets, it is unlikely that any of the $> 6\sigma$ candidates are real dispersed signals.

As a physically motivated filtering step, we examined the DM values of the candidates output by PRESTO. Although it is difficult to predict the total DM of coherent emission associated with GRB 210419A as we do not know its redshift, we know that it is at cosmological distances. We can therefore use the DM contribution from the Milky Way in the GRB direction as a lower limit, which is $DM_{MW} \sim 62\,pc\,cm^{-3}$ according to the YMW16 electron density model (Yao et al., 2017). All prompt signal candidates must therefore have a DM $> 62\,pc\,cm^{-3}$. We arrived at 11 candidates at this stage.

As a final filtering step, we used a friends-of-friends algorithm (Burke-Spolaor et al., 2011; Bannister et al., 2012) to identify possible false positives. This algorithm exploits the fact that statistical fluctuations above the threshold are likely to appear only in a single DM trial and time stamp whereas a real signal would be partially detected in adjacent trials. Therefore, only candidates detected in a group of three or more adjacent DMs and times are likely to be real. Following

147

both filtering criteria described above, there remained no valid candidate.

4.5.2 Determination of system sensitivity

We converted the $6\,\sigma$ threshold on the SNRs output by PRESTO into flux density limits using the radiometer equation,

$$S_{\mathrm{min}} = (\mathrm{S/N}) \times \frac{\mathrm{SEFD}}{\sqrt{n_{\mathrm{p}} t_{\mathrm{int}} \Delta\nu}}, \qquad (4.1)$$

where n_{p} is the number of polarisations sampled, t_{int} is the integration time in units of µs, and $\Delta\nu$ is the bandwidth in units of MHz (see e.g. Meyers et al. 2017). The overall system equivalent flux density (SEFD) is determined by the ratio of the system temperature T_{sys} and gain G,

$$\mathrm{SEFD} = \frac{T_{\mathrm{sys}}}{G} = \frac{\eta T_{\mathrm{ant}} + (1-\eta) T_{\mathrm{amb}} + T_{\mathrm{rec}}}{G}, \qquad (4.2)$$

where η is the direction and frequency dependent radiation efficiency of the MWA array, and T_{ant}, T_{amb} and T_{rec} represent the antenna, ambient and receiver temperatures, respectively. The radiation efficiency η at the position of GRB 210419A at our observing frequency of 185 MHz is 0.987 (Ung et al., 2019), the receiver temperature (which is well characterised across the MWA band) is 23 K, and the ambient temperature (calculated from the metadata of our observation) is 311 K.

The calculation of the antenna temperature and gain requires a good knowledge of the tied-array synthesised beam pattern, i.e. the product of the array factor and an individual MWA tile power pattern. The array factor contains the phase information that points the telescope to a target position, and the tile pattern can be simulated as described in Sutinjo et al. (2015). Assuming a sky temperature map at our observing frequency based on the global sky model of de Oliveira-Costa et al. (2008), we convolved it with the tied-array beam pattern (e.g. Sokolowski et al. 2015) to estimate the antenna temperature and the tied-array gain (for a full description of this procedure see Meyers et al. 2017).

Altogether, we found the SEFD for our coherently beamformed data to be 986 Jy for the full (128 tiles) MWA.

We need to consider a few other factors in order to calculate our final sensitivity for this observation. First is the bandwidth consideration. As we flagged 16 of the 128 fine channels, the effective bandwidth is reduced to 87.5% of the full 30.72 MHz. To correct for this, we need to apply a scaling factor of $0.875^{-1/2} \approx 1.07$ when converting to flux density limits. In estimating the SEFD, we used 128 tiles of the full MWA for our simulation. However, there were 45 bad tiles during our observation of GRB 210419A. In the ideal case where the sensitivity scales with the number of tiles, this means we have lost 35% sensitivity. Additionally, a coherency factor is introduced to quantify the deviation of the theoretical expectation from the actual improvement with respect to incoherent sums, and can be estimated by comparing the SNRs of a bright pulse in the coherently and incoherently beamformed data (for details see Meyers et al. 2017). We chose the brightest pulsar (PSR J0437–4715; Bhat et al. 2014) in our field of view and produced an estimate of 0.639 for the coherency factor. This pulsar detection also demonstrates that our data processing and searching pipeline were operating correctly. Taking into account the above considerations, we arrived at a flux density upper limit of $6\sigma = 25$ Jy on a 1 ms timescale.

To better characterise our sensitivity to prompt radio signals, we converted the flux density limit to a fluence limit

$$F = 25\,(w_{\mathrm{obs}}/1\,\mathrm{ms})^{1/2}\,\mathrm{Jy\,ms}, \tag{4.3}$$

which is dependent on the pulse duration (w_{obs}). The observed pulse duration is given by

$$w_{\mathrm{obs}} = \sqrt{[w_{\mathrm{int,rest}}(1+z)]^2 + w_{\mathrm{sample}}^2 + w_{\mathrm{DS}}^2 + w_{\mathrm{scatter}}^2}, \tag{4.4}$$

where $w_{\mathrm{int,rest}}$, w_{sample}, w_{DS} and w_{scatter} are the rest-frame intrinsic pulse duration,

observational sampling time, dispersion smearing, and pulse scattering, respectively (Hashimoto et al., 2020a). Here we assume that the scattering would not limit the observability of prompt radio signals (Sokolowski et al., 2018). As the observed pulse width varies with the redshift, our prompt emission fluence limit is also redshift dependent (see Section 4.7.2.1).

4.6   Results

4.6.1   Prompt signal search

As described in Section 4.5.1, we performed a single pulse search on the high time resolution VCS triggered observation of *Swift*-detected GRB 210419A. Of these 143 trials $> 6\sigma$, only 11 had a DM$> 62 \, \text{pc} \, \text{cm}^{-3}$. As mentioned in Section 4.5.1, none of these candidates passed the friends-of-friends algorithm filtering, however, we still visually inspected the 11 candidates for signs of a dispersion sweep in the dynamic spectrum. None were seen reaffirming they are not viable dispersed signal candidates.

In conclusion, for the DM range of 62–5000 $\text{pc} \, \text{cm}^{-3}$, corresponding to all extragalactic distances up to $z \sim 4$, we do not detect any associated prompt radio emission from GRB 210419A. For an intrinsic pulse width of $w_{\text{int,rest}} = 0.5$–10 ms (typical for FRBs; Hashimoto et al. 2019, 2020b), our non-detection points to a 6σ fluence upper limit of 32–224 Jy ms, which can be used to constrain theoretical coherent emission models (see Section 4.7.2).

4.6.2   Long timescale emission during the X-ray flare

In order to search for long duration coherent radio signals associated with the X-ray flare described in Section 4.2, we generated an MWA image that covers the lifetime of the flare and potential dispersion delay for several redshifts as shown in Figure 4.3 (see Section 4.4.3). We performed a forced fit to the synthesised beam at the *Swift*-XRT position of GRB 210419A using the radio transient
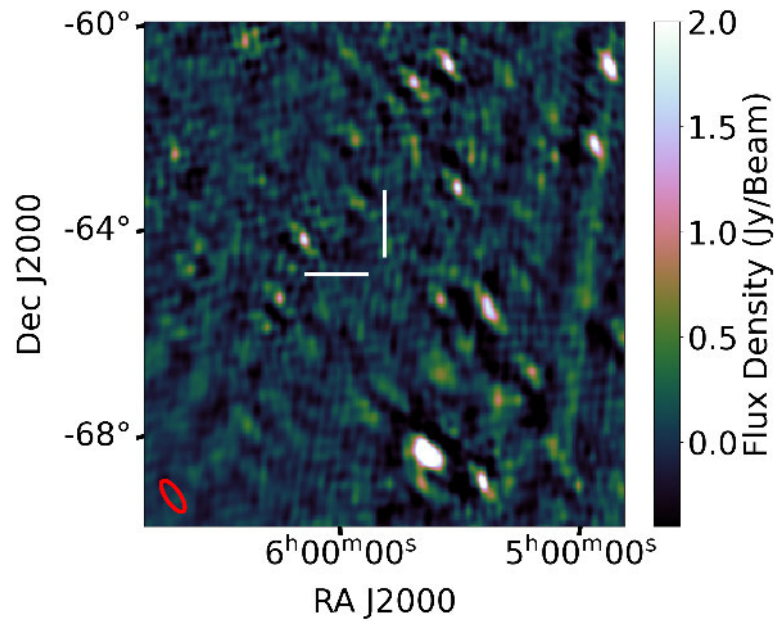
Figure 4.3: The MWA image showing the region surrounding GRB 210419A integrated over the duration of the X-ray flare assuming a redshift of $z = 1.7$ as described in Sections 4.4.3 and 4.6.2 (see radio fluence predictions in Section 4.7.2.2). The two white lines point to the GRB position localised by the *Swift*–XRT to within a synthesised beam of the MWA, where the RMS noise was measured to be $190 \, \mathrm{mJy \, beam^{-1}}$. The ellipse in the lower left corner shows the synthesized beam size of $23.4 \times 9.4 \, \mathrm{arcmin}$.

detection work-flow Robbie (Hancock et al., 2019b). For the three tested red-shifts of $z = 0.1$, 1.7, and 4, we obtained a flux density of $93 \pm 165 \, \text{mJy beam}^{-1}$, $115 \pm 169 \, \text{mJy beam}^{-1}$, and $46 \pm 171 \, \text{mJy beam}^{-1}$, respectively, which are consistent with zero within the uncertainties and therefore indicating a non-detection. We used Robbie (Hancock et al., 2019b) to calculate a local RMS noise of $190 \, \text{mJy beam}^{-1}$ in the image that assumes the GRB is at $z = 1.7$ (Figure 4.3), and therefore derived a 3σ upper limit of $570 \, \text{mJy beam}^{-1}$ for the long timescale radio emission during the X-ray flare. The RMS noise in the other two images assuming redshifts of $z = 0.1$ and $z = 4$ are similar, $185 \, \text{mJy beam}^{-1}$ and $192 \, \text{mJy beam}^{-1}$, respectively. The flux density upper limit can be used to constrain model parameters applicable to the GRB jet during the X-ray flare phase (see Section 4.7.2.2).

4.7 Discussion

4.7.1 Propagation effects

There are several propagation effects limiting the observability of the coherent, prompt radio emission we are searching for, such as absorption due to induced Compton scattering (Condon & Ransom, 2016) and absorption below the plasma frequency in the dense environment of the emission site (Condon & Ransom, 2016). Such considerations are particularly import for long GRBs as observations show they often occur in star forming regions near the centres of their host galaxies (generally with low metallicity; e.g. Berger 2009, Levesque et al. 2010), consistent with their core collapse origin. Due to the strong wind emission from a massive star prior to its collapse (Weaver et al., 1977), the circum-burst media of long GRBs exhibit a large density range typically between $\sim 10^{-1}$–$10^2 \, \text{cm}^{-3}$ (Laskar et al., 2015). In the following, we investigate the effect of both absorption mechanisms on any prompt radio emission emitted by GRB 210419A.

It has been shown that in the dense environments of long GRBs, induced

Compton and Raman scattering can severely reduce the detectability of radio pulses at $\sim$MHz frequencies (Macquart, 2007). For long GRBs in dense environments, only if the GRB jet is ultrarelativistic or the intrinsic opening angle of the emission is extremely small, could the predicted radio emission be visible. Given our incomplete knowledge of the GRB Lorentz factors (only lower limits have been observed, e.g. Ackermann et al. 2010, Zhao et al. 2011 and Zou et al. 2011) and the precise jet opening angles (they are likely confined to a narrow region; see Beniamini & Nakar 2019; Salafia et al. 2020), it is unknown whether the radio emission can evade induced Compton scattering. Nonetheless, a detection would provide valuable information on the Lorentz factor and the opening angle of the GRB jet. Specifically, it would indicate the evasion of induced Compton scattering, implying that the intrinsic emission angle is less than or equal to $\Delta\Omega \lesssim 5 \times 10^{-4}(T_{\mathrm{B}}/10^{25}\,\mathrm{K})^{-1/2}\,\mathrm{sr}$ where $T_{\mathrm{B}} = 10^{24}$–$10^{29}\,\mathrm{K}$ is the brightness temperature of the radio emission (Thompson, 1994; Macquart, 2007). If the radio emission is isotropic in the rest frame of the jet, this means that the minimum possible Lorentz factor of the jet is $\Gamma \gtrsim 10^3(D/100\,\mathrm{Mpc})$ where D is the luminosity distance of the GRB (Macquart, 2007).

The column density obtained from the X-ray spectrum of GRB 210419A can be used to estimate the plasma absorption of the radio emission along the line of sight. The X-ray spectrum of GRB 210419A is best fitted with an absorbed power law with a photon index of $2.60^{+0.29}_{-0.27}$ and an absorption column of $1.9^{+0.7}_{-0.6} \times 10^{21}\,\mathrm{cm}^{-2}$ (Beardmore et al., 2021), which is in excess of the Galactic value of $7.8 \times 10^{20}\,\mathrm{cm}^{-2}$ (Willingale et al., 2013). If we ignore the contribution of intervening systems (the interstellar and intergalactic media) along the line of sight, the intrinsic absorbing column density for GRB 210419A would be $\sim 1.1 \times 10^{21}\,\mathrm{cm}^{-2}$, which is smaller than the typical value of $5^{+10.8}_{-3.4} \times 10^{21}\,\mathrm{cm}^{-2}$ evaluated from a sample of long GRBs (Campana et al., 2012) and comparable to the typical value of $2.5^{+3.8}_{-1.5} \times 10^{21}\,\mathrm{cm}^{-2}$ for a sample of short GRBs (Asquini et al., 2019). As shown by Zhang (2014) in the specific context of GRBs, the plasma frequency in the

GRB environment must be lower than the radio frequency for the radio emission to escape, i.e. $1/2\pi \times \sqrt{4\pi n_e e^2/m_e} < \nu_{\rm obs}$, where n_e is the electron number density, and e and m_e are the electric charge and mass of electrons (Vlasov, 1968). At the MWA observing frequency of $\nu_{\rm obs} = 185\,{\rm MHz}$, that would require an electron number density $n_e \lesssim 4 \times 10^8\,{\rm cm}^{-3}$, corresponding to an electron column density of $\lesssim 4 \times 10^{21}\,{\rm cm}^{-2}$ if we assume the length scale of the GRB environment to be $\sim 10^{13}\,{\rm cm}$ (Zhang, 2014). While the electron column density along our line of sight derived from the XRT spectrum of GRB 210419A is less than this value, the uncertainty associated with the length scale makes it difficult to conclude whether our observing frequency is above the plasma frequency. For the following analysis, we assume that it is above the plasma frequency in order to investigate the constraints our observations place on coherent radio emission predicted by the jet-ISM interaction model.

4.7.2   Constraints on the jet-ISM interaction model

The GRB jet-ISM interaction model has been described under the magnetar assumption in Chapter 3. However, this model also works in the case of no magnetar formation (Usov & Katz, 2000). Here we revisit this model without any assumption of magnetars, which would further generalise our model discussion (see Chapter 6 for more discussion).

4.7.2.1   Radio emission associated with the prompt gamma-ray emission

As suggested by Usov & Katz (2000), the interaction between a Poynting flux dominated jet and the ISM can generate a coherent radio pulse as well as the prompt gamma-ray emission. In this scenario, the bolometric radio fluence Φ_r (erg cm^{-2}) is proportional to the bolometric gamma-ray fluence Φ_γ (erg cm^{-2}) in the energy range of 0.1–$10^4\,$keV, the widest energy range for current GRB detection satellites (e.g. Rowlinson et al. 2019). This power ratio is roughly estimated

to be $\simeq 0.1\epsilon_B$ (Usov & Katz, 2000), where ϵ_B is the fraction of magnetic energy in the relativistic jet. In the typical spectrum of low-frequency waves generated at the shock front, there is a peak frequency determined by the magnetic field

$$\nu_{\max} \simeq [0.5 - 1]\frac{1}{1+z}\epsilon_B^{1/2} \times 10^6 \, \text{Hz} \tag{4.5}$$

(in the observer's frame; Rowlinson et al. 2019). For our observing frequency $\nu = 185 \, \text{MHz}$, which is above the peak radio frequency, the observed radio fluence is given by

$$\Phi_\nu = \frac{\beta - 1}{\nu_{\max}}\Phi_r \left(\frac{\nu}{\nu_{\max}}\right)^{-\beta} \text{erg cm}^{-2} \, \text{Hz}^{-1}. \tag{4.6}$$

Note that the bolometric radio fluence Φ_r is the fluence integrated over frequency and thus has a different unit to Φ_ν. Assuming a typical spectral index of $\beta = 1.6$ (Usov & Katz, 2000), the power ratio between Φ_r and Φ_γ can be written in terms of the radio fluence at our observing frequency:

$$\delta = \frac{5}{3}\nu^{1.6}\nu_{\max}^{-0.6}\frac{\Phi_\nu}{\Phi_\gamma}. \tag{4.7}$$

Thus, the predicted radio fluence is given by

$$\Phi_{185\text{MHz}} \simeq [0.9 - 1.4] \times 10^{-10}\delta(1+z)^{-0.6}\epsilon_B^{0.3}\Phi_\gamma. \tag{4.8}$$

In order to calculate the unabsorbed bolometric gamma-ray fluence ($0.1 - 10^4 \, \text{keV}$) for GRB 210419A, we applied a correction factor to the gamma-ray fluence measured by *Swift*-BAT in the $15 - 150 \, \text{keV}$ energy band. Assuming a simple power-law model for the spectrum of the prompt emission as given by Palmer et al. (2021) and the absorption column derived from the spectral fit to the *Swift*-XRT PC observation of GRB 210419A (Beardmore et al., 2021, see also Section 4.2), we used the WebPIMMS tool (Mukai, 1993) to obtain a fluence correction factor of $6.2^{+6.5}_{-1.2}$. Note that the errors come from the uncertainty on the spectral index, which dominates the errors on the absorption column.

Both the model-predicted prompt radio emission and our fluence upper limit at 185 MHz (see Eq. 4.3) depend on redshift, which is an unknown quantity for GRB 210419A. Under the assumption that we would be able to capture the dispersion delayed radio emission generated at the prompt gamma-ray emission phase (when the GRB jet first interacts with the ISM), the 89 s delay of our observation with respect to the GRB detection (see Section 4.3) means we can only detect signals with a minimum DM of $734\,\mathrm{pc\,cm^{-3}}$. After subtracting the Galactic contribution (see Section 4.5.1), this corresponds to events at $z \gtrsim 0.6$. We are therefore able to search for prompt radio signals associated with the jet-ISM interaction within the redshift range of $0.6 < z < 4$ for GRB 210419A.

In order to constrain the model-predicted prompt emission in Eq. 4.8, we need to convert the sensitivity of our observation to a fluence upper limit using Eq. 4.3, which is dependent on the unknown rest-frame intrinsic pulse width $w_{\mathrm{int,rest}}$. In the absence of detected prompt emission from long GRBs, we base our choice of $w_{\mathrm{int,rest}}$ on known rest-frame intrinsic durations of FRBs with known redshifts and no scattering features (~ 0.5–10 ms; Hashimoto et al. 2019, 2020b). We therefore assume durations of $w_{\mathrm{int,rest}} = 0.5\,\mathrm{ms}$ and $10\,\mathrm{ms}$ for our fluence upper limits when constraining the model predictions.

With the assumed redshifts and intrinsic pulse widths, we illustrate how our fluence upper limits derived from our MWA observation of GRB 210419A can constrain the model predictions for the fraction of magnetic energy in the relativistic jet in Figure 4.4. For a redshift range of $0.6 < z < 4$ and an intrinsic pulse width of $0.5\,\mathrm{ms} < w_{\mathrm{int,rest}} < 10\,\mathrm{ms}$, we derived a 6σ fluence upper limit of 77–224 Jy ms (see Section 4.5.2), resulting in a constraint on the fraction of magnetic energy in the relativistic jet launched by GRB 210419A $\epsilon_{\mathrm{B}} \lesssim 0.05$ and $\epsilon_{\mathrm{B}} \lesssim 0.1$ at the lowest and highest redshift, respectively. These upper limits on ϵ_{B} are comparable to $\epsilon_{\mathrm{B}} \lesssim [0.24-0.47]$ derived in Rowlinson et al. (2019) for long GRB 180706A. Note that our constraints on ϵ_{B} are only valid if the jet-ISM interaction is indeed active in the GRB under study.
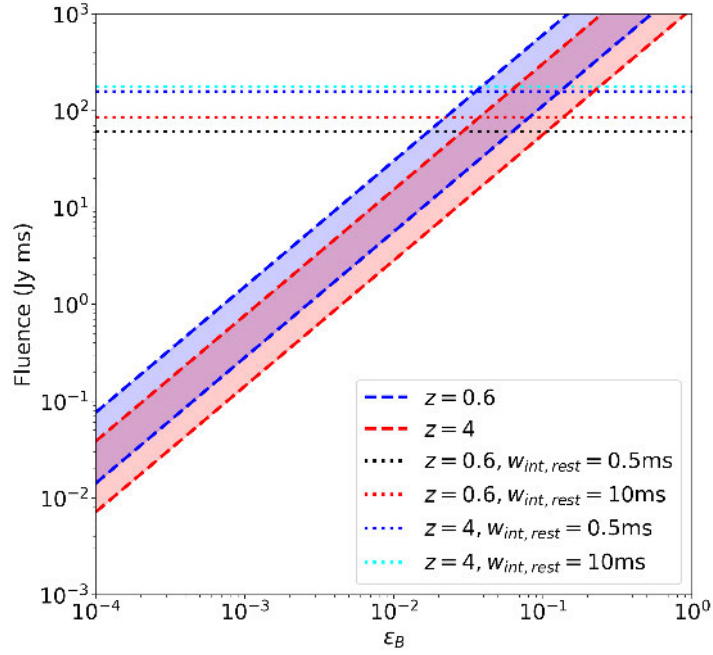
Figure 4.4: The predicted fluence of a prompt signal produced by the interaction between the relativistic jet of GRB 210419A and the ISM at 185 MHz as a function of the fraction of magnetic energy. The shaded regions illustrate those predictions assuming the maximum and minimum redshift considered in this investigation, with the uncertainties resulting from the peak frequency of the prompt radio emission at the shock front (see Eq. 4.5) and the measured gamma-ray fluence (see Section 4.2), which has been corrected to a bolometric gamma-ray fluence (see Section 4.7.2.1). The horizontal dotted lines in different colors represent the fluence upper limits we obtained from the VCS observation of GRB 210419A for different combinations of redshift and intrinsic pulse width.

As one of the key open questions in the GRB field, i.e. whether the relativistic jet is Poynting flux or baryon dominated, GRB jet magnetisation has been investigated extensively (e.g. Lyutikov et al. 2003, Bégué & Pe'er 2015, Pe'er 2017). Zhang & Pe'er (2009) reported a lower limit of $\epsilon_B \gtrsim [0.94 - 0.95]$ at the photosphere radius based on the non-detection of a thermal component in gamma rays ($\sim 50\,\mathrm{keV}$) from GRB 080916C. Note that ϵ_B evolves with the radius from the central engine and may become much smaller at the deceleration radius where the relativistic ejecta collides into the ISM (Kumar & Zhang, 2015). A detailed simulation of spectra of GRB prompt emission using a hybrid relativistic outflow containing both fireball and Poynting-flux components finds $\epsilon_B \gtrsim 0.5$ at a distance of $10^{15}\,\mathrm{cm}$ from the central engine (a possible prompt gamma-ray emission site covered by our MWA observation; Gao & Zhang 2015). Therefore, our constraint on the magnetisation of GRB jets potentially undermines the Poynting flux dominated scenario investigated in this simulation but at a low significance, particularly given our assumptions on the spectral index β, the GRB redshift and the pulse width.

4.7.2.2 Radio emission during the X-ray flare

As the X-ray light curve of GRB 210419A displays flaring activity as shown in Figure 4.1 (shaded region), we explore the GRB jet properties in the context of any radio emission associated with X-ray flaring in this section.

While X-ray flares are commonly observed following GRBs, their physical origin still remains unclear, with suggestions including internal dissipation (prompt-emission-like; Falcone et al. 2007; Chincarini et al. 2010; Margutti et al. 2010) and external shock (afterglow-like; Giannios 2006; Panaitescu 2006; Bernardini et al. 2011) mechanisms. There is a criterion to distinguish these two scenarios based on the flare variability and occurrence time (Δt_{FWHM} the full width at half maximum of the pulse and t_{pk} the time of the flare maximum; Ioka et al. 2005; Lazzati & Perna 2007). If $\Delta t_{\mathrm{FWHM}}/t_{\mathrm{pk}} < 1$, as is the case for GRB 210419A

(see Figure 4.1), the flare is difficult to accommodate within the external shock model. Therefore, here we assume an internal shock origin for the flare observed in the X-ray light curve of GRB 210419A (the same as for the prompt gamma-ray emission), which means the jet-ISM interaction model discussed in Section 4.7.2.1 may also apply to the X-ray flare (as described by Starling et al., 2020).

For this scenario, we use the X-ray fluence derived for the X-ray flare in Section 4.2 to calculate the fluence of the predicted radio signal using the Usov & Katz (2000) model equations given in Section 4.7.2.1. In order to convert the X-ray fluence measured in the $0.3 - 10 \, \text{keV}$ energy band to a bolometric gamma-ray fluence ($0.1 - 10^4 \, \text{keV}$), we again used WebPIMMS and the power law spectral fit to the *Swift*-XRT data provided by Beardmore et al. (2021, see also Section 4.2) to derive a correction factor of $4.0^{+2.0}_{-0.8}$. Note that we used the photon index from the spectrum derived from the PC mode observation as the recorded data covers the duration of the X-ray flare we are investigating (see Figure 4.1).

When placing fluence limits on the associated radio emission, we do not consider signals of millisecond duration for this scenario. Given that the fluence from the X-ray flare is much lower than what is supplied by the prompt gamma-ray emission, it would provide a less stringent constraint on ϵ_B (see Eq. 4.8) than that calculated in Section 4.7.2.1. However, it is possible that the predicted radio pulse has a much longer duration, similar to that of the X-ray flare (Starling et al., 2020). Any signals on such a long timescale would not be dispersion limited at reasonable GRB redshifts, and would have a flux density equal to the undispersed pulse (see eq. 16 in Rowlinson & Anderson 2019). We can therefore readily search for associated radio emission in an MWA image created over the same timescale as the X-ray flare duration.

In Figure 4.3 we show the region surrounding GRB 210419A made from an offline correlation of the VCS data with an integration time that covers the duration of the X-ray flare, assuming a dispersion delay corresponding to a typical long GRB redshift of $z = 1.7$ (see Section 4.4.3). We compare the 3σ flux density

upper limit derived from the MWA image in Figure 4.3 (which is similar to the upper limits from the images that assume redshifts of $z = 0.1$ and $z = 4$) to the predicted model emission associated with the X-ray flare for a range of redshifts in Figure 4.5. The MWA was on target and observing GRB 210419A before the X-ray flare, which occurred 335 s post-burst so there is no lower limit on the redshift range we are able to constrain (unlike in Section 4.7.2.1). We therefore plot the model predictions corresponding to the lowest ($z = 0.1$), typical ($z = 1.7$), and highest ($z = 4$) observed long GRB redshifts. As can be seen from Figure 4.5, we are able to constrain the fraction of magnetic energy to $\epsilon_B \lesssim 10^{-3}$, $\epsilon_B \lesssim 2 \times 10^{-3}$ and $\epsilon_B \lesssim 3 \times 10^{-3}$ during the flaring activity at the lowest, average, and highest redshifts. These constraints are more stringent than those derived during the prompt gamma-ray emission phase in Section 4.7.2.1. Note that our constraints on ϵ_B are only valid under the assumption that there is indeed radio emission during the X-ray flare of GRB 210419A.

Starling et al. (2020) predicted that 44% of X-ray flares detected by *Swift*–XRT should have had detectable low frequency radio emission by LOFAR assuming magnetically dominated GRB jets. Here, assuming a magnetic energy fraction of $\epsilon_B = 10^{-2}$ comparable to the constraint shown in Figure 4.5, our MWA rapid-response observation should be able to detect the predicted radio emission from 30% of X-ray flares. Assuming a magnetically driven outflow at the base of the jet where it is launched (e.g. Komissarov et al. 2009; Tchekhovskoy et al. 2010), our non-detection of radio emission during the X-ray flare might imply the existence of magnetic energy dissipation in the GRB jet, which results in insufficient magnetic energy for radio emission during X-ray flares (e.g. Kumar & Zhang 2015).
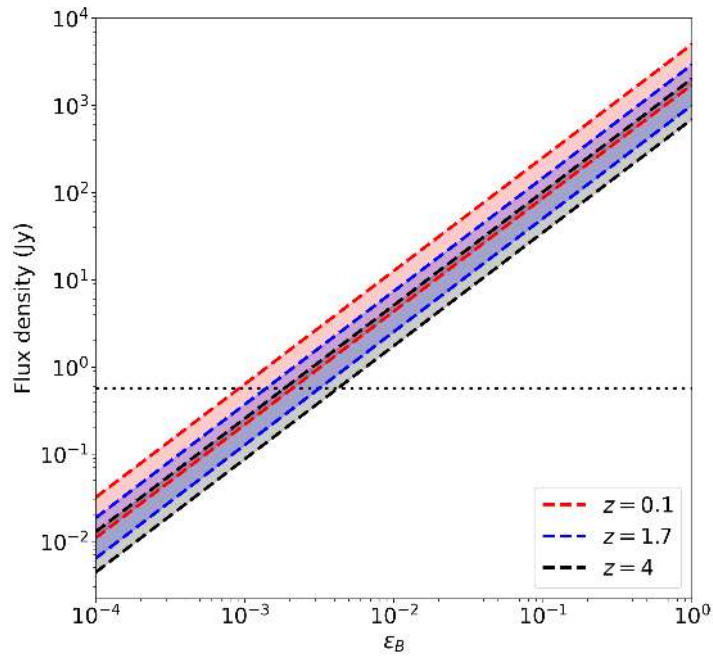
Figure 4.5: The predicted flux density of the radio signal produced during the X-ray flare from GRB 210419A as a function of the fraction of magnetic energy. The shaded region in different colors represent the model predictions assuming the lowest, typical and highest long GRB redshift, with the uncertainties again resulting from the predicted peak frequency of the prompt radio emission at the shock front (see Eq. 4.5) and the measured X-ray fluence (see Section 4.2), which has been corrected to a bolometric gamma-ray fluence (see Section 4.7.2.2). The horizontal dotted line shows the 3σ flux density upper limit derived from the MWA image integrated over the duration of the X-ray flare.

4.7.3 Future prospects

4.7.3.1 Improvements to future VCS triggers

We expect there to be much more sensitive observations with the full MWA in the future. During our observation of GRB 210419A, several of the receivers were down due to beamformer faults on-site, which resulted in a 35% sensitivity loss. With the full MWA operational, we could have reached a sensitivity of $\sim 40\,\mathrm{Jy\,ms}$ for a $10\,\mathrm{ms}$ wide pulse, comparable to the prediction in Rowlinson & Anderson (2019). This would represent a factor of ~ 3 in improvement in sensitivity compared to our results for GRB 210419A, which would further constrain the fraction of magnetic energy in the relativistic jet of GRBs during the prompt gamma-ray phase (see Section 4.7.2.1) to $\epsilon_{\mathrm{B}} \lesssim [0.01 - 0.03]$ under the assumption that the jet-ISM interaction indeed operates in the GRB under study.

We expect to trigger the VCS on more *Swift* GRBs in the future, with a particular focus on short GRBs as associated prompt radio signals are more likely to escape their less dense surrounding environments (Zhang, 2014). With a compact binary merger origin, short GRBs have additional channels to produce coherent radio emission such as the interactions of the neutron star magnetic fields just preceding the merger (Lyutikov, 2013). Assuming a typical short GRB redshift of $z = 0.7$ (Gompertz et al., 2020), the MWA response time of $89\,\mathrm{s}$ would allow us to capture the signals produced as early as $\sim 13\,\mathrm{s}$ prior to the prompt gamma-ray emission. Based on the number of short GRBs detected by *Swift* per year (~ 9; Lien et al. 2016) and assuming 30% sky coverage of the MWA, we would expect to trigger on $2 - 3$ short GRBs per year.

While the VCS data are most sensitive to prompt radio emission, they can be used to search for long timescale or persistent emission after offline correlation and imaging, as was done in Section 4.7.2.2. However, since the observation of GRB 210419A was taken when the MWA was in the compact configuration, the resulting image has a low angular resolution ($\sim 10\,\mathrm{arcmin}$) and is limited by classical confusion (see Figure 4.3; Condon 1974; Franceschini 1982), making the

upper limit derived from the RMS noise less constraining than what we would expect from an observation taken in the extended configuration. Assuming a typical flare duration of 247 s (for the distribution of flare durations see Yi et al. 2016) and the general relation that image noise scales with integration time as $\propto \Delta t_{\text{int}}^{-1/2}$, we expect a sensitivity of $\sim 0.1 \, \text{Jy beam}^{-1}$ on the 247 s timescale in the extended configuration (a factor of 2 times better than our observation of GRB 210419A in the compact configuration) based on the upper limits derived on 30 min timescales from previous MWA observations (see Chapter 3). Note that our sensitivity estimation does not take into account sidelobe confusion. In the future we expect to undertake VCS observations in the extended configuration, which will increase the sensitivity to any long timescale emission by an order of magnitude and thus improve our constraint on the coherent radio emission associated with X-ray flares.

4.8   Summary and conclusions

In this chapter, we have searched for prompt radio bursts associated with GRB 210419A in the frequency range of 170 to 200 MHz using the rapid-response mode on the MWA, triggering VCS observations. This is the first time that the MWA VCS has been used in the rapid-response follow up of a GRB. The MWA rapid-response observing mode makes it possible to capture the early time emission, which would be missed by other low frequency radio telescopes with slower response times and/or all-sky instruments that necessarily have lower sensitivities (for a comparison of response times for different low-frequency telescopes see figure 10 in Anderson et al. 2021b).

As a result of this work, we come to the following main conclusions:

1. We have performed a single pulse search on the high time resolution data but found no prompt emission associated with GRB 210419A. We derive a fluence upper limit of 77–224 Jy ms on prompt radio bursts associated

with GRB 210419A, assuming a pulse width of 0.5–10 ms and a redshift of $0.6 < z < 4$. This allows us to test the jet-ISM interaction model assuming a spectral index of $\beta = 1.6$ (Usov & Katz, 2000). The fluence limit results in the fraction of magnetic energy constraint of $\epsilon_B \lesssim [0.05-0.1]$ in the relativistic jet (see Figure 4.4), disfavoring the Poynting flux dominated composition for the jet though at a low significance.

2. We have also inspected the MWA images made via offline correlation of the VCS data for signals occurring during the X-ray flare of GRB 210419A assuming redshifts of $z = 0.1$, 1.7, and 4 but found no emission at the GRB position (see Figure 4.3), obtaining a 3σ flux density upper limit of $570\,\mathrm{mJy\,beam^{-1}}$. This allows us to test the same jet-ISM interaction model, which also predicts radio emission during X-ray flares (Starling et al., 2020). The flux density limit results in a constraint on the magnetic energy fraction during the X-ray flare of $\epsilon_B \lesssim 10^{-3}$ over a redshift range of $0.1 < z < 4$ (see Figure 4.5), suggesting magnetic energy dissipation in the GRB jet.

3. Compared to previous MWA searches for prompt radio bursts using the standard correlator with a temporal resolution of only 0.5 s (see Chapter 3), our VCS observation of GRB 210419A with a temporal resolution of 100 μs is equally as sensitive to our best constrained burst GRB 190627A using image dedispersion techniques (see Chapter 3), and demonstrates the potential for even more sensitive VCS observations in the future.

In conclusion, our non-detection of coherent radio emission associated with GRB 210419A seems to challenge the Poynting flux dominated scenario commonly assumed for GRB jets (Usov 1994; Thompson 1994; Drenkhahn & Spruit 2002), which is a prerequisite for the radio emission mechanisms proposed by Usov & Katz (2000) and Starling et al. (2020). However, there are some other possible reasons for our non-detection. Given the unknown redshift of GRB 210419A and observations of long GRBs at redshifts of $z > 6$ (Salvaterra, 2015), it may be

too distant to have detectable radio emission. Given the X-ray absorption might not reflect the true density in the GRB environment (e.g. Rahin & Behar 2019; Dalton & Morris 2020), it is possible that GRB 210419A resides in a high density surrounding medium that prevents low-frequency emission from escaping.

In order to detect the predicted radio emission or fully explore the parameter space of the emission model, we need more MWA rapid-response VCS observations of GRBs, especially short GRBs with redshift measurements.

Chapter 5

A targeted search for repeating fast radio bursts with the MWA

This chapter is a reproduction of J. Tian, G. E. Anderson, P. J. Hancock, J. C. A. Miller-Jones, M. Sokolowski, C. W. James, N. D. R. Bhat, N. A. Swainston, D. Ung, B. W. Meyers (2022), "A targeted search for repeating fast radio bursts with the MWA", Monthly Notices of the Royal Astronomical Society, Volume 518, Issue 3, page 4278-4289, DOI: https://doi.org/10.1093/mnras/stac3392. I have adapted the chapter to make it better fit into this thesis, avoiding repetition of the materials already included in Chapters 1 and 2 and keeping all references consistent within this thesis.

5.1 Introduction

As discussed in Section 1.1.4, there are potential links between GRBs and FRBs, as evidenced by the observational (CHIME/FRB Collaboration et al., 2020; Bochenek et al., 2020; The CHIME/FRB Collaboration et al., 2021a) and theoretical (Zhang, 2020b; Beloborodov, 2020; Lyubarsky, 2020) association of FRBs with magnetars, one type of remnant that could be formed by GRBs (Rowlinson et al., 2013). In this chapter we present a targeted search for low-frequency (144–

215 MHz) FRB emission from five repeating FRBs. We used 23.3 hr of archival data taken with the MWA VCS between 2014 September and 2020 May. This is the first time that the MWA VCS has been used to search for FRB signals from known repeaters, which enables much more sensitive FRB searches than previously performed with the standard MWA correlator mode (Tingay et al., 2015; Rowlinson et al., 2016; Sokolowski et al., 2018). We performed a standard single pulse search with a temporal and spectral resolution of 400 μs and 10 kHz, respectively, over a broad DM range centred at the known DM of each studied repeating FRB. With the fluence upper limits derived from the VCS data, we were able to study the burst rates, low-frequency spectra and local environments of the five repeaters. Finally, this chapter highlights the importance of VCS follow-up or archival searches for low frequency bursts from known repeaters, which would provide unprecedented information on FRB emission mechanisms and/or physics.

5.1.1   Low-frequency FRB searches

Up until very recently, FRB repeating sources have been detected at frequencies between 300 MHz (Chawla et al., 2020; Pilia et al., 2020; Parent et al., 2020) and 8 GHz (Gajjar et al., 2018). However, simultaneous observations of repeating FRBs in different bands suggest that individual pulses are narrow-band, yet are scattered across a wide range of frequencies with time (Gourdji et al., 2019). For example, FRB 20180916B has been detected up to 5.3 GHz (Bethapudi et al., 2022), yet the absence of simultaneous detections at frequencies 2.3 and 8.4 GHz demonstrates its frequency dependent activity (Pearlman et al., 2020). While Chawla et al. (2020) detected FRB 20180916B at 300–400 MHz using the Green Bank Telescope, no emission was seen contemporaneously at 110–188 MHz using the Low Frequency Array (LOFAR). Such narrow-band emission has also been demonstrated for FRB 20121102A (Gourdji et al., 2019; Majid et al., 2020) and FRB 20190711A (Kumar et al., 2021a).

To date, there have been many searches for FRB emission below 300 MHz,

including simultaneous, multiband, targeted (Law et al., 2017; Sokolowski et al., 2018; Houben et al., 2019) and wide-field blind (Coenen et al., 2014; Karastergiou et al., 2015; Tingay et al., 2015; Rowlinson et al., 2016; Sanidas et al., 2019) searches using LOFAR, the Murchison Wide-field Array (MWA) and the Long-wavelength Array. In addition, searches for prompt and dispersed (FRB-like) signals predicted to be associated with gamma-ray bursts have also been conducted with MWA and LOFAR via rapid-response observations (Kaplan et al., 2015; Rowlinson et al., 2019, 2021; Anderson et al., 2021b; Tian et al., 2022a,b), none of which have yielded a detection. However, recently Pleunis et al. (2021b) reported the detection of 18 bursts from FRB 20180916B between 110–188 MHz using LOFAR, the only detections of any FRB below 300 MHz to date. This confirms the existence and the detectability of low frequency bursts from repeating FRBs at cosmological distances, which are not limited by propagation effects or the FRB emission mechanism. Additionally, this same repeater appears to undergo chromatic periodic activity where its activity window is wider and occurs later with decreasing frequency. This is demonstrated by the ~ 3 day delay in the peak activity between bursts observed by CHIME/FRB at 600 MHz and those observed by LOFAR at 150 MHz (Pleunis et al., 2021b; Pastor-Marazuela et al., 2021).

There are several reasons for the dearth of FRB detections at low frequencies. First is an increase in the sky background temperature at low radio frequencies (e.g. de Oliveira-Costa et al. 2008; Cong et al. 2021). This can increase the noise level in low frequency observations and reduce the observed signal-to-noise ratio (S/N). As FRB signals propagate through intervening ionized media before reaching the Earth, the effects of scatter broadening of the pulse profiles and intrachannel dispersive smearing, which are more significant at low frequencies, can also reduce the peak S/N. In addition, repeating FRBs are also known to suddenly turn on and enter periods of long-term ($>$ a few years) activity (e.g., FRB 20201124A; Lanman et al. 2022). This makes it difficult to define proper

169

burst rates for sources that exhibit burst clustering, which may be more/less active at higher/lower frequencies (e.g., FRB 20121102A and FRB 20180916B; Josephy et al. 2019; Pearlman et al. 2020). All of these present challenges to FRB searches at low radio frequencies.

Nonetheless, low frequency FRB searches are very important. A real detection at low frequencies would complement high frequency detections for broadband measurements of the FRB spectrum, allowing more reliable studies of the burst energetics and the emission mechanism. It would also allow us to better constrain the local environments of FRBs based on propagation effects such as free-free absorption. As this effect is more obvious at lower frequencies (optical depth scales as $\tau_{\rm ff} \propto \nu^{-2.1}$) , FRB measurements at low frequencies would place more stringent constraints on the size of the emission site (Pleunis et al., 2021b). Low frequency FRB emission is also sensitive to other propagation effects such as the dispersion, scattering and Faraday rotation, and could provide precise measurements of the dispersion measure, scattering timescale and rotation measure of FRBs (Petroff et al., 2022). Therefore, low frequency FRB searches are well motivated scientifically in spite of the observational challenges.

5.1.2 SMART survey

The MWA VCS mode has been extensively used for pulsar studies and searches (Bhat et al., 2016; Xue et al., 2017; McSweeney et al., 2017; Meyers et al., 2018; Swainston et al., 2021). In September 2018, an all sky pulsar search project, the Southern-sky MWA Rapid Two-meter (SMART) survey (Bhat et al., 2022), was commenced to search the entire sky south of $+30°$ in declination for pulsars, with regular data collection planned until ~ 2023. This survey, along with targeted observations toward a number of already known pulsars, generates a large amount of VCS observations in the MWA archive. These all-sky archival data at the highest time resolution available with the MWA, combined with the MWA's large field of view are an invaluable resource to exploit for transient studies and

enable the search for low frequency bursts from known repeating FRB sources. The observations we selected for FRB searches were taken between 2014 September and 2020 May, spanning the MWA Phase I and Phase II, which differ in array configuration, and baseline length and distribution. The MWA Phase I presents an angular resolution of $\sim 2\,\mathrm{arcmin}$ at $185\,\mathrm{MHz}$ (Tingay et al., 2013). The MWA phase II has two configurations: extended and compact configurations with angular resolutions of ~ 1 and $\sim 10\,\mathrm{arcmin}$, respectively (Wayth et al., 2018). Both can be used for FRB searches.

In this chapter, we use the archival MWA observations taken with the VCS to search for FRB signals from known repeating FRBs. In Section 5.2, we describe our selection of MWA observations in the data archive and the data processing and analysis we used for the FRB search. Our results are then presented in Section 5.3. We discuss the implications of our results for FRB sources and emission models in Section 5.4, followed by conclusions in Section 5.5.

5.2 Observations and data reduction

5.2.1 Sample selection

We used the first complete FRB catalogue[1] (including FRB events published in the Transient Name Server[2], FRBCAT and the CHIME/FRB Catalogue; Petroff et al. 2016; Amiri et al. 2021) to identify targets for our FRB search, i.e. those repeaters that could be viewed by the MWA. Since the majority of repeaters have been detected by CHIME, which looks at the Northern sky (CHIME/FRB is sensitive to sky locations with declinations $> -11°$; Amiri et al. 2021), only a few of them are located in the MWA observable sky. We filtered through the population of known repeating FRBs using the criterion of their maximum elevation above the MWA's horizon of $> 30°$ (for the choice of the elevation

---

[1]https://www.herta-experiment.org/frbstats/
[2]https://www.wis-tns.org/

limit, see Hancock et al. 2019a), and obtained a list of five repeating FRBs (see Table 5.1).

The five repeating FRBs display varying burst widths, fluences and degrees of activity and repetition rates, as shown in Table 5.1. FRB 20190711A was first detected by ASKAP in the frequency range 1.1–1.3 GHz (Macquart et al., 2020), and hundreds of hours of follow-up observations with ASKAP and Parkes detected only one repeat burst at 1.4 GHz in the Parkes observations (Kumar et al., 2021a), indicating an extremely low repetition rate. We do not report a burst rate for this repeater in Table 5.1. FRB 20190116A, 20190117A, 20190213A and 20201124A were first detected by CHIME in the frequency range 400–800 MHz, with a burst rate simply estimated by the ratio of the number of detected bursts to the exposure time of the CHIME system on the source (CHIME/FRB Collaboration et al., 2019c; Fonseca et al., 2020a). The brightest repeater in this sample, FRB 20201124A, was subsequently detected by multiple instruments including the Karl G. Jansky Very Large Array (VLA) at 1.5 GHz (Law et al., 2021), the Australian Square Kilometre Array Pathfinder (ASKAP) at 864.5 MHz (Kumar et al., 2021d,b) and the Five-hundred-meter Aperture Spherical radio Telescope (FAST) at 1.2 GHz (Xu et al., 2021), and reported to enter a sudden period of high activity in 2021 March (Marthi et al., 2021; Piro et al., 2021; Lanman et al., 2022). Thanks to these radio observations between 864.5 MHz and 1.5 GHz, FRB 20201124A is the only repeater in our sample that has a measured spectral index $\alpha = -5.82^{+0.68}_{-0.84}$ (Kumar et al., 2021c). For the CHIME repeaters, the burst rates quoted in Table 5.1 assume an average rate that does not take into account the likely variable nature of a potential activity window, and thus may not apply to the time windows of the MWA observations inspected in our analysis (see discussions in Section 5.4.1). Note that the CHIME rates in Table 5.1 are all based on CHIME observations except for FRB 20201124A, which is estimated for the period of high activity after 2021 March while its rate prior to discovery is as low as $< 3.4 \, \text{day}^{-1}$ (Marthi et al., 2021; Piro et al., 2021; Lanman et al., 2022).

FRB	Instrument[1]	RA (deg)	Dec (deg)	Frequency[2]	Burst rate[3] (hr^{-1})	Fluence[4] (Jy ms)	Burst Width[4] (ms)	DM ($\mathrm{pc\,cm}^{-3}$)
190116A	CHIME	192.33 ± 0.15	27.15 ± 0.24	400–700 MHz	0.25	0.8–2.8	1.5–4	441
190117A	CHIME	331.71 ± 0.15	17.37 ± 0.26	400–800 MHz	0.26	5.0–12	0.64–5.2	393.6
190213A	CHIME	31.72 ± 0.25	20.08 ± 0.30	400–600 MHz	0.12	0.6–3.0	4–10	651.45
190711A	ASKAP	329.4195	-80.358	1.1–1.4 GHz	/[5]	1.4–34	1.0–6.5	593.1
201124A	CHIME	76.99 ± 0.52	26.19 ± 0.53	550–750 MHz	16[6]	2.6–108	6.1–59.3	411

Table 5.1: Details of the five known repeaters that can be observed by the MWA. References for the repeater properties: a: CHIME/FRB Collaboration et al. (2019c); b: Fonseca et al. (2020a); c: Macquart et al. (2020); Kumar et al. (2021a); d: Chime/Frb Collabortion (2021); Kumar et al. (2021d); Marthi et al. (2021); Piro et al. (2021); Lanman et al. (2021).

1: The radio instrument that discovered and localised each repeater.

2: The frequency of detected emission from each repeater.

3: The burst rate inferred by the ratio between the number of detected bursts and the total exposure time of each repeater. The burst rates are all based on CHIME observations except for FRB 190711A and 201124A (see the notes below). An estimation of expected bursts during the MWA observations is given in Table 5.3 assuming the burst rate is constant.

4: The range of fluences and widths observed for each repeater in the MWA VCS data.

5: The burst rate of FRB 190711A is extremely low given ∼ 300 hr of follow up observations using different telescopes identified only one repeat burst (Kumar et al., 2021a).

6: The burst rate of FRB 201124A is estimated for the period of high activity after 2021 March, while its rate prior to discovery (based on the non-detection over the pre-discovery total observed time) is low as $< 3.4\,\mathrm{day}^{-1}$ (Marthi et al., 2021; Piro et al., 2021; Lanman et al., 2021).

5.2.2 MWA observations

We used the MWA All-Sky Virtual Observatory[3] (ASVO) to search for all VCS observations that overlap with the positional errors of the five repeating FRBs, and found 61 observations in the MWA data archive. We then estimated the sensitivity of each VCS observation in the directions of the five repeating FRBs based on the Full Embedded Element model of the MWA (Sokolowski et al., 2017). We selected only those observations with at least 20% of the maximum sensitivity in the primary beam. This resulted in a total of 25 observations with integrations between 15 min and 1.5 hr (23.3 hr in total) and central frequencies between 144 MHz and 215 MHz, as listed in Table 5.2. Of these observations, 12 were taken in the MWA Phase II compact configuration, and the others were recorded in the higher angular resolution of Phase I and the Phase II extended configuration.

5.2.3 Data processing

For the data processing we used the VCS data processing pipeline, which was initially developed for pulsar searches (for details see Chapter 2). The calibrator source selected to calibrate each MWA observation is listed in Table 5.2. Here we briefly summarise the beamforming process.

We used the coherent beamforming to phase all MWA tiles to the known positions of the five repeating FRBs, as listed in Table 5.1. The number of coherent beams we needed to form for each FRB depended on the positional error of the FRB and the angular resolution of the MWA observation. The ASKAP repeater, FRB 190711A, has a small positional error of 0.38 arcsec (Macquart et al., 2020), well within the synthesized beam of the MWA, so we only needed to beamform the VCS data at a single position. The other CHIME repeaters have a positional error of ~ 10 arcmin. Depending on the configuration of the MWA, this corresponded to 2–16 beams for the phase II compact configuration

---

[3]https://asvo.mwatelescope.org/

Table 5.2: MWA observations used for the FRB search and the search results.

FRB	Date	Start time (UT)	Obs. ID	Config.	Dur. (s)	Freq. (MHz)	Elev. (deg)	Cal.	Beams	Min. detectable flux density (Jy)	Candidates above 6σ	Candidates with friends
20190116A	2018-04-05	15:27:58	1206977296	IIE	3600	185	36.1	HydA	550	29.36	40368	26
	2018-03-27	15:49:58	1206201016	IIE	3600	185	35.9	HydA	550	27.20	42693	194
20190117A	2015-10-13	11:49:27	1128772184	I	3600	185	45.0	PicA	540	29.48	41633	51
	2017-08-01	17:41:58	1185644536	IIC	3600	144	44.0	3C444	2	25.70	137	0
	2017-08-08	17:19:58	1186248016	IIC	3600	185	44.8	PicA	2	22.43	169	0
	2017-11-18	11:01:58	1195038136	IIE	3600	185	43.3	3C444	540	23.25	41266	44
	2018-09-24	13:51:02	1221832280	IIC	4800	154	45.4	3C444	2	24.82	214	0
	2018-10-08	14:01:02	1223042480	IIC	4800	154	40.8	PicA	2	26.46	208	0
20190213A	2016-11-22	12:35:03	1163853320	IIC	4800	185	42.8	3C444	6	24.80	2611	17
	2018-11-01	14:37:02	1225118240	IIC	4800	154	42.8	PicA	6	26.15	619	0
	2019-09-10	19:08:46	1252177744	IIC	4800	154	41.8	PicA	6	33.19	1024	0
20190711A	2014-09-23	11:14:56	1095506112	I	3600	185	34.5	PicA	1	45.01	72	0
	2015-07-01	21:38:15	1119821912	I	2400	185	34.4	3C444	1	25.62	54	0
	2015-10-13	11:49:27	1128772184	I	3600	185	36.3	PicA	1	29.50	103	0
	2016-09-16	11:36:31	1158061008	IIC	1440	172	33.9	HerA	1	52.68	178	0
	2017-08-08	17:19:58	1186248016	IIC	3600	185	36.2	PicA	1	22.13	75	0
	2017-11-18	11:01:58	1195038136	IIE	3600	185	35.9	3C444	1	23.25	965	0
	2018-11-23	12:05:58	1227009976	IIC	4800	154	33.9	3C444	1	27.89	115	9
	2019-07-25	14:46:14	1248101192	IIE	5400	215	34.2	PicA	1	55.86	856	0
	2020-04-29	21:02:28	1272229366	IIE	1500	167	34.4	3C444	1	42.67	38	0
	2020-05-02	21:01:58	1272488536	IIE	1500	167	34.7	3C444	1	40.35	31	0
20201124A	2014-11-07	16:53:20	1099414416	I	1200	185	34.3	HydA	576	18.41	54021	2
	2015-10-03	20:29:11	1127939368	I	3600	157	36.7	PicA	576	21.15	41171	17
	2016-10-14	20:01:19	1160510496	IIC	1200	185	36.8	PicA	16	21.07	3524	183
	2016-12-08	15:39:59	1165246816	IIC	900	154	36.9	HydA	16	22.00	293	0

1: The MWA observation date, observation ID and array configuration, including phase I ('I'), or phase II extended ('IIE') or compact ('IIC');

2: The duration of each MWA observation;

3: The central frequency of each MWA observation;

4: The maximum elevation of the FRB in the MWA's field of view during the observation;

5: The calibrator used to calibrate the MWA observations;

6: The number of synthesised beams within the positional error of the FRB;

7: The minimum detectable flux density calculated using the radiometer equation for each observation (see Section ??);

8: The number of candidates above 6σ resulting from the single pulse search on each observation and those passing the friends-of-friends algorithm (see Section 4.5.1).

and ~ 550 beams for the phase I and phase II extended configuration, as shown in Table 5.2.

5.2.4 FRB search

The single pulse search was performed using the PRESTO software package (Ransom, 2001). We did not perform any RFI excision (see Chapter 2), but any spurious events caused by RFI can be identified from the final candidates via visual inspection.

First we dedispersed the time series using the PREPDATA routine in PRESTO. We determined the DM search range of each observation based on the nominal DM of the target FRB (see Table 5.3). Specifically, we searched around the known DM with approximately $\pm 50\,\mathrm{pc\,cm^{-3}}$ but shifted that limit to within the closest multiple of $10\,\mathrm{pc\,cm^{-3}}$, covering a DM range of $100\,\mathrm{pc\,cm^{-3}}$. Given that there is no evidence of DM evolution for the five repeating FRBs analysed in this paper, and the largest DM variation observed for FRB 20190711A and FRB 20201124A is 7 and $10\,\mathrm{pc\,cm^{-3}}$, respectively (likely caused by varying burst morphology; Kumar et al. 2021a,c), the DM range we chose is sufficient for the repeat bursts searched for here. We adopted a DM step size of $0.1\,\mathrm{pc\,cm^{-3}}$, resulting in 1000 DM trials for each observation. To reduce the data size, the dedispersed time series were downsampled to a lower time resolution of $400\,\mu\mathrm{s}$. This would not affect our search for repeating bursts given the shortest burst width is $0.64\,\mathrm{ms}$ in our sample of repeating FRBs (see Table 5.1) and the general trend of increasing burst widths at lower frequencies (e.g. Chawla et al. 2020; Pleunis et al. 2021b).

We performed a traditional single pulse search using PRESTO's SINGLE_PULSE_SEARCH.PY, which convolves the dedispersed time series with boxcars of different widths. We chose different pulse width search ranges for the five repeating FRBs based on their brightness and the sensitivity of the MWA observations. While we searched up to a pulse width of $1.3\,\mathrm{s}$ (the maximum scatter broadening expected at the MWA observing frequency; see Section 5.2.6 and Table 5.3) for the two bright-

est FRBs in our sample, i.e. FRB 20190711A and FRB 20201124A, we only searched up to 150 ms for the other three FRBs as any signals scattered beyond 150 ms are expected to have a flux density of $< 0.2\,\mathrm{Jy}$, $< 1.4\,\mathrm{Jy}$ and $< 0.2\,\mathrm{Jy}$ for FRB 20190116A, 20190117A and 20190213A, respectively (assuming a spectral index of $\alpha = -2$; see Table 5.3), which is below the MWA sensitivity of $\sim 1.4\,\mathrm{Jy}$ on 150 ms timescales. Single pulse events detected with a S/N above six were classified as candidates (e.g. Chawla et al. 2020, Meyers et al. 2018, Bannister et al. 2012). We then applied a friends-of-friends algorithm (Burke-Spolaor et al., 2011; Bannister et al., 2012) to identify possible false positives. In the case of more than five individual boxcar/DM trials clustering into a candidate (e.g. Kumar et al. 2021a), we reserved it for further inspection (see Figure 5.1 for an example candidate).

We tested our data processing and FRB detection pipeline by searching for single giant pulses from the Crab pulsar in a 154 MHz MWA observation listed in Table 5.2 (Obs ID: 1165246816). We ran our FRB search pipeline over a chosen DM range of $56.77 \pm 5\,\mathrm{pc\,cm^{-3}}$ (from the ATNF Pulsar Catalogue[4]; Manchester et al. 2005). We successfully detected 89 single pulses with $\mathrm{S/N} > 10$ from this 15 min observation (see Appendix D and Figure D.1 for the dedispersed dynamic spectrum of the brightest Crab pulse). In order to calculate the expected giant pulse rate from the Crab at the observing frequency of 154 MHz, we took the Crab pulse rate of $0.35\,\mathrm{s^{-1}}$ at 185 MHz for a fluence $> 520\,\mathrm{Jy\,ms}$, the spectral index of -0.7 ± 1.4 and the power-law fluence distribution $N(> F_\nu) \propto F_\nu^{-\beta}$ with $\beta = 2.88 \pm 0.12$, all calculated by Meyers et al. (2017). We obtained a pulse rate of 0.03–$0.17\,\mathrm{s^{-1}}$ for a fluence $> 1000\,\mathrm{Jy\,ms}$ (corresponding to the 10σ sensitivity of the tested observation). Therefore, the expected number of detectable giant pulses from the Crab at 154 MHz within our 15 min observation is 27–153, which is consistent with our detection of 89 pulses, and thus verifying the utility of our VCS data processing and FRB detection pipeline.

---

[4]https://www.atnf.csiro.au/research/pulsar/psrcat/
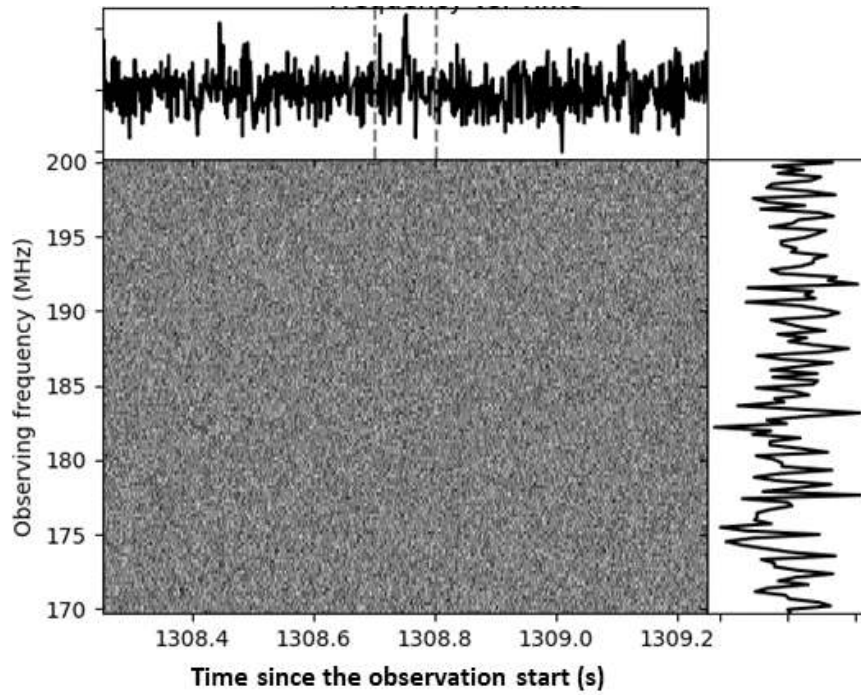
Figure 5.1: An example dynamic spectrum of a candidate burst detected in an MWA observation (Obs ID: 1163853320) beamformed at the position of FRB 20190213A. Data have been dedispersed to a DM of $635.4\,\mathrm{pc\,cm^{-3}}$. The dynamic spectrum has been averaged to a time resolution of $3\,\mathrm{ms}$ and a frequency resolution of $0.24\,\mathrm{MHz}$. The frequency-averaged pulse profile is shown on the top panel with the candidate located between the two vertical dashed lines. The time-averaged spectrum is shown on the right panel.

5.2.5 Determination of system sensitivity

Corresponding to the 6σ threshold on S/N, we determined a flux density upper limit for each of the selected MWA observations using the radiometer equation (see Section 4.5). Taking into account the sensitivity loss induced by flagging bad tiles and channels during the calibration process (see Section 4.4), we arrived at a 6σ flux density upper limit for each observation, as shown in Table 5.2.

5.2.6 Pulse width and fluence estimates

As mentioned above, the sensitivity of the MWA observations is characterised by flux density. However, in the field of FRB astrophysics it is common to use fluence for presenting results. We can convert the flux density limit to a fluence limit using Eq. 4.3 (pulse duration dependent) in Chapter 4. The pulse durations of the five repeating FRBs have been measured at their observed frequencies, as shown in Table 5.1. We can estimate the pulse duration at the MWA observing frequency using Eq. 4.4 in Chapter 4. Here we are mainly concerned about three factors: w_{obs} is the observed pulse duration at higher frequencies, and w_{DS} and w_{scatter} account for the pulse broadening due to dispersive smearing and pulse scattering at the MWA observing frequency. The dispersion smearing across the MWA channel, $\Delta\nu = 10\,\mathrm{kHz}$, can be calculated at the nominal DM values listed in Table 5.1 for the five repeaters using (e.g. Anderson et al. 2018b)

$$w_{\mathrm{DS}} = 8.3 \times 10^3 \times \left(\frac{\Delta\nu}{\mathrm{MHz}}\right) \times \left(\frac{\nu}{\mathrm{MHz}}\right)^{-3} \times \left(\frac{\mathrm{DM}}{\mathrm{pc\,cm^{-3}}}\right)\,\mathrm{s}. \qquad (5.1)$$

For a typical observing frequency of the MWA, $\nu = 185\,\mathrm{MHz}$, the corresponding dispersion smearing is $\sim 5\,\mathrm{ms}$.

FRBs also experience scattering. However, given the unknown environment of FRBs the scattering timescale is largely uncertain. We may infer the lower limit of the scattering timescale based on the Galactic contribution. Using the NE2001 model of electron density fluctuations (Cordes & Lazio, 2002), we obtained a

minimum scattering timescale at $1\,\text{GHz}$ of $4.3 \times 10^{-5}\,\text{ms}$, $2.6 \times 10^{-4}\,\text{ms}$, $1.7 \times 10^{-4}\,\text{ms}$, $3.2 \times 10^{-4}\,\text{ms}$ and $5.8 \times 10^{-3}\,\text{ms}$ for the five repeaters. The upper limits on scattering timescales have been derived for FRB 190116A, 190117A, 190213A and 201124A to be $<11\,\text{ms}$, $<7.4\,\text{ms}$, $<4.0\,\text{ms}$ and $<11.1\,\text{ms}$ at $600\,\text{MHz}$ (CHIME/FRB Collaboration et al., 2019c; Fonseca et al., 2020a; Marthi et al., 2021). Given FRB 190711A has no scattering fitting due to its complex time-domain structure (Day et al., 2020) or low S/N (Kumar et al., 2021a), we assumed a typical scattering timescale of $<10\,\text{ms}$ (Amiri et al., 2021). Assuming the scattering timescale depends on frequency as ν^{-4} (Bhat et al., 2004), we can obtain a range of scattering timescales at the MWA observing frequency. The final lower and upper limits on the scatter broadening can be found in Table 5.3. Note that the final range in Table 5.3 was calculated individually for each observation before being combined.

With the estimated dispersion smearing and scattering timescales, we can derive a range of pulse widths for each observation using Eq. 4.4, which can be further used to derive the final range of fluence limits for each observation using Eq. 4.3. The ranges of fluence limits derived from different observations covering the same repeating FRB were combined to obtain the final range of fluence limits for the repeater, as shown in Table 5.3.

5.3 Results

We performed FRB searches on 25 VCS observations at the positions of five repeating FRBs, of which four were discovered by CHIME and one by ASKAP. Following the automated pulse search, we further filtered all candidates with a S/N above 6σ using the friends-of-friends algorithm. The number of remaining candidates at the position of each repeater is listed in Table 5.2, totalling 543 candidates discovered in $23.3\,\text{hr}$ of VCS data. We visually inspected their pulse profiles and dynamic spectra, and found no evidence of a dispersion sweep, suggesting they are not real signals. An example dynamic spectrum of a candidate

FRB	Obs.[1] (hr)	Expected bursts[2]	DM search range (pc cm^{-3})	Bounds of scattering[3] (ms)	Bounds of pulse widths[4] (ms)	Fluence upper limit[5] (Jy ms)	Fluence expected[6] (Jy ms) $\alpha = -1$	$\alpha = -1.53$	$\alpha = -2$
190116A	2	0.5	400–500	0.04–1217	5.97–1217	42–648	2–8	4–15	7–25
190117A	6.8	1.8	350–450	0.22–819	5.20–819	32–534	16–50	30–106	53–208
190213A	4.2	0.5	600–700	0.15–442	9.43–442	48–441	2–10	3–18	4–32
190711A	9.2	/	550–650	0.27–1106	5.06–1106	32–1175	8–276	21–837	47–2240
201124A	1.9	30	350–450	4.95–1228	9.52–1229	36–488	9–456	18–978	43–1924

Table 5.3: Derived burst properties of the five repeaters at the MWA observing frequency.

1: The total exposure time of MWA to each FRB;

2: The expected number of bursts assuming a constant burst rate (see Table 5.1);

3: The scattering timescale at the MWA observing frequency inferred from the observed scattering at higher frequencies and the contribution from the Milky way (see Section 5.2.5);

4: The pulse width at the MWA observing frequency derived by taking into account the pulse broadening due to dispersive smearing and pulse scattering (see Section 5.2.6);

5: The fluence upper limit for each FRB combined from the limit derived for each observation (see Section 5.2.6);

6: The expected fluence of the observed FRBs extrapolated to the MWA observing frequency (185 MHz) assuming a power-law spectrum with different spectral indices (see Section 5.4.2).

burst detected in an MWA observation (Obs ID: 1163853320) with S/N = 6.59 is shown in Figure 5.1.

We derived a flux density limit for each of the 25 MWA VCS observations searched for FRB signals, as shown in Table 5.2. For FRB 20201124A, the flux density limits ranged between 18.41–22 Jy. We also inferred a range of pulse widths of 9.52–1229 ms at the MWA observing frequency of 185 MHz for this repeater. With the derived flux density limits and pulse widths, we finally arrived at a range of fluence limits of 36–488 Jy ms for FRB 20201124A. We did a similar analysis for the remaining FRBs, and present all results in Table 5.3. Note that the three faint repeaters in our sample, i.e. FRB 20190116A, 20190117A and 20190213A, were only searched up to a pulse width of 150 ms (see Section 4.5.1). The uncertainties in the final fluence limits span more than an order of magnitude, which can be attributed to the largely uncertain scattering timescales. In the best case, i.e. minimal scattering, we would have detected any bursts with a fluence $\gtrsim 50$ Jy ms. Note that the low-frequency bursts detected by LOFAR from FRB 20180916B can reach a fluence of 308 ± 10 Jy ms (Pleunis et al., 2021b), much higher than this fluence threshold.

In summary, no bursts from the five repeaters were detected in MWA observations. Based on their known properties, we inferred a range of fluence upper limits for each repeater, as shown in Table 5.3, which can be used to constrain the burst properties of the repeating FRB population.

5.4 Discussion

We have performed a search for bursts from five repeating FRBs at low frequencies with the MWA, obtaining a range of fluence upper limits on each of these repeaters (see Table 5.3). Given their burst rates estimated by CHIME or ASKAP observations (see Table 5.1), we calculated the expected bursts during the MWA observations assuming the burst rate is constant and frequency independent, as shown in Table 5.3. We can see there is a non-negligible chance of bursting dur-

ing the MWA observations of these repeaters, especially for FRB 201124A, which can potentially emit 30 bursts within 1.9 hr (Lanman et al., 2021). Therefore, the fact that we did not detect any bursts could suggest that our assumption of a constant burst rate is wrong, the FRB emission has a shallow spectrum, or the circumburst environment prevents the low frequency radio emission from escaping. In this section, we discuss the constraints placed on the properties of these repeaters by the MWA non-detections.

5.4.1 Burst rate

The first explanation for our non-detection may be that the repeaters were not active during the MWA observations. If that is the case, we can further constrain the burst rates of the five repeaters at the MWA observing frequency of $\sim 185\,\mathrm{MHz}$ to $< 0.50\,\mathrm{hr}^{-1}$, $< 0.15\,\mathrm{hr}^{-1}$, $< 0.24\,\mathrm{hr}^{-1}$, $< 0.11\,\mathrm{hr}^{-1}$ and $< 0.53\,\mathrm{hr}^{-1}$ for FRB 190116A, 190117A, 190213A, 190711A and 201124A, respectively, assuming the rate is constant. The most stringent constraint on the burst rate of FRB 190711A is comparable to the lowest observed rate for a CHIME repeater ($0.05\,\mathrm{hr}^{-1}$ for FRB 190212A; Fonseca et al. 2020b). Note that these two burst rates are measured at different frequencies, and there seems to be a decreasing trend in burst rates towards lower frequencies though it is not conclusive (e.g. Pearlman et al. 2020; Pleunis et al. 2021b).

There is also another possibility that the repeaters were in quiescence during the MWA observations. That is, the five repeaters have variable burst rates, depending on their episodic bursting behavior. This has been shown to be the case for FRB 201124A. While this FRB has been observed to emit 48 bursts within three hours (Marthi et al., 2021), its rate prior to discovery is low as $< 3.4\,\mathrm{day}^{-1}$ (Lanman et al., 2021). Despite the above uncertainties in the FRB activity, it is intriguing to assume the repeaters emitted signals during the MWA observations and investigate their spectral properties (see Section 5.4.2) and emission environments (see Section 5.4.3).

5.4.2 Spectral properties

Here we consider that our non-detections of FRB emission is due to low fluences in the MWA observing band. In the case of broadband FRB emission, we can constrain the spectral index using the fluence upper limits we derived for the five repeaters and their observed fluences at higher frequencies. The mean spectral index of FRB emission has been determined to be $-1.5^{+0.2}_{-0.3}$ from the summed power of 23 ASKAP FRBs over a frequency range of 1.1–1.5 GHz (Macquart et al., 2019) and $-1.53^{+0.29}_{-0.19}$ by a simulation on a sample of 82 FRBs detected by Parkes, ASKAP, CHIME and UTMOST over 0.4–1.5 GHz (Bhattacharyya et al., 2021). Here we extrapolated the fluences observed at higher frequencies to the MWA observing frequency of 185 MHz for three different spectral index values of -1, -1.53 and -2 (the same range of spectral indices explored by Sokolowski et al. 2018) and include them in Table 5.3 where they can be compared to the fluence upper limits derived from our data. While low frequency bursts from FRB 20190116A and 20190213A were likely undetectable in the searched MWA datasets based on the assumed mean spectral index, bursts from the other repeaters may well be detectable if they were active during the MWA observations. Although the scatter broadening of pulses can significantly reduce our sensitivity to FRB emission (as demonstrated by the large range of fluence upper limits shown in Table 5.3), our non-detection of low frequency bursts from the two brightest repeaters FRB 20190711A and 20201124A cannot be explained by scattering alone unless their spectral indices are $\alpha \gtrsim -1$, which is consistent with the conclusion in Sokolowski et al. (2018).

There is another possibility that the spectrum of repeating FRBs needs to be generalised beyond a simple power law. This could be attributed to a low instantaneous bandwidth as has been observed for FRB 20121102A, 20180916B and 20190711A with a typical fractional bandwidth of $\sim 20\%$ (Law et al., 2017; Gourdji et al., 2019; Majid et al., 2020; Kumar et al., 2021a) and/or clustering of spectra of repeat bursts as has been observed for FRB 20121102A (peaking

around 1650 MHz) and 20201124A (peaking around 650 and 500 MHz; Aggarwal 2021; Lanman et al. 2022). In the former case, the narrowband feature is similar to that observed for giant pulses from some pulsars (e.g. Geyer et al. 2021; Thulasiram & Lin 2021), and might hint at similarities in emission mechanisms between repeating FRBs and giant pulses.

5.4.3 Free-free absorption

A low-frequency break in the spectrum of FRB emission is a plausible explanation for our non-detection. It has been suggested that free-free absorption by electrons in the circumburst environment can suppress low-frequency emission (Ravi & Loeb, 2019; Rajwade et al., 2020a). Here we derive an upper limit on the size of a nebula that the repeater may be embedded in in the context of free-free absorption (e.g. Sokolowski et al. 2018).

The optical depth due to free-free absorption is given by

$$
\begin{aligned}
\tau_{\mathrm{ff}} = {} & 1.1 \times 10^{-5} \times \left(\frac{T}{10^4 \mathrm{K}} \right)^{-1.35} \times \left(\frac{\nu}{185\,\mathrm{MHz}} \right)^{-2.1} \\
& \times \frac{\mathrm{DM}_{\mathrm{ex}}^2}{f_{\mathrm{eff}}\, L_{\mathrm{pc}}},
\end{aligned}
\tag{5.2}
$$

where T is the electron temperature, ν is the observing frequency normalised to 185 MHz, L_{pc} is the size of the absorbing material, f_{eff} accounts for the volume filling correction, and $\mathrm{DM}_{\mathrm{ex}}$ is the DM contribution from the absorbing material (Condon & Ransom, 2016). $\mathrm{DM}_{\mathrm{ex}}$ can be estimated by the DM values in excess of the Milky Way contributions in the directions of FRBs (Cordes & Lazio, 2002) and a further Milky Way halo contribution of $15\,\mathrm{pc\,cm^{-3}}$ (Shannon et al., 2018).

If free-free absorption is responsible for the absence of low frequency emission, we can place a constraint on the size of the absorbing medium by requiring $\tau_{\mathrm{ff}} > \ln(F_{\mathrm{exp}}/F_{\mathrm{lim}})$, where F_{exp} is the expected fluence at the observing frequency for a spectral index of $-1.53^{+0.29}_{-0.19}$ (Bhattacharyya et al., 2021) and F_{lim} is the

fluence upper limit derived from the MWA observation (see Table 5.3). In the case of minimum scattering, we find $f_{\text{eff}} L_{\text{pc}} < 1.00 \times (T/10^4\text{K})^{-1.35}$ pc (using $F_{\text{exp}} = 106$ Jy ms), $0.92 \times (T/10^4\text{K})^{-1.35}$ pc (using $F_{\text{exp}} = 837$ Jy ms) and $[0.22\text{--}2.50] \times (T/10^4\text{K})^{-1.35}$ pc for FRB 190117A, 190711A, and 201124A, respectively. Note that the fluence upper limits on the other two repeaters are not sufficient for constraining the size of their absorbing media.

We can compare our constraints on the size of an ionized nebula with those derived for other repeaters, such as FRB 121102 and FRB 180916B. The lowest frequency detection of FRB 121102 was reported at 600 MHz by CHIME (Josephy et al., 2019). However, a search for low-frequency emission from FRB 121102 with LOFAR resulted in a fluence upper limit of 42 Jy ms at 150 MHz (Houben et al., 2019). If we adopt the DM value derived from Balmer line measurements for the DM contribution from the host galaxy, $\text{DM}_{\text{host}} \lesssim 324\,\text{pc cm}^{-3}$ (Tendulkar et al., 2017), the size of the ionized region surrounding FRB 121102 can be constrained to $\lesssim 2.85\,\text{pc}$, which is comparable to the constraints derived above. Different than FRB 121102 and the repeaters studied here, FRB 180916B was reported to have low-frequency emission between 110–188 MHz, suggesting a lower limit on the size of an ionized nebula $\gg 0.16 \times (T/10^4\text{K})^{-1.35}$ pc (Pleunis et al., 2021b). If the population of repeating FRBs analysed here have a similar environment as FRB 180916B, we would expect a nebula size of $\sim$ pc, comparable to the Crab Nebula.

5.4.4 Comparison of FRB searches with the MWA

The MWA has been employed to search for FRBs previously in the image domain (Tingay et al., 2015; Rowlinson et al., 2016; Sokolowski et al., 2018). Here we present the first FRB search using the MWA VCS observations. Compared to the imaging mode, the VCS data features a much higher time resolution, increasing our sensitivity to short duration ($\sim$ms) FRB emission which would otherwise be diluted by the 0.5 s coarse sampling of the standard correlator. Table 5.4 displays

Reference	Obs. (hr)	Freq. (MHz)	Time/Freq. resolution	Sensitivity (Jy ms)
Tingay et al. 2015	10.5	156	2 s / 1.28 MHz	700
Rowlinson et al. 2016	100	182	28 s / 1.28 MHz	7980
Sokolowski et al. 2018	3.5	185	0.5 s / 1.28 MHz	450–6500
This work	24.1	144–215	400 μs / 10 kHz	32–1175

Table 5.4: Comparison between FRB searches using the MWA.

a comparison of our search with previous works. Note that while Tingay et al. (2015) and Rowlinson et al. (2016) performed a blind search for FRB emission in the wide field of view of the MWA, Sokolowski et al. (2018) specifically targeted the bright FRBs detected by ASKAP via a shadowing observing strategy. We can see the VCS observations used in this work demonstrate the best sensitivity. In the case of minimal scattering, the VCS observation is more than an order of magnitude more sensitive than the standard observation, and thus is most promising for searching for FRBs in the future.

5.4.5 Future prospects

Considering the ongoing searches for FRBs with multiple different facilities, e.g., Parkes (Keane et al., 2018), ASKAP (Bannister et al., 2017), CHIME (CHIME/FRB Collaboration et al., 2018), UTMOST (Caleb et al., 2016) and FAST (Jiang et al., 2019), we expect more repeating FRBs to be discovered that can be observed by the MWA in the future. Since most FRBs are discovered by CHIME, here we focus on the prospect of CHIME repeating FRB follow-up using the MWA. At the location of MWA, we are able to observe only those FRBs with low declinations ($\lesssim 30$ deg), amounting to ~20% of the whole population based on the sky distribution of FRBs (see figure 10 in Amiri et al. 2021). Therefore, given that 18 repeating FRBs have been discovered by CHIME during its first year of operation (CHIME/FRB Collaboration et al., 2019c; Fonseca et al., 2020a), we expect to be able to follow up ~ 4 new repeating FRBs using the MWA per year assuming that the discovery rate is constant. Note that we would ideally target repeating

FRBs that were away from the Galactic plane where the sky temperature is much higher, as well as choose those that show lower levels of scattering.

A very interesting source among the population of repeating FRBs is FRB 20180916B, which features a periodicity of 16.3 day and low frequency emission detected by LOFAR in the frequency range of 110–188 MHz (Pleunis et al., 2021b), overlapping with the MWA observing band. Note that it is unobservable by the MWA due to its location in the northern hemisphere. However, the fluences of the bursts from this FRB ranging from 26 to 308 Jy ms are close to the fluence upper limits we derived from the MWA VCS observations studied in this analysis, making it intriguing to explore the detectability of these bursts by the MWA if they appeared in the MWA field of view. In Figure 5.2, we plot the pulse widths and fluences of the 18 detected bursts (black points) and the fluence upper limits derived from the MWA observations included in this work (blue region). Considering the sensitivity of the MWA observations in this work are limited by the low elevations of the targeted FRBs in the MWA field of view, we also plot a typical sensitivity near the zenith of the full MWA for comparison (Meyers et al. 2017, 2018; dashed red line). While the observations in this work would only have been sensitive enough to detect the seven brightest bursts, a typical VCS observation near the zenith could have detected up to 12 bursts, and therefore $\sim 70\%$ of the bursts reported by Pleunis et al. (2021b) from the repeating FRB 20180916B at low frequencies (< 200 MHz). Therefore, if another repeating source with emission properties similar to FRB 20180916B becomes known in the MWA sky in the future, follow-up campaigns with the MWA would be capable of detecting low frequency bursts.

Apart from follow-up observations of repeaters, we plan to conduct an all-sky FRB search with the MWA. The rate of FRB detections by the MWA can be estimated using

$$\frac{R_{\nu 1}^{F1}}{R_{\nu 2}^{F2}} = \left(\frac{\nu 1}{\nu 2}\right)^{-\alpha\beta} \times \left(\frac{F1}{F2}\right)^{\beta-1}, \tag{5.3}$$
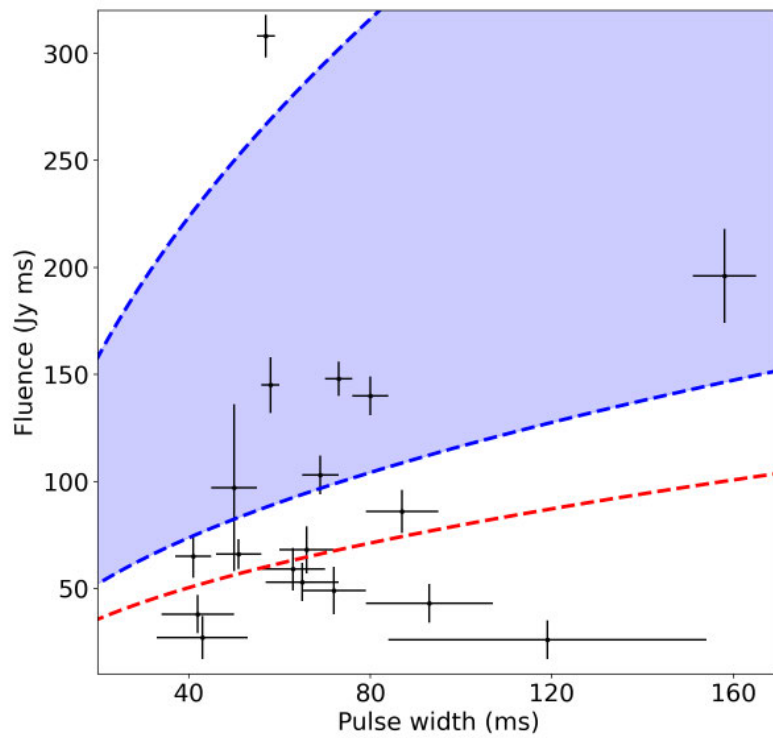
Figure 5.2: The fluences of the bursts reported by Pleunis et al. (2021b) from the repeating FRB 20180916B between 110–188 MHz versus their pulse widths. The black points represent the 18 bursts detected by LOFAR, the blue region represents the range of fluence upper limits derived from the MWA observations analysed in this work, and the dashed red line represents a typical VCS sensitivity near the zenith of the MWA.

where $R_{\nu 1}^{F1}$ ($R_{\nu 2}^{F2}$) is the sky rate above a fluence of $F1$ ($F2$) at a radio frequency of $\nu 1$ ($\nu 2$), α is the average spectral index ($-1.53_{-0.19}^{+0.29}$; Bhattacharyya et al. 2021), and β is the power-law index parameterizing the fluence distribution ($-1.40 \pm 0.11_{-0.09}^{+0.06}$; Amiri et al. 2021). Here we adopted the latest sky rate of $820 \pm 60_{-200}^{+220}\,\mathrm{sky}^{-1}\,\mathrm{day}^{-1}$ for FRBs (including both repeaters and non-repeaters) with a fluence $> 5\,\mathrm{Jy\,ms}$ and a scattering time less than $10\,\mathrm{ms}$ at $600\,\mathrm{MHz}$, which is based on the first large sample of FRBs (Amiri et al., 2021) and consistent with the rate reported from the Green Bank North Celestial Cap (GBNCC) survey in the 300–400 MHz band (Parent et al., 2020). Scaling this rate down to the MWA observing frequency of 185 MHz and a typical fluence upper limit of $50\,\mathrm{Jy\,ms}$ as shown in Figure 5.2 using Eq. 5.3, we expect a rate of $15\text{–}78\,\mathrm{sky}^{-1}\,\mathrm{day}^{-1}$. Given the $\sim 1\%$ instantaneous sky coverage of the MWA (Tingay et al., 2013, 2015), we expect on average 1–7 days of VCS observations would yield an FRB detection. It is noteworthy that the computational cost of processing such a large amount of data is still a challenge (Trott et al., 2013).

5.5   Conclusions

In this chapter, we have searched for low-frequency emission from five repeating FRBs using the VCS observations in the MWA archive. This is the first time that the MWA VCS has been used to search for bursts from repeating FRBs. The 25 MWA VCS observations analysed ranged in integration times between 15 min and 1.5 hr (23.3 hr in total). As a result of this work, we come to the following main conclusions:

1. If FRB 190711A and FRB 201124A were active during the MWA observations, then we can constrain their spectral index to $\alpha \gtrsim -1$, shallower than the mean spectral index estimated on a sample of FRBs (Bhattacharyya et al., 2021).

2. The fluence upper limits derived from the MWA observations in the case of

minimum scattering on the FRB emission (contributed only by the Milky Way) enable us to constrain the size of the absorbing medium to $< 1.00 \times (T/10^4 \mathrm{K})^{-1.35}$ pc, $< 0.92 \times (T/10^4 \mathrm{K})^{-1.35}$ pc and $< [0.22\text{–}2.50] \times (T/10^4 \mathrm{K})^{-1.35}$ pc for FRB 190117A, 190711A, and 201124A respectively, which is comparable to the size limit on FRB 121102 (Tendulkar et al., 2017; Houben et al., 2019) and lower limit for FRB 180916B (Pleunis et al., 2021b).

3. Compared to previous MWA searches for low-frequency FRB emission using the standard correlator with a minimum temporal resolution of only $0.5\,\mathrm{s}$ (Tingay et al., 2015; Rowlinson et al., 2016; Sokolowski et al., 2018), our VCS observations with a temporal resolution of $100\,\mathrm{\mu s}$ are more than an order of magnitude more sensitive to FRB signals except in the case of severe pulse broadening due to scattering beyond $\sim 0.5\,\mathrm{s}$.

4. A comparison between the typical sensitivity of the MWA VCS observation at the zenith and the fluences detected by LOFAR from FRB 180916B reveals that the MWA would be able to detect $\sim 70\%$ of the low frequency bursts from a repeater like FRB 180916B.

In conclusion, our non-detections are likely due to the limited total integration time of our VCS observations, during which the repeaters were likely inactive. However, we cannot rule out the possibility of a shallow spectrum or a dense environment. In order to detect the low-frequency counterparts of repeating FRBs or clearly constrain their burst properties, we need a combination of the reanalysis of archival VCS observations, which will continue to be collected over the duration of the SMART survey, and potentially dedicated VCS observing campaigns. Higher frequency instruments such as CHIME and ASKAP can be used to determine the active windows of repeating FRBs when targeted observations with the MWA will be most useful. Currently, the high time resolution dataset that covers a large part of the Southern Sky, which is only made possible via access to high time resolution data archives, presents a unique opportunity for

transient science. Given this rich dataset, a blind search is a logical and efficient way of identifying low frequency FRBs and repeaters.

Chapter 6

Discussion and conclusions

I have performed a low frequency search for coherent, prompt radio emission from different transient events, including GRBs (see Chapters 3 and 4) and repeating FRBs (see Chapter 5), using the MWA rapid-response observing mode and the archival MWA data, respectively. The main technique for prompt radio transient searches used in this thesis is dedispersion in the image domain (see Chapter 3) or the high time resolution and coherently beamformed voltage data (see Chapters 4 and 5). This is the most sensitive attempt that the image dedispersion has been used for searching for prompt radio emission associated with GRBs, demonstrating one of the best sensitivities achieved to date. With the upper limits derived from the MWA observations of GRBs, I tested various models that predict coherent radio emission associated with GRBs. I found the composition of GRB jets is possibly baryon dominated, which moves forward our understanding of one of the fundamental open questions in the GRB field, i.e. what is the composition of the GRB jet? I also used the upper limits derived from the MWA observations of repeating FRBs to constrain the spectral properties of the FRB emission and the FRB environments. This PhD research was aimed at exploiting the capabilities of the MWA rapid-response observing mode in low frequency searches for dispersed radio transients in the context of GRBs and FRBs.

6.1 Revisiting coherent emission models of GRBs

We described the theoretical models that predict coherent radio emission from short and long GRBs in Section 1.1.4 and in Chapters 3 and 4 that include a sample of 10 GRBs. Testing these models with rapid follow-ups of a sample of GRBs with the MWA provides new insights into the theories. Here I discuss the implications of our non-detections of coherent radio emission from a sample of GRBs on the emission models. Note that the first emission model introduced in Section 1.1.4.3, interactions of binary NSs, is only applicable to short GRBs, while the other models are applicable to both short and long GRBs.

6.1.1 Relativistic jet and ISM interaction

I start with the most extensively studied model, interactions between the relativistic jet launched by GRBs and the ISM (e.g. Bannister et al. 2012; Palaniswamy et al. 2014; Rowlinson & Anderson 2019; Rowlinson et al. 2019, 2021; Anderson et al. 2021a). The big sample of GRBs studied at low radio frequencies (< 300 MHz), including twelve short and two long ones (from both MWA and LOFAR triggers; Kaplan et al. 2015; Anderson et al. 2021a; Rowlinson et al. 2019, 2021; also see Chapters 3 and 4), allowed us to draw some solid conclusions, i.e. the GRB jet is possibly baryon dominated during both the prompt gamma-ray emission phase and X-ray flares of GRBs.

Compared to the other coherent emission models, the GRB jet-ISM interaction involves the least assumptions as this model does not require the formation of a magnetar. Note that in Chapter 3 we did assume a typical magnetar model for deriving the radio emission resulting from the GRB jet-ISM interaction, but in order to generalise our discussion (e.g. GRBs could also form BHs; Cannizzo et al. 2011) we can directly assume typical GRB parameters (as done in Chapter 4; also see Rowlinson et al. 2019, 2021). Moreover, detections of the prompt gamma-ray emission spontaneously indicate that any radio signals produced in the jet would point towards us. Therefore, we are most likely to detect the prompt

radio emission predicted by the jet-ISM interaction model. The MWA is ideal for capturing this emission given its rapid response mode and high sensitivity on short timescales, as demonstrated in Chapters 3 and 4. Surprisingly, we did not detect this predicted emission from a large sample of GRBs, which drive us to rethink the GRB jet-ISM interaction model.

First we revisit the fast response mode of the MWA. Considering a typical response time of the MWA between 30–60 s as shown in Chapter 3, if the prompt radio emission is produced concurrently with the prompt gamma-ray emission, we would capture the dispersion delayed emission from GRBs for redshifts $z \gtrsim$ 0.2–0.4 at an observing frequency of 185 MHz. Given the known redshift distribution of short (Rowlinson et al., 2013) and long (Le & Mehta, 2017) GRBs, we should be able to capture the radio emission predicted for most GRBs ($\sim 90\%$). Therefore, the rapid response mode of the MWA is sufficient for capturing the prompt radio emission produced by the relativistic jet and ISM interaction.

Next, we compare the sensitivity of the MWA with the predicted fluence of the prompt radio emission produced by the relativistic jet and ISM interaction, as shown in Figure 6.1. Note that we include both model predictions from Chapters 3 and 4, i.e. with or without magnetar formation. As shown in Chapter 3, the predicted radio fluence is proportional to the magnetisation of the GRB jet, i.e. the fraction of magnetic energy in the jet (ϵ_B). If $\epsilon_B \lesssim 10^{-3}$, the sensitivity of the MWA imaging mode would be insufficient for detecting the predicted emission, as shown in Figure 6.1. However, this requirement on ϵ_B would undoubtedly point to a baryon dominated jet (e.g. Rowlinson et al. 2020). We also notice that in the case of no magnetar formation, the prompt signal prediction would be much fainter (two orders of magnitude; see Figure 6.1), and we need more sensitive telescopes such as the SKA-Low for probing this emission (see Section 6.3.4).

It may be worth considering propagation effects applicable to the GRB environment, i.e. absorption below the plasma frequency and induced Compton

scattering, as these effects may obscure real signals. The absorption below the plasma frequency is determined by the electron number density in the GRB environment. At the MWA observing frequency of 185 MHz, in order for the plasma frequency to be below this frequency, the electron number density must be $n_e \lesssim 4 \times 10^8 \, \text{cm}^{-3}$, as shown in Chapter 4. While short GRBs are known to occur in low density environments (Zhang, 2014; Fong et al., 2015), it is uncertain whether the environments of long GRBs can fulfill the requirement on the electron number density. Based on X-ray absorptions, we might expect some long GRBs could arise from a low density environment, such as GRB 210419A (see Chapter 4) and GRB 180706A (Rowlinson et al., 2019). Therefore, the absorption below the plasma frequency may be negligible for short GRBs and some of the long GRBs.

Induced Compton scattering can also strongly limit the detectability of the coherent radio emission emanating from the GRB environment, as discussed in Chapter 4. In order for the coherent radio emission to evade induced Compton scattering, the Lorentz factor of the GRB jet should be $\Gamma \gtrsim 10^3 (D/100 \, \text{Mpc})$ (assuming the radiation within the jet is isotropic; Lyubarsky 2008). The distribution of bulk Lorentz factors of GRB jets before deceleration has been found to have a typical value of ~ 300 (150) for a uniform (wind-type) circumburst medium using the peak time observed in the optical or GeV light curves of GRBs (Ghirlanda et al., 2018), which could possibly fulfill the above requirement for evading induced Compton scattering. Therefore, while the propagation effects can prevent the coherent radio emission from being detected, we anticipate them to be negligible for some GRBs.

Given the above considerations, our non-detections of the prompt radio emission from a sample of GRBs with the rapid follow up of the MWA might suggest a low magnetisation of GRB jets. That is, the GRB jet is possibly baryon dominated. Note that we cannot rule out the possibility that some GRBs are at high redshifts and/or they do not form magnetars resulting in fainter radio emission.

Another possibility is that they reside in a dense environment that prevents radio emission from escaping.

6.1.1.1 Flare model

Apart from searching for the coherent radio emission produced during the prompt gamma-ray emission phase of GRBs, we performed another search for radio emission associated with GRB flares using triggered MWA VCS observations, as described in Chapter 4. This study was enabled by the MWA rapid-response mode. The flares are observed in the X-ray and likely produced by internal shocks, as is the prompt gamma-ray emission. This is the first time that the flare model has been studied at such low frequencies. Since the X-ray flare occurred $\sim$5 min after the prompt gamma-ray emission of GRB 210419A, the rapid-response MWA observation meant it was on-target in time to capture any radio emission associated with the flare. Here I discuss the constraint placed by the MWA VCS observation on the flare model.

If the relativistic jet is baryon dominated at the earlier prompt gamma-ray emission phase as discussed above, given that the magnetic energy thought to power the prompt gamma-ray and X-ray emission dissipates with time (e.g. Kumar & Zhang 2015), it makes sense that by the time we observe the X-ray flaring activity, the magnetic energy remaining in the jet is minimal. If the fraction of magnetic energy in the relativistic jet during the flaring activity of GRB 210419A is $\epsilon_B \lesssim 10^{-3}$ (possibly baryon dominated), we need even more sensitive observations than the MWA VCS observation of GRB 210419A to detect the predicted coherent radio emission, as demonstrated in Chapter 4. Therefore, our non-detections of coherent radio emission associated with the prompt gamma-ray emission of a sample of GRBs and the X-ray flare of GRB 210419A suggest the possibility of baryon dominated jets.
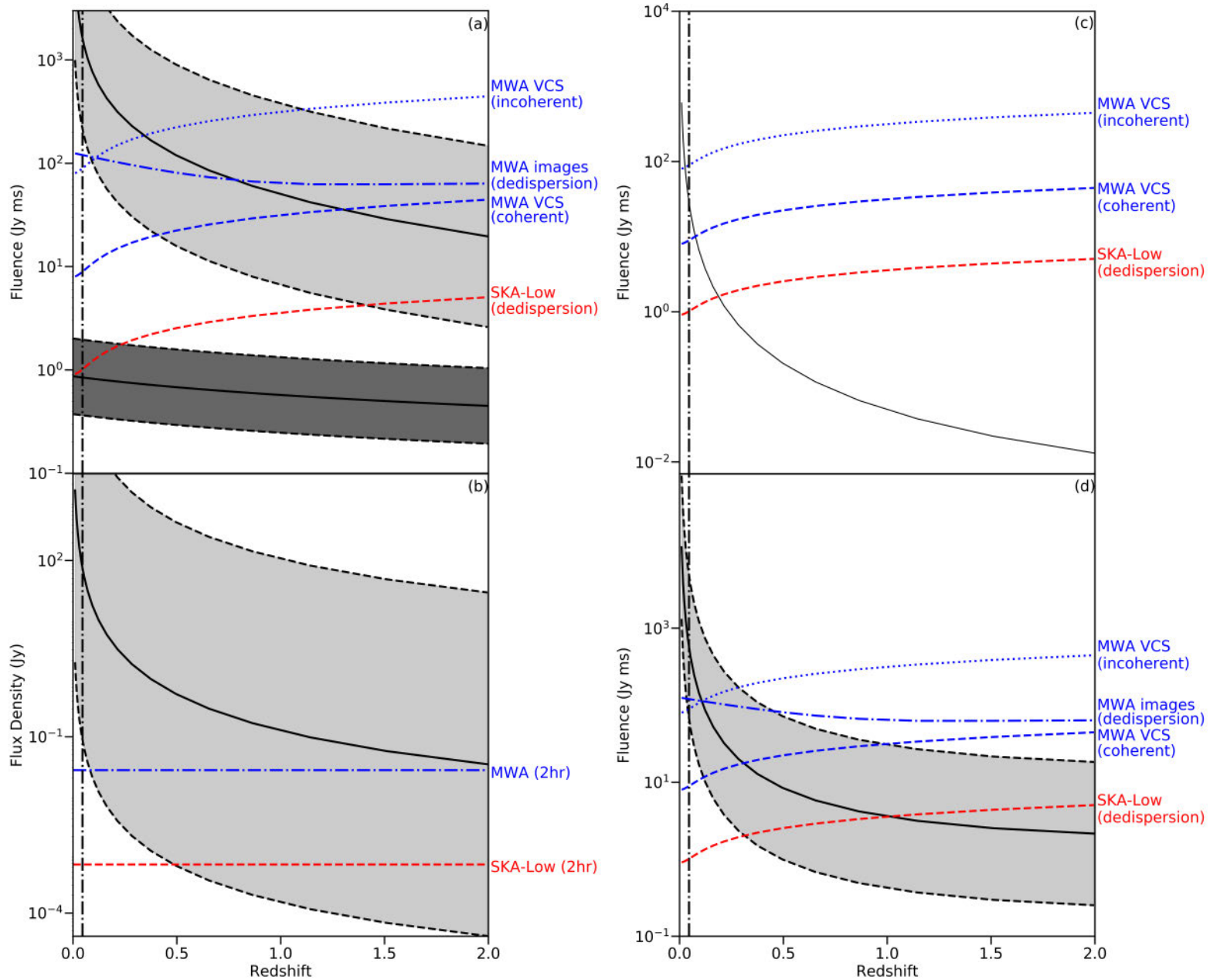
Figure 6.1: Comparisons between the MWA sensitivity and the fluence or flux density predictions of the four coherent emission models described in Chapter 3. We plot the sensitivity of the MWA imaging data on 0.25 s (for image dedispersion) and 2 hr timescales (blue dash-dot lines), the VCS sensitivity for incoherent (blue dotted lines) and coherent (blue dashed lines) beamforming, and the sensitivity of the SKA-Low imaging data (red dashed lines). Note that the sensitivities quoted here are all at 6σ levels, as adopted in Chapters 3 and 4. Continued on the following page.

Figure 6.1: The four labelled panels correspond to the four emission models. a) The GRB jet - ISM interaction. The light and dark shaded regions represent the model predictions with (see Chapter 3) and without (see Chapter 4) the magnetar assumption, respectively. The blue dash-dot line represents the expected sensitivity of performing image dedispersion on 0.25 s timescales with MWAX. b) The persistent pulsar emission from the magnetar remnant. The blue dash-dot and red dashed lines represent the sensitivity of MWA and SKA-Low on 2 hr timescales, respectively. c) The interaction of NS magnetospheres. d) The magnetar collapse. The vertical dash-dot lines in all four panels represent the expected maximum redshift of GWs to be detectable by aLIGO/Virgo observing run O4 (Abbott et al., 2020b).

6.1.2 Persistent pulsar emission

The persistent pulsar emission model is the best constrained by our data among the four models introduced in Section 1.1.4.3. Thanks to the big sample of GRBs from both MWA and LOFAR triggers (including twelve short and two long ones; Kaplan et al. 2015; Anderson et al. 2021a; Rowlinson et al. 2019, 2021; also see Chapters 3 and 4) and the MWA rapid response mode, we performed the most comprehensive study of this model to date. First the pulsar emission is on until the magnetar remnant collapses into a BH (~ 1000–$10\,000$ s depending on the equation of state of NSs; Ravi & Lasky 2014; Lasky et al. 2014), which allows the MWA enough time to capture this emission. In addition, the persistence nature of this emission enables deep searches in images of a long integration time, resulting in stringent flux density upper limits, as shown in Figure 6.1. Note that this model is also well constrained in previous searches for GRB associated coherent radio emission (not limited to MWA), especially by LOFAR (Rowlinson et al., 2019, 2021).

The lack of detections of the predicted persistent emission from a sample of 14 GRBs is puzzling, driving us to reconsider the assumptions and/or uncertainties involved in the pulsar emission model. First is the magnetar remnant assumption. A systematic study of the X-ray light curves of *Swift* short GRBs shows that at least half of them can be fitted with a magnetar model (the rest are uncertain due to insufficient data; Rowlinson et al. 2013). As a conservative estimation, we may

199

expect seven magnetar remnants to be formed by the sample of GRBs explored in this thesis. Next we consider the redshifts of these magnetar remnants. As demonstrated in Chapter 3, the MWA and LOFAR observations should be able to detect the model predicted emission for a large subset of typical magnetar parameters, at least up to a redshift of $z \sim 0.6$. Based on the distribution of known GRB redshifts (Gompertz et al., 2020), we expect only one third to have redshifts of $z > 0.6$. That is, five out of the seven magnetar remnants should be located within a redshift of 0.6, and half of them, i.e. 2–3, have persistent emission brighter than a typical magnetar remnant and thus are detectable. The final issue needing to be considered is the orientation of the radiation beam of the magnetar remnant, i.e. whether the emission is pointing towards the Earth. One possibility is that the radiation beam is along the magnetic axis of the magnetar remnant (like typical pulsars), which is likely to align with the magnetar rotation axis due to dynamo activity induced magnetic field amplification (Cheng & Yu, 2014; Giacomazzo et al., 2015). That means the radiation beam of the magnetar remnant is also likely to align with the GRB jet, and thus point towards the Earth. Given the above considerations, we should be able to detect the persistent emission from 2–3 GRBs in our sample. Therefore, our non-detections of the predicted persistent emission from such a big sample of GRBs suggest some of the assumptions involved in this magnetar emission model might need to be re-examined, e.g. the fraction of GRBs that form long-lived magnetars may be very small, much less than the assumed 50%.

The equation of state of NSs and the formation of magnetars have been a long standing question in the GRB field. Searching for the pulsar emission following GRBs may be the most direct way to solving this problem as a detection would immediately confirm the formation of magnetars and open an important window for studying the equation of state of NSs.

6.1.3 Interactions of NS magnetic fields

Short GRBs likely originate from merging NSs (Narayan et al., 1992). The radio emission resulting from interactions of NS magnetic fields just prior to their merger is least explored with observations. As this emission happens prior to the BNS merger and thus the GRB emission, pointed instruments are highly unlikely to capture it. However, the rapid response of the MWA, combined with the dispersion delay of low frequency radio prompt emission with respect to the gamma-ray emission, provides an opportunity to study this emission model on GRBs at large redshifts. Considering a typical response time of the MWA between 30–60 s as shown in Chapter 3, we can achieve a negative latency for GRBs with redshifts $z \gtrsim 0.2$–0.4 at an observing frequency of 185 MHz. Specifically, for a typical short GRB redshift of $z = 0.7$ (Rowlinson et al., 2013), the rapid response follow-up observations with the MWA would allow direct studies of the radio emission produced up to ~ 70 s prior to the burst.

The fluence upper limits derived from the MWA observations of short GRBs have been compared with the model predicted radio emission in Chapter 3. Assuming typical parameters of the merging NSs such as the mass $M_{\mathrm{NS}} = 1.4 \, \mathrm{M}_\odot$, radius $R_{\mathrm{NS}} = 10^6$ cm, magnetic field $B_{\mathrm{NS}} = 10^{12}$ G and radio emission efficiency $\epsilon_{\mathrm{r}} = 10^{-4}$ for typical pulsars (Taylor et al., 1993), we found this model predicts the prompt emission fluence produced by the revived pulsar in the merging binary ($\ll 100$ Jy ms at a typical short GRB redshift) to be much fainter than our upper limits. Therefore, our non-detections of this radio emission did not rule out its existence. The possibility of using future MWA VCS observations for constraining this model is explored in Section 6.3.1 (see Figure 6.1). More sensitive telescopes with a similar fast response mode such as the SKA-Low would be promising in exploring the potential for prompt radio signals emitted prior to the BNS merger (see Section 6.3.4).

6.1.4 Magnetar collapse

The magnetar collapse could be the final phase in the evolution of GRBs that form an unstable magnetar remnant. X-ray observations seem to suggest that the spin down induced collapse of the magnetar into a black hole may not occur until 2 h post-burst (Zhang, 2014), as shown in Chapter 3. Therefore, our 30 min MWA observations immediately following GRB triggers are unlikely to capture the brief flash of coherent radio emission produced by magnetic reconnection within the pulsar magnetosphere during the collapse.

In order to detect this model emission, we need to overcome a few difficulties. First is the largely uncertain collapse time, depending on the unknown equation of state of magnetar remnants formed by the merging NSs or core-collapse supernovae. This uncertainty makes it difficult to schedule a follow up that just captures the one-off burst at a minimal cost, i.e. least observing time requested (specifically a problem for VCS data due to the large data volume). Additionally, the predicted fluence of this prompt radio emission is quite low. As shown in Rowlinson et al. (2021), the predicted emission would reach a fluence of $\gtrsim 100\,\mathrm{Jy\,ms}$ only within a redshift of $z < 0.05$ for typical magnetar parameters such as the amount of available energy in the magnetic field ($E_{\mathrm{B}} = 1.7 \times 10^{47}\,\mathrm{erg}$), the fraction of magnetic energy converted into the radio emission ($\epsilon = 10^{-6}$) and the spectral index of the coherent radio emission ($\alpha = -2$; Rowlinson et al. 2021). Despite the above difficulties, we have devised several ways of probing the emission predicted to be produced by the magnetar collapse in Section 6.3.1.

6.2 Low-frequency studies of repeating FRBs

We have performed a search for low radio frequency emission from five repeating FRBs with the VCS data in the MWA archive (mainly from the SMART survey; also see Chapter 5). This is one of the most extensive searches for low frequency FRB emission from known repeaters. Our observations may suggest that repeat-

ing FRBs have very shallow spectra, that the five repeating FRBs are affected by free-free absorption and could be sitting in persistent nebulae, or (more likely) the five repeaters were not active during the MWA observations.

I start with the most plausible scenario, i.e. the repeaters being inactive during the MWA observations. None of the five repeaters studied in Chapter 5 are known to show periodic activity as is the case for some sources (e.g. FRB 20121102A and FRB 20180916B; Rajwade et al. 2020b; Chime/Frb Collaboration et al. 2020), so we do not know when they were active. Given their observed low burst rates, we would expect only a few bursts to be emitted by these repeaters during the MWA observations. Indeed, it is more likely all repeaters may have active and inactive periods, further reducing the likelihood of a detection. However, we can use the MWA observations to place further constraints on the duty cycle of the five repeating FRBs. Particularly, we can update the burst rate of FRB 190116A, 190117A, 190213A and 201124A to a lower value of $0.20\,\mathrm{hr}^{-1}$, $0.19\,\mathrm{hr}^{-1}$, $0.09\,\mathrm{hr}^{-1}$ and $9.80\,\mathrm{hr}^{-1}$, respectively. Note that here we have ignored the dependence of burst rates on observing frequencies and fluences (Pearlman et al., 2020; Pleunis et al., 2021b). The burst rate of FRB 190711A is extremely low, and not included here (see Chapter 5).

We might still expect some of the repeaters could be active during the MWA observations, such as FRB 190117A and FRB 201124A with an expected number of bursts of 1.8 and 30, respectively (see Chapter 5). In this case, our results demonstrate a shallow spectrum for the FRB emission, given the expected low frequency burst must be below the sensitivity of the MWA observations. Specifically, we can constrain the spectral index of the FRB emission to $\alpha \gtrsim -1$, as shown in Chapter 5. This constraint is larger than the typical spectral index measured over a large sample of FRBs (~ -1.5; Macquart et al. 2020; Bhattacharyya et al. 2021), and also larger than the spectral index measured for FRB 201124A (~ -5.8; Kumar et al. 2021c). Given that previous measurements of the spectral index are all based on high frequency ($> 300\,\mathrm{MHz}$) observations, this disagree-

ment might suggest that the FRB spectrum is shallower at low frequencies than at high frequencies, or there is a break in the spectrum. This could be further related to pulsar emission, which resembles FRBs in many respects such as the high brightness temperature and the potential association with compact objects. Also many pulsars have been observed to show spectral breaks in the frequency range of 100–300 MHz (Bilous et al., 2016; Murphy et al., 2017).

Our results can also be used to constrain the FRB environment if we assume free-free absorption attenuates the low frequency radio burst to below the sensitivity of the MWA observations. This requires clustering of the absorbing material at the burst site, as given by the constraint on the size of the ionized nebula hosting the repeating FRBs studied in Chapter 5. This small sized nebula of ∼pc is comparable to the Crab Nebula. If the repeaters studied in Chapter 5 are associated with magnetars formed via core-collapse supernovae, the large amount of material produced prior to the explosion would be able to absorb the low frequency radio bursts via free-free absorption (Woosley et al., 2002). Given the plausible link between repeating FRBs and magnetars in both observations (Bochenek et al., 2020; CHIME/FRB Collaboration et al., 2020) and theories (Metzger et al., 2019; Lu et al., 2020; Beloborodov, 2020; Lyubarsky, 2020), this scenario of free-free absorption is possibly in operation and can naturally explain our results even if low frequency bursts with a typical spectral index were emitted by the repeaters during the MWA observations. Note that this scenario also implies a potential link between repeating FRBs and long GRBs. In summary, the results of our low frequency FRB search suggest a lower burst rate than previously calculated for the five repeating FRBs investigated in Chapter 5.

6.3 Future prospects

I have discussed how current MWA observations can be used for GRB and repeating FRB studies in Section 6.1 and 6.2. In order to further our understanding of GRB models, GW science and the source of repeating FRBs, while paving the

way for SKA activities, it is important to continue improving the existing transient experiment. In this section I discuss different future prospects of the MWA and SKA-Low in GRB, GW and FRB research.

6.3.1 Improving the MWA VCS triggering program for GRBs

First we discuss how the GRB triggering program with the MWA VCS can be used to advance our knowledge of the coherent emission models investigated in this thesis. We compare the sensitivity of the MWA VCS under coherent and incoherent beamforming to the four model predictions in Figure 6.1. As can be seen, the VCS data are more sensitive to the prompt radio emission associated with GRBs than the imaging data. Yet currently there is only one published VCS observation of a long GRB 210419A (see Chapter 4). We need more VCS triggers and observations of GRBs to increase the sample size and further test the emission models (see Section 1.1.4.3), especially for short GRBs detected by *Swift* (more emission mechanisms and less subjection to absorption). Here I discuss the prospective science that would come from triggering on more GRBs with the MWA VCS.

6.3.1.1 GRB triggering rates and improved sample size

First we need more VCS observations of *Swift* GRBs, which compared to *Fermi* GRBs have much more accurate localisation (see Section 1.3). Based on the number of GRBs detected by *Swift* from 2005 to 2014 (Lien et al., 2016), there are ~ 100 GRB triggers per year, of which ~ 90 are long and ~ 10 short. Assuming 30% sky coverage of the MWA, we expect there to be ~ 27 long and ~ 3 short GRBs likely to be in the MWA observable sky every year. If we factor in the downtime of the array (including breakdowns, upgrades and software failures, which could add up to half a year), the final number of triggers would be 13–14 and 1–2 for long and short GRBs, respectively.

While long GRBs are more common, they are more likely to suffer from absorption (see Section 6.1.1). Meanwhile, short GRBs are more likely to have detectable radio emission with more predicted emission scenarios but are much rarer events. Given that we already have useful statistics from the first five years of MWA triggering on both *Swift* and *Fermi* GRBs, we can make true MWA trigger rate estimates. For *Swift* GRBs, the trigger rate is 12 per year, of which 11 are long and one short, consistent with the above estimation. For *Fermi* GRBs, the trigger rate is 29 and 12 per year for long and short GRBs, respectively. As we can see, the trigger rate for *Fermi* detected short GRBs is much higher than for *Swift* detected short GRBs. Note that we have attempted to filter out long GRBs in MWA triggering on *Fermi* GRBs (Hancock et al., 2019a), so the proportion of short GRB triggers is much higher than in actual GRB detections by *Fermi*.

In order to increase the GRB sample, we need to trigger on *Fermi* GRBs as well as *Swift* GRBs with the MWA VCS. The main obstacle is the large position errors of *Fermi* GRBs, which contain a prohibitively large number of synthesised beams needing coherent beamforming. We may solve this problem by only triggering on those events with small position errors, even if it means waiting for a few position updates. Note that this could delay the MWA observation by $\sim 10\,\mathrm{s}$–$10\,\mathrm{min}$ and affect our search for the emission predicted to be produced by the interaction of NS magnetic fields and the GRB jet-ISM interaction. The threshold of position errors for filtering *Fermi* GRBs should depend on the array configuration, e.g. $< 1\,\mathrm{deg}$ for the extended configuration and $< 10\,\mathrm{deg}$ for the compact configuration. That means that the compact configuration is in fact preferable for GRB triggered follow-up with the VCS.

In the case when a GRB is not above the MWA horizon at the time of detection, we can calculate how long it will take for the GRB to rise. If that is within the next two hours, we can schedule a VCS observation at the time the GRB has risen. In this case, we are still sensitive to the persistent emission from the

magnetar remnant. Also we may optimise the observation time to capture the emission produced when the magnetar collapses, i.e. scheduling a VCS observation around 2 hr post-burst, the expected time of the collapse (Zhang 2014; see the section below).

6.3.1.2 Optimising VCS observations to target prompt emission models

The four emission models investigated in this thesis operate at different phases of during BNS mergers or core-collapse supernovae (see Section 1.1.4.3). Based on that we can optimise the MWA VCS observing strategy to better target each of the predicted signals.

First we consider the GRB jet-ISM interaction. For probing this model, we need to improve the MWA latency (Hancock et al., 2019a). We may investigate the time taken by every step in the triggering process (e.g. the latencies associated with the MWA front end receiving the VOEvent, the parsing of VOEvents and the scheduling of MWA observations) and find out which steps could be further optimised. As shown in Figure 6.1, the MWA VCS observation with coherent beamforming would be able to detect the predicted emission (with a magnetar engine; see Chapter 3) up to a redshift of $z \sim 1$ assuming typical model parameters including the spin period and magnetic field of a typical magnetar remnant, the gamma-ray fluence and the fraction of magnetic energy in the relativistic jet. Note that in this section all predictions are based on the full MWA array. Based on the redshift distribution of GRBs in the *Swift* era, around one third of GRBs have a redshift of $z < 1$ (Le & Mehta, 2017). That means if we can trigger on six GRBs, the probability of at least one GRB having $z < 1$ would be $\sim 90\%$. Based on the expected MWA trigger rate of GRBs estimated in the previous section, that could take six years and six months for *Swift* detected short and long GRBs, respectively. Including *Fermi* detected short GRBs could double our trigger rate and reduce the time needed for six GRB triggers to three months. Note that the

model prediction without a magnetar engine is too faint to be detected by the MWA VCS, and will be explored in Section 6.3.4 with the SKA-Low.

Next we consider the pulsar emission model (the best constrained; see Section 6.1.2). In order to optimise our chance of a detection of the persistent emission from the magnetar remnant, we plan to schedule a further 2 hr observation in the standard correlator mode following the first 15 min VCS trigger if the GRB is likely to be short. This could improve our sensitivity to any persistent emission by a factor of two compared to the 30 min MWA observation analysed in Chapter 3. With such a high sensitivity, we would be able to detect the predicted emission from the magnetar remnant at all reasonable redshifts for a large parameter space (see Figure 6.1). The final chance of detection may depend on whether magnetar remnants are formed by GRBs, the orientation of the magnetar radiation beam and the low radio frequency emission being able to escape from the GRB environment.

For the earliest signal produced by the interaction of NS magnetic fields (only applicable to short GRBs), improving the MWA latency is also important. As demonstrated in Figure 6.1, the MWA VCS observation with coherent beamforming would be able to detect the predicted emission only within a small redshift range of $z \lesssim 0.1$. That means we can hardly test the NS magnetic field interaction model with the MWA VCS due to insufficient sensitivity. SKA-Low is more promising for this model (see Section 6.3.4).

The 2 hr standard observation planned above can also be used for probing the prompt signal produced when the magnetar remnant collapses. With the highest temporal resolution of the standard correlator (0.25 s for MWAX; private communication), we would be able to detect the predicted signal using image dedispersion (see Chapter 3) for a redshift range of $z \lesssim 0.5$, as shown in Figure 6.1. We could also schedule another 15–30 min VCS observation around 2 hr post-burst, which would increase the detectable redshift range to $z \lesssim 1$ (see Figure 6.1). Again, SKA-Low will be more promising for probing this model, as discussed in

Section 6.3.4.

6.3.2   MWA VCS triggers on GWs

BNS mergers can produce GWs as well as short GRBs, as confirmed by the near-coincident detection of GW170817 and GRB 170817A (see Section 1.1.4.4). Therefore, in addition to triggering on GRBs, we can also trigger on GW events and search for the radio emission predicted to be produced by BNS mergers. We compare the sensitivity of the MWA VCS with coherent and incoherent beamforming to GW associated prompt radio signals predicted by the four emission models (see Section 6.1) in Figure 6.1. In this section, I discuss the prospect of triggering on GW detections with the MWA VCS during the aLIGO/Virgo observing run O4 (expected to commence in 2022; Abbott et al. 2020b).

We can probe all the same models with follow-up observations of GWs as have been investigated in this thesis. Note that here we are only concerned with GW signals resulting from BNS mergers, not those from binary BH or BH-NS mergers. However, a big advantage of triggering on GW events over GRBs is the much closer distance of GWs ($\lesssim 190\,\mathrm{Mpc}$, BNS predicted horizon limit for O4; Abbott et al. 2020b), which means the associated radio emission would be much brighter than from distant GRBs, as shown in Figure 6.1. Given the proximity of the events, a non-detection with an MWA VCS trigger could mean we need to make significant amendments to the model assumptions (depending on the orientation of the event). It could be that the BNS merger does not produce a magnetar remnant. We may also be able to constrain the fraction of magnetic energy in the relativistic jet launched by the merger to be $\ll 10^{-3}$, which would suggest GRB jets are baryonic rather than Poynting flux dominated.

While the expected results from GW triggers look exciting, we need to overcome a few challenges in this experiment. First is the even more stringent requirement on the fast response of the telescope (compared to GRB triggers; see Section 1.3). As the proximity of GW events means little dispersion delay, the

MWA needs to respond to GW detections almost instantly, for which there are some hardware and software limitations (Hancock et al., 2019a). However, instead of triggering on GW signals emitted at the final moment of a BNS merger, we could trigger on the signals emitted during the inspiral phase, i.e. negative-latency triggering (James et al., 2019). This could help alleviate the requirement on response times, allowing the MWA enough time to catch any associated prompt radio signals, especially those produced by the relativistic jet-ISM interaction and NS interaction model.

Another difficulty is the poor localisation of GW events, which can hardly be covered by the MWA. We need high time resolution observations of a large portion of the sky that is still sensitive enough to detect the signals we are searching for. The traditional method is to point the MWA to the most probable position of GWs, which can be obtained by fitting an all-sky probability map of the GW signal. We can attain the best sensitivity of the MWA for our search for any associated radio emission but bear a risk of missing the emission if the GW is not near the most probable position. In addition, the computational time for processing the GW position probability density map would delay the telescope being on target so we would miss any signal emitted either just prior to or during the merger event. A strategy proposed by James et al. (2019) was to switch off all but one of the sixteen dipoles on each tile, which would widen the MWA field of view to the entire sky down to the horizon limit. Note that the proximity of GW events is likely to outweigh the sensitivity loss in this case (James et al., 2019). As a balanced strategy, we may divide the full MWA array into multiple subarrays and point them in different directions (private communication) in order to cover half of the hemisphere. Thus we can obtain a slightly bigger field of view at a slightly lower sensitivity. However, dealing with the data from the subarrays would be a problem as we would need multiple copies of the data and then flag out all the tiles pointed in different directions. This is a bit clumsy and may take large amounts of disk space but it is still feasible.

210

Here we propose another observing mode for GW triggers, i.e. the VCS mode with incoherent beamforming. While the incoherent beamforming is less sensitive than the coherent beamforming (by a factor of ~ 10; see Figure 6.1), we can preserve a large field of view. As the GW associated radio emission is expected to be much brighter than the GRB associated emission as discussed above, the lower sensitivity of incoherent beamforming could still yield meaningful results. As shown in Figure 6.1, incoherent beamforming of the MWA VCS data is sensitive enough to make a real detection of the prompt signals predicted to be produced by the relativistic jet-ISM interaction, the NS magnetosphere interaction and the collapse of the magnetar remnant, or place constraints on these models.

6.3.3   MWA follow-up of repeating FRBs

Detecting low frequency bursts from repeating FRBs is extremely important as the low frequency emission can be used to study the spectral properties and local environments of repeaters as well as improve the estimation of FRB rates (see Section 6.2). Yet currently there is only one FRB that has been detected at $< 300\,\mathrm{MHz}$ frequencies (Pleunis et al., 2021b). The MWA VCS, with a wide field of view and a high time resolution, is an ideal instrument for low frequency FRB searches.

We plan to study repeating FRBs using both archival VCS data and new pointed follow-up observations. First we expect there to be ~ 20 new repeating FRBs likely to be discovered per year based on the results published by CHIME (CHIME/FRB Collaboration et al., 2019c; Fonseca et al., 2020a). We can use the archival VCS data resulting from the SMART survey (Bhat et al., 2022) to search for low frequency bursts from these newly discovered repeaters. Although the MWA and CHIME are located in different hemispheres, given the huge sky coverage of the SMART survey (the entire sky south of $+30°$ in declination; see Chapter 5) we expect $\sim 20\%$ of the CHIME FRBs to be in the MWA observable sky, i.e. ~ 4 newly discovered repeating FRBs per year. Currently there are

$\sim 168\,\mathrm{hr}$ of VCS data in the MWA archive available for this FRB search program. We also plan to perform routine targeted observations of known repeating FRBs to obtain monthly coverage. Note that a few additional observations in the pulsar queue may also increase our coverage of repeating FRBs.

Apart from repeating FRBs of sporadic bursting behavior, some FRBs might be discovered to show periodic activity in the future, similar to FRB 20121102A and FRB 20180916B. In this case, we can target the periodic window of these well characterised repeaters with the MWA. Certainly, the repeaters must be visible to the MWA. This strategy has been proved to be successful through the detection of low frequency bursts from FRB 20180916B by LOFAR (Pleunis et al., 2021b). As shown in Chapter 5, the sensitivity of the MWA VCS observation is sufficient for detecting most of the low frequency bursts detected by LOFAR (see Figure 5.2). Therefore, if another periodically bursting FRB with similar emission properties to FRB 20180916B occurs in the MWA field, targeting the periodic window with the MWA VCS would be highly likely to yield a detection.

Another strategy would be to perform rapid follow-up VCS observations of repeating FRBs that are shown by other instruments to have entered a sudden period of high activity. Note that the "rapid" here refers to a timescale of $\sim$ days, different from the rapid follow-ups of GRBs. One of the five repeating FRBs studied in Chapter 5, FRB 201124A, is such a case. It shows a highly variable burst rate. Specifically, during the period from 2021 March 20 to 2021 May 27 FRB 201124A is estimated to have a burst rate between $92\,\mathrm{day}^{-1}$ and $201\,\mathrm{day}^{-1}$, while the burst rate prior to discovery was only $< 3.4\,\mathrm{day}^{-1}$ (Lanman et al., 2021). This long (months) period of high activity allows scheduled follow up observations, yielding detections of repeat bursts by different telescopes over a broad range of frequencies (Marthi et al., 2021; Piro et al., 2021; Lanman et al., 2021). Inspired by this success, we plan to keep monitoring the latest report of FRB activities and follow up on any repeaters with the MWA VCS that show signs of sudden high activity.

6.3.4 Transient strategies for SKA-Low

Our experience in observing the coherent radio emission associated with GRBs and low frequency emission from repeating FRBs is applicable to the low frequency component of the SKA (SKA-Low; Dewdney et al. 2009)[1]. As a low frequency (50–350 MHz) radio telescope, the SKA-Low would feature an unprecedented collecting area and sensitivity (Sokolowski et al., 2021), which makes it interesting to discuss the prospective science the SKA-Low would be able to explore in the context of GRBs and repeating FRBs. Note that there may be a pulsar mode (similar to the VCS) for the SKA-Low, but here we are only concerned about the SKA-Low imaging mode as this mode has been discussed in detail recently (Sokolowski et al., 2021, 2022).

The biggest improvement of the SKA-Low is sensitivity. For a single coarse channel of 0.926 MHz within the SKA-Low operational range of 160–230 MHz, we expect a sensitivity of 42 ± 15 Jy on a 2 s timescale (Sokolowski et al., 2021). Since the SKA-Low will consist of 512 stations and have an instantaneous bandwidth of ~ 50 MHz, we expect a sensitivity (scaling with the bandwidth as $\propto \Delta\nu^{-1/2}$ and the number of baselines as $\propto N_{\mathrm{baseline}}^{-1/2}$ in the correlator mode) of ~ 0.02 Jy on 2 s timescales for the full SKA-Low. If we scale the sensitivity with integration time as $\propto \Delta t_{\mathrm{int}}^{-1/2}$, we expect a sensitivity of ~ 0.002 Jy on 2 min timescales (integration time of individual MWA observations; see Chapter 3). This is an improvement of more than an order of magnitude on the sensitivity of the MWA imaging mode, even compared to the best images created from the MWA observations of GRB 190627A (0.084 Jy on 2 min timescales; see Chapter 3). For a comparison of the sensitivity between the imaging mode of MWA and SKA-Low see Figure 6.1.

Another improvement is the employment of a high time resolution ($\sim$millisecond) imaging mode for the SKA-Low (Sokolowski et al., 2021). The time resolution of the MWA imaging data is only 0.5 s, limiting the sensitivity to transient signals on shorter timescales. For example, a pulsed signal with a duration of 10 ms would

---

[1]https://www.skatelescope.org/

be diluted by the 0.5 s coarse sampling of the MWA imaging data to $\approx 14\%$ of its intrinsic intensity. The high time resolution of SKA-Low images will prevent such a sensitivity loss. Therefore, the SKA-Low imaging mode, with an unprecedented sensitivity and a high time resolution, would be extremely sensitive to any prompt radio signals, as shown in Figure 6.1.

6.3.4.1 Prospect on the GRB triggering experiment

As discussed in Section 6.3.1, the SKA-Low is very promising in probing the coherent emission models applicable to GRBs, especially the NS magnetosphere interaction and the magnetar remnant collapse, which predict extremely faint emission. We compare the expected sensitivity of the SKA-Low to the coherent emission model predictions in Figure 6.1. Here I assume the SKA-Low will have a similar fast response as the MWA and discuss the prospect of the SKA-Low in the GRB triggering experiment.

First I consider the prospect of probing the GRB jet-ISM interaction model with the SKA-Low. In Figure 6.1, we compare the expected sensitivity of the SKA-Low to the typical sensitivity of the MWA VCS data (coherent beamforming; see Chapter 5) and the predicted radio emission produced by the GRB jet-ISM interaction model. Note that we presume the SKA-Low will have a time resolution of 1 ms in the imaging mode, and we would perform image dedispersion with the imaging data. In the case of lower resolutions, e.g. ~ 10 ms, we would expect a downgrading factor of ~ 3 in the sensitivity. We can see from Figure 6.1 that the SKA-Low will be more than an order of magnitude more sensitive to prompt radio transients than the MWA VCS data. In the case of a magnetar central engine (light shaded region), while the MWA observations can detect the predicted emission up to a redshift of $z \sim 1.5$ for typical model parameters (see Chapter 3), the SKA-Low will be able to detect the emission up to a similar redshift but for almost the full parameter space. Even in the case of no magnetars (dark shaded region), the SKA-Low would have a chance of detection

from GRBs at a redshift of $z \lesssim 0.3$. Therefore, SKA-Low observations of GRBs will have a high chance of detecting the predicted emission or place constraints on the model.

Next I explore the prospect of detecting the persistent radio emission predicted to be produced by the magnetar remnant with the SKA-Low. A comparison between the SKA-Low sensitivity and the predicted flux density for the model emission is shown in Figure 6.1. Note that we adopt a 2 hr integration time for the SKA-Low, as discussed in Section 6.3.1. We can see the SKA-Low is more sensitive than the LOFAR (2 h integration time; Rowlinson et al. 2019), and would be able to detect the persistent radio emission for the full magnetar parameter space up to a redshift of $z \sim 0.5$.

We also compare the SKA-Low sensitivity with the faint radio emission predicted by the NS magnetosphere interaction and the magnetar remnant collapse in Figure 6.1. We can see the SKA-Low allows us to detect the emission predicted by these two models from GRBs at a redshift of $z \lesssim 0.3$ and $z \lesssim 1$, respectively. If the SKA-Low can respond to GRB detections as fast as the MWA, we would expect the SKA-Low to be able to detect the earliest radio emission from BNS mergers within a redshift range of $0.2 \lesssim z \lesssim 0.3$ (see Section 6.1.3). In the case of GW events, this means the SKA-Low would be able to detect associated radio emission for future GW observing runs that will likely have a larger horizon than O4.

6.3.4.2 Prospect on repeating FRB searches

The extremely high sensitivity of the SKA-Low on millisecond timescales (in the imaging mode and with image dedispersion), as shown in Figure 6.2, can also be used for FRB search. Here we discuss the potential of a targeted search for repeating FRBs and a blind survey with the SKA-Low.

First we explore the detectability of repeating FRBs like FRB 20180916B by the SKA-Low. As shown in Figure 6.2, SKA-Low would be able to detect all the
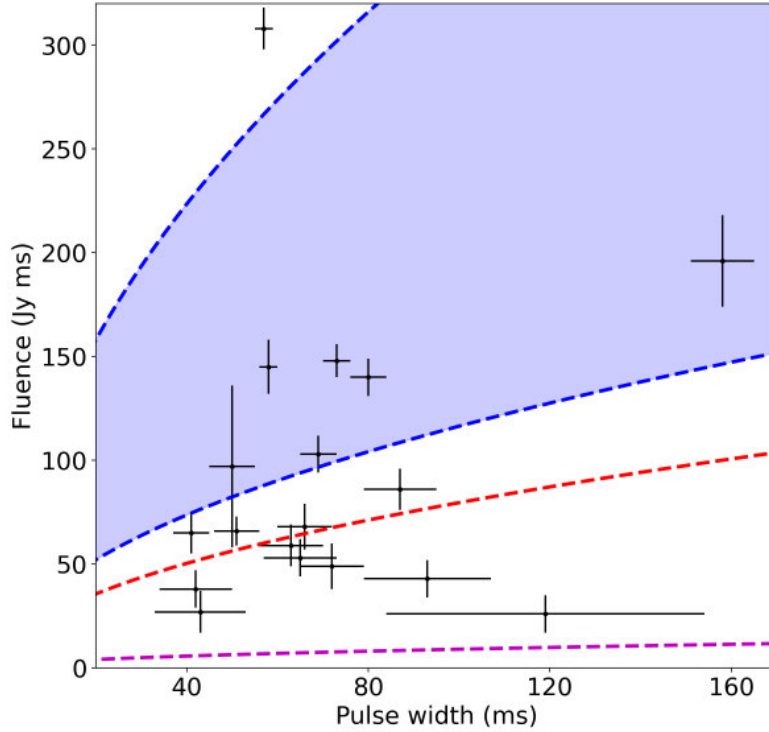
Figure 6.2: Same as Figure 5.2 in Chapter 5 except the additional magenta dashed line representing the expected sensitivity of the SKA-Low. The black points represent the 18 bursts detected by LOFAR, the blue region represents the range of fluence upper limits derived from the MWA observations analysed in Chapter 5, and the dashed red line represents a typical sensitivity near the zenith of the MWA.

low frequency bursts detected by LOFAR from FRB 20180916B (Pleunis et al., 2021b). Even fainter bursts will also be readily detected. The many more low frequency bursts likely to be detected by the SKA-Low from known repeating FRBs may help characterise their active windows and lead to discoveries of more (quasi-)periodic FRBs.

For a blind survey we can estimate the expected detection rate of FRBs with the SKA-Low based on current estimation of FRB rates (including both repeaters and non-repeaters). As discussed in Chapter 5, the FRB detection rate depends on the observing frequency and sensitivity of the telescope. Adopt-

216

ing an observing frequency of $160 \, \text{MHz}$ (as tested in Sokolowski et al. 2021) and a typical sensitivity of $5 \, \text{Jy ms}$ (see Figure 6.2), we expect a sky rate of $\sim 4 \times 10^3$–$4 \times 10^4 \, \text{sky}^{-1} \, \text{day}^{-1}$ for repeating FRBs that can be detected by the SKA-Low. Given the huge field of view of the SKA-Low ($\approx 10^4 \, \text{deg}^2$, around 25% of the full sky; Sokolowski et al. 2021), $1 \, \text{hr}$ of SKA-Low observation would result in ~ 40–400 FRB detections. This would significantly expand the repeating FRB population at low frequencies. Note that the actual detection rate by the SKA-Low may differ considerably from this prediction as the spectrum of FRB emission at low frequencies ($< 300 \, \text{MHz}$) is still poorly explored and propagation effects may absorb some of the low frequency bursts (Sokolowski et al. 2018; Pleunis et al. 2021b; also see Chapter 5).

The high time resolution of the SKA-Low imaging data would allow a direct FRB search in the image domain (using image dedispersion as used in Chapter 3 on MWA imaging data) with the maximum sensitivity instead of using the voltage data. This can significantly reduce the computational cost for FRB searches in a large area of the sky when compared to coherent beamforming at a large number of independent pointings (see Chapter 5). Naively, we might expect a boost in the FRB search speed by a factor equal to the number of synthesised beams in the FRB search area as techniques described in Chapter 3 can be performed directly on the high time resolution images. Therefore, the high time resolution imaging mode of the SKA-Low would make the data processing more manageable than the traditional FRB search method using the voltage data. Note that storing a large amount of high time resolution SKA-Low images may still be a limiting factor on this search strategy.

6.4 Conclusions

This thesis has presented targeted searches for coherent low frequency radio transients with the MWA. We have observed nine short GRBs with the rapid response of the MWA in the imaging mode and one long GRB with the VCS, doubling the

number of sensitive low frequency ($< 300\,\mathrm{MHz}$) searches for coherent, prompt radio emission (Kaplan et al., 2015; Anderson et al., 2018b; Rowlinson et al., 2019, 2021; Anderson et al., 2021a), and performed one of the most deepest searches on both short ($\sim$ms) and long ($\sim 30\,\mathrm{min}$) timescales for GRB associated radio emission. We also performed one of the most extensive searches for repeat bursts at low frequencies ($< 300\,\mathrm{MHz}$) from known repeating FRBs with archival MWA VCS data. These works have proved that the MWA is a powerful tool in transient searches, demonstrating that further observations of GRBs and repeating FRBs are promising for future detections. The main conclusions from this thesis are summarised as follows.

6.4.1 Feasibility of MWA in the GRB triggering experiment

As demonstrated in Chapters 3 and 4, the fast response of the MWA to GRB detections by *Swift*-BAT and/or *Fermi*-GBM allows us to catch any dispersed radio signals produced simultaneously with the GRB for a minimum redshift between 0.2 and 0.6. Furthermore, for GRBs at a larger redshift, e.g. a typical short GRB redshift of $z = 0.7$, the MWA could even catch radio signals emitted prior to the GRB, during the inspiral phase of the BNS merger.

In Chapter 3, we constrained the prompt radio signals predicted by the jet-ISM interaction model to $\lesssim 100\,\mathrm{Jy\,ms}$ using the MWA imaging data and the image dedispersion technique. This upper limit was improved in Chapter 4, where we used the MWA VCS and coherent beamforming for a dispersed pulse search, and derived some of the most stringent upper limits, constraining the fraction of magnetic energy in the relativistic jet of GRB 210419A to $\epsilon_\mathrm{B} \lesssim [0.05\text{--}0.1]$ during the prompt gamma-ray emission phase and $\epsilon_\mathrm{B} \lesssim 10^{-3}$ during the X-ray flare with the MWA VCS observation of this GRB. This might suggest a baryon dominated jet, providing a clue for the jet composition problem for GRB 210419A. Note that this was achieved with only two thirds of the full MWA tiles. Therefore,

even in the case of no detections of GRB associated prompt signals, MWA VCS triggered observations of GRBs can significantly contribute to our understanding of the GRB jet composition.

Apart from prompt radio emission, we used the MWA to search for persistent radio emission predicted to be produced by the magnetar remnant formed via BNS mergers or core-collapse supernovae, as demonstrated in Chapter 3. The deep MWA images created using the standard correlator with an integration time of 30 min can detect the predicted emission from GRBs up to a redshift of $z \sim 2$. In summary, the MWA, equipped with the rapid-response mode has the capability to either detect the predicted coherent radio emission produced by GRBs or place significant constraints on the emission models.

6.4.2 Feasibility of MWA in targeted searches for repeating FRBs

As demonstrated in Chapter 5, the large amount of archival MWA VCS data resulting from the SMART survey, combined with the GRB triggering experiment naturally provides generous sky coverage and exposure time over multiple epochs to search for low frequency bursts from known repeating FRBs. This is the first systematic search for low frequency bursts from a large sample of repeating FRBs, allowing us to constrain the spectral index and the size of the absorbing medium in the FRB environment for these repeaters.

In Chapter 5, we compared the sensitivity of the MWA VCS observations to the expected fluence of five repeating FRBs in the frequency range of 144–215 MHz assuming a typical spectral index, predicting that MWA could detect the two brightest FRBs, i.e. FRB 190711A and FRB 201124A, if they were active during the MWA observations. We also found a considerable fraction of the low frequency bursts emitted by FRB 20180916B that were detected by LOFAR (Pleunis et al., 2021b) were bright enough to be detectable by the MWA, which is encouraging for low frequency VCS detections of bursts from repeating FRBs in the future. In

conclusion, MWA is an incredible instrument for prompt radio transient searches, and it is paving the way for even more exciting transient science with SKA-Low.

Appendices

Appendix A

MWA images

In Figures A.1 and A.2, we show the first 2 min snapshots of the nine short GRBs in our sample. These images were visually inspected to judge the data quality for our sample selection (see Section 3.2). The positions of those GRBs localised by *Swift* are indicated by white lines or a circle in Figure A.1, and the ROIs of those GRBs localised by *Fermi* or the IPN are indicated by the overlap between the GRB error positions (white curves) and the MWA primary beams 50% response (red curves) in Figure A.2 (see Section 3.4.1). Note that the observations of GRB 190903A and 191004A were taken in the MWA compact configuration so their images have a larger resolution (synthesised beam) than those taken during Phase I or in the extended configuration.
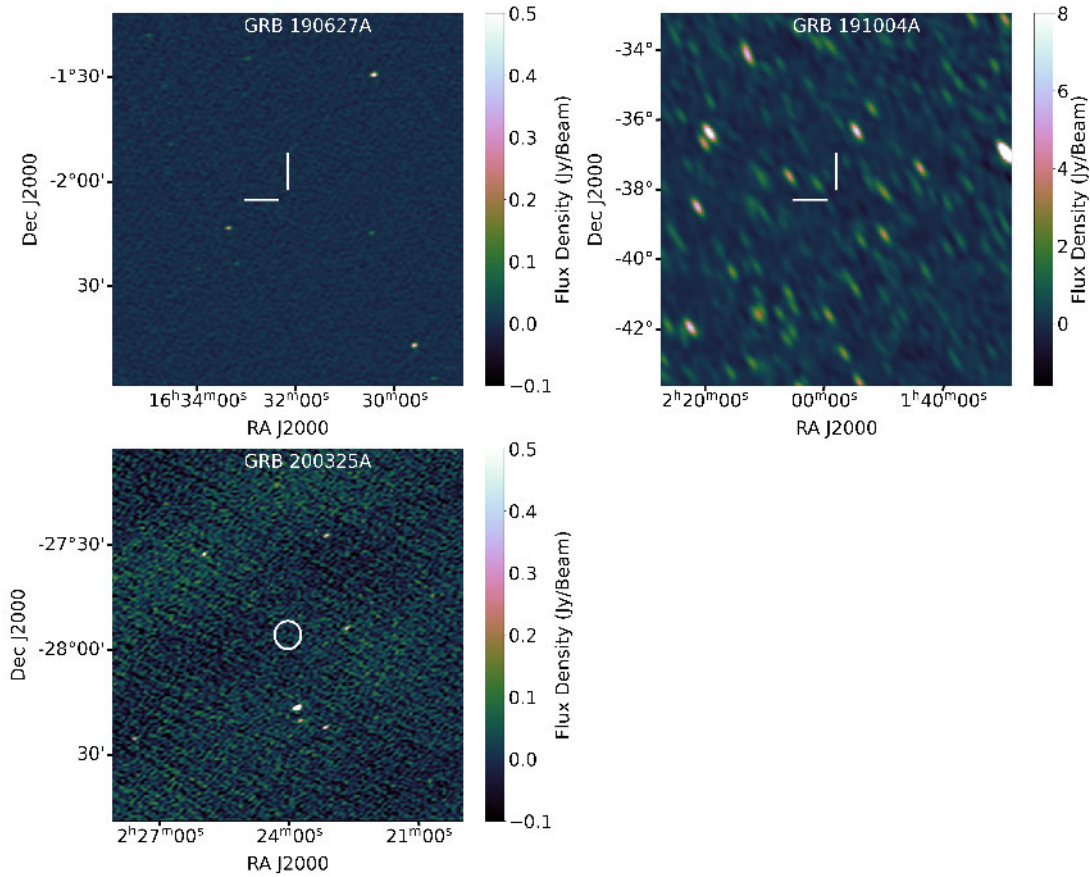
Figure A.1: The first 2 min snapshots showing the regions surrounding the three GRBs localised by *Swift*. The white lines in the top 2 panels point to the positions of GRB 190627A and 191004A localised by *Swift*–XRT to within a synthesised beam of the MWA, and the white circle in the bottom panel indicates the position of GRB 200325A localised by *Swift*–BAT to within 50 synthesised beams.
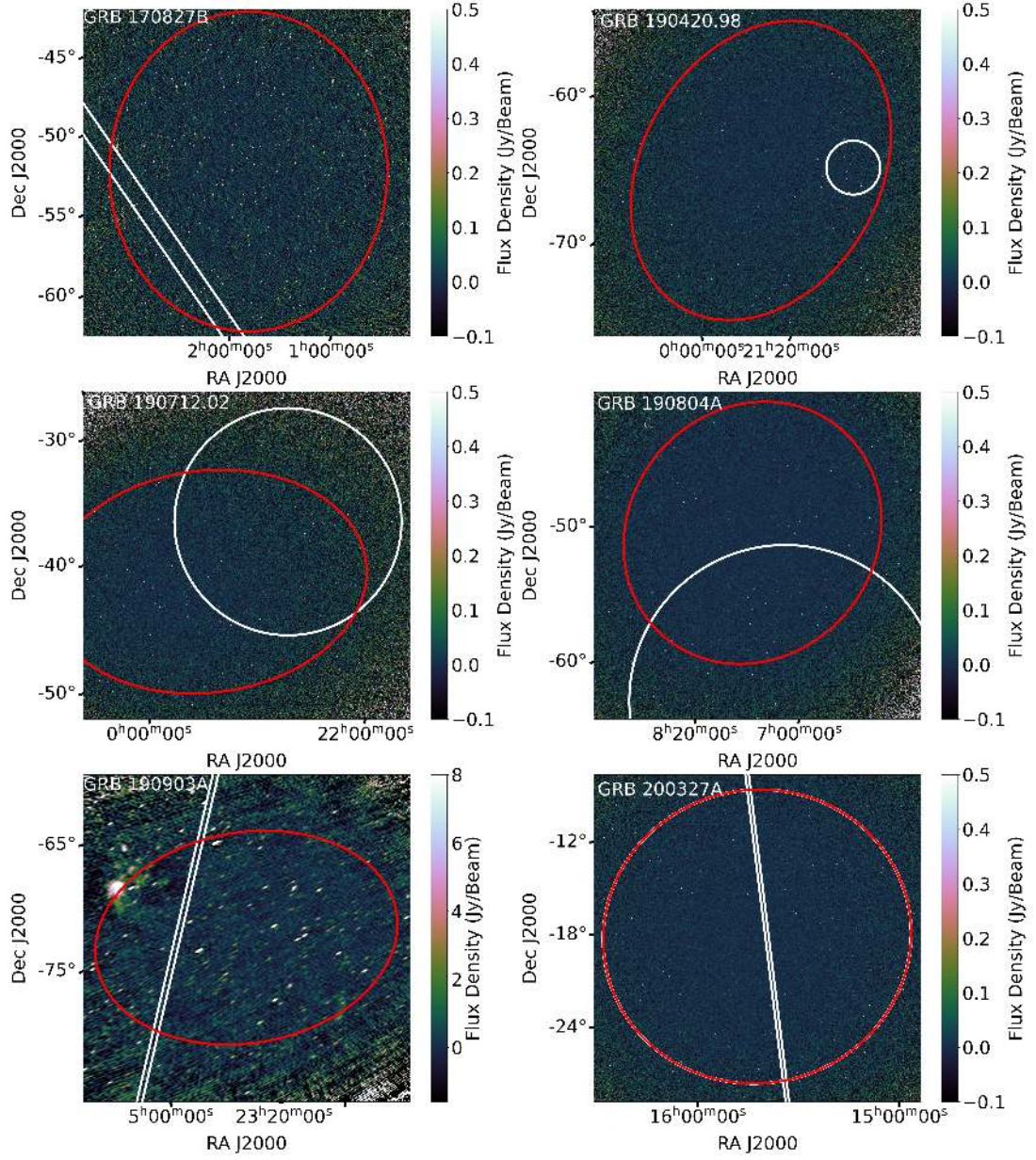
Figure A.2: Similar to Figure A.1, here we present the first 2 min snapshots of field covering the *Fermi* GRBs in our sample. The white lines show the boundaries of the GRB localisation by *Fermi* or the IPN, the red lines show the boundaries of the MWA primary beam 50% response, and their overlaps show the ROIs within which we searched for transients and variables (see Section 3.4.1).

Appendix B

Transient and variable candidates for Fermi GRBs

In Table B.1, we provide the light curve variability parameters derived via priorized fitting at the position of the two *Swift* GRBs on timescales of $2\,\mathrm{min}$, $30\,\mathrm{s}$ and $5\,\mathrm{s}$, i.e. the modulation index (m), the de-biased modulation index (m_d; which takes into account the errors on each data-point), and the probability of observing such variability in a non-variable (steady) source (p_val; see Section 3.4.1 for details).

In Table B.2 of this appendix, we report the number of transient and variable candidates that were detected by ROBBIE within each *Fermi* GRB ROI in our sample. The expected number of false positive transient and variable candidates assuming Gaussian statistics are also provided (see Section 3.4.2 for details).

GRB	Timescale	Variability statistics		
		m	m_d	p_val
190627A	2min	6.47	-1.6	0.7
	30s	5.82	2.53	0.75
	5s	-20.04	-6.24	0.53
191004A	2min	-0.62	-0.54	0.05
	30s	-0.78	-0.4	0.02
	5s	-0.42	0.51	0.41

Table B.1: Light curve variability statistics derived via priorized fitting at the positions of the *Swift* GRBs for different monitoring timescales. Quoted are the modulation index (m), the de-biased modulation index (m_d), and the probability of being a non-variable source (p_val; see Section 3.4.1).

GRB	ROI	Timescale	Expected false transients above 6σ	Expected false transients in GRB ROI	Detected transients in GRB ROI	Expected false variables in GRB ROI	Detected variables in GRB ROI
170827B	$\sim 2 \times 10^4$	2min	3×10^{-4}	1.44	0	0	0
		30s	10^{-3}	0.66	0	1.92	0
		5s	7×10^{-3}	1.68	0	4.14	0
190420.98	$\sim 2 \times 10^5$	2min	2×10^{-3}	0	0	0	0
		30s	8×10^{-3}	0	0	0.97	1
		5s	5×10^{-2}	0.04	1	2.23	1
190712.02	$\sim 4 \times 10^6$	2min	6×10^{-2}	0	0	0	0
		30s	0.24	0	0	0.55	0
		5s	1.44	1.1	1	6.6	5
190804A	$\sim 3 \times 10^6$	2min	3×10^{-2}	0.31	0	0.31	0
		30s	0.12	0.31	0	0	0
		5s	0.72	1.55	2	4.03	4
190903A	$\sim 10^3$	2min	2×10^{-5}	0	0	0.05	0
		30s	8×10^{-5}	0	0	0.07	0
		5s	5×10^{-4}	0.01	0	0.06	0
200325A	~ 50	2min	7×10^{-7}	0	0	0	0
		30s	3×10^{-6}	0	0	0	0
		5s	2×10^{-5}	0	0	0	0
200327A	$\sim 10^4$	2min	2×10^{-4}	0.06	0	0	0
		30s	8×10^{-4}	0.42	0	0.12	0
		5s	5×10^{-3}	1.67	0	0.72	0

Table B.2: The number of detected transients and variables within each *Fermi* GRB ROI on different timescales as output by ROBBIE, which are compared to the expected false positive transient and variable rates as defined in Section 3.4.2.
1: The size of the ROI is in units of synthesised beams;
2: The expected number of false positive transient candidates above 6σ in the ROI that is calculated assuming Gaussian statistics;
3: The expected transient false positive rate in the ROI based on the number of false positive candidates in the MWA 50% primary beam;
4: The detected number of transient candidates in the ROI by ROBBIE;
5: The expected variable false positive rate in the ROI based on the number of false positive candidates in the MWA 50% primary beam;
6: The detected number of variable candidates in the ROI by ROBBIE.

Appendix C

Candidates of dispersed pulse search

In Figure C.1, we provide the candidates output by PRESTO with SNR above 6σ from our dispersed pulse search on the rapid-response MWA VCS observation of GRB 210419A. The candidates found from another set of time series created on the same dataset using (unphysical) negative DM trials are also included for comparison (see Section 4.6.1).

In Figure C.2, we present the distribution of SNRs of all candidates shown in the left panel of Figure C.1. We also plot a histogram for those candidates with $DM > 62\,\mathrm{pc\,cm^{-3}}$ (red points in Figure C.1), which are more likely to originate from cosmological distances (see Section 4.5.1).
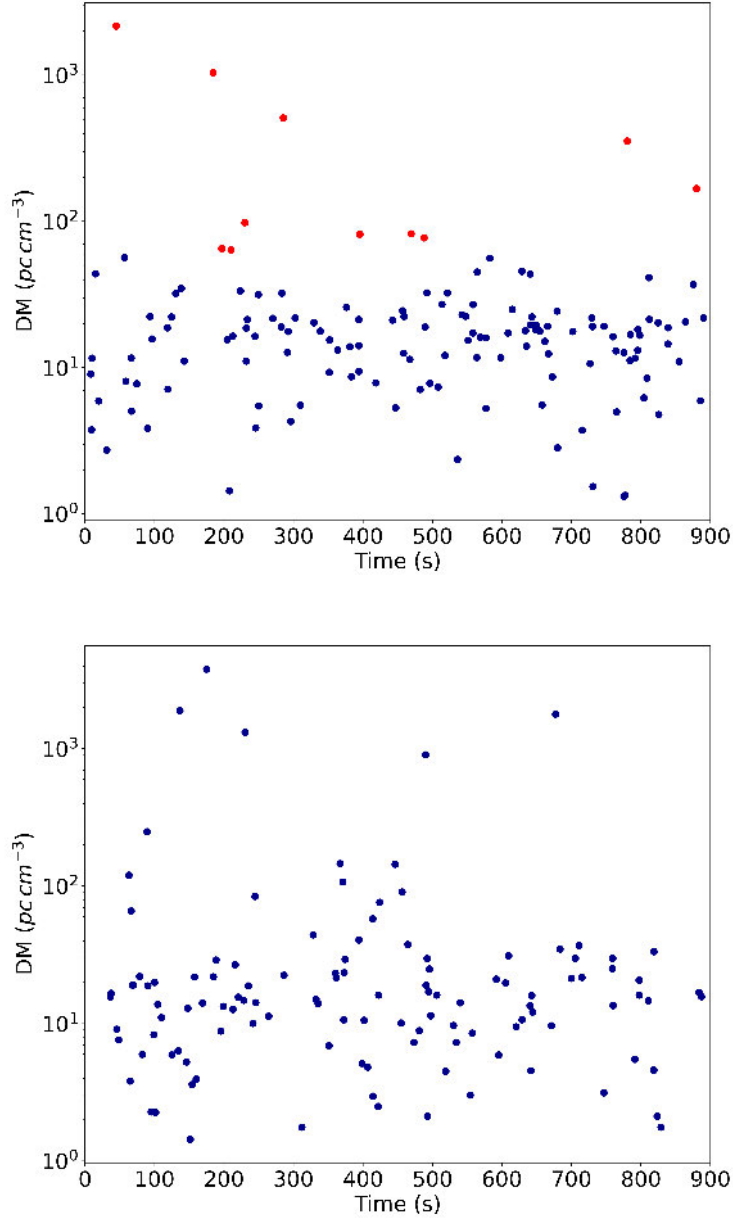
Figure C.1: Single pulse candidates with SNR above 6σ (blue circles) produced by positive (left) and negative (right) DM trials, respectively. The 11 candidates with $DM > 62 \, pc \, cm^{-3}$ are marked with red colors.
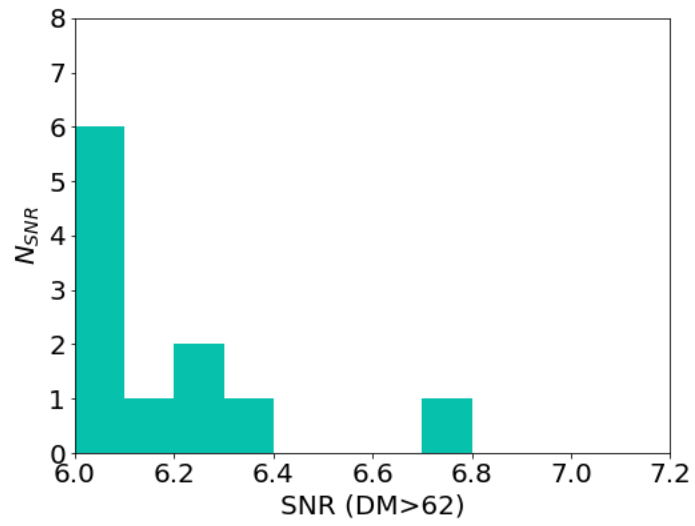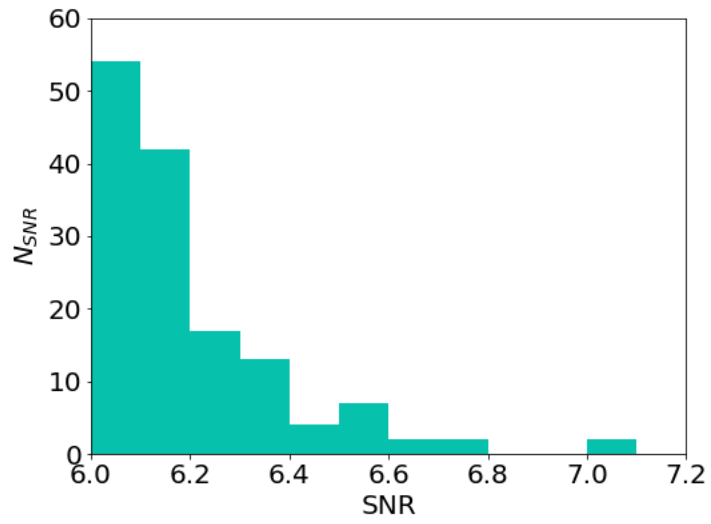
Figure C.2: Distribution of SNRs of all candidates above 6σ (left) and those with $\mathrm{DM} > 62\,\mathrm{pc\,cm^{-3}}$ (right), respectively.

Appendix D

The brightest pulse detected from the Crab pulsar with the MWA observation

In Figure D.1, we present the dynamic spectrum of the brightest pulse detected from the Crab pulsar with an MWA observation (Obs ID: 1165246816) at a DM of $56.76\,\mathrm{pc\,cm^{-3}}$, S/N of 21.84 and time since the observation start of $319.59\,\mathrm{s}$ (see Section 4.5.1).
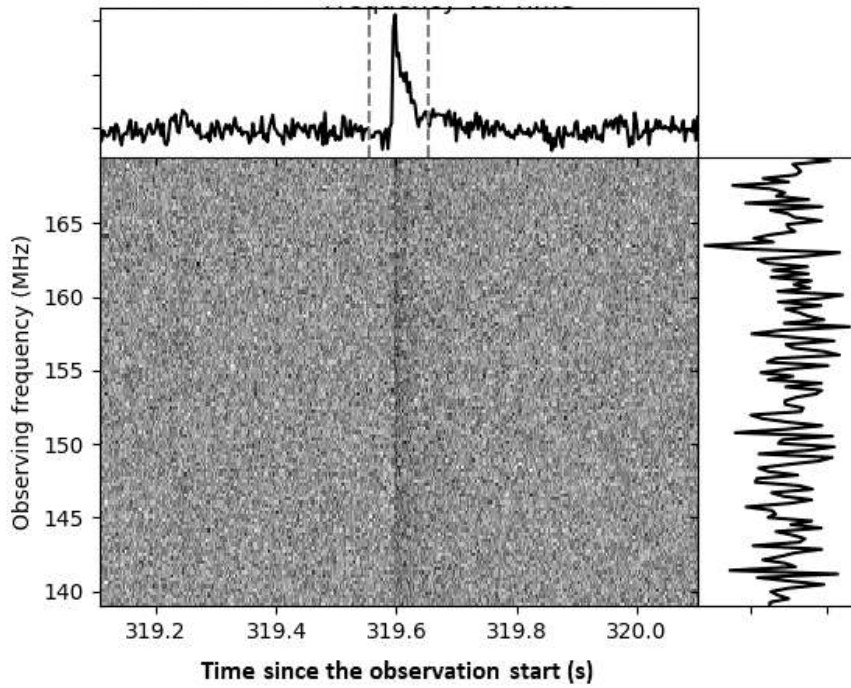
Figure D.1: The dynamic spectrum of the brightest pulse detected with an MWA observation from the Crab pulsar. Data have been dedispersed to a DM of $56.76\,\mathrm{pc\,cm^{-3}}$. The dynamic spectrum has been averaged to a time resolution of $3\,\mathrm{ms}$ and a frequency resolution of $0.24\,\mathrm{MHz}$. The frequency-averaged pulse profile is shown on the top panel (between the two vertical dashed lines), and the time-averaged spectrum is shown on the right panel.

Appendix E

Acknowledgement of facilities and funding

cipient of an Australian Research Council Future Fellowship (project number FT140101082) funded by the Australian Government.

Appendix F

Copyright Information

F.1 Table of Attribution

To Whom It May Concern

I, Jun Tian, have outlined in the table below the contribution of the co-author to Chapter 3 of this thesis, "Early-time Searches for Coherent Radio Emission from Short GRBs with the Murchison Widefield Array", which is a reproduction of an already published work by Tian et al. 2022 (Publications of the Astronomical Society of Australia, Volume 39, article id. e003, DOI: https://doi.org/10.1017/pasa.2021.58).

	Conception & Design	Acquisition of Data & Method	Data Conditioning & Manipulation	Analysis & Statistical Method	Interpretation & Discussion
G. E. Anderson	✓	✓	✓	✓	✓
G. E. Anderson Acknowledgement: I acknowledge that these represent my contribution to the above research output and I have approved the final version. Signed:					

I, Jun Tian, have outlined in the table below the contribution of the co-author to Chapter 4 of this thesis, "High time resolution search for prompt radio emission from the long GRB 210419A with the Murchison Widefield Array", which is a reproduction of an already published work by Tian et al. 2022 (accepted in Monthly Notices of the Royal Astronomical Society, DOI: https://academic.oup.com/mnras/advance-article-abstract/doi/10.1093/mnras/stac1483/6595331).

	Conception & Design	Acquisition of Data & Method	Data Conditioning & Manipulation	Analysis & Statistical Method	Interpretation & Discussion
G. E. Anderson	✓	✓	✓	✓	✓
G. E. Anderson Acknowledgement: I acknowledge that these represent my contribution to the above research output and I have approved the final version. Signed:					

I, Jun Tian, have outlined in the table below the contribution of the co-author to Chapter 5 of this thesis, "A targeted search for repeating fast radio bursts with the MWA" (Monthly Notices of the Royal Astronomical Society, Volume 518, pp 4278-4289, DOI: https://doi.org/10.1093/mnras/stac3392).

	Conception & Design	Acquisition of Data & Method	Data Conditioning & Manipulation	Analysis & Statistical Method	Interpretation & Discussion
G. E. Anderson:	✓	✓	✓	✓	✓
G. E. Anderson Acknowledgement: I acknowledge that these represent my contribution to the above research output and I have approved the final version.					
Signed:					

To Whom It May Concern

I, Jun Tian, have outlined in the table below the contribution of the co-author to Chapter 3 of this thesis, "Early-time Searches for Coherent Radio Emission from Short GRBs with the Murchison Widefield Array", which is a reproduction of an already published work by Tian et al. 2022 (Publications of the Astronomical Society of Australia, Volume 39, article id. e003, DOI: https://doi.org/10.1017/pasa.2021.58).

	Conception & Design	Acquisition of Data & Method	Data Conditioning & Manipulation	Analysis & Statistical Method	Interpretation & Discussion
P. J. Hancock	✓	✓	✓	✓	✓
P. J. Hancock Acknowledgement: I acknowledge that these represent my contribution to the above research output and I have approved the final version. Signed: ███████					

I, Jun Tian, have outlined in the table below the contribution of the co-author to Chapter 4 of this thesis, "High time resolution search for prompt radio emission from the long GRB 210419A with the Murchison Widefield Array", which is a reproduction of an already published work by Tian et al. 2022 (accepted in Monthly Notices of the Royal Astronomical Society, DOI: https://academic.oup.com/mnras/advance-article-abstract/doi/10.1093/mnras/stac1483/6595331).

	Conception & Design	Acquisition of Data & Method	Data Conditioning & Manipulation	Analysis & Statistical Method	Interpretation & Discussion
P. J. Hancock	✓	✓	✓	✓	✓
P. J. Hancock Acknowledgement: I acknowledge that these represent my contribution to the above research output and I have approved the final version. Signed: ███████					

I, Jun Tian, have outlined in the table below the contribution of the co-author to Chapter 5 of this thesis, "A targeted search for repeating fast radio bursts with the MWA" (Monthly Notices of the Royal Astronomical Society, Volume 518, pp 4278-4289, DOI: https://doi.org/10.1093/mnras/stac3392).

	Conception & Design	Acquisition of Data & Method	Data Conditioning & Manipulation	Analysis & Statistical Method	Interpretation & Discussion
P. J. Hancock	✓	✓	✓	✓	✓
P. J. Hancock Acknowledgement: I acknowledge that these represent my contribution to the above research output and I have approved the final version. Signed: ███████					

To Whom It May Concern

I, Jun Tian, have outlined in the table below the contribution of the co-author to Chapter 3 of this thesis, "Early-time Searches for Coherent Radio Emission from Short GRBs with the Murchison Widefield Array", which is a reproduction of an already published work by Tian et al. 2022 (Publications of the Astronomical Society of Australia, Volume 39, article id. e003, DOI: https://doi.org/10.1017/pasa.2021.58).

	Conception & Design	Acquisition of Data & Method	Data Conditioning & Manipulation	Analysis & Statistical Method	Interpretation & Discussion
J. C. A. Miller-Jones	✓	✓		✓	✓
J. C. A. Miller-Jones Acknowledgement: I acknowledge that these represent my contribution to the above research output and I have approved the final version. Signed: ██████					

I, Jun Tian, have outlined in the table below the contribution of the co-author to Chapter 4 of this thesis, "High time resolution search for prompt radio emission from the long GRB 210419A with the Murchison Widefield Array", which is a reproduction of an already published work by Tian et al. 2022 (accepted in Monthly Notices of the Royal Astronomical Society, DOI: https://academic.oup.com/mnras/advance-article-abstract/doi/10.1093/mnras/stac1483/6595331).

	Conception & Design	Acquisition of Data & Method	Data Conditioning & Manipulation	Analysis & Statistical Method	Interpretation & Discussion
J. C. A. Miller-Jones	✓	✓		✓	✓
J. C. A. Miller-Jones Acknowledgement: I acknowledge that these represent my contribution to the above research output and I have approved the final version. Signed: ██████					

I, Jun Tian, have outlined in the table below the contribution of the co-author to Chapter 5 of this thesis, "A targeted search for repeating fast radio bursts with the MWA" (Monthly Notices of the Royal Astronomical Society, Volume 518, pp 4278-4289, DOI: https://doi.org/10.1093/mnras/stac3392).

	Conception & Design	Acquisition of Data & Method	Data Conditioning & Manipulation	Analysis & Statistical Method	Interpretation & Discussion
J. C. A. Miller Jones	✓	✓		✓	✓
J. C. A. Miller Jones Acknowledgement: I acknowledge that these represent my contribution to the above research output and I have approved the final version. Signed: ■■■■■					

To Whom It May Concern

I, Jun Tian, have outlined in the table below the contribution of the co-author to Chapter 3 of this thesis, "Early-time Searches for Coherent Radio Emission from Short GRBs with the Murchison Widefield Array", which is a reproduction of an already published work by Tian et al. 2022 (Publications of the Astronomical Society of Australia, Volume 39, article id. e003, DOI: https://doi.org/10.1017/pasa.2021.58).

	Conception & Design	Acquisition of Data & Method	Data Conditioning & Manipulation	Analysis & Statistical Method	Interpretation & Discussion
M. Sokolowski	✓	✓	✓	✓	✓
M. Sokolowski Acknowledgement: I acknowledge that these represent my contribution to the above research output and I have approved the final version. Signed: ███████					

I, Jun Tian, have outlined in the table below the contribution of the co-author to Chapter 4 of this thesis, "High time resolution search for prompt radio emission from the long GRB 210419A with the Murchison Widefield Array", which is a reproduction of an already published work by Tian et al. 2022 (accepted in Monthly Notices of the Royal Astronomical Society, DOI: https://academic.oup.com/mnras/advance-article-abstract/doi/10.1093/mnras/stac1483/6595331).

	Conception & Design	Acquisition of Data & Method	Data Conditioning & Manipulation	Analysis & Statistical Method	Interpretation & Discussion
M. Sokolowski	✓	✓	✓	✓	✓
M. Sokolowski Acknowledgement: I acknowledge that these represent my contribution to the above research output and I have approved the final version. Signed: ███████					

I, Jun Tian, have outlined in the table below the contribution of the co-author to Chapter 5 of this thesis, "A targeted search for repeating fast radio bursts with the MWA" (Monthly A'otices of the Royal Astronomical Society, Volume 518, pp 4278-4289, DOI: https://doi.org/10.1093/mnras/stac3392).

	Conception & Design	Acquisition of Data & Method	Data Conditioning & Manipulation	Analysis & Statistical Method	Interpretation & Discussion
M. Sokolowski	✓	✓	✓	✓	✓
M. Sokolowski Acknowledgement: I acknowledge that these represent my contribution to the above research output and I have approved the 'final' version. Signed: ███████████████					

To Whom It May Concern

I, Jun Tian, have outlined in the table below the contribution of the co-author to Chapter 3 of this thesis, "Early-time Searches for Coherent Radio Emission from Short GRBs with the Murchison Widefield Array", which is a reproduction of an already published work by Tian et al. 2022 (Publications of the Astronomical Society of Australia, Volume 39, article id. e003, DOI: https://doi.org/10.1017/pasa.2021.58).

	Conception & Design	Acquisition of Data & Method	Data Conditioning & Manipulation	Analysis & Statistical Method	Interpretation & Discussion
A. Rowlinson	✓	✓	✓	✓	✓
A. Rowlinson Acknowledgement: I acknowledge that these represent my contribution to the above research output and I have approved the final version. Signed: ███████					

I, Jun Tian, have outlined in the table below the contribution of the co-author to Chapter 4 of this thesis, "High time resolution search for prompt radio emission from the long GRB 210419A with the Murchison Widefield Array", which is a reproduction of an already published work by Tian et al. 2022 (accepted in Monthly Notices of the Royal Astronomical Society, DOI: https://academic.oup.com/mnras/advance-article-abstract/doi/10.1093/mnras/stac1483/6595331).

	Conception & Design	Acquisition of Data & Method	Data Conditioning & Manipulation	Analysis & Statistical Method	Interpretation & Discussion
A. Rowlinson	✓				✓
A. Rowlinson Acknowledgement: I acknowledge that these represent my contribution to the above research output and I have approved the final version. Signed: ███████					

To Whom It May Concern

I, Jun Tian, have outlined in the table below the contribution of the co-author to Chapter 3 of this thesis, "Early-time Searches for Coherent Radio Emission from Short GRBs with the Murchison Widefield Array", which is a reproduction of an already published work by Tian et al. 2022 (Publications of the Astronomical Society of Australia, Volume 39, article id. e003, DOI: https://doi.org/10.1017/pasa.2021.58).

	Conception & Design	Acquisition of Data & Method	Data Conditioning & Manipulation	Analysis & Statistical Method	Interpretation & Discussion
A. Williams	✓	✓			
A. Williams Acknowledgement: I acknowledge that these represent my contribution to the above research output and I have approved the final version. Signed: ███████████████					

I, Jun Tian, have outlined in the table below the contribution of the co-author to Chapter 4 of this thesis, "High time resolution search for prompt radio emission from the long GRB 210419A with the Murchison Widefield Array", which is a reproduction of an already published work by Tian et al. 2022 (accepted in Monthly Notices of the Royal Astronomical Society, DOI: https://academic.oup.com/mnras/advance-article-abstract/doi/10.1093/mnras/stac1483/6595331).

	Conception & Design	Acquisition of Data & Method	Data Conditioning & Manipulation	Analysis & Statistical Method	Interpretation & Discussion
A. Williams	✓	✓			
A. Williams Acknowledgement: I acknowledge that these represent my contribution to the above research output and I have approved the final version. Signed: ███████████████					

To Whom It May Concern

I, Jun Tian, have outlined in the table below the contribution of the co-author to Chapter 3 of this thesis, "Early-time Searches for Coherent Radio Emission from Short GRBs with the Murchison Widefield Array", which is a reproduction of an already published work by Tian et al. 2022 (Publications of the Astronomical Society of Australia, Volume 39, article id. e003, DOI: https://doi.org/10.1017/pasa.2021.58).

	Conception & Design	Acquisition of Data & Method	Data Conditioning & Manipulation	Analysis & Statistical Method	Interpretation & Discussion
J. Morgan		✓	✓	✓	
J. Morgan Acknowledgement: I acknowledge that these represent my contribution to the above research output and I have approved the final version. Signed:					

I, Jun Tian, have outlined in the table below the contribution of the co-author to Chapter 4 of this thesis, "High time resolution search for prompt radio emission from the long GRB 210419A with the Murchison Widefield Array", which is a reproduction of an already published work by Tian et al. 2022 (accepted in Monthly Notices of the Royal Astronomical Society, DOI: https://academic.oup.com/mnras/advance-article-abstract/doi/10.1093/mnras/stac1483/6595331).

	Conception & Design	Acquisition of Data & Method	Data Conditioning & Manipulation	Analysis & Statistical Method	Interpretation & Discussion
J. Morgan		✓	✓	✓	
J. Morgan Acknowledgement: I acknowledge that these represent my contribution to the above research output and I have approved the final version. Signed:					

To Whom It May Concern

I, Jun Tian, have outlined in the table below the contribution of the co-author to Chapter 3 of this thesis, "Early-time Searches for Coherent Radio Emission from Short GRBs with the Murchison Widefield Array", which is a reproduction of an already published work by Tian et al. 2022 (Publications of the Astronomical Society of Australia, Volume 39, article id. e003, DOI: https://doi.org/10.1017/pasa.2021.58).

	Conception & Design	Acquisition of Data & Method	Data Conditioning & Manipulation	Analysis & Statistical Method	Interpretation & Discussion
N. Hurley-Walker		✓	✓	✓	
N. Hurley-Walker Acknowledgement: I acknowledge that these represent my contribution to the above research output and I have approved the final version. Signed: ██████████					

I, Jun Tian, have outlined in the table below the contribution of the co-author to Chapter 4 of this thesis, "High time resolution search for prompt radio emission from the long GRB 210419A with the Murchison Widefield Array", which is a reproduction of an already published work by Tian et al. 2022 (accepted in Monthly Notices of the Royal Astronomical Society, DOI: https://academic.oup.com/mnras/advance-article-abstract/doi/10.1093/mnras/stac1483/6595331).

	Conception & Design	Acquisition of Data & Method	Data Conditioning & Manipulation	Analysis & Statistical Method	Interpretation & Discussion
N. Hurley-Walker		✓	✓	✓	
N. Hurley-Walker Acknowledgement: I acknowledge that these represent my contribution to the above research output and I have approved the final version. Signed: ██████████					

To Whom It May Concern

I, Jun Tian, have outlined in the table below the contribution of the co-author to Chapter 3 of this thesis, "Early-time Searches for Coherent Radio Emission from Short GRBs with the Murchison Widefield Array", which is a reproduction of an already published work by Tian et al. 2022 (Publications of the Astronomical Society of Australia, Volume 39, article id. e003, DOI: https://doi.org/10.1017/pasa.2021.58).
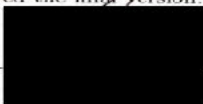
	Conception & Design	Acquisition of Data & Method	Data Conditioning & Manipulation	Analysis & Statistical Method	Interpretation & Discussion
D. L. Kaplan	✓	✓		✓	✓
D. L. Kaplan Acknowledgement: I acknowledge that these represent my contribution to the above research output and I have approved the final version. Signed: ███████					

I, Jun Tian, have outlined in the table below the contribution of the co-author to Chapter 4 of this thesis, "High time resolution search for prompt radio emission from the long GRB 210419A with the Murchison Widefield Array", which is a reproduction of an already published work by Tian et al. 2022 (accepted in Monthly Notices of the Royal Astronomical Society, DOI: https://academic.oup.com/mnras/advance-article-abstract/doi/10.1093/mnras/stac1483/6595331).

	Conception & Design	Acquisition of Data & Method	Data Conditioning & Manipulation	Analysis & Statistical Method	Interpretation & Discussion
D. L. Kaplan	✓	✓		✓	✓
D. L. Kaplan Acknowledgement: I acknowledge that these represent my contribution to the above research output and I have approved the final version. Signed: ███████					

To Whom It May Concern

I, Jun Tian, have outlined in the table below the contribution of the co-author to Chapter 3 of this thesis, "Early-time Searches for Coherent Radio Emission from Short GRBs with the Murchison Widefield Array", which is a reproduction of an already published work by Tian et al. 2022 (Publications of the Astronomical Society of Australia, Volume 39, article id. e003, DOI: https://doi.org/10.1017/pasa.2021.58).

	Conception & Design	Acquisition of Data & Method	Data Conditioning & Manipulation	Analysis & Statistical Method	Interpretation & Discussion
Tara Murphy	✓	✓	✓	✓	
Tara Murphy Acknowledgement: I acknowledge that these represent my contribution to the above research output and I have approved the final version. Signed:				3rd June 2022	

To Whom It May Concern

I, Jun Tian, have outlined in the table below the contribution of the co-author to Chapter 3 of this thesis, "Early-time Searches for Coherent Radio Emission from Short GRBs with the Murchison Widefield Array", which is a reproduction of an already published work by Tian et al. 2022 (Publications of the Astronomical Society of Australia, Volume 39, article id. e003, DOI: https://doi.org/10.1017/pasa.2021.58).

	Conception & Design	Acquisition of Data & Method	Data Conditioning & Manipulation	Analysis & Statistical Method	Interpretation & Discussion
S. J. Tingay	✓	✓			✓
S. J. Tingay Acknowledgement: I acknowledge that these represent my contribution to the above research output and I have approved the final version. Signed: ███████████					

I, Jun Tian, have outlined in the table below the contribution of the co-author to Chapter 4 of this thesis, "High time resolution search for prompt radio emission from the long GRB 210419A with the Murchison Widefield Array", which is a reproduction of an already published work by Tian et al. 2022 (accepted in Monthly Notices of the Royal Astronomical Society, DOI: https://academic.oup.com/mnras/advance-article-abstract/doi/10.1093/mnras/stac1483/6595331).

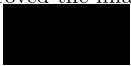|	Conception & Design	Acquisition of Data & Method	Data Conditioning & Manipulation	Analysis & Statistical Method	Interpretation & Discussion
S. J. Tingay	✓	✓			✓
S. J. Tingay Acknowledgement: I acknowledge that these represent my contribution to the above research output and I have approved the final version. Signed: ███████████					

To Whom It May Concern

I, Jun Tian, have outlined in the table below the contribution of the co-author to Chapter 3 of this thesis, "Early-time Searches for Coherent Radio Emission from Short GRBs with the Murchison Widefield Array", which is a reproduction of an already published work by Tian et al. 2022 (Publications of the Astronomical Society of Australia, Volume 39, article id. e003, DOI: https://doi.org/10.1017/pasa.2021.58).

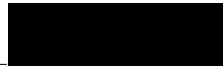|	Conception & Design	Acquisition of Data & Method	Data Conditioning & Manipulation	Analysis & Statistical Method	Interpretation & Discussion
M. Johnston-Hollitt	✓	✓			
M. Johnston-Hollitt Acknowledgement: I acknowledge that these represent my contribution to the above research output and I have approved the final version.					
Signed: ████████ 20 June 2022					

To Whom It May Concern

I, Jun Tian, have outlined in the table below the contribution of the co-author to Chapter 3 of this thesis, "Early-time Searches for Coherent Radio Emission from Short GRBs with the Murchison Widefield Array", which is a reproduction of an already published work by Tian et al. 2022 (Publications of the Astronomical Society of Australia, Volume 39, article id. e003, DOI: https://doi.org/10.1017/pasa.2021.58).
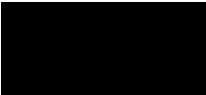
	Conception & Design	Acquisition of Data & Method	Data Conditioning & Manipulation	Analysis & Statistical Method	Interpretation & Discussion
K. W. Bannister	✓	✓			
K. W. Bannister Acknowledgement: I acknowledge that these represent my contribution to the above research output and I have approved the final version. Signed:					

I, Jun Tian, have outlined in the table below the contribution of the co-author to Chapter 4 of this thesis, "High time resolution search for prompt radio emission from the long GRB 210419A with the Murchison Widefield Array", which is a reproduction of an already published work by Tian et al. 2022 (accepted in Monthly Notices of the Royal Astronomical Society, DOI: https://academic.oup.com/mnras/advance-article-abstract/doi/10.1093/mnras/stac1483/6595331).

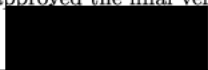|	Conception & Design	Acquisition of Data & Method	Data Conditioning & Manipulation	Analysis & Statistical Method	Interpretation & Discussion
K. W. Bannister	✓	✓			
K. W. Bannister Acknowledgement: I acknowledge that these represent my contribution to the above research output and I have approved the final version. Signed:					

To Whom It May Concern

I, Jun Tian, have outlined in the table below the contribution of the co-author to Chapter 3 of this thesis, "Early-time Searches for Coherent Radio Emission from Short GRBs with the Murchison Widefield Array", which is a reproduction of an already published work by Tian et al. 2022 (Publications of the Astronomical Society of Australia, Volume 39, article id. e003, DOI:).

	Conception & Design	Acquisition of Data & Method	Data Conditioning & Manipulation	Analysis & Statistical Method	Interpretation & Discussion
M. E. Bell	✓	✓			
M. E. Bell Acknowledgement: I acknowledge that these represent my contribution to the above research output and I have approved the final version. Signed: ████████					

I, Jun Tian, have outlined in the table below the contribution of the co-author to Chapter 4 of this thesis, "High time resolution search for prompt radio emission from the long GRB 210419A with the Murchison Widefield Array", which is a reproduction of an already published work by Tian et al. 2022 (accepted in Monthly Notices of the Royal Astronomical Society, DOI:).

	Conception & Design	Acquisition of Data & Method	Data Conditioning & Manipulation	Analysis & Statistical Method	Interpretation & Discussion
M. E. Bell	✓	✓			
M. E. Bell Acknowledgement: I acknowledge that these represent my contribution to the above research output and I have approved the final version. Signed: ████████					

To Whom It May Concern

I, Jun Tian, have outlined in the table below the contribution of the co-author to Chapter 3 of this thesis, "Early-time Searches for Coherent Radio Emission from Short GRBs with the Murchison Widefield Array", which is a reproduction of an already published work by Tian et al. 2022 (Publications of the Astronomical Society of Australia, Volume 39, article id. e003, DOI: https://doi.org/10.1017/pasa.2021.58).

	Conception & Design	Acquisition of Data & Method	Data Conditioning & Manipulation	Analysis & Statistical Method	Interpretation & Discussion
B. W. Meyers	✓	✓	✓	✓	
B. W. Meyers Acknowledgement: I acknowledge that these represent my contribution to the above research output and I have approved the final version. Signed: ███ 02 June 2022					

I, Jun Tian, have outlined in the table below the contribution of the co-author to Chapter 4 of this thesis, "High time resolution search for prompt radio emission from the long GRB 210419A with the Murchison Widefield Array", which is a reproduction of an already published work by Tian et al. 2022 (accepted in Monthly Notices of the Royal Astronomical Society, DOI: https://academic.oup.com/mnras/advance-article-abstract/doi/10.1093/mnras/stac1483/6595331).

	Conception & Design	Acquisition of Data & Method	Data Conditioning & Manipulation	Analysis & Statistical Method	Interpretation & Discussion
B. W. Meyers	✓	✓	✓	✓	
B. W. Meyers Acknowledgement: I acknowledge that these represent my contribution to the above research output and I have approved the final version. Signed: ███ 02 June 2022					

To Whom It May Concern

I, Jun Tian, have outlined in the table below the contribution of the co-author to Chapter 4 of this thesis, "High time resolution search for prompt radio emission from the long GRB 210419A with the Murchison Widefield Array", which is a re production of an already published work by Tian et al. 2022 (accepted in Monthly Notices of the Royal Astronomical Society, DOI: https://academic.oup.com/ mnras/advance-article-abstract/doi/10.1093/mnras/stac1483/6595331).

	Concept ion & Design	Acquisition of Data & Method	Data Conditioning & Manipulation	Analysis & Statistical Method	Interpretati on & Discussion
N. A. Swainston		X	X	X	
N. A. Swainston Acknowledgement: I acknowledge that these represent my contribution to the above research output and I have approved the final version. Signed: ▉					

I, Jun Tian, have outlined in the table below the contribution of the co-author to Chapter 5 of this thesis, "A targeted search for repeating fast

radio bursts with the MWA" (Monthly Notices of the Royal Astronomical Society, Volume 518, pp 4278-4289, DOI: https://doi.org/10.1093/mnras/stac3392).

	Concept ion & Design	Acquisition of Data & Method	Data Conditioning & Manipulation	Analysis & Statistical Method	Interpretati on & Discussion
N. A. Swainston		X	X	X	
N. A. Swainston Acknowledgement: I acknowledge that these represent my contribution to the above research output and I have approved the final version. Signed: ███					

To Whom It May Concern

I, Jun Tian, have outlined in the table below the contribution of the co-author to Chapter 4 of this thesis, "High time resolution search for prompt radio emission from the long GRB 210419A with the Murchison Widefield Array", which is a re-production of an already published work by Tian et al. 2022 (accepted in Monthly Notices of the Royal Astronomical Society, DOI: https://academic.oup.com/mnras/advance-article-abstract/doi/10.1093/mnras/stac1483/6595331).
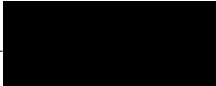
	Conception & Design	Acquisition of Data & Method	Data Conditioning & Manipulation	Analysis & Statistical Method	Interpretation & Discussion
N. D. R. Bhat		✓	✓	✓	
N. D. R. Bhat Acknowledgement: I acknowledge that these represent my contribution to the above research output and I have approved the final version. Signed: ███████████					

I, Jun Tian, have outlined in the table below the contribution of the co-author to Chapter 5 of this thesis, "A targeted search for repeating fast radio bursts with the MWA" (Monthly Notices of the Royal Astronomical Society, Volume 518, pp 4278-4289, DOI: https://doi.org/10.1093/mnras/stac3392).
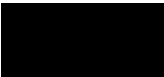
	Conception & Design	Acquisition of Data & Method	Data Conditioning & Manipulation	Analysis & Statistical Method	Interpretation & Discussion
N. D. R. Bhat		✓	✓	✓	
N. D. R. Bhat Acknowledgement: I acknowledge that these represent my contribution to the above research output and I have approved the final version. Signed: ███████████					

To Whom It May Concern

I, Jun Tian, have outlined in the table below the contribution of the co-author to Chapter 4 of this thesis, "High time resolution search for prompt radio emission from the long GRB 210419A with the Murchison Widefield Array", which is a reproduction of an already published work by Tian et al. 2022 (accepted in Monthly Notices of the Royal Astronomical Society, DOI:).

	Conception & Design	Acquisition of Data & Method	Data Conditioning & Manipulation	Analysis & Statistical Method	Interpretation & Discussion
D. Ung		✓	✓	✓	
D. Ung Acknowledgement: I acknowledge that these represent my contribution to the above research output and I have approved the final version. Signed: ███					

To Whom It May Concern

I, Jun Tian, have outlined in the table below the contribution of the co-author to Chapter 4 of this thesis, "High time resolution search for prompt radio emission from the long GRB 210419A with the Murchison Widefield Array", which is a reproduction of an already published work by Tian et al. 2022 (accepted in Monthly Notices of the Royal Astronomical Society, DOI: https://academic.oup.com/mnras/advance-article-abstract/doi/10.1093/mnras/stac1483/6595331).

	Conception & Design	Acquisition of Data & Method	Data Conditioning & Manipulation	Analysis & Statistical Method	Interpretation & Discussion
M. Walker	✓	✓			
M. Walker Acknowledgement: I acknowledge that these represent my contribution to the above research output and I have approved the final version. Signed:					

To Whom It May Concern

I, Jun Tian, have outlined in the table below the contribution of the co-author to Chapter 5 of this thesis, "A targeted search for repeating fast radio bursts with the MWA" (Monthly Notices of the Royal Astronomical Society, Volume 518, pp 4278-4289, DOI, https://doi.org/10.1093/mnras/stac3392).

	Conception & Design	Acquisition of Data & Method	Data Conditioning & Manipulation	Analysis & Statistical Method	Interpretation & Discussion
C. W. James					✓
C. W. James Acknowledgement: I acknowledge that these represent my contribution to the above research output and I have approved the final version. Signed: ███████████████████████████					

Bibliography

B. P. Abbott, et al. (2016a). 'Observation of Gravitational Waves from a Binary Black Hole Merger'. **116**(6):061102.

B. P. Abbott, et al. (2016b). 'GW151226: Observation of Gravitational Waves from a 22-Solar-Mass Binary Black Hole Coalescence'. **116**(24):241103.

B. P. Abbott, et al. (2020a). 'GW190425: Observation of a Compact Binary Coalescence with Total Mass $\sim$ 3.4 M$_\odot$'. *The Astrophysical Journal Letters* **892**(1):L3.

B. P. Abbott, et al. (2019). 'GWTC-1: A Gravitational-Wave Transient Catalog of Compact Binary Mergers Observed by LIGO and Virgo during the First and Second Observing Runs'. *Physical Review X* **9**(3):031040.

B. P. Abbott, et al. (2020b). 'Prospects for observing and localizing gravitational-wave transients with Advanced LIGO, Advanced Virgo and KAGRA'. *Living Reviews in Relativity* **23**(1):3.

B. P. Abbott, et al. (2017). 'GW170817: Observation of Gravitational Waves from a Binary Neutron Star Inspiral'. **119**(16):161101.
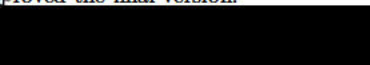
B. P. Abbott et al. (2017). 'Gravitational Waves and Gamma-Rays from a Binary Neutron Star Merger: GW170817 and GRB 170817A'. *The Astrophysical Journal Letter* **848**(2):L13.

B. P. Abbott et al. (2018). 'GW170817: Measurements of Neutron Star Radii and Equation of State'. *Physical Review Letter* **121**(2):161101.

A. A. Abdo, et al. (2009a). 'A limit on the variation of the speed of light arising from quantum gravity effects'. *Nature* **462**(7271):331–334.

A. A. Abdo, et al. (2009b). 'Fermi Observations of High-Energy Gamma-Ray Emission from GRB 080916C'. *Science* **323**(5922):1688.

M. Ackermann, et al. (2011). 'Detection of a Spectral Break in the Extra Hard Component of GRB 090926A'. *The Astrophysical Journal* **729**(2):114.

M. Ackermann, et al. (2010). 'Fermi Observations of GRB 090510: A Short-Hard Gamma-ray Burst with an Additional, Hard Power-law Component from 10 keV TO GeV Energies'. *The Astrophysical Journal* **716**(2):1178–1190.

K. Aggarwal (2021). 'Observational Effects of Banded Repeating FRBs'. *The Astrophysical Journal Letters* **920**(1):L18.

T. Ahumada, et al. (2021). 'Discovery and confirmation of the shortest gamma ray burst from a collapsar'. *arXiv e-prints* p. arXiv:2105.05067.

K. Akiyama, et al. (2022a). 'First Sagittarius A* Event Horizon Telescope Results. I. The Shadow of the Supermassive Black Hole in the Center of the Milky Way'. *The Astrophysical Journal Letters* **930**(2):L12.

K. Akiyama, et al. (2022b). 'First Sagittarius A* Event Horizon Telescope Results. II. EHT and Multiwavelength Observations, Data Processing, and Calibration'. *The Astrophysical Journal Letters* **930**(2):L13.

K. Akiyama, et al. (2022c). 'First Sagittarius A* Event Horizon Telescope Results. III. Imaging of the Galactic Center Supermassive Black Hole'. *The Astrophysical Journal Letters* **930**(2):L14.

K. Akiyama, et al. (2022d). 'First Sagittarius A* Event Horizon Telescope Results. IV. Variability, Morphology, and Black Hole Mass'. *The Astrophysical Journal Letters* **930**(2):L15.

M. Amiri, et al. (2021). 'The First CHIME/FRB Fast Radio Burst Catalog'. *The Astrophysical Journal Supplement Series* **257**(2):59.

G. E. Anderson, et al. (2021a). 'Rapid-response radio observations of short GRB 181123B with the Australia Telescope Compact Array'. *Monthly Notices of the Royal Astronomical Society* **503**(3):4372–4386.

G. E. Anderson, et al. (2021b). 'Murchison Widefield Array rapid-response observations of the short GRB 180805A'. *Publications of the Astronomical Society of Australia* **38**:e026.

G. E. Anderson, et al. (2018a). 'The Arcminute Microkelvin Imager catalogue of gamma-ray burst afterglows at 15.7 GHz'. *Monthly Notices of the Royal Astronomical Society* **473**(2):1512–1536.

G. E. Anderson, et al. (2014). 'Probing the bright radio flare and afterglow of GRB 130427A with the Arcminute Microkelvin Imager'. *Monthly Notices of the Royal Astronomical Society* **440**(3):2059–2065.

M. M. Anderson, et al. (2018b). 'A Simultaneous Search for Prompt Radio Emission Associated with the Short GRB 170112A Using the All-sky Imaging Capability of the OVRO-LWA'. *The Astrophysical Journal* **864**(1):22.

K. Asano, et al. (2009). 'Hadronic Models for the Extra Spectral Component in the Short GRB 090510'. *The Astrophysical Journal Letters* **705**(2):L191–L194.

L. Asquini, et al. (2019). 'X-ray absorbing column densities of a complete sample of short gamma ray bursts'. *Astronomy and Astrophysics* **625**:A6.

R. Athreya (2009). 'A New Approach to Mitigation of Radio Frequency Interference in Interferometric Data'. *The Astrophysical Journal* **696**(1):885–890.

W. B. Atwood, et al. (2009). 'The Large Area Telescope on the Fermi Gamma-Ray Space Telescope Mission'. *The Astrophysical Journal* **697**(2):1071–1102.

G. A. Baird, et al. (1975). 'A search for VHF radio pulses in coincidence with celestial gamma-ray bursts.'. *The Astrophysical Journal Letters* **196**:L11–L13.

C. A. Balanis (2005). *Antenna theory: analysis and design.*

K. W. Bannister, et al. (2019). 'A single fast radio burst localized to a massive galaxy at cosmological distance'. *Science* **365**(6453):565–570.

K. W. Bannister et al. (2017). 'ON THE DETECTABILITY OF PROMPT COHERENT GAMMA-RAY BURST RADIO EMISSION'. *The Astrophysical Journal Letter* **841**(2):L12.

K. W. Bannister & G. J. Madsen (2014). 'A Galactic origin for the fast radio burst FRB010621'. *Monthly Notices of the Royal Astronomical Society* **440**(1):353–358.

K. W. Bannister, et al. (2012). 'Limits on Prompt, Dispersed Radio Pulses from Gamma-Ray Bursts'. *The Astrophysical Journal* **757**(1):38.

K. W. Bannister, et al. (2017). 'The Detection of an Extremely Bright Fast Radio Burst in a Phased Array Feed Survey'. *The Astrophysical Journal Letters* **841**(1):L12.

C. Barnbaum & R. F. Bradley (1998). 'A New Approach to Interference Excision in Radio Astronomy: Real-Time Adaptive Cancellation'. *The Astronomical Journal* **116**(5):2598–2614.

A. Barrau, et al. (2014). 'Fast radio bursts and white hole signals'. **90**(12):127503.

S. D. Barthelmy, et al. (2005a). 'The Burst Alert Telescope (BAT) on the SWIFT Midex Mission'. *Space Science Reviews* **120**(3-4):143–164.

S. D. Barthelmy, et al. (2005b). 'An origin for short γ-ray bursts unassociated with current star formation'. *Nature* **438**(7070):994–996.

S. D. Barthelmy, et al. (2019). 'GRB 190627A: Swift-BAT refined analysis (short-soft burst).'. *GRB Coordinates Network* **24899**:1.

C. G. Bassa, et al. (2017). 'FRB 121102 Is Coincident with a Star-forming Region in Its Host Galaxy'. *The Astrophysical Journal Letters* **843**(1):L8.

S. D. Bates, et al. (2013). 'The pulsar spectral index distribution'. *Monthly Notices of the Royal Astronomical Society* **431**(2):1352–1358.

A. P. Beardmore, et al. (2021). 'GRB 210419A: Swift-XRT refined Analysis'. *GRB Coordinates Network* **29835**:1.

D. Bégué & A. Pe'er (2015). 'Poynting-flux-dominated Jets Challenged by their Photospheric Emission'. *The Astrophysical Journal* **802**(2):134.

K. Belczynski, et al. (2010). 'On the Origin of the Highest Redshift Gamma-Ray Bursts'. *The Astrophysical Journal* **708**(1):117–126.

M. E. Bell, et al. (2019). 'The Murchison Widefield Array Transients Survey (MWATS). A search for low-frequency variability in a bright Southern hemisphere sample'. *Monthly Notices of the Royal Astronomical Society* **482**(2):2484–2501.

A. M. Beloborodov (2017). 'ON THE DETECTABILITY OF PROMPT COHERENT GAMMA-RAY BURST RADIO EMISSION'. *The Astrophysical Journal Letter* **843**(2):L26.

A. M. Beloborodov (2020). 'Blast Waves from Magnetar Flares and Fast Radio Bursts'. *The Astrophysical Journal* **896**(2):142.

P. Beniamini & E. Nakar (2019). 'Observational constraints on the structure of gamma-ray burst jets'. *Monthly Notices of the Royal Astronomical Society* **482**(4):5430–5440.

P. Beniamini, et al. (2020). 'Periodicity in recurrent fast radio bursts and the origin of ultralong period magnetars'. *Monthly Notices of the Royal Astronomical Society* **496**(3):3390–3401.

E. Berger (2009). 'The Host Galaxies of Short-Duration Gamma-Ray Bursts: Luminosities, Metallicities, and Star-Formation Rates'. *The Astrophysical Journal* **690**(1):231–237.

E. Berger (2014). 'Short-Duration Gamma-Ray Bursts'. *Annual Review of Astronomy and Astrophysics* **52**:43–105.

E. Berger, et al. (2013). 'An r-process Kilonova Associated with the Short-hard GRB 130603B'. *The Astrophysical Journal Letters* **774**(2):L23.

E. Berger, et al. (2005). 'Afterglows, Redshifts, and Properties of Swift Gamma-Ray Bursts'. *The Astrophysical Journal* **634**(1):501–508.

M. G. Bernardini, et al. (2011). 'Gamma-ray burst long lasting X-ray flaring activity'. *Astronomy and Astrophysics* **526**:A27.

M. G. Bernardini, et al. (2012). 'The X-ray light curve of gamma-ray bursts: clues to the central engine'. *Astronomy and Astrophysics* **539**:A3.

S. Bethapudi, et al. (2022). 'High frequency study of FRB 20180916B using the 100-m Effelsberg radio telescope'. *arXiv e-prints* p. arXiv:2207.13669.

N. D. R. Bhat, et al. (2004). 'Multifrequency Observations of Radio Pulse Broadening and Constraints on Interstellar Electron Density Microstructure'. *The Astrophysical Journal* **605**(2):759–783.

N. D. R. Bhat et al. (2022). 'The Southern-sky MWA Rapid Two-meter (SMART) survey'. In preparation.

N. D. R. Bhat, et al. (2016). 'Scintillation Arcs in Low-frequency Observations of the Timing-array Millisecond Pulsar PSR J0437-4715'. *The Astrophysical Journal* **818**(1):86.

246

N. D. R. Bhat, et al. (2014). 'The Low-frequency Characteristics of PSR J0437-4715 Observed with the Murchison Wide-field Array'. *The Astrophysical Journal Letters* **791**(2):L32.

S. Bhattacharyya, et al. (2021). 'A maximum likelihood estimate of the parameters of the FRB population'. *Monthly Notices of the Royal Astronomical Society* .

A. V. Bilous, et al. (2016). 'A LOFAR census of non-recycled pulsars: average profiles, dispersion measures, flux densities, and spectra'. *Astronomy and Astrophysics* **591**:A134.

C. H. Blake, et al. (2005). 'An infrared flash contemporaneous with the γ-rays of GRB 041219a'. *Nature* **435**(7039):181–184.

R. D. Blandford & R. L. Znajek (1977). 'Electromagnetic extraction of energy from Kerr black holes.'. *Monthly Notices of the Royal Astronomical Society* **179**:433–456.

J. S. Bloom, et al. (2001). 'The Prompt Energy Release of Gamma-Ray Bursts using a Cosmological k-Correction'. *The Astronomical Journal* **121**(6):2879–2888.

C. D. Bochenek, et al. (2020). 'A fast radio burst associated with a Galactic magnetar'. *Nature* **587**(7832):59–62.

P. Bolli (2020). 'Test-Driven Design of an Active Dual-Polarized Log-Periodic Antenna for the Square Kilometre Array'. *IEEE Open Journal of Antennas and Propagation* **1**:253–263.

Ž. Bošnjak, et al. (2009). 'Prompt high-energy emission from gamma-ray bursts in the internal shock model'. *Astronomy and Astrophysics* **498**(3):677–703.

D. S. Briggs (1995). 'High Fidelity Interferometric Imaging: Robust Weighting and NNLS Deconvolution'. In *American Astronomical Society Meeting*

Abstracts, vol. 187 of *American Astronomical Society Meeting Abstracts*, p. 112.02.

F. H. Briggs, et al. (2000). 'Removing Radio Interference from Contaminated Astronomical Spectra Using an Independent Reference Signal and Closure Relations'. *The Astronomical Journal* **120**(6):3351–3361.

N. Bucciantini, et al. (2008). 'Relativistic jets and long-duration gamma-ray bursts from the birth of magnetars'. *Monthly Notices of the Royal Astronomical Society* **383**(1):L25–L29.

N. Bucciantini, et al. (2009). 'Magnetized relativistic jets and long-duration GRBs from magnetar spin-down during core-collapse supernovae'. *Monthly Notices of the Royal Astronomical Society* **396**(4):2038–2050.

S. Burke-Spolaor, et al. (2011). 'The High Time Resolution Universe Pulsar Survey - III. Single-pulse searches and preliminary analysis'. *Monthly Notices of the Royal Astronomical Society* **416**(4):2465–2476.

S. Burke-Spolaor & K. W. Bannister (2014). 'The Galactic Position Dependence of Fast Radio Bursts and the Discovery of FRB011025'. *The Astrophysical Journal* **792**(1):19.

D. N. Burrows, et al. (2005). 'The Swift X-Ray Telescope'. *Space Science Reviews* **120**(3-4):165–195.

N. R. Butler & D. Kocevski (2007). 'X-Ray Hardness Evolution in GRB Afterglows and Flares: Late-Time GRB Activity without N_H Variations'. *The Astrophysical Journal* **663**(1):407–419.

M. Caleb et al. (2017). 'Searches for prompt radio emission at 151 MHz from the gamma-ray bursts GRB 950430 and GRB 950706'. *Monthly Notices of the Royal Astronomical Society* **468**(4):3746.

M. Caleb, et al. (2016). 'Fast Radio Transient searches with UTMOST at 843 MHz'. *Monthly Notices of the Royal Astronomical Society* **458**(1):718–725.

M. Caleb & E. Keane (2021). 'A Decade and a Half of Fast Radio Burst Observations'. *Universe* **7**(11):453.

S. Campana, et al. (2012). 'The X-ray absorbing column density of a complete sample of bright Swift gamma-ray bursts'. *Monthly Notices of the Royal Astronomical Society* **421**(2):1697–1702.

S. Campana, et al. (2006). 'The X-ray afterglow of the short gamma ray burst 050724'. *Astronomy and Astrophysics* **454**(1):113–117.

J. K. Cannizzo, et al. (2011). 'Fall-back Disks in Long and Short Gamma-Ray Bursts'. *The Astrophysical Journal* **734**(1):35.

Z. Cano (2013). 'A new method for estimating the bolometric properties of Ibc supernovae'. *Monthly Notices of the Royal Astronomical Society* **434**(2):1098–1116.

S. B. Cenko, et al. (2019a). 'GRB 191004A: Swift detection of a burst with an optical detection'. *GRB Coordinates Network* **25945**:1.

S. B. Cenko, et al. (2019b). 'GRB 191004A: Swift detection of a burst with an optical detection'. *GRB Coordinates Network* **25945**:1.

D. J. Champion, et al. (2016). 'Five new fast radio bursts from the HTRU high-latitude survey at Parkes: first evidence for two-component bursts'. *Monthly Notices of the Royal Astronomical Society* **460**(1):L30–L34.

P. Chandra & D. A. Frail (2012). 'A Radio-selected Sample of Gamma-Ray Burst Afterglows'. *The Astrophysical Journal* **746**(2):156.

S. Chatterjee et al. (2017). 'Observations of fast radio bursts at frequencies down to 400 megahertz'. *Nature* **541**(2):58.

P. Chawla, et al. (2020). 'Detection of Repeating FRB 180916.J0158+65 Down to Frequencies of 300 MHz'. *The Astrophysical Journal Letters* **896**(2):L41.

W.-X. Chen & A. M. Beloborodov (2007). 'Neutrino-cooled Accretion Disks around Spinning Black Holes'. *The Astrophysical Journal* **657**(1):383–399.

Q. Cheng & Y.-W. Yu (2014). 'How can Newly Born Rapidly Rotating Neutron Stars Become Magnetars?'. *The Astrophysical Journal Letters* **786**(2):L13.

Chime/Frb Collaboration, et al. (2020). 'Periodic activity from a fast radio burst source'. *Nature* **582**(7812):351–355.

CHIME/FRB Collaboration, et al. (2018). 'The CHIME Fast Radio Burst Project: System Overview'. *The Astrophysical Journal* **863**(1):48.

CHIME/FRB Collaboration, et al. (2019a). 'A second source of repeating fast radio bursts'. *Nature* **566**(7743):235–238.

CHIME/FRB Collaboration, et al. (2019b). 'Observations of fast radio bursts at frequencies down to 400 megahertz'. *Nature* **566**(7743):230–234.

CHIME/FRB Collaboration, et al. (2019c). 'CHIME/FRB Discovery of Eight New Repeating Fast Radio Burst Sources'. *The Astrophysical Journal Letters* **885**(1):L24.

CHIME/FRB Collaboration, et al. (2020). 'A bright millisecond-duration radio burst from a Galactic magnetar'. *Nature* **587**(7832):54–58.

Chime/Frb Collabortion (2021). 'Recent high activity from a repeating Fast Radio Burst discovered by CHIME/FRB'. *The Astronomer's Telegram* **14497**:1.

G. Chincarini, et al. (2010). 'Unveiling the origin of X-ray flares in gamma-ray bursts'. *Monthly Notices of the Royal Astronomical Society* **406**(4):2113–2148.

G. Chincarini, et al. (2007). 'The First Survey of X-Ray Flares from Gamma-Ray Bursts Observed by Swift: Temporal Properties and Morphology'. *The Astrophysical Journal* **671**(2):1903–1920.

Q. Chu, et al. (2016). 'Capturing the electromagnetic counterparts of binary neutron star mergers through low-latency gravitational wave triggers'. *Monthly Notices of the Royal Astronomical Society* **459**(1):121–139.

A. J. Cianciara, et al. (2017). 'Simulation and Testing of a Linear Array of Modified Four-Square Feed Antennas for the Tianlai Cylindrical Radio Telescope'. *Journal of Astronomical Instrumentation* **6**(3):1750003–40.

T. Coenen, et al. (2014). 'The LOFAR pilot surveys for pulsars and fast radio transients'. *Astronomy and Astrophysics* **570**:A60.

M. H. Cohen, et al. (1971). 'The Small-Scale Structure of Radio Galaxies and Quasi-Stellar Sources at 3.8 Centimeters'. *The Astrophysical Journal* **170**:207.

J. J. Condon (1974). 'Confusion and Flux-Density Error Distributions'. *The Astrophysical Journal* **188**:279–286.

J. J. Condon & S. M. Ransom (2016). *Essential Radio Astronomy*.

Y. Cong, et al. (2021). 'An Ultralong-wavelength Sky Model with Absorption Effect'. *The Astrophysical Journal* **914**(2):128.

J. M. Cordes & S. Chatterjee (2019). 'Fast Radio Bursts: An Extragalactic Enigma'. *Annual Review of Astronomy and Astrophysics* **57**:417–465.

J. M. Cordes & T. J. W. Lazio (2002). 'NE2001.I. A New Model for the Galactic Distribution of Free Electrons and its Fluctuations'. *arXiv e-prints* pp. astro–ph/0207156.

J. M. Cordes, et al. (2017). 'Lensing of Fast Radio Bursts by Plasma Structures in Host Galaxies'. *The Astrophysical Journal* **842**(1):35.

T. Cornwell (1995). 'Imaging Concepts'. In J. A. Zensus, P. J. Diamond, & P. J. Napier (eds.), *Very Long Baseline Interferometry and the VLBA*, vol. 82 of *Astronomical Society of the Pacific Conference Series*, p. 39.

T. Cornwell & E. B. Fomalont (1999). 'Self-Calibration'. In G. B. Taylor, C. L. Carilli, & R. A. Perley (eds.), *Synthesis Imaging in Radio Astronomy II*, vol. 180 of *Astronomical Society of the Pacific Conference Series*, p. 187.

T. J. Cornwell, et al. (2005). 'W Projection: A New Algorithm for Wide Field Imaging with Radio Synthesis Arrays'. In P. Shopbell, M. Britton, & R. Ebert (eds.), *Astronomical Data Analysis Software and Systems XIV*, vol. 347 of *Astronomical Society of the Pacific Conference Series*, p. 86.

T. J. Cornwell, et al. (2008). 'The Noncoplanar Baselines Effect in Radio Interferometry: The W-Projection Algorithm'. *IEEE Journal of Selected Topics in Signal Processing* **2**(5):647–657.

E. Costa, et al. (1997). 'Discovery of an X-ray afterglow associated with the γ-ray burst of 28 February 1997'. *Nature* **387**(6635):783–785.

D. A. Coulter, et al. (2017). 'Swope Supernova Survey 2017a (SSS17a), the optical counterpart to a gravitational wave source'. *Science* **358**(2):1556.

M. Cruces, et al. (2021). 'Repeating behaviour of FRB 121102: periodicity, waiting times, and energy distribution'. *Monthly Notices of the Royal Astronomical Society* **500**(1):448–463.

G. Cusumano, et al. (2006). 'Swift XRT Observations of the Afterglow of GRB 050319'. *The Astrophysical Journal* **639**(1):316–322.

Z. G. Dai & T. Lu (1998). 'Gamma-ray burst afterglows and evolution of post-burst fireballs with energy injection from strongly magnetic millisecond pulsars'. *Astronomy and Astrophysics* **333**:L87–L90.

Z. G. Dai, et al. (2006). 'X-ray Flares from Postmerger Millisecond Pulsars'. *Science* **311**(5764):1127–1129.

T. Dalton & S. L. Morris (2020). 'Using realistic host galaxy metallicities to improve the GRB X-ray equivalent total hydrogen column density and constrain the intergalactic medium density'. *Monthly Notices of the Royal Astronomical Society* **495**(2):2342–2353.

C. K. Day, et al. (2020). 'High time resolution and polarization properties of ASKAP-localized fast radio bursts'. *Monthly Notices of the Royal Astronomical Society* **497**(3):3335–3350.

A. de Oliveira-Costa, et al. (2008). 'A model of diffuse Galactic radio emission from 10 MHz to 100 GHz'. *Monthly Notices of the Royal Astronomical Society* **388**(1):247–260.

J. DeLaunay, et al. (2020a). 'GRB 200325A: Swift/BAT detection and probable arcminute localization of a short GRB from GUANO'. *GRB Coordinates Network* **27444**:1.

J. DeLaunay, et al. (2020b). 'GRB 200325A: Swift/BAT detection and probable arcminute localization of a short GRB from GUANO'. *GRB Coordinates Network* **27444**:1.

J. J. DeLaunay, et al. (2016). 'Discovery of a Transient Gamma-Ray Counterpart to FRB 131104'. *The Astrophysical Journal Letter* **832**(2):L1.

W. Deng & B. Zhang (2014). 'Cosmological Implications of Fast Radio Burst/Gamma-Ray Burst Associations'. *The Astrophysical Journal Letters* **783**(2):L35.

C. A. C. Dessenne, et al. (1996). 'Searches for prompt radio emission at 151 MHz from the gamma-ray bursts GRB 950430 and GRB 950706.'. *Monthly Notices of the Royal Astronomical Society* **281**(3):977–984.

P. Dewdney et al. (2010). 'SKA Memo 130, SKA Phase 1: Preliminary System Description, www.skatelescope.org/pages/page memos.htm' .

P. E. Dewdney, et al. (2009). 'The Square Kilometre Array'. *IEEE Proceedings* **97**(8):1482–1496.

G. Drenkhahn & H. C. Spruit (2002). 'Efficient acceleration and radiation in Poynting flux powered GRB outflows'. *Astronomy and Astrophysics* **391**:1141–1153.

S. W. Duchesne, et al. (2020). 'Murchison Widefield Array detection of steep-spectrum, diffuse, non-thermal radio emission within Abell 1127'. *Publications of the Astronomical Society of Australia* **37**:e037.

T. Eftekhari, et al. (2018). 'Associating Fast Radio Bursts with Extragalactic Radio Sources: General Methodology and a Search for a Counterpart to FRB 170107'. *The Astrophysical Journal* **860**(1):73.

D. Eichler, et al. (1989). 'Nucleosynthesis, neutrino bursts and γ-rays from coalescing neutron stars'. *Nature* **340**(6229):126–128.

S. W. Ellingson (2005). 'Antennas for the Next Generation of Low-Frequency Radio Telescopes'. *IEEE Transactions on Antennas and Propagation* **53**(8):2480–2489.

P. Esposito, et al. (2020). 'A Very Young Radio-loud Magnetar'. *The Astrophysical Journal Letters* **896**(2):L30.

P. A. Evans, et al. (2009). 'Methods and results of an automatic analysis of a complete sample of Swift-XRT observations of GRBs'. *Monthly Notices of the Royal Astronomical Society* **397**(3):1177–1201.

P. A. Evans, et al. (2017). 'Swift and NuSTAR observations of GW170817: Detection of a blue kilonova'. *Science* **358**(2):1565.

P. A. Evans, et al. (2010). 'The Swift Burst Analyser. I. BAT and XRT spectral and flux evolution of gamma ray bursts'. *Astronomy and Astrophysics* **519**:A102.

H. Falcke & L. Rezzolla (2014). 'Fast radio bursts: the last sign of supramassive neutron stars'. *Astronomy and Astrophysics* **562**:A137.

A. D. Falcone, et al. (2006). 'The Giant X-Ray Flare of GRB 050502B: Evidence for Late-Time Internal Engine Activity'. *The Astrophysical Journal* **641**(2):1010–1017.

A. D. Falcone, et al. (2007). 'The First Survey of X-Ray Flares from Gamma-Ray Bursts Observed by Swift: Spectral Properties and Energetics'. *The Astrophysical Journal* **671**(2):1921–1938.

Y. Z. Fan & D. M. Wei (2005). 'Late internal-shock model for bright X-ray flares in gamma-ray burst afterglows and GRB 011121'. *Monthly Notices of the Royal Astronomical Society* **364**(1):L42–L46.

W. Farah, et al. (2019). 'Five new real-time detections of fast radio bursts with UTMOST'. *Monthly Notices of the Royal Astronomical Society* **488**(3):2989–3002.

R. P. Fender, et al. (2006). 'A transient relativistic radio jet from Cygnus X-1'. *Monthly Notices of the Royal Astronomical Society* **369**(2):603–607.

G. J. Fishman & C. A. Meegan (1995). 'Gamma-Ray Bursts'. *Annual Review of Astronomy and Astrophysics* **33**:415–458.

W. Fong & E. Berger (2013). 'The Locations of Short Gamma-Ray Bursts as Evidence for Compact Object Binary Progenitors'. *The Astrophysical Journal* **776**(1):18.

W. Fong, et al. (2010). 'Hubble Space Telescope Observations of Short Gamma-Ray Burst Host Galaxies: Morphologies, Offsets, and Local Environments'. *The Astrophysical Journal* **708**(1):9–25.

W. Fong, et al. (2015). 'A Decade of Short-duration Gamma-Ray Burst Broadband Afterglows: Energetics, Circumburst Densities, and Jet Opening Angles'. *The Astrophysical Journal* **815**(2):102.

W. Fong, et al. (2021). 'The Broadband Counterpart of the Short GRB 200522A at z = 0.5536: A Luminous Kilonova or a Collimated Outflow with a Reverse Shock?'. *The Astrophysical Journal* **906**(2):127.

E. Fonseca, et al. (2020a). 'Nine New Repeating Fast Radio Burst Sources from CHIME/FRB'. *The Astrophysical Journal Letters* **891**(1):L6.

E. Fonseca, et al. (2020b). 'Nine New Repeating Fast Radio Burst Sources from CHIME/FRB'. *The Astrophysical Journal Letters* **891**(1):L6.

D. B. Fox, et al. (2005). 'The afterglow of GRB 050709 and the nature of the short-hard γ-ray bursts'. *Nature* **437**(7060):845–850.

D. A. Frail, et al. (1997). 'The radio afterglow from the γ-ray burst of 8 May 1997'. *Nature* **389**(6648):261–263.

A. Franceschini (1982). 'Source counts at and beyond the confusion limit.'. *Astrophysics and Space Science* **86**(1):3–11.

P. A. Fridman & W. A. Baan (2001). 'RFI mitigation methods in radio astronomy'. *Astronomy and Astrophysics* **378**:327–344.

A. S. Fruchter, et al. (2006). 'Long γ-ray bursts and core-collapse supernovae have different environments'. *Nature* **441**(7092):463–468.

V. Gajjar, et al. (2018). 'Highest Frequency Detection of FRB 121102 at 4-8 GHz Using the Breakthrough Listen Digital Backend at the Green Bank Telescope'. *The Astrophysical Journal* **863**(1):2.

T. J. Galama, et al. (1998). 'An unusual supernova in the error box of the γ-ray burst of 25 April 1998'. *Nature* **395**(6703):670–672.

H. Gao & B. Zhang (2015). 'Photosphere Emission from a Hybrid Relativistic Outflow with Arbitrary Dimensionless Entropy and Magnetization in GRBs'. *The Astrophysical Journal* **801**(2):103.

N. Gehrels, et al. (2004). 'The Swift Gamma-Ray Burst Mission'. *The Astrophysical Journal* **611**(2):1005–1020.

N. Gehrels, et al. (2009). 'Gamma-Ray Bursts in the Swift Era'. *Annual Review of Astronomy and Astrophysics* **47**(1):567–617.

N. Gehrels & S. Razzaque (2013). 'Gamma-ray bursts in the swift-Fermi era'. *Frontiers of Physics* **8**(6):661–678.

N. Gehrels, et al. (2005). 'A short γ-ray burst apparently associated with an elliptical galaxy at redshift z = 0.225'. *Nature* **437**(7060):851–854.

R. Genzel, et al. (1981a). 'Proper motions and distances of H2O maser sources. II. W51 MAIN.'. *The Astrophysical Journal* **247**:1039–1051.

R. Genzel, et al. (1981b). 'Proper motions and distances of H2O maser sources. I. The outflow in Orion-KL.'. *The Astrophysical Journal* **244**:884–902.

M. Geyer, et al. (2021). 'The Thousand-Pulsar-Array programme on MeerKAT - III. Giant pulse characteristics of PSR J0540-6919'. *Monthly Notices of the Royal Astronomical Society* **505**(3):4468–4482.

G. Ghirlanda, et al. (2018). 'Bulk Lorentz factors of gamma-ray bursts'. *Astronomy and Astrophysics* **609**:A112.

P. Ghumatkar, et al. (2019). 'GRB 190613B: AstroSat CZTI detection'. *GRB Coordinates Network* **25289**:1.

B. Giacomazzo, et al. (2015). 'Producing Magnetar Magnetic Fields in the Merger of Binary Neutron Stars'. *The Astrophysical Journal* **809**(1):39.

D. Giannios (2006). 'Flares in GRB afterglows from delayed magnetic dissipation'. *Astronomy and Astrophysics* **455**(1):L5–L8.

K. Golap, et al. (2005). 'Post Correlation RFI Excision'. In N. Kassim, M. Perez, W. Junor, & P. Henning (eds.), *From Clark Lake to the Long Wavelength Array: Bill Erickson's Radio Science*, vol. 345 of *Astronomical Society of the Pacific Conference Series*, p. 366.

A. Goldstein, et al. (2017). 'An Ordinary Short Gamma-Ray Burst with Extraordinary Implications: Fermi-GBM Detection of GRB 170817A'. *The Astrophysical Journal Letters* **848**(2):L14.

B. P. Gompertz, et al. (2020). 'A Search for Neutron Star-Black Hole Binary Mergers in the Short Gamma-Ray Burst Population'. *The Astrophysical Journal* **895**(1):58.

K. Gourdji, et al. (2019). 'A Sample of Low-energy Bursts from FRB 121102'. *The Astrophysical Journal Letters* **877**(2):L19.

K. Gourdji, et al. (2020). 'Constraining a neutron star merger origin for localized fast radio bursts'. *Monthly Notices of the Royal Astronomical Society* **497**(3):3131–3141.

W.-M. Gu, et al. (2016). 'A Neutron Star-White Dwarf Binary Model for Repeating Fast Radio Burst 121102'. *The Astrophysical Journal Letters* **823**(2):L28.

V. Gupta, et al. (2021). 'Estimating fast transient detection pipeline efficiencies at UTMOST via real-time injection of mock FRBs'. *Monthly Notices of the Royal Astronomical Society* **501**(2):2316–2326.

G. Hallinan, et al. (2017). 'A radio counterpart to a neutron star merger'. *Science* **358**(6370):1579–1583.

P. J. Hancock, et al. (2019a). 'A VOEvent-based automatic trigger system for the Murchison Widefield Array'. *Publications of the Astronomical Society of Australia* **36**:e046.

P. J. Hancock, et al. (2013). 'Two Populations of Gamma-Ray Burst Radio Afterglows'. *The Astrophysical Journal* **776**(2):106.

P. J. Hancock, et al. (2019b). 'ROBBIE: A batch processing work-flow for the detection of radio transients and variables'. *Astronomy and Computing* **27**:23.

P. J. Hancock, et al. (2018). 'Source Finding in the Era of the SKA (Precursors): Aegean 2.0'. *Publications of the Astronomical Society of Australia* **35**:e011.

T. H. Hankins, et al. (2003). 'Nanosecond radio bursts from strong plasma turbulence in the Crab pulsar'. *Nature* **422**(6928):141–143.

T. Hashimoto, et al. (2020a). 'Fast radio bursts to be detected with the Square Kilometre Array'. *Monthly Notices of the Royal Astronomical Society* **497**(4):4107–4116.

T. Hashimoto, et al. (2020b). 'Luminosity-duration relations and luminosity functions of repeating and non-repeating fast radio bursts'. *Monthly Notices of the Royal Astronomical Society* **494**(2):2886–2904.

T. Hashimoto, et al. (2019). 'Luminosity-duration relation of fast radio bursts'. *Monthly Notices of the Royal Astronomical Society* **488**(2):1908–1916.

K. E. Heintz, et al. (2020). 'Host Galaxy Properties and Offset Distributions of Fast Radio Bursts: Implications for Their Progenitors'. *The Astrophysical Journal* **903**(2):152.

G. Hellbourg, et al. (2014). 'Reference antenna-based subspace tracking for RFI mitigation in radio astronomy'. In *Signal and Information Processing (Global-SIP*, pp. 1286–1290.

J. W. T. Hessels, et al. (2019). 'FRB 121102 Bursts Show Complex Time-Frequency Structure'. *The Astrophysical Journal Letters* **876**(2):L23.

J. Hjorth, et al. (2003). 'A very energetic supernova associated with the γ-ray burst of 29 March 2003'. *Nature* **423**(6942):847–850.

J. Hjorth, et al. (2005). 'The optical afterglow of the short γ-ray burst GRB 050709'. *Nature* **437**(7060):859–861.

D. W. Hogg (1999). 'Distance measures in cosmology'. *arXiv e-prints* pp. astro–ph/9905116.

A. W. Hotan, et al. (2004). 'PSRCHIVE and PSRFITS: An Open Approach to Radio Pulsar Data Storage and Analysis'. *Publications of the Astronomical Society of Australia* **21**(3):302–309.

L. J. M. Houben, et al. (2019). 'Constraints on the low frequency spectrum of FRB 121102'. *Astronomy and Astrophysics* **623**:A42.

K. Hurley, et al. (2013). 'The Interplanetary Network Supplement to the Fermi GBM Catalog of Cosmic Gamma-Ray Bursts'. *The Astrophysical Journal Supplement Series* **207**(2):39.

N. Hurley-Walker, et al. (2017). 'GaLactic and Extragalactic All-sky Murchison Widefield Array (GLEAM) survey - I. A low-frequency extragalactic catalogue'. *Monthly Notices of the Royal Astronomical Society* **464**(1):1146–1167.

N. Hurley-Walker & P. J. Hancock (2018). 'De-distorting ionospheric effects in the image plane'. *Astronomy and Computing* **25**:94–102.

N. Hurley-Walker, et al. (2019). 'GaLactic and Extragalactic All-sky Murchison Widefield Array (GLEAM) survey II: Galactic plane 345° ¡ l ¡ 67°, 180° ¡ l ¡ 240°'. *Publications of the Astronomical Society of Australia* **36**:e047.

S. Inoue (2004). 'Probing the cosmic reionization history and local environment of gamma-ray bursts through radio dispersion'. *Monthly Notices of the Royal Astronomical Society* **348**(3):999–1008.

T. Inoue, et al. (2011). 'Three-dimensional Simulations of Magnetohydrodynamic Turbulence Behind Relativistic Shock Waves and Their Implications for Gamma-Ray Bursts'. *The Astrophysical Journal* **734**(2):77.

K. Ioka (2003). 'The Cosmic Dispersion Measure from Gamma-Ray Burst Afterglows: Probing the Reionization History and the Burst Environment'. *The Astrophysical Journal Letters* **598**(2):L79–L82.

K. Ioka, et al. (2005). 'Variabilities of Gamma-Ray Burst Afterglows: Long-acting Engine, Anisotropic Jet, or Many Fluctuating Regions?'. *The Astrophysical Journal* **631**(1):429–434.

K. Ioka & B. Zhang (2020). 'A Binary Comb Model for Periodic Fast Radio Bursts'. *The Astrophysical Journal Letters* **893**(1):L26.

N. Jackson (2008). 'Principles of Interferometry'. In F. Bacciotti, L. Testi, & E. Whelan (eds.), *Jets from Young Stars II*, vol. 742, p. 193.

C. W. James, et al. (2019). 'Using negative-latency gravitational wave alerts to detect prompt radio bursts from binary neutron star mergers with the Murchison Widefield Array'. *Monthly Notices of the Royal Astronomical Society* **489**(1):L75–L79.

F. Jankowski, et al. (2018). 'Spectral properties of 441 radio pulsars'. *Monthly Notices of the Royal Astronomical Society* **473**(4):4436–4458.

J. Japelj, et al. (2019). 'GRB 190627A: VLT/FORS2 spectroscopic redshift.'. *GRB Coordinates Network* **24916**:1.

P. Jiang, et al. (2019). 'Commissioning progress of the FAST'. *Science China Physics, Mechanics, and Astronomy* **62**(5):959502.

Z.-P. Jin, et al. (2016). 'The Macronova in GRB 050709 and the GRB-macronova connection'. *Nature Communications* **7**:12898.

Z.-P. Jin, et al. (2015). 'The Light Curve of the Macronova Associated with the Long-Short Burst GRB 060614'. *The Astrophysical Journal Letters* **811**(2):L22.

C. H. Jordan, et al. (2017). 'Characterization of the ionosphere above the Murchison Radio Observatory using the Murchison Widefield Array'. *Monthly Notices of the Royal Astronomical Society* **471**(4):3974–3987.

A. Josephy, et al. (2019). 'CHIME/FRB Detection of the Original Repeating Fast Radio Burst Source FRB 121102'. *The Astrophysical Journal Letters* **882**(2):L18.

D. A. Kann (2013). 'Multi-Wavelength Observations of Short-Duration Gamma-Ray Bursts: Recent Results'. In A. J. Castro-Tirado, J. Gorosabel, & I. H. Park (eds.), *EAS Publications Series*, vol. 61 of *EAS Publications Series*, pp. 309–317.

D. A. Kann, et al. (2011). 'The Afterglows of Swift-era Gamma-Ray Bursts. II. Type I GRB versus Type II GRB Optical Afterglows'. *The Astrophysical Journal* **734**(2):96.

D. L. Kaplan, et al. (2016). 'Strategies for Finding Prompt Radio Counterparts to Gravitational Wave Transients with the Murchison Widefield Array'. *Publications of the Astronomical Society of Australia* **33**:e050.

D. L. Kaplan, et al. (2015). 'A Deep Search for Prompt Radio Emission from the Short GRB 150424A with the Murchison Widefield Array'. *The Astrophysical Journal Letters* **814**(2):L25.

A. Karastergiou, et al. (2015). 'Limits on fast radio bursts at 145 MHz with ARTEMIS, a real-time software backend'. *Monthly Notices of the Royal Astronomical Society* **452**(2):1254–1262.

J. I. Katz (1997). 'Yet Another Model of Gamma-Ray Bursts'. *The Astrophysical Journal* **490**(2):633–641.

J. I. Katz (2016). 'Fast radio bursts — A brief review: Some questions, fewer answers'. *Modern Physics Letters A* **31**(14):1630013.

E. F. Keane, et al. (2018). 'The SUrvey for Pulsars and Extragalactic Radio Bursts - I. Survey description and overview'. *Monthly Notices of the Royal Astronomical Society* **473**(1):116–135.

E. F. Keane, et al. (2011). 'Rotating Radio Transients: new discoveries, timing solutions and musings'. *Monthly Notices of the Royal Astronomical Society* **415**(4):3065–3080.

E. F. Keane & E. Petroff (2015). 'Fast radio bursts: search sensitivities and completeness'. *Monthly Notices of the Royal Astronomical Society* **447**(3):2852–2856.

K. I. Kellermann & I. I. K. Pauliny-Toth (1969). 'The Spectra of Opaque Radio Sources'. *The Astrophysical Journal Letters* **155**:L71.

K. Kiuchi, et al. (2012). 'Three-dimensional evolution of differentially rotating magnetized neutron stars'. **86**(6):064008.

R. W. Klebesadel, et al. (1973). 'Observations of Gamma-Ray Bursts of Cosmic Origin'. *The Astrophysical Journal Letters* **182**:L85.

W. Kluźniak & M. Ruderman (1998). 'The Central Engine of Gamma-Ray Bursters'. *The Astrophysical Journal Letters* **505**(2):L113–L117.

J. Kocz, et al. (2010). 'Radio Frequency Interference Removal through the Application of Spatial Filtering Techniques on the Parkes Multibeam Receiver'. *The Astronomical Journal* **140**(6):2086–2094.

S. S. Komissarov, et al. (2009). 'Magnetic acceleration of ultrarelativistic jets in gamma-ray burst sources'. *Monthly Notices of the Royal Astronomical Society* **394**(3):1182–1212.

T. M. Koshut, et al. (1996). 'Systematic Effects on Duration Measurements of Gamma-Ray Bursts'. *The Astrophysical Journal* **463**:570.

C. Kouveliotou, et al. (1993). 'Identification of Two Classes of Gamma-Ray Bursts'. *The Astrophysical Journal Letters* **413**:L101.

S. R. Kulkarni, et al. (1998). 'Identification of a host galaxy at redshift z = 3.42 for the γ-ray burst of 14 December 1997'. *Nature* **393**(6680):35–39.

S. R. Kulkarni, et al. (1999). 'Discovery of a Radio Flare from GRB 990123'. *The Astrophysical Journal Letters* **522**(2):L97–L100.

P. Kumar & T. Piran (2000). 'ENERGETICS AND LUMINOSITY FUNCTION OF GAMMA-RAY BURSTS'. *The Astrophysical Journal* **535**:152.

P. Kumar, et al. (2021a). 'Extremely band-limited repetition from a fast radio burst source'. *Monthly Notices of the Royal Astronomical Society* **500**(2):2525–2531.

P. Kumar, et al. (2021b). 'A second fast radio burst from the source of FRB 201124A detected by ASKAP'. *The Astronomer's Telegram* **14508**:1.

P. Kumar, et al. (2021c). 'Circularly polarized radio emission from the repeating fast radio burst source FRB 20201124A'. *arXiv e-prints* p. arXiv:2109.11535.

P. Kumar, et al. (2021d). 'ASKAP detection of a repeat burst from the FRB 20201124A source'. *The Astronomer's Telegram* **14502**:1.

P. Kumar, et al. (2019). 'Faint Repetitions from a Bright Fast Radio Burst Source'. *The Astrophysical Journal Letters* **887**(2):L30.

P. Kumar & B. Zhang (2015). 'The physics of gamma-ray bursts & relativistic jets'. *Physics Reports* **561**:1–109.

S. Laha, et al. (2021). 'GRB 210419A: Swift detection of a burst'. *GRB Coordinates Network* **29828**:1.

A. E. Lanman, et al. (2021). 'A sudden period of high activity from repeating Fast Radio Burst 20201124A'. *arXiv e-prints* p. arXiv:2109.09254.

A. E. Lanman, et al. (2022). 'A Sudden Period of High Activity from Repeating Fast Radio Burst 20201124A'. *The Astrophysical Journal* **927**(1):59.

T. Laskar, et al. (2015). 'Energy Injection in Gamma-Ray Burst Afterglows'. *The Astrophysical Journal* **814**(1):1.

P. D. Lasky, et al. (2014). 'Nuclear equation of state from observations of short gamma-ray burst remnants'. **89**(4):047302.

C. Law, et al. (2021). 'VLA/realfast localization and deep imaging of FRB 20201124A'. *The Astronomer's Telegram* **14526**:1.

C. J. Law, et al. (2017). 'A Multi-telescope Campaign on FRB 121102: Implications for the FRB Population'. *The Astrophysical Journal* **850**(1):76.

C. J. Law, et al. (2020). 'A Distant Fast Radio Burst Associated with Its Host Galaxy by the Very Large Array'. *The Astrophysical Journal* **899**(2):161.

D. Lazzati & R. Perna (2007). 'X-ray flares and the duration of engine activity in gamma-ray bursts'. *Monthly Notices of the Royal Astronomical Society* **375**(1):L46–L50.

T. Le & V. Mehta (2017). 'Revisiting the Redshift Distribution of Gamma-Ray Bursts in the Swift Era'. *The Astrophysical Journal* **837**(1):17.

H. K. Lee, et al. (2000). 'The Blandford-Znajek process as a central engine for a gamma-ray burst'. *Physics Reports* **325**(3):83–114.

E. M. Levesque, et al. (2010). 'The Host Galaxies of Gamma-Ray Bursts. I. Interstellar Medium Properties of Ten Nearby Long-Duration Gamma-Ray Burst Hosts'. *The Astronomical Journal* **139**(2):694–711.

Y. Levin, et al. (2020). 'Precessing Flaring Magnetar as a Source of Repeating FRB 180916.J0158+65'. *The Astrophysical Journal Letters* **895**(2):L30.

L.-B. Li, et al. (2018). 'A model of fast radio bursts: collisions between episodic magnetic blobs'. *Research in Astronomy and Astrophysics* **18**(6):061.

L.-X. Li & B. Paczyński (1998). 'Transient Events from Neutron Star Mergers'. *The Astrophysical Journal Letters* **507**(1):L59–L62.

E.-W. Liang, et al. (2008). 'A Comprehensive Analysis of Swift XRT Data. III. Jet Break Candidates in X-Ray and Optical Afterglow Light Curves'. *The Astrophysical Journal* **675**(1):528–552.

E. W. Liang, et al. (2006). 'Testing the Curvature Effect and Internal Origin of Gamma-Ray Burst Prompt Emissions and X-Ray Flares with Swift Data'. *The Astrophysical Journal* **646**(1):351–357.

E.-W. Liang, et al. (2007). 'A Comprehensive Analysis of Swift XRT Data. II. Diverse Physical Origins of the Shallow Decay Segment'. *The Astrophysical Journal* **670**(1):565–583.

A. Lien, et al. (2016). 'The Third Swift Burst Alert Telescope Gamma-Ray Burst Catalog'. *The Astrophysical Journal* **829**(1):7.

M. Lingam & A. Loeb (2017). 'Fast Radio Bursts from Extragalactic Light Sails'. *The Astrophysical Journal Letters* **837**(2):L23.

V. M. Lipunov & I. E. Panchenko (1996). 'Pulsars revived by gravitational waves'. *Astronomy & Astrophysics* **312**:937.

C. J. Lonsdale, et al. (2009). 'The Murchison Widefield Array: Design Overview'. *IEEE Proceedings* **97**(8):1497–1506.

D. R. Lorimer, et al. (2007). 'A Bright Millisecond Radio Burst of Extragalactic Origin'. *Science* **318**(5851):777.

D. R. Lorimer & M. Kramer (2012). *Handbook of Pulsar Astronomy*.

H.-J. Lü, et al. (2010). 'A New Classification Method for Gamma-ray Bursts'. *The Astrophysical Journal* **725**(2):1965–1970.

H.-J. Lü & B. Zhang (2014). 'A Test of the Millisecond Magnetar Central Engine Model of Gamma-Ray Bursts with Swift Data'. *The Astrophysical Journal* **785**(1):74.

H.-J. Lü, et al. (2015). 'The Millisecond Magnetar Central Engine in Short GRBs'. *The Astrophysical Journal* **805**(2):89.

W. Lu, et al. (2020). 'A unified picture of Galactic and cosmological fast radio bursts'. *Monthly Notices of the Royal Astronomical Society* **498**(1):1397–1405.

S. G. Lucek & A. R. Bell (2000). 'Non-linear amplification of a magnetic field driven by cosmic ray streaming'. *Monthly Notices of the Royal Astronomical Society* **314**(1):65–74.

R. Luo, et al. (2020). 'Diverse polarization angle swings from a repeating fast radio burst source'. *Nature* **586**(7831):693–696.

N. Lyons, et al. (2010). 'Can X-ray emission powered by a spinning-down magnetar explain some gamma-ray burst light-curve features?'. *Monthly Notices of the Royal Astronomical Society* **402**(2):705–712.

Y. Lyubarsky (2008). 'Induced Scattering of Short Radio Pulses'. *The Astrophysical Journal* **682**(2):1443–1449.

Y. Lyubarsky (2014). 'Searches for prompt radio emission at 151 MHz from the gamma-ray bursts GRB 950430 and GRB 950706'. *Monthly Notices of the Royal Astronomical Society* **442**(4):L9.

Y. Lyubarsky (2020). 'Fast Radio Bursts from Reconnection in a Magnetar Magnetosphere'. *The Astrophysical Journal* **897**(1):1.

M. Lyutikov (2013). 'The Electromagnetic Model of Short GRBs, the Nature of Prompt Tails, Supernova-less Long GRBs, and Highly Efficient Episodic Accretion'. *The Astrophysical Journal* **768**(1):63.

M. Lyutikov, et al. (2003). 'Polarization of Prompt Gamma-Ray Burst Emission: Evidence for Electromagnetically Dominated Outflow'. *The Astrophysical Journal* **597**(2):998–1009.

A. I. MacFadyen, et al. (2005). 'X-ray flares following short gamma-ray bursts from shock heating of binary stellar companions'. *arXiv e-prints* pp. astro–ph/0510192.

A. I. MacFadyen & S. E. Woosley (1999). 'Collapsars: Gamma-Ray Bursts and Explosions in "Failed Supernovae"'. *The Astrophysical Journal* **524**(1):262–289.

J. P. Macquart (2007). 'On the Detectability of Prompt Coherent Gamma-Ray Burst Radio Emission'. *The Astrophysical Journal Letters* **658**(1):L1–L4.

J. P. Macquart, et al. (2020). 'A census of baryons in the Universe from localized fast radio bursts'. *Nature* **581**(7809):391–395.

J. P. Macquart, et al. (2019). 'The Spectral Properties of the Bright Fast Radio Burst Population'. *The Astrophysical Journal Letters* **872**(2):L19.

B. Mailyan & C. Meegan (2019). 'GRB 190903A: Fermi GBM detection.'. *GRB Coordinates Network* **25636**:1.

W. A. Majid, et al. (2020). 'A Dual-band Radio Observation of FRB 121102 with the Deep Space Network and the Detection of Multiple Bursts'. *The Astrophysical Journal Letters* **897**(1):L4.

D. Malesani, et al. (2004). 'SN 2003lw and GRB 031203: A Bright Supernova for a Faint Gamma-Ray Burst'. *The Astrophysical Journal Letters* **609**(1):L5–L8.

R. N. Manchester, et al. (2005). 'The Australia Telescope National Facility Pulsar Catalogue'. *The Astronomical Journal* **129**(4):1993–2006.

V. Mangano, et al. (2007). 'Swift XRT Observations of the Afterglow of XRF 050416A'. *The Astrophysical Journal* **654**(1):403–412.

B. Marcote, et al. (2020). 'A repeating fast radio burst source localized to a nearby spiral galaxy'. *Nature* **577**(7789):190–194.

B. Marcote, et al. (2017). 'The Repeating Fast Radio Burst FRB 121102 as Seen on Milliarcsecond Angular Scales'. *The Astrophysical Journal Letters* **834**(2):L8.

R. Margutti, et al. (2011). 'X-ray flare candidates in short gamma-ray bursts'. *Monthly Notices of the Royal Astronomical Society* **417**(3):2144–2160.

R. Margutti, et al. (2010). 'Lag-luminosity relation in γ-ray burst X-ray flares: a direct link to the prompt emission'. *Monthly Notices of the Royal Astronomical Society* **406**(4):2149–2167.

J. M. Marr, et al. (2015). *Fundamentals of Radio Astronomy: Observational Methods*.

V. R. Marthi, et al. (2021). 'Burst properties of the highly active FRB20201124A using uGMRT'. *Monthly Notices of the Royal Astronomical Society* .

K. Masui, et al. (2015). 'Dense magnetized plasma associated with a fast radio burst'. *Nature* **528**(7583):523–525.

E. P. Mazets, et al. (1974). 'Flare of cosmic gamma radiation as observed with "Cosmos-461" satellite'. *Soviet Journal of Experimental and Theoretical Physics Letters* **19**:77.

M. M. McKinnon (2014). 'The Analytical Solution to the Temporal Broadening of a Gaussian-Shaped Radio Pulse by Multipath Scattering from a Thin Screen in the Interstellar Medium'. **126**(939):476.

M. A. McLaughlin, et al. (2006). 'Transient radio bursts from rotating neutron stars'. *Nature* **439**(7078):817–820.

J. P. McMullin, et al. (2007). 'CASA Architecture and Applications'. In R. A. Shaw, F. Hill, & D. J. Bell (eds.), *Astronomical Data Analysis Software and Systems XVI*, vol. 376 of *Astronomical Society of the Pacific Conference Series*, p. 127.

S. J. McSweeney, et al. (2017). 'Low-frequency Observations of the Subpulse Drifter PSR J0034-0721 with the Murchison Widefield Array'. *The Astrophysical Journal* **836**(2):224.

M. V. Medvedev, et al. (2005). 'Long-Time Evolution of Magnetic Fields in Relativistic Gamma-Ray Burst Shocks'. *The Astrophysical Journal Letters* **618**(2):L75–L78.

C. Meegan, et al. (2009). 'The Fermi Gamma-ray Burst Monitor'. *The Astrophysical Journal* **702**(1):791–804.

C. A. Meegan, et al. (1992). 'Spatial distribution of γ-ray bursts observed by BATSE'. *Nature* **355**(6356):143–145.

D. B. Melrose (1978). 'Amplified linear acceleration emission applied to pulsars.'. *The Astrophysical Journal* **225**:557–573.

D. B. Melrose (2017). 'Coherent emission mechanisms in astrophysical plasmas'. *Reviews of Modern Plasma Physics* **1**(1):5.

P. Mészáros & M. J. Rees (1997). 'Optical and Long-Wavelength Afterglow from Gamma-Ray Bursts'. *The Astrophysical Journal* **476**(1):232–237.

B. D. Metzger, et al. (2017). 'Millisecond Magnetar Birth Connects FRB 121102 to Superluminous Supernovae and Long-duration Gamma-Ray Bursts'. *The Astrophysical Journal* **841**(1):14.

B. D. Metzger, et al. (2011). 'The protomagnetar model for gamma-ray bursts'. *Monthly Notices of the Royal Astronomical Society* **413**(3):2031–2056.

B. D. Metzger, et al. (2019). 'Fast radio bursts as synchrotron maser emission from decelerating relativistic blast waves'. *Monthly Notices of the Royal Astronomical Society* **485**(3):4091–4106.

B. D. Metzger & C. Zivancev (2016). 'Pair fireball precursors of neutron star mergers'. *Monthly Notices of the Royal Astronomical Society* **461**(4):4435.

M. R. Metzger, et al. (1997). 'Spectral constraints on the redshift of the optical counterpart to the γ-ray burst of 8 May 1997'. *Nature* **387**(6636):878–880.

B. W. Meyers, et al. (2018). 'Hunting for Radio Emission from the Intermittent Pulsar J1107-5907 at Low Frequencies'. *The Astrophysical Journal* **869**(2):134.

B. W. Meyers, et al. (2017). 'Spectral Flattening at Low Frequencies in Crab Giant Pulses'. *The Astrophysical Journal* **851**(1):20.

D. Michilli et al. (2018). 'Observations of fast radio bursts at frequencies down to 400 megahertz'. *Nature* **553**(2):182.

K. Mikhailov & A. Sclocco (2018). 'The Apertif Monitor for Bursts Encountered in Real-time (AMBER) auto-tuning optimization with genetic algorithms'. *Astronomy and Computing* **25**:139–148.

M. Milosavljević & E. Nakar (2006). 'The Cosmic-Ray Precursor of Relativistic Collisionless Shocks: A Missing Link in Gamma-Ray Burst Afterglows'. *The Astrophysical Journal* **651**(2):979–984.

D. A. Mitchell, et al. (2008). 'Real-Time Calibration of the Murchison Widefield Array'. *IEEE Journal of Selected Topics in Signal Processing* **2**(5):707–717.

Y. Mizuno, et al. (2011). 'Magnetic-field Amplification by Turbulence in a Relativistic Shock Propagating Through an Inhomogeneous Medium'. *The Astrophysical Journal* **726**(2):62.

J. Moldon (2012). *Structure and nature of gamma-ray binaries by means of VLBI observations*. Ph.D. thesis, Universitat de Barcelona.

K. P. Mooley et al. (2018a). 'Superluminal motion of a relativistic jet in the neutron-star merger GW170817'. *Nature* **561**(2):355.

K. P. Mooley, et al. (2018b). 'A Strong Jet Signature in the Late-time Light Curve of GW170817'. *The Astrophysical Journal Letter* **868**(2):L11.

K. P. Mooley, et al. (2018c). 'A mildly relativistic wide-angle outflow in the neutron-star merger event GW170817'. *Nature* **554**(2):207.

K. Mukai (1993). 'PIMMS and Viewing: proposal preparation tools'. *Legacy* **3**:21–31.

T. Murphy, et al. (2017). 'Low-Frequency Spectral Energy Distributions of Radio Pulsars Detected with the Murchison Widefield Array'. *Publications of the Astronomical Society of Australia* **34**:e020.

E. Nakar (2007). 'Short-hard gamma-ray bursts'. *Physics Reports* **442**(1-6):166–236.

E. Nakar, et al. (2018). 'From to Radio: The Electromagnetic Counterpart of GW170817'. *The Astrophysical Journal* **867**:18.

J. Nambissan T., et al. (2021). 'SARAS 3 CD/EoR Radiometer: Design and Performance of the Receiver'. *arXiv e-prints* p. arXiv:2104.01756.

R. Narayan, et al. (1992). 'Gamma-Ray Bursts as the Death Throes of Massive Binary Stars'. *The Astrophysical Journal Letters* **395**:L83.

P. Narayana Bhat, et al. (2016). 'The Third Fermi GBM Gamma-Ray Burst Catalog: The First Six Years'. *The Astrophysical Journal Supplement Series* **223**(2):28.

K. Nimmo, et al. (2021). 'Highly polarized microstructure from the repeating FRB 20180916B'. *Nature Astronomy* **5**:594–603.

K. Nimmo, et al. (2022). 'Burst timescales and luminosities as links between young pulsars and fast radio bursts'. *Nature Astronomy* **6**:393–401.

J. P. Norris, et al. (1994). 'Detection of Signature Consistent with Cosmological Time Dilation in Gamma-Ray Bursts'. *The Astrophysical Journal* **424**:540.

J. A. Nousek, et al. (2006). 'Evidence for a Canonical Gamma-Ray Burst Afterglow Light Curve in the Swift XRT Data'. *The Astrophysical Journal* **642**(1):389–400.

K. S. Obenberger, et al. (2014). 'Limits on Gamma-Ray Burst Prompt Radio Emission Using the LWA1'. *The Astrophysical Journal* **785**(1):27.

P. T. O'Brien, et al. (2006). 'The Early X-Ray Emission from GRBs'. *The Astrophysical Journal* **647**(2):1213–1237.

A. R. Offringa, et al. (2012). 'Post-correlation filtering techniques for off-axis source and RFI removal'. *Monthly Notices of the Royal Astronomical Society* **422**(1):563–580.

A. R. Offringa, et al. (2014). 'WSCLEAN: an implementation of a fast, generic wide-field imager for radio astronomy'. *Monthly Notices of the Royal Astronomical Society* **444**(1):606–619.

A. R. Offringa & O. Smirnov (2017). 'An optimized algorithm for multiscale wideband deconvolution of radio astronomical images'. *Monthly Notices of the Royal Astronomical Society* **471**(1):301–316.

A. R. Offringa, et al. (2015). 'The Low-Frequency Environment of the Murchison Widefield Array: Radio-Frequency Interference Analysis and Mitigation'. *Publications of the Astronomical Society of Australia* **32**(1):8.

S. A. Olausen & V. M. Kaspi (2014). 'The McGill Magnetar Catalog'. *The Astrophysical Journal Supplement Series* **212**(1):6.

S. M. Ord, et al. (2015). 'The Murchison Widefield Array Correlator'. *Publications of the Astronomical Society of Australia* **32**:e006.

S. M. Ord, et al. (2019). 'MWA tied-array processing I: Calibration and beam-formation'. *Publications of the Astronomical Society of Australia* **36**:e030.

J. P. Osborne, et al. (2021). 'GRB 210419A: Enhanced Swift-XRT position'. *GRB Coordinates Network* **29830**:1.

W. S. Paciesas, et al. (2012). 'The Fermi GBM Gamma-Ray Burst Catalog: The First Two Years'. *The Astrophysical Journal Supplement Series* **199**(1):18.

B. Paczynski (1991). 'Cosmological gamma-ray bursts.'. **41**:257–267.

D. Palaniswamy, et al. (2014). 'A Search for Fast Radio Bursts Associated with Gamma-Ray Bursts'. *The Astrophysical Journal* **790**(1):63.

D. M. Palmer, et al. (2005). 'A giant γ-ray flare from the magnetar SGR 1806 - 20'. *Nature* **434**(7037):1107–1109.

D. M. Palmer, et al. (2021). 'GRB 210419A: Swift-BAT refined analysis'. *GRB Coordinates Network* **29838**:1.

A. Panaitescu (2005). 'Jets, structured outflows and energy injection in gamma-ray burst afterglows: numerical modelling'. *Monthly Notices of the Royal Astronomical Society* **363**(4):1409–1423.

A. Panaitescu (2006). 'The energetics and environment of the short-GRB afterglows 050709 and 050724'. *Monthly Notices of the Royal Astronomical Society* **367**(1):L42–L46.

A. Panaitescu & P. Kumar (2002). 'Properties of Relativistic Jets in Gamma-Ray Burst Afterglows'. *The Astrophysical Journal* **571**(2):779–789.

E. Parent, et al. (2020). 'First Discovery of a Fast Radio Burst at 350 MHz by the GBNCC Survey'. *The Astrophysical Journal* **904**(2):92.

I. Pastor-Marazuela, et al. (2021). 'Chromatic periodic activity down to 120 megahertz in a fast radio burst'. *Nature* **596**(7873):505–508.

C. Patel, et al. (2018). 'PALFA Single-pulse Pipeline: New Pulsars, Rotating Radio Transients, and a Candidate Fast Radio Burst'. *The Astrophysical Journal* **869**(2):181.

A. B. Pearlman, et al. (2020). 'Multiwavelength Radio Observations of Two Repeating Fast Radio Burst Sources: FRB 121102 and FRB 180916.J0158+65'. *The Astrophysical Journal Letters* **905**(2):L27.

A. Pe'er (2017). 'Constraining Magnetization of Gamma-Ray Bursts Outflows Using Prompt Emission Fluence'. *The Astrophysical Journal* **850**(2):200.

U.-L. Pen, et al. (2009). 'The GMRT EoR experiment: limits on polarized sky brightness at 150 MHz'. *Monthly Notices of the Royal Astronomical Society* **399**(1):181–194.

E. Petroff, et al. (2016). 'FRBCAT: The Fast Radio Burst Catalogue'. *Publications of the Astronomical Society of Australia* **33**:e045.

E. Petroff, et al. (2019). 'Fast radio bursts'. **27**(1):4.

E. Petroff, et al. (2022). 'Fast radio bursts at the dawn of the 2020s'. **30**(1):2.

E. Petroff, et al. (2015). 'A survey of FRB fields: limits on repeatability'. *Monthly Notices of the Royal Astronomical Society* **454**(1):457–462.

E. Petroff, et al. (2014). 'An Absence of Fast Radio Bursts at Intermediate Galactic Latitudes'. *The Astrophysical Journal Letters* **789**(2):L26.

S. Phinney & J. H. Taylor (1979). 'A sensitive search for radio pulses from primordial black holes and distant Supernovae'. *Nature* **277**(5692):117–118.

E. Pian, et al. (2006). 'An optical supernova associated with the X-ray flash XRF 060218'. *Nature* **442**(7106):1011–1013.

M. Pilia, et al. (2020). 'The Lowest-frequency Fast Radio Bursts: Sardinia Radio Telescope Detection of the Periodic FRB 180916 at 328 MHz'. *The Astrophysical Journal Letters* **896**(2):L40.

T. Piran (1999). 'Gamma-ray bursts and the fireball model'. *Physics Reports* **314**(6):575–667.

T. Piran (2003). 'The Energy of Gamma-ray Bursts'. In E. P. van den Heuvel, L. Kaper, E. Rol, & R. A. M. J. Wijers (eds.), *From X-ray Binaries to Gamma-Ray Bursts: Jan van Paradijs Memorial Symposium*, vol. 308 of *Astronomical Society of the Pacific Conference Series*, p. 355.

L. Piro, et al. (2021). 'The fast radio burst FRB 20201124A in a star-forming region: Constraints to the progenitor and multiwavelength counterparts'. *Astronomy and Astrophysics* **656**:L15.

Z. Pleunis, et al. (2021a). 'Fast Radio Burst Morphology in the First CHIME/FRB Catalog'. *The Astrophysical Journal* **923**(1):1.

Z. Pleunis, et al. (2021b). 'LOFAR Detection of 110-188 MHz Emission and Frequency-dependent Activity from FRB 20180916B'. *The Astrophysical Journal Letters* **911**(1):L3.

I. Plotnikov & L. Sironi (2019). 'The synchrotron maser emission from relativistic shocks in Fast Radio Bursts: 1D PIC simulations of cold pair plasmas'. *Monthly Notices of the Royal Astronomical Society* **485**(3):3816–3833.

N. Pol, et al. (2019). 'Estimates of Fast Radio Burst Dispersion Measures from Cosmological Simulations'. *The Astrophysical Journal* **886**(2):135.

R. Popham, et al. (1999). 'Hyperaccreting Black Holes and Gamma-Ray Bursts'. *The Astrophysical Journal* **518**(1):356–374.

S. B. Popov, et al. (2018). 'Fast radio bursts'. *Physics Uspekhi* **61**(10):965.

N. Pradel, et al. (2006). 'Astrometric accuracy of phase-referenced observations with the VLBA and EVN'. *Astronomy and Astrophysics* **452**(3):1099–1106.

B. Qin, et al. (1998). 'The Collapse of Neutron Stars in High-Mass Binaries as the Energy Source for the Gamma-Ray Bursts'. *The Astrophysical Journal Letters* **494**(1):L57–L59.

J. L. Racusin, et al. (2009). 'Jet Breaks and Energetics of Swift Gamma-Ray Burst X-Ray Afterglows'. *The Astrophysical Journal* **698**(1):43–74.

R. Rahin & E. Behar (2019). 'Cosmological Evolution of the Absorption of γ-Ray Burst X-Ray Afterglows'. *The Astrophysical Journal* **885**(1):47.

C. A. Raithel, et al. (2018). 'Tidal Deformability from GW170817 as a Direct Probe of the Neutron Star Radius'. *The Astrophysical Journal Letter* **857**(2):L23.

K. M. Rajwade, et al. (2020a). 'Limits on absorption from a 332-MHz survey for fast radio bursts'. *Monthly Notices of the Royal Astronomical Society* **493**(3):4418–4427.

K. M. Rajwade, et al. (2020b). 'Possible periodic activity in the repeating FRB 121102'. *Monthly Notices of the Royal Astronomical Society* **495**(4):3551–3558.

S. Ransom (2011). 'PRESTO: PulsaR Exploration and Search TOolkit'.

S. M. Ransom (2001). *New search techniques for binary pulsars*. Ph.D. thesis, Harvard University.

J. C. Rastinejad, et al. (2022). 'A Kilonova Following a Long-Duration Gamma-Ray Burst at 350 Mpc'. *arXiv e-prints* p. arXiv:2204.10864.

V. Ravi, et al. (2019). 'A fast radio burst localized to a massive galaxy'. *Nature* **572**(7769):352–354.

V. Ravi & P. D. Lasky (2014). 'The birth of black holes: neutron star collapse times, gamma-ray bursts and fast radio bursts'. *Monthly Notices of the Royal Astronomical Society* **441**(3):2433–2439.

V. Ravi & A. Loeb (2019). 'Explaining the Statistical Properties of Fast Radio Bursts with Suppressed Low-frequency Emission'. *The Astrophysical Journal* **874**(1):72.

V. Ravi, et al. (2015). 'A Fast Radio Burst in the Direction of the Carina Dwarf Spheroidal Galaxy'. *The Astrophysical Journal Letters* **799**(1):L5.

S. Razzaque, et al. (2010). 'Synchrotron Radiation from Ultra-High Energy Protons and the Fermi Observations of GRB 080916C'. *The Open Astronomy Journal* **3**(1):150–155.

M. J. Rees & P. Meszaros (1992). 'Relativistic fireballs - Energy conversion and time-scales.'. *Monthly Notices of the Royal Astronomical Society* **258**:41.

J. E. Rhoads (1999). 'The Dynamics and Light Curves of Beamed Gamma-Ray Burst Afterglows'. *The Astrophysical Journal* **525**(2):737–749.

G. E. Romero et al. (2016). 'GW170817: Measurements of Neutron Star Radii and Equation of State'. *Physical Review D* **93**(2):023001.

P. W. A. Roming, et al. (2005). 'The Swift Ultra-Violet/Optical Telescope'. *Space Science Reviews* **120**(3-4):95–142.

P. W. A. Roming, et al. (2009). 'The First Swift Ultraviolet/Optical Telescope GRB Afterglow Catalog'. *The Astrophysical Journal* **690**(1):163–188.

P. W. A. Roming, et al. (2006). 'GRB 060313: A New Paradigm for Short-Hard Bursts?'. *The Astrophysical Journal* **651**(2):985–993.

A. Rowlinson & G. E. Anderson (2019). 'Constraining coherent low-frequency radio flares from compact binary mergers'. *Monthly Notices of the Royal Astronomical Society* **489**(3):3316–3333.

A. Rowlinson, et al. (2016). 'Limits on Fast Radio Bursts and other transient sources at 182 MHz using the Murchison Widefield Array'. *Monthly Notices of the Royal Astronomical Society* **458**(4):3506–3522.

A. Rowlinson, et al. (2014). 'Constraining properties of GRB magnetar central engines using the observed plateau luminosity and duration correlation'. *Monthly Notices of the Royal Astronomical Society* **443**(2):1779–1787.

A. Rowlinson, et al. (2019). 'LOFAR early-time search for coherent radio emission from GRB 180706A'. *Monthly Notices of the Royal Astronomical Society* **490**(3):3483–3492.

A. Rowlinson, et al. (2013). 'Signatures of magnetar central engines in short GRB light curves'. *Monthly Notices of the Royal Astronomical Society* **430**(2):1061–1087.

A. Rowlinson, et al. (2010). 'The unusual X-ray emission of the short Swift GRB 090515: evidence for the formation of a magnetar?'. *Monthly Notices of the Royal Astronomical Society* **409**(2):531–540.

A. Rowlinson, et al. (2020). 'LOFAR early-time search for coherent radio emission from Short GRB 181123B'. *arXiv e-prints* p. arXiv:2008.12657.

A. Rowlinson, et al. (2021). 'LOFAR early-time search for coherent radio emission from short GRB 181123B'. *Monthly Notices of the Royal Astronomical Society* **506**(4):5268–5277.

M. A. Ruderman & P. G. Sutherland (1975). 'Theory of pulsars: polar gaps, sparks, and coherent microwave radiation.'. *The Astrophysical Journal* **196**:51–72.

M. A. Ruderman, et al. (2000). 'A Central Engine for Cosmic Gamma-Ray Burst Sources'. *The Astrophysical Journal* **542**(1):243–250.

A. Sagiv & E. Waxman (2002). 'Collective Processes in Relativistic Plasma and Their Implications for Gamma-Ray Burst Afterglows'. *The Astrophysical Journal* **574**(2):861–872.

T. Sakamoto, et al. (2011). 'The Gamma-Ray Burst Catalog Obtained with the Gamma-Ray Burst Monitor Aboard BeppoSAX'. *The Astrophysical Journal Supplement* **195**:2.

T. Sakamoto, et al. (2019). 'GRB 191004A: Swift-BAT refined analysis'. *GRB Coordinates Network* **25953**:1.

O. S. Salafia, et al. (2020). 'Gamma-ray burst jet propagation, development of angular structure, and the luminosity function'. *Astronomy and Astrophysics* **636**:A105.

R. Salvaterra (2015). 'High redshift Gamma-Ray Bursts'. *Journal of High Energy Astrophysics* **7**:35–43.

S. Sanidas, et al. (2019). 'The LOFAR Tied-Array All-Sky Survey (LOTAAS): Survey overview and initial pulsar discoveries'. *Astronomy and Astrophysics* **626**:A104.

R. Santana, et al. (2014). 'Magnetic Fields in Relativistic Collisionless Shocks'. *The Astrophysical Journal* **785**(1):29.

R. Sari & T. Piran (1999). 'Predictions for the Very Early Afterglow and the Optical Flash'. *The Astrophysical Journal* **520**(2):641–649.

R. Sari, et al. (1999). 'Jets in Gamma-Ray Bursts'. *The Astrophysical Journal Letters* **519**(1):L17–L20.

R. Sari, et al. (1998). 'Spectra and Light Curves of Gamma-Ray Burst Afterglows'. *The Astrophysical Journal Letters* **497**(1):L17–L20.

N. Sarin, et al. (2020). 'Interpreting the X-ray afterglows of gamma-ray bursts with radiative losses and millisecond magnetars'. *Monthly Notices of the Royal Astronomical Society* **499**(4):5986–5992.

P. Scholz, et al. (2016). 'The Repeating Fast Radio Burst FRB 121102: Multiwavelength Observations and Additional Bursts'. *The Astrophysical Journal* **833**(2):177.

A. Sclocco, et al. (2016). 'Real-time dedispersion for fast radio transient surveys, using auto tuning on many-core accelerators'. *Astronomy and Computing* **14**:1–7.

R. Seaman, et al. (2011). 'Sky Event Reporting Metadata Version 2.0'. IVOA Recommendation 11 July 2011.

S. Sekhar & R. Athreya (2018). 'Two Procedures to Flag Radio Frequency Interference in the UV Plane'. *The Astronomical Journal* **156**(1):9.

S. Sett, et al. (2022). 'Searching for pulsars with the Murchison Widefield Array'. *in preparation* .

R. M. Shannon, et al. (2018). 'The dispersion-brightness relation for fast radio bursts from a wide-field survey'. *Nature* **562**(7727):386–390.

D. M. Siegel, et al. (2014). 'Magnetically Driven Winds from Differentially Rotating Neutron Stars and X-Ray Afterglows of Short Gamma-Ray Bursts'. *The Astrophysical Journal Letters* **785**(1):L6.

N. Smith (2014). 'Mass Loss: Its Effect on the Evolution and Fate of High-Mass Stars'. *Annual Review of Astronomy and Astrophysics* **52**:487–528.

A. M. Soderberg, et al. (2006). 'The Afterglow, Energetics, and Host Galaxy of the Short-Hard Gamma-Ray Burst 051221a'. *The Astrophysical Journal* **650**(1):261–271.

M. Sokolowski, et al. (2018). 'No Low-frequency Emission from Extremely Bright Fast Radio Bursts'. *The Astrophysical Journal Letters* **867**(1):L12.

M. Sokolowski, et al. (2017). 'Calibration and Stokes Imaging with Full Embedded Element Primary Beam Model for the Murchison Widefield Array'. *Publications of the Astronomical Society of Australia* **34**:e062.

M. Sokolowski, et al. (2022). 'What is the SKA-Low sensitivity for your favourite radio source?'. *Publications of the Astronomical Society of Australia* **39**:e015.

M. Sokolowski, et al. (2015). 'BIGHORNS - Broadband Instrument for Global HydrOgen ReioNisation Signal'. *Publications of the Astronomical Society of Australia* **32**:e004.

M. Sokolowski, et al. (2021). 'A Southern-Hemisphere all-sky radio transient monitor for SKA-Low prototype stations'. *Publications of the Astronomical Society of Australia* **38**:e023.

E. Sonbas, et al. (2019a). 'GRB 190627A: Swift detection of a burst.'. *GRB Coordinates Network* **24888**:1.

E. Sonbas, et al. (2019b). 'GRB 190627A: Swift detection of a burst.'. *GRB Coordinates Network* **24888**:1.

L. G. Spitler, et al. (2014). 'Fast Radio Burst Discovered in the Arecibo Pulsar ALFA Survey'. *The Astrophysical Journal* **790**(2):101.

L. G. Spitler et al. (2014). 'Probing the Intergalactic Medium with Fast Radio Bursts'. *The Astrophysical Journal* **790**:101.

L. G. Spitler, et al. (2016). 'A repeating fast radio burst'. *Nature* **531**(7593):202–205.

K. Z. Stanek, et al. (2003). 'Spectroscopic Discovery of the Supernova 2003dh Associated with GRB 030329'. *The Astrophysical Journal Letters* **591**(1):L17–L20.

R. L. C. Starling, et al. (2020). 'LOFAR detectability of prompt low-frequency radio emission during gamma-ray burst X-ray flares'. *Monthly Notices of the Royal Astronomical Society* **494**(4):5787–5792.

G. Stratta, et al. (2007). 'A study of the prompt and afterglow emission of the short GRB 061201'. *Astronomy and Astrophysics* **474**(3):827–835.

R. Strausbaugh & A. Cucchiara (2021). 'GRB 210419A: LCO Optical Upper Limit'. *GRB Coordinates Network* **29829**:1.

A. Sutinjo, et al. (2015). 'Understanding instrumental Stokes leakage in Murchison Widefield Array polarimetry'. *Radio Science* **50**(1):52–65.

D. Svinkin, et al. (2017). 'IPN Triangulation of GRB 170827B (short).'. *GRB Coordinates Network* **21735**:1.

N. Swainston et al. (2022). 'MWA Tied-Array Processing IV: A Multi-Pixel Beamformer for Pulsar Surveys and Ionospheric Corrected Localisation'. In preparation.

N. A. Swainston, et al. (2021). 'Discovery of a Steep-spectrum Low-luminosity Pulsar with the Murchison Widefield Array'. *The Astrophysical Journal Letters* **911**(2):L26.

C. A. Swenson & P. W. A. Roming (2014). 'Gamma-Ray Burst Flares: X-Ray Flaring. II.'. *The Astrophysical Journal* **788**(1):30.

N. R. Tanvir, et al. (2013). 'A 'kilonova' associated with the short-duration γ-ray burst GRB 130603B'. *Nature* **500**(7464):547–549.

G. B. Taylor, et al. (1999). *Synthesis Imaging in Radio Astronomy II.*

J. H. Taylor, et al. (1993). 'Catalog of 558 Pulsars'. *The Astrophysical Journal Supplement Series* **88**:529.

A. Tchekhovskoy, et al. (2010). 'Magnetohydrodynamic simulations of gamma-ray burst jets: Beyond the progenitor star'. *New Astronomy* **15**(8):749–754.

S. P. Tendulkar, et al. (2017). 'The Host Galaxy and Redshift of the Repeating Fast Radio Burst FRB 121102'. *The Astrophysical Journal Letters* **834**(2):L7.

The CHIME/FRB Collaboration, et al. (2021a). 'Sub-second periodicity in a fast radio burst'. *arXiv e-prints* p. arXiv:2107.08463.

The CHIME/FRB Collaboration, et al. (2021b). 'Sub-second periodicity in a fast radio burst'. *arXiv e-prints* p. arXiv:2107.08463.

A. R. Thompson, et al. (2017). *Interferometry and Synthesis in Radio Astronomy, 3rd Edition.*

C. Thompson (1994). 'A model of gamma-ray bursts.'. *Monthly Notices of the Royal Astronomical Society* **270**:480–498.

C. Thompson (2017a). 'Giant Primeval Magnetic Dipoles'. *The Astrophysical Journal* **844**(1):65.

C. Thompson (2017b). 'Tiny Electromagnetic Explosions'. *The Astrophysical Journal* **844**(2):162.

D. Thornton, et al. (2013). 'A Population of Fast Radio Bursts at Cosmological Distances'. *Science* **341**(6141):53–56.

P. Thulasiram & H.-H. Lin (2021). 'Narrow-band giant pulses from the Crab pulsar'. *Monthly Notices of the Royal Astronomical Society* **508**(2):1947–1953.

J. Tian, et al. (2022a). 'Early-time searches for coherent radio emission from short GRBs with the Murchison Widefield Array'. *Publications of the Astronomical Society of Australia* **39**:e003.

J. Tian, et al. (2022b). 'High time resolution search for prompt radio emission from the long GRB 210419A with the Murchison Widefield Array'. *Monthly Notices of the Royal Astronomical Society* **514**(2):2756–2768.

S. J. Tingay, et al. (2013). 'The Murchison Widefield Array: The Square Kilometre Array Precursor at Low Radio Frequencies'. *Publications of the Astronomical Society of Australia* **30**:e007.

S. J. Tingay, et al. (2015). 'A Search for Fast Radio Bursts at Low Frequencies with Murchison Widefield Array High Time Resolution Imaging'. *The Astronomical Journal* **150**(6):199.

T. Totani (2013). 'Cosmological Fast Radio Bursts from Binary Neutron Star Mergers'. **65**:L12.

S. E. Tremblay, et al. (2015). 'The High Time and Frequency Resolution Capabilities of the Murchison Widefield Array'. *Publications of the Astronomical Society of Australia* **32**:e005.

E. Troja, et al. (2007). 'Swift Observations of GRB 070110: An Extraordinary X-Ray Afterglow Powered by the Central Engine'. *The Astrophysical Journal* **665**(1):599–607.

C. M. Trott, et al. (2013). 'Prospects for the Detection of Fast Radio Bursts with the Murchison Widefield Array'. *The Astrophysical Journal Letters* **776**(1):L16.

D. Ung, et al. (2019). 'Radiation Efficiency Calculation of the Murchison Widefield Array Using a Power Wave Based Framework'. In *IEEE*, pp. 401–402.

V. V. Usov (1992). 'Millisecond pulsars with extremely strong magnetic fields as a cosmological source of γ-ray bursts'. *Nature* **357**(6378):472–474.

V. V. Usov (1994). 'On the Nature of Nonthermal Radiation from Cosmological Gamma-Ray Bursters'. *Monthly Notices of the Royal Astronomical Society* **267**:1035.

V. V. Usov & J. I. Katz (2000). 'Low frequency radio pulses from gamma-ray bursts?'. *Astronomy and Astrophysics* **364**:655–659.

D. A. Uzdensky & A. I. MacFadyen (2006). 'Stellar Explosions by Magnetic Towers'. *The Astrophysical Journal* **647**(2):1192–1212.

M. P. van Haarlem, et al. (2013). 'LOFAR: The LOw-Frequency ARray'. *Astronomy and Astrophysics* **556**:A2.

J. van Paradijs, et al. (1997). 'Transient optical emission from the error box of the γ-ray burst of 28 February 1997'. *Nature* **386**(6626):686–689.

L. Van Waerbeke & A. Zhitnitsky (2019). 'Fast radio bursts and the axion quark nugget dark matter model'. **99**(4):043535.

H. K. Vedantham, et al. (2016). 'The Fluence and Distance Distributions of Fast Radio Bursts'. *The Astrophysical Journal* **830**(2):75.

P. Veres, et al. (2020a). 'GRB 200325A: Fermi GBM observation'. *GRB Coordinates Network* **27453**:1.

P. Veres, et al. (2020b). 'GRB 200327A: Fermi GBM detection'. *GRB Coordinates Network* **27466**:1.

W. T. Vestrand, et al. (2005). 'A link between prompt optical and prompt γ-ray emission in γ-ray bursts'. *Nature* **435**(7039):178–180.

W. T. Vestrand, et al. (2006). 'Energy input and response from prompt and early optical afterglow emission in γ-ray bursts'. *Nature* **442**(7099):172–175.

A. A. Vlasov (1968). 'Reviews of Topical Problems: the Vibrational Properties of AN Electron Gas'. *Soviet Physics Uspekhi* **10**(6):721–733.

R. C. Walker (1995). 'Practical VLBI Imaging'. In J. A. Zensus, P. J. Diamond, & P. J. Napier (eds.), *Very Long Baseline Interferometry and the VLBA*, vol. 82 of *Astronomical Society of the Pacific Conference Series*, p. 247.

X.-Y. Wang, et al. (2009). 'GRB 080916C: On the Radiation Origin of the Prompt Emission from keV/MeV TO GeV'. *The Astrophysical Journal Letters* **698**(2):L98–L102.

E. Waxman (2017). 'On the Origin of Fast Radio Bursts (FRBs)'. *The Astrophysical Journal* **842**(1):34.

R. B. Wayth, et al. (2018). 'The Phase II Murchison Widefield Array: Design overview'. *Publications of the Astronomical Society of Australia* **35**:33.

R. Weaver, et al. (1977). 'Interstellar bubbles. II. Structure and evolution.'. *The Astrophysical Journal* **218**:377–395.

J. C. Wheeler, et al. (2000). 'Asymmetric Supernovae, Pulsars, Magnetars, and Gamma-Ray Bursts'. *The Astrophysical Journal* **537**(2):810–823.

A. R. Whitney, et al. (1971). 'Quasars Revisited: Rapid Time Variations Observed Via Very-Long-Baseline Interferometry'. *Science* **173**(3993):225–230.

R. Willingale, et al. (2013). 'Calibration of X-ray absorption in our Galaxy'. *Monthly Notices of the Royal Astronomical Society* **431**(1):394–404.

S. E. Woosley (1993). 'Gamma-Ray Bursts from Stellar Mass Accretion Disks around Black Holes'. *The Astrophysical Journal* **405**:273.

S. E. Woosley & J. S. Bloom (2006). 'The Supernova Gamma-Ray Burst Connection'. *Annual Review of Astronomy and Astrophysics* **44**(1):507–556.

S. E. Woosley, et al. (2002). 'The evolution and explosion of massive stars'. *Reviews of Modern Physics* **74**(4):1015–1071.

E. L. Wright (2006). 'A Cosmology Calculator for the World Wide Web'. **118**(850):1711–1715.

H. Xu, et al. (2021). 'FAST detection and localization of FRB20201124A'. *The Astronomer's Telegram* **14518**:1.

M. Xue, et al. (2017). 'A Census of Southern Pulsars at 185 MHz'. *Publications of the Astronomical Society of Australia* **34**:e070.

M. Xue, et al. (2019). 'MWA tied-array processing II: Polarimetric verification and analysis of two bright southern pulsars'. *Publications of the Astronomical Society of Australia* **36**:e025.

S. Yamasaki, et al. (2018). 'Repeating and non-repeating fast radio bursts from binary neutron star mergers'. **70**(3):39.

Y.-P. Yang & B. Zhang (2016). 'Extracting Host Galaxy Dispersion Measure and Constraining Cosmological Parameters using Fast Radio Burst Data'. *The Astrophysical Journal Letters* **830**(2):L31.

J. M. Yao, et al. (2017). 'A New Electron-density Model for Estimation of Pulsar and FRB Distances'. *The Astrophysical Journal* **835**(1):29.

S.-X. Yi, et al. (2016). 'Comprehensive Study of the X-Ray Flares from Gamma-ray Bursts Observed by Swift'. *The Astrophysical Journal Supplement Series* **224**(2):20.

S. A. Yost, et al. (2003). 'A Study of the Afterglows of Four Gamma-Ray Bursts: Constraining the Explosion and Fireball Model'. *The Astrophysical Journal* **597**(1):459–473.

Y.-W. Yu, et al. (2014). 'Implications of fast radio bursts for superconducting cosmic strings'. **2014**(11):040.

Y. W. Yu & Z. G. Dai (2007). 'Shallow decay phase of GRB X-ray afterglows from relativistic wind bubbles'. *Astronomy and Astrophysics* **470**(1):119–122.

B. Zackay & E. O. Ofek (2017). 'An Accurate and Efficient Algorithm for Detection of Radio Bursts with an Unknown Dispersion Measure, for Single-dish Telescopes and Interferometers'. *The Astrophysical Journal* **835**(1):11.

B. Zhang (2014). 'A Possible Connection between Fast Radio Bursts and Gamma-Ray Bursts'. *The Astrophysical Journal Letters* **780**(2):L21.

B. Zhang (2020a). 'Fast Radio Bursts from Interacting Binary Neutron Star Systems'. *The Astrophysical Journal Letters* **890**(2):L24.

B. Zhang (2020b). 'The physical mechanisms of fast radio bursts'. *Nature* **587**(7832):45–53.

B. Zhang, et al. (2006). 'Physical Processes Shaping Gamma-Ray Burst X-Ray Afterglow Light Curves: Theoretical Implications from the Swift X-Ray Telescope Observations'. *The Astrophysical Journal* **642**(1):354–370.

B. Zhang, et al. (2007). 'GRB Radiative Efficiencies Derived from the Swift Data: GRBs versus XRFs, Long versus Short'. *The Astrophysical Journal* **655**(2):989–1001.

B. Zhang, et al. (2016a). 'GRB Observational Properties'. *Space Science Reviews* **202**(1-4):3–32.

B. Zhang & P. Mészáros (2001). 'Gamma-Ray Burst Afterglow with Continuous Energy Injection: Signature of a Highly Magnetized Millisecond Pulsar'. *The Astrophysical Journal Letters* **552**(1):L35–L38.

B. Zhang & P. Mészáros (2004). 'Gamma-Ray Bursts: progress, problems & prospects'. *International Journal of Modern Physics A* **19**(15):2385–2472.

B. Zhang & A. Pe'er (2009). 'Evidence of an Initially Magnetically Dominated Outflow in GRB 080916C'. *The Astrophysical Journal Letters* **700**(2):L65–L68.

B. Zhang, et al. (2009). 'Discerning the Physical Origins of Cosmological Gamma-ray Bursts Based on Multiple Observational Criteria: The Cases of z = 6.7 GRB 080913, z = 8.2 GRB 090423, and Some Short/Hard GRBs'. *The Astrophysical Journal* **703**(2):1696–1724.

B.-B. Zhang, et al. (2016b). 'Synchrotron Origin of the Typical GRB Band Function—A Case Study of GRB 130606B'. *The Astrophysical Journal* **816**(2):72.

B.-B. Zhang, et al. (2011). 'A Comprehensive Analysis of Fermi Gamma-ray Burst Data. I. Spectral Components and the Possible Physical Origins of LAT/GBM GRBs'. *The Astrophysical Journal* **730**(2):141.

C. Zhang, et al. (2020). 'Applying saliency-map analysis in searches for pulsars and fast radio bursts'. *Astronomy and Astrophysics* **642**:A26.

F.-W. Zhang, et al. (2012). 'Revisiting the Long/Soft-Short/Hard Classification of Gamma-Ray Bursts in the Fermi Era'. *The Astrophysical Journal* **750**(2):88.

X.-H. Zhao, et al. (2011). 'The Bulk Lorentz Factors of Fermi-LAT Gamma Ray Bursts'. *The Astrophysical Journal* **726**(2):89.

Y.-C. Zou, et al. (2011). 'A Revised Limit of the Lorentz Factors of Gamma-ray Bursts with Two Emitting Regions'. *The Astrophysical Journal Letters* **726**(1):L2.